DISS. ETH NO 22002

New insights to functional CRF, somatostatin 14, and

β-endorphin aggregation

A thesis submitted to attain the degree of

DOCTOR OF SCIENCES OF ETH ZURICH

(Dr. sc. ETH Zurich)

presented by

NADEZDA NESPOVITAYA

Diploma in Biochemistry, Lomonosov Moscow State University

born on *09.06.1986*

citizen of Russia

accepted on the recommendation of

Prof. Dr. Roland Riek, examiner
Prof. Dr. Paola Picotti, co-examiner

2014

Acknowledgements

I have had many occasions to collaborate and benefit from fruitful and encouraging discussions with Dr. Konstantin Barylyuk. His support and intellectual input to all my projects cannot be overestimated.

I would also like to thank members of the group of Prof. Dr. Massimo Morbidelli for sharing some of their lab equipment.

My sincere thanks also go to Dr. Silvia Campioni. Not only does she share her scientific experience with me, but she also is a great companion during our late stay in the lab, in a bar, on a skating rink, in rowing and cycling classes, and many other places.

I am thankful to Dr. Jason Greenwald, Dr. Silvia Campioni, Marielle Wälti, Viviane Zelenay, Diego Sánchez Carvallo and Riccardo Cadalbert and other members of the biolab in Riek's group for the everyday collaborative work and smooth running of the biolab. I thank Dr. Cédric Eichmann and Dr. Alexander Sobol for guiding me in the world of liquid-state NMR. Not only does Cédric answer all my countless questions regarding NMR, but he also is a fantastic labmate to chat, have a drink or a walk.

I am grateful to Marielle Wälti, who is a very inspiring and motivating person. I enjoy her rowing classes a lot. They help me to be fit and sustain high workload in the lab. Marielle is an amazing teacher, colleague and friend. Kiitos Marielle! Once more, many thanks go to Cédric, who motivates me to lift heavier, push harder, do more reps, who spots me while I am arrogantly attempting to lift as much as he does.

Many thanks to Dr. Erich Meister, Dr. Alice Soragni, Dr. Lei Wang, Viviane Zelenay, Kong Ooi Tan for organizing and running DDR and SDG experiments in the PC practicum.

I deeply appreciate the help of Dr. Konstantin Barylyuk, Marielle Wälti and Dr. Silvia Campioni with proofreading of this thesis and all advices that helped to improve the text. Thanks a lot to Dr. Cédric Eichmann and Kristina Comiotto for translating the abstract into German.

My acknowledgement would not be complete without thanking my husband and my mom for support in the everyday life. I always know I have my family to count on. None of my accomplishments would be possible without you. In particular, I would not have written this thesis without the continuous support and assistance from my husband, Konstantin Barylyuk, who faced so many challenges with me before and during all four years of my PhD.

Abstract

Amyloids are insoluble fibrous protein aggregates that share in common the so-called cross-β sheet structure. Protein depositions found initially in patients with neurological disorders created the bad reputation of amyloids [1]. Although amyloids are very well organized and structured species [1, 2], they were exclusively recognized as products of protein misfolding for a long time [3, 4]. The recent discovery of functional amyloids contradicted this theory suggesting that the β-sheet organization of amyloids can be functional and not just serve as a depot of misfolded proteins [5]. Functional amyloids confer an advantage to their host rather than leading to a pathology or death of the organism [3, 6-11]. Up to date, functional amyloids have been found in various organisms from bacteria to human [7].

Hormone amyloids are unique among other functional amyloids, because their aggregated state is not terminal but intermediate and reversible. Peptide hormones are densely packed as amyloids in secretory granules for storage inside gland tissue cells. Upon triggering, the secretory granules are released into the extracellular environment, where the amyloids must dissociate into monomeric peptides in order to ensure proper signaling. The mechanisms allowing peptide hormones to exist in two distinctly different states and switch between them in a controlled fashion are unknown.

Functional hormone amyloids formed by three peptides distinct in their amino acid sequence, properties, and solution-phase tertiary structure are studied here: (*i*) corticotropin-releasing factor (CRF), which forms an extended α-helix in solution [12] and upon binding to the receptor [13], (*ii*) somatostatin 14 (SS14) – a cyclic peptide characterized by a β-hairpin structure [14, 15], and (*iii*) β-endorphin found in a random-coil conformation in solution [16]. The relationship between the structure of hormone amyloids and their ability to assemble reversibly and disassemble upon secretion is the primary interest of this thesis.

Solid-state nuclear magnetic resonance (ssNMR) spectroscopy is considered the method of choice for determining the high-resolution structure of amyloids. We developed efficient methods for high-yield synthesis of CRF, SS14, and β-endorphin based on heterologous expression of recombinant fusion proteins in bacterial cell culture. The methods afford tens of milligrams of the peptides and are suitable for producing samples uniformly labeled with stable ^{13}C and ^{15}N isotopes for structural studies with

heteronuclear ssNMR. A separate chapter (**Chapter 4**) describes the synthesis method for SS14, which offered additional challenges due to the necessity to form the intramolecular disulfide bridge by chemical oxidation and the need to optimize the nucleotide sequence of the expression vector in order to suppress the synthesis of an unexpected side product.

Determining the high-resolution structure of functional hormone amyloids by ssNMR is no easy endeavor. First steps towards high-resolution structures of CRF and SS14 amyloid fibrils are described in **Chapter 3** and **Chapter 5**, respectively. The morphology of CRF fibrillar aggregates has been studied by electron microscopy (EM) under various fibrillization conditions and at different time points of aggregation. Strong facilitation of CRF amyloid aggregation by heparin has been found. Structural polymorphism of SS14 amyloid fibrils has been revealed by solid-state ssNMR spectroscopy. Based on a 1:1 ratio between the intensities of NMR signals attributed to different polymorphs, an asymmetric dimer has been proposed as an elementary unit of SS14 amyloid. The results indicate that the structure of hormone amyloids may be very sensitive to the experimental conditions used for preparing fibrils, which adds to complexity of the studied phenomenon. Careful selection of aggregation conditions prior to structure elucidation by ssNMR is therefore necessary to ensure biologically relevant, functional structure of fibrils.

Chapter 6 and **Chapter 7** are dedicated to comprehensive studies of the β-endorphin functional amyloid. Various biophysical, biochemical, and molecular biology methods including visualization of fibril morphology by EM, secondary structure determination by ssNMR, a newly developed assay for monitoring aggregation and dissociation kinetics, point mutagenesis, etc., are employed to investigate the molecular mechanism of reversible amyloid formation by β-endorphin. Various factors, such as the presence of salts, osmolytes, sugars, and heparin, have been found to promote aggregation of the peptide. Simple buffer exchange has been demonstrated to be sufficient to induce rapid dissociation of β-endorphin amyloid fibrils. Conversely, heparin has been shown to irreversibly stabilize them, which is attributed to the difference in fibril structure revealed by ssNMR. In all examined salt-induced β-endorphin fibrils, at least three polymorphic forms distinct from the heparin-promoted ones have been found. These observations question the suitability of heparin as biologically relevant aggregation helper molecule in the case of functional hormone amyloids.

In the present work, dynamic assembly and disassembly of a functional hormone amyloid on a relatively short timescale has been demonstrated for the first time.

Aggregation and dissociation rates of β-endorphin showed clear dependence on the ionization state of the peptide. Structural studies of β-endorphin amyloid fibrils obtained in solutions containing polyvalent anions have revealed overall similarity of these fibrils irrespective of anion type or solution pH. Thus, high peptide concentration and efficient neutralization of peptide electrostatic charges by counter-anions are proposed as the major factors triggering amyloid fibril formation, which is reverted by dilution and buffer exchange.

Amyloide sind fibrillenartige Protein Aggregate, die sich durch eine sogenannte Kreuz-β-Blatt-Struktur auszeichnen. Da Proteinablagerungen zuerst bei Patienten mit neurologischen Dysfunktionen gefunden wurden, wurden Amyloide stets mit einer Krankheit assoziiert [1]. Obwohl Amyloide sehr gut organisierte strukturelle Spezies bilden [1, 2], wurden sie für lange Zeit als falsch-gefaltete Protein-Produkte betrachtet [3, 4]. Die kürzlich entdeckten funktionalen Amyloide deuten darauf hin, dass die Kreuz-β-Blatt Organisation funktional sein kann und nicht nur als Depot falsch-gefalteter Proteine dient [5]. Funktionale Amyloide stellen daher ein Vorteil für ihre Wirte dar und führen nicht zwingend zu einer Krankheit oder zum Tod des Organismus [3, 6-11]. Bis zum heutigen Zeitpunkt wurden funktionale Amyloide in verschiedenen Organismen gefunden – von Bakterien bis zum Menschen [7].

Hormone sind einzigartig unter den funktionalen Amyloiden, da ihr Aggregationszustand nicht final sondern intermediär und reversibel ist. Peptid-Hormone sind dicht gepackt wie Amyloide und kommen in den sekretorischen Granula innerhalb der Drüsenzellen vor. Bei Bedarf werden die sekretorischen Granula in die extrazelluläre Umgebung abgegeben wobei sich die Amyloide in monomere Peptide auflösen, um die korrekte Signalinformation bereitzustellen. Der Mechanismus, der das Koexistieren und den Wechsel zweier verschiedener Zustände erlaubt, ist bis dato nicht bekannt.

In der vorliegenden Arbeit wurden funktionale Amyloide anhand dreier Peptide, die sich in der Aminosäuren-Sequenz, deren Eigenschaften und deren flüssig-phasen Tertiär-Struktur unterscheiden, untersucht: (*i*) Corticotropin-Releasing Faktor (CRF) formt sowohl frei in Lösung [12] wie auch in gebundenem Zustand mit dem Rezeptor [13] eine α-Helix; (*ii*) Somatostatin 14 (SS14), ein zyklisches Peptid, charakterisiert durch eine β-Hairpin Struktur [14, 15] und (*iii*) β-Endorphin, das einen nicht gefaltete Zustand in Lösung einnimmt [16]. Das Hauptinteresse dieser Arbeit bilden die Beziehung zwischen der Hormonstruktur und ihrer Fähigkeit sich bei Sekretion reversibel zusammenzufügen und aufzulösen.

Festkörper NMR Spektroskopie wurde verwendet um hochaufgelöste Amyloid-Strukturen zu ermitteln. Wir entwickelten effiziente Methoden für die Synthese grosser Mengen an CRF, SS14 und β-Endorphin, die alle auf der heterologen Herstellung rekombinanter Fusionsproteine in bakteriellen Zellkulturen bestehen. Aus diesen

Methoden resultierten Milligramm Mengen an ^{13}C und ^{15}N markiertem Protein, wie sie in Festkörper NMR für strukturelle Studien nötig sind. Die Synthesen-Methoden für SS14, die eine intermolekulare Disulfid-Brücke durch chemische Oxidation nötig machen und eine Optimierung der Nukleotid-Sequenz des Expressionsvektors voraussetzen damit unerwünschte Nebenprodukte während der Synthese unterdrückt werden, werden separat in **Kapitel 4** beschrieben.

Die Bestimmung hochaufgelöster Strukturen funktionaler Amyloide mittels Festkörper NMR stellen eine grosse Herausforderung dar. Erste Schritte in Richtung hochaufgelöster Strukturen von CRF- und SS14-Amyloid-Fibrillen sind in den **Kapitel 4** und **Kapitel 5** beschrieben. Die Morphologie von fibrillenartigen CRF Aggregaten wurden mittels Elektronenmikroskopie (EM) bei verschiedenen Fibrillisations-Bedingungen und unterschiedlichen Aggregations-Zeitpunkten studiert. Es konnte dabei aufgezeigt werden, dass durch Zugabe von Heparin die CRF Amyloid-Aggregation stark unterstützt wird. Zusätzlich zeigte die Messung von Festkörper NMR Spektren strukturelle Polymorphismen von SS14 Amyloid-Fibrillen. Basierend auf einem 1:1 Verhältnis zwischen den NMR Signalen, die den verschiedenen Polymorphismen zugeschrieben werden konnten, wurde ein asymmetrisches Dimer als elementare Einheit von SS14 Amyloiden vorgeschlagen. Die Resultate weisen darauf hin, dass die Struktur von Amyloid-Hormonen sehr stark von den experimentellen Bedingungen während der Fibrillen-Präparation abhängt und somit die Komplexität der Fragestellung erhöht. Daher ist eine sorgfältig Auswahl von Aggregations-Bedingungen, die biologisch relevante und funktionale Strukturen von Fibrillen garantieren, nötig bevor die Struktur-Bestimmung mittels Festkörper NMR durchgeführt werden kann.

Kapitel 6 und **Kapitel 7** befassen sich mit umfassenden Studien von funktionalen β-Endorphin Amyloiden. Die reversible Amyloid-Bildung von β-Endorphin wurde mittels unterschiedlicher biophysikalischer, biochemischer und molecular-biologischen Methoden wie Fibrillen-Morphologie Bestimmung durch EM, Festkörper NMR Sekundär-Struktur Bestimmung, neu entwickelter Prüfung von Aggregations- und Dissoziation-Kinetik, Punktmutationen usw. untersucht. Dabei wurde herausgefunden dass verschieden Faktoren wie das Vorhandensein von Salz, Osmolyten und Heparin die Peptid-Aggregation beschleunigen. Es wurde herausgefunden, dass das Wechseln von Puffern ausreicht, um eine schnelle Dissoziation von β-Endorphin Amyloid-Fibrillen einzuleiten. Auf der anderen Seite wurde gezeigt, dass Heparin β-Endorphin Amyloid-Fibrillen irreversibel stabilisiert, das durch die unterschiedlichen Strukturen, aufgeklärt

durch Festkörper NMR, begründet werden kann. In allen untersuchten Salz-induzierten β-Endorphin Fibrillen wurden mindestens drei polymorph unterscheidbare Formen, verschieden von Heparin-unterstützten Fibrillen, gefunden. Diese Beobachtungen stellen die Eignung von Heparin als biologisch relevantes Aggregations-Hilfe-Molekül im Falle funktionaler Amyloid-Hormone in Frage.

In der vorliegenden Arbeit wurde zum ersten Mal der dynamische Zusammenbau und Abbau funktionaler Amyloid-Hormone während eines relativ kleinen Zeitintervalls beschrieben. Die Aggregations- und Dissoziationsraten von β-Endorphin sind vom Ionisationszustand des Peptids abhängig. Strukturelle Studien von β-Endorphin Amyloiden in löslichem Zustand, im Vorhandensein von polyvalenten Anionen lassen darauf schliessen, dass die Fibrillen unabhängig von Anion Typ oder pH-Wert der Lösung sich ähnlich sind. Daher wird vorgeschlagen, dass hohe Peptidkonzentrationen und effiziente Neutralisation der elektrostatischen Peptidladungen durch anders geladene Anionen die Hauptfaktoren für die Aktivizirung der Amyloid-Fibrillen-Bildung sind.

Chapter 1

Introduction and background

Amyloid

The term amyloid is 160 years old. It was introduced by the German physician Rudolph Virchow in 1854 for the first time. The specimen of the brain tissue, which had an abnormal microscopic appearance, attracted Virchow's attention. The identification test revealed pale blue staining of the sample upon treatment with iodine, and violet upon the subsequent interaction with sulfuric acid. Virchow erroneously concluded that the studied material was composed of starch and named it amyloid, from Latin *amylum* [17]. Later, experiments of Friedreich and Kekule demonstrated the protein nature of the "amyloid mass" [1].

First amyloid samples were represented by organs and tissues obtained by autopsy of patients afflicted with a variety of clinical symptoms mainly associated with neurology and aging. Initially, it was concluded that amyloids were structurally amorphous. However, polarization light microscopic studies demonstrated that accumulations of amyloids stained by Congo red (CR) exhibited birefringence effect with respect to the orientation of the deposits. Thus, amyloids were assigned to structured species and CR staining became the first criterion of amyloid [1]. With time, more information regarding common properties of different amyloids had been accumulated. The biopsy specimen of patients and model animals with extensive amyloidosis showed wavy bundles of delicate fibrils in the electron microscope. The dimensions of these fibrils were similar among different species, 7-14 nm in width and up to 2 μm in length [18]. Thus, amyloids gained another characteristic feature in common, their fibrillar morphology. Finally, the typical arrangement of amyloid filaments was revealed by X-ray diffraction. The diffraction pattern was photographed when amyloid filaments were oriented parallel and perpendicular to the X-ray beam. The characteristic split of diffraction rings at 4.7 and 9.8 Å was obtained only when the sample was perpendicular to the beam, which gave rise to the term "cross-β sheet" [2].

The following modern definition of the amyloid summarizes all common structural features of these protein aggregates: "an amyloid is an unbranched protein fiber whose repeating structure consists of β-strands that run perpendicular to the fiber axis, forming a cross-β sheet of indefinite length" [8] (**Figure 1.1**).
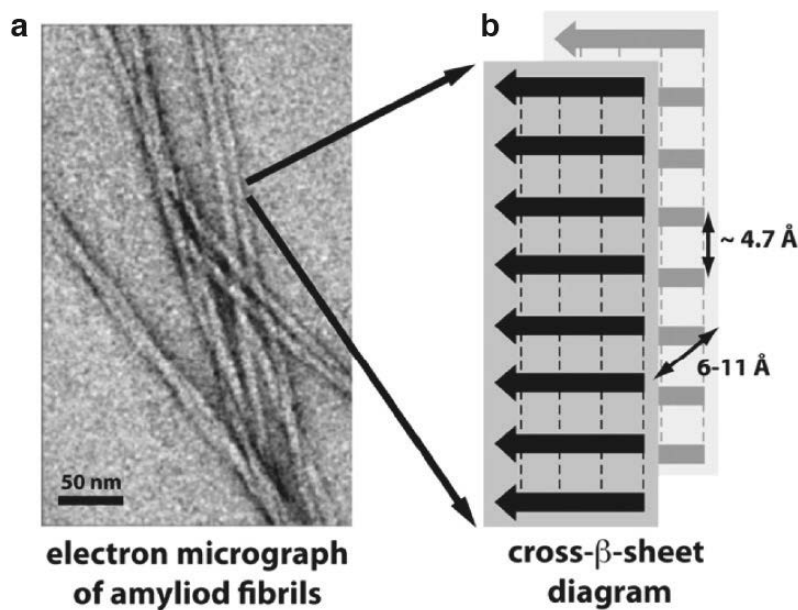
Figure 1.1. Common structural features defining amyloid fibrils. (**a**) Negatively stained transmission electron micrograph of unbranched amyloid fibrils. Scale bar – 50 nm. (**b**) Scheme of cross-β sheets in a fibril. Bold arrows picture β-strands formed by individual protein molecules, dashed lines indicate the backbone hydrogen bonds, double arrows show the characteristic distances in the amyloid fibril determined by X-ray diffraction. Adapted from [8].

Pioneering biochemical studies of amyloid deposits by amino acid sequencing showed that these accumulations were composed of different proteins, which are normally soluble (e.g. immunoglobulin light chains, β2-microglobulin, lysozyme, fibrinogen-α, transthyretin, insulin, etc.). The reason of the transition between soluble functional proteins to disease-associated amyloid deposits was not clear. It was hypothesized that amyloid aggregates served as a trapping depot of misfolded proteins, which were not rescued by the quality control machinery during synthesis [4]. Therefore, the toxicity caused by amyloids was explained by rather mechanical reason: insoluble aggregates, which were resistant to proteolytic clearance, led to the damage of vital organs [1].

Interestingly, soluble proteins bearing different primary sequence, different soluble 3D structure, and different function can adopt similar cross-β sheet conformation upon aggregation. It seems to be a generic feature of polypeptides to adopt an amyloid fold. Numerous studies showing amyloid formation by many peptides and proteins that are not associated with a disease support this idea [19]. The core structure of the fibrils is stabilized primarily by hydrogen bonds involving the polypeptide backbone. Therefore, the similarity in structure among aggregates of polypeptides with different primary sequences can be explained by fixed backbone distances, which are common to all polypeptides. Although the ability to form amyloid seems to be generic for polypeptides,

the propensity to do so can vary considerably [4]. The relative aggregation rates correlate with physicochemical properties of the protein such as charge, secondary structure, and hydrophobicity [20]. Increasing evidence that the amyloid state might be more stable than the functional native state, even under physiological conditions, indicates that the latter may not represent the global minimum on the free energy landscape, but simply be a metastable state separated from the amyloid form by a high activation barrier [21]. Moreover, rising evidence of the toxic effect of many amyloid-related diseases is not associated with fibrillar structures but is rather due to oligomeric precursors [22-24] speaks for the hypothesis that amyloid is a unique protein fold, which serves as a detoxification depot [22]. Due to the fact that amyloidogenic proteins lack sequence or structural homology, it has been hypothesized that amyloids have existed for as long as proteins, and were probably a prominent fold early in the evolution of life [7, 25].

Functional amyloids

In 1997, two prion proteins featuring amyloid structure were identified as potentially functional, the Sup35p from the yeast *Saccharomyces cerevisiae* [26] and HET-s from the fungus *Podospora anserina* [27]. Each of these proteins forms a cytoplasmic amyloid, leading to a particular phenotype that is acquired upon mating and passed from mother to daughter cells upon division. The prion aggregation state and the resulting phenotype are heritable in an epigenetic, non-Mendelian manner. Sup35p is a translation factor that ensures the termination of protein synthesis at stop codons. Aggregation of Sup35p prevents translation termination and results in stop codon read-through, which generates altered proteins leading to emergence of a new phenotype [7, 26]. The HET-s protein can exist in soluble and amyloid form, while HET-S is always soluble. Fusion of the fungus containing HET-s aggregates with another colony bearing soluble HET-S causes the heterokaryon incompatibility reaction. In this reaction, HET-s amyloid induces the transformation of HET-S into β-solenoid structure, which perforates the cell membrane upon interaction [10]. Therefore, the fusion of two fungal strains with different *het*-genes is aborted. The heterokaryon incompatibility reaction is thought to serve as a cellular defense mechanism to prevent viral attacks, different forms of parasitism and preserve genetic individuality of the host organism [28]. Therefore, Sup35p and HET-s proteins do not lead to the host death, but rather ensure proper biological functioning of organisms expressing them.

Many other proteins were identified as functional amyloids conferring an advantage to their host [3, 7, 11]. Bacterial curli are amyloid structures involved in cell adhesion [3]. The *Aplysia*'s cytoplasmic polyadenylation element-binding protein is involved in long-term memory [29], and human Pmel17 protein is responsible for melanosome maturation [30]. Functional amyloids are not a result of protein misfolding, as is the case, for example, in the pathological aggregation of β2-microglobulin or serum amyloid A protein in systemic amyloidosis. Instead, they represent the final functional state of a protein. It is hence fair to divide amyloids into two categories: pathological and functional amyloids [3, 11].

In 2009, a new class of functional amyloid has been discovered: the hormone amyloids [31]. Hormone amyloids are unique, since their aggregated state is not terminal but intermediate and reversible. Interestingly, similar type of behavior has been described 3 years later for low complexity sequence domains of some RNA-binding proteins, such as FUS, TDP-43, etc. These domains form dynamic amyloid structures, so-called hydrogels, when treated with 5-aryl-isoxazol compounds, while their dissociation is triggered by incubation with sodium dodecyl sulfate (SDS) at +37 °C [32]. The authors demonstrated the principle difference between the resistance of prions (Sup35) and hydrogels to the SDS treatment. Notably, some hydrogels such as those formed by the hnRNP A2 protein were dissolved by simple buffer replacement.

Maji et al. [31] demonstrated for the first time that the secretory granules purified from pituitary glands contained amyloids, as revealed by amyloid-specific staining with CR and the characteristic X-ray fiber diffraction pattern [33]. The authors hypothesized that specific aggregation and disaggregation of peptide hormones may be a crucial process without which their sorting, storage, and controlled release upon signaling would not be functional. To test this hypothesis, they screened a broad variety of human peptide hormones for amyloid formation and demonstrated that 35 peptide hormones aggregated in the presence of heparin. The working hypothesis was that hormone amyloids must be capable of assembling and disassembling on relatively short timescales in order to ensure functional signal transduction. However, the measured aggregation and disaggregation kinetics observed in model systems were too slow to be relevant in this context [31].

The hypothesis of functional structured hormone aggregates was already proposed in early 1980-s. Oakley et al. explored over 20 neuropeptides prepared in millimolar concentrations in saline solution under the electron microscope [34]. They found that many hormones were capable of forming unbranched fibrillar structures with a diameter

of 5-7 nm. Combining their finding with the previously obtained X-ray diffraction patterns revealing β-sheet structure of some neurohormonal aggregates, Oakley et al. suggested the possible occurrence of peptide fibrils *in vivo*, because it would explain the maintenance of relatively high neurotransmitter concentrations in synaptic vesicles. Moreover, the ability to form β-sheet structures was proposed to be an important factor determining the interaction of peptides with specific receptor sites. For instance, the regions of potential β-structure in neuropeptide molecules were considered to be important in receptor binding [35].

In summary, it is now evident that the amyloid fold has been selected during evolution for a variety of functions. Multiple examples of functional amyloids utilized for major cellular activities hint that evolution has selected and preserved this structure for physiological purposes [6].

Secretory pathway and hormone sorting

Secretory granules containing hormones appear in the cellular secretory pathway. All cells have secretory pathway to the cell membrane or to lysosomes. Proteins in this pathway are synthesized on polysomes attached to the endoplasmic reticulum (ER) and passed through the ER membrane into its lumen (**Figure 1.2**). In the ER, a polypeptide chain folds and is subjected to co- or post-translational modifications (glycosylation, formation of disulfide bonds, amidation, etc.) [36]. Vesicular and tubular structures transport synthesized proteins further to the *trans*-Golgi network (TGN) via stacks of the Golgi complex (GC). At this point, several kinds of sorting into different vesicles occur leading to lysosome formation and secretion to the plasma membrane. In secretory cells, such as neuroendocrine, exocrine, mast cells, etc., an additional process takes place at the TGN – the formation of secretory granules [37]. These secretory granules can be visualized by antibody staining and/or by electron microscopy [38-40]. The protein concentration in secretory granules is quite high – 50-100 mg/ml [41, 42]. How such a high concentration can be achieved by the cell is a major question of endocrinology [37].
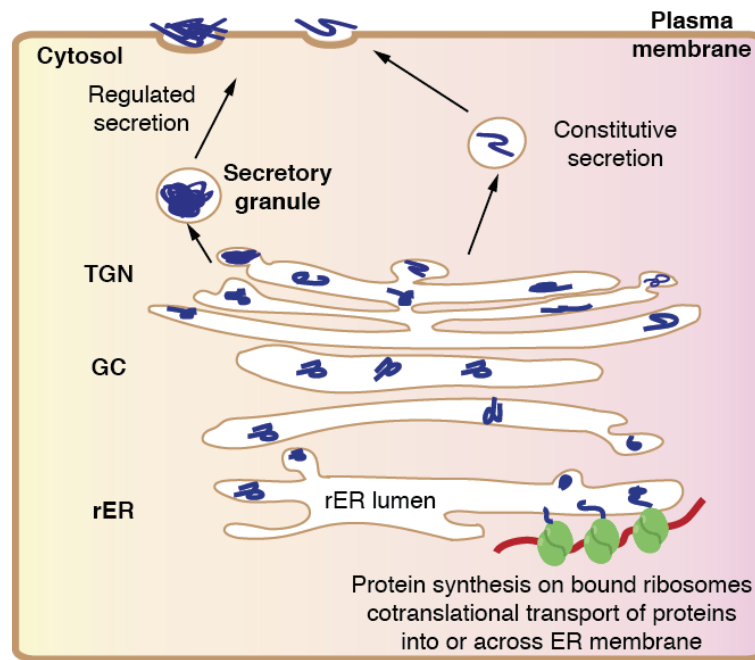
Figure 1.2. Schematic representation of the secretory pathway in a cell. Protein synthesis starts in cytosol and continues in the rough endoplasmic reticulum (rER). A polypeptide chain enters the rER co-translationally and folds. Co- and post-translational modification of a polypeptide can occur in the ER and Golgi complex (GC). In the *trans*-Golgi network (TGN), proteins are sorted for constitutive secretion or densely packed into membrane-enclosed secretory granules for temporary storage. Adapted from [43].

Two models of hormone sorting in the secretory pathway were proposed and corroborated. However, none of them seems to be exclusive.

The first model named "sorting-by-entry" suggests that secreted proteins may be selected and locally concentrated by binding to some putative specific receptors in the TGN membrane, while other proteins are excluded. For example, the amphipathic loop of pro-opiomelanocortin (POMC) was shown to be responsible for hormone sorting. The loop is formed at the N-terminus of the POMC sequence and secured by two disulfide bridges [44]. Carboxypeptidase E, which is involved in the processing of POMC into mature hormones [45], was reported to bind to this loop and promote granule formation [46]. Chromogranin A (CgA) was proposed as a potential candidate for the receptor-mediated sorting of POMC. Exogenously expressed POMC was neither stored nor secreted in a regulated manner in CgA-deficient cells, while overexpression of CgA in an originally CgA- and secretory granule-deficient endocrine cell line restored regulated secretion of transfected POMC [39].

The alternative mechanism suggests that proteins secreted in a regulated manner are sorted passively, while constitutively secreted proteins are actively removed from the protein pool of the TGN lumen by specific interactions with membrane-associated receptors. Thus, this mechanism is referred to as "sorting-by-retention". For example, in

pancreatic β-cells, soluble proinsulin hexamers and an unsorted fraction of lysosomal prohydrolases enter immature secretory granules together. Processing of the prohormone to insulin and C-peptide allows newly synthesized insulin to condense and sequester. In contrast, C-peptide, which remains soluble, shows increased predisposition to escape from maturing granules via the constitutive-like secretory pathway. At the same time, lysosomal hydrolases appear to be pulled out of maturing granules, too [47]. The apparent low selectivity in the "sorting-by-retention" model can be overcome by the structure of aggregate: specific hormone aggregation provides a unique 3D fold, which can be recognized and elongated only by the molecules of the same hormone. In addition, the "sorting-by-retention" mechanism is supported by the fact that none of receptors governing the regulated hormone sorting postulated by the "sorting-by-entry" hypothesis has been identified up to date [47].

Both "sorting-by-entry" and "sorting-by-retention" models agree that hormones are concentrated and aggregate in the TGN, which seems to be extremely important for correct functioning of the secretory pathway. Too early aggregation may cause pathology. For example, aberrant aggregation of vasopressin in the ER has been shown to induce familial neurohypophyseal diabetes insipidus [48]. Vasopressin is a hormone, which regulates water homeostasis by stimulating water reabsorption from the renal collecting ducts [49]. Lack of vasopressin causes diabetes insipidus, which is characterized by the production of large amounts of dilute urine [49]. The hormone is synthesized as a precursor protein. Upon translocation into the ER, the signal sequence is cleaved and provasopressin is glycosylated [50]. The crystal structure of neurophysin II, the carrier protein of vasopressin derived from the same precursor protein [50], with bound vasopressin reveals that vasopressin-neurophysin II folds into a compact globular protein with eight disulfide bonds [51]. Folded prohormone consisting of vasopressin and neurophysin II sequences is exported to the TGN where the mature hormones are proteolytically excised from the complex by prohormone convertases [52] upon sorting into secretory granules. Mutational analysis of provasopressin indicates that its correct folding in the ER is very dependent on structure stabilization by covalent crosslinks between vasopressin and neurophysin II cysteines [48]. Over 60 different pathogenic mutations of the human vasopressin gene have been reported [53]. Newly synthesized mutant precursors form abnormal disulfide-linked homo-oligomers, which turn later into large aggregates visible by light microscopy [48]. Immunogold electron microscopy revealed fibrillar organization of these aggregates. Fibril formation could also be

reproduced *in vitro* using the purified precursor. These findings suggest that dominant neurohypophyseal diabetes insipidus belongs to the group of neurodegenerative diseases associated with amyloid aggregation [48]. It has been hypothesized that the pathology in diabetes insipidus is the result of intrinsic aggregation of vasopressin originally responsible for the sorting of mature hormone, which have not been fully prevented by the proper folding of the precursor molecule. Aggregation of wild-type vasopressin occurs in the TGN, but incorrectly folded mutant aggregates into the amyloid at an earlier stage. These aggregates remain in the ER and lead to cell death [11, 48].

As it is seen from the vasopressin example, the location of hormone aggregation is very important. Inappropriate early hormone condensation causes the fatal disease [48]. This brings up some questions. For instance, why does the hormone aggregation occur specifically in the TGN or secretory granules? What prevents hormone aggregation at early stages of polypeptide transportation from the ER to TGN? Highly conservative conditions preserved in the ER, GC, and secretory granules in different cell types indicate that environmental conditions in these cell compartments play a role in ordered aggregation of maturing hormones. Rising concentration of Ca^{2+} [54] and lowering of the pH [55] along the secretory pathway are considered to be the driving force of the specific hormone aggregation [41, 54, 56-58]. For example, the aggregation of luteinizing and follicle stimulating hormones was stimulated by lowering the pH to mildly acidic condition (pH 6.0-5.0), while $CaCl_2$ promoted the aggregation of POMC [57]. The protective role in aggregation is attributed to precursors of mature hormones [11]. The prohormone sequence of somatostatin was experimentally demonstrated to be necessary for the transportation of the hormone through the GC. The sequence of somatostatin was replaced by the α-globin protein in the prohormone sequence. This chimeric protein was preserved during the transportation form the ER to GC and yielded "mature" α-globin upon naturally occurred enzymatic processing. At the same time, α-globin linked to β-lactamase signal peptide was degraded intracellularly with a half-life of 4-5 min [59]. Additionally, it was hypothesized that molecular crowding effect can minimize protein aggregation in the ER [60]. Therefore, the change of environmental conditions (pH, ionic strength, etc.) can be responsible for the specific triggering of hormone aggregation.

In vivo, hormones are released in response to different stimuli [61-63]. The functional state of a hormone is most often a monomer [64, 65]. Therefore, the hormone aggregation must be reversible [37]. This was experimentally demonstrated *in vitro* for the aggregates of CgA [57] and some human hormones, such as somatostatin 14,

prolactin, β-endorphin, etc. [31]. However, disaggregation kinetics observed in these studies were either not measured [57] or rather slow in the biological context [31].

Carbohydrates and GAGs in amyloid aggregation

The GC is the major site of carbohydrate synthesis. A number of polysaccharides, in particular glycosaminoglycans (GAGs), is produced here [36]. Spatial co-localization of the two processes – polysaccharide synthesis providing high local concentrations of carbohydrates and maturation of secreted protein precursors – hints at the involvement of polysaccharides in the specific protein aggregation occurring in secretory granules [31]. Indeed, it has been demonstrated that transgenic mast cells, which cannot synthesize fully sulfated heparin (an example of GAGs), lack secretory granules and are not able to store appreciable amounts of proteases normally found in the wild-type cell line [66].

GAGs are a heterogeneous group of linear polysaccharides, whose disaccharide building blocks consist of an amino sugar (*N*-acetylglucosamine or *N*-acetylgalactosamine) and an uronic acid (in particular, glucuronic acid or iduronic acid) or galactose (**Scheme 1.1**). Virtually all mammalian cells produce GAGs and after attaching them to a protein core, they secrete proteoglycans into the extracellular matrix, insert them into the plasma membrane, or store them in secretory granules. GAGs present in secretory granules are thought to help sequester and regulate the availability of positively charged components, such as proteases and bioactive amines, through interaction with the negatively charged glycosaminoglycan chains [67]. Secretory granules filled with GAGs are mainly stored in the connective tissue (mast cells, granulocytes, lymphocytes, platelets, etc.), where they are responsible for cell motility, adhesion, cell-to-cell interactions, and providing the scaffold for endothelial cells [67, 68].
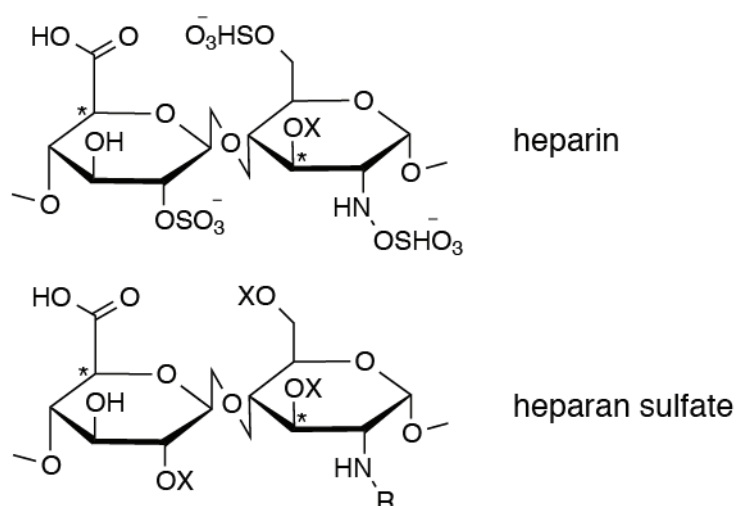
Scheme 1.1. Structures of disaccharide repeating units of heparin and heparan sulfate. Asterisks indicate positions of possible epimerization. X = H or SO_3, R = $COCH_3$ or SO_3. Heparan sulfate is less sulfated (40-60 % $GlcNSO_3$, 0.8-1.8 sulfate:hexosamine ratio) and contains less iduronic acid (30-50 %). Heparin is more sulfated ($\geq$80 % $GlcNSO_3$, 1.8-2.6 sulfate:hexosamine ratio) and contains more iduronic acid ($\geq$70 %) [67].

Nearly all types of amyloid deposits were found to contain heparan sulfate. The latter is believed to promote fibrillogenesis by associating with the amyloid precursors and/or potentially contributing to the conformational change required for their assembly into fibrils [69]. Histological analysis of tissues affected by different amyloid deposits revealed co-localization of amyloid fibrils and sulfated GAGs [70-74] (**Figure 1.3**).
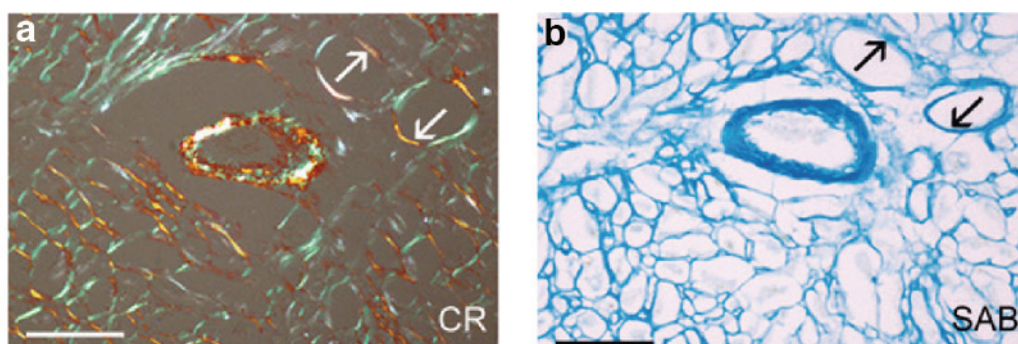
Figure 1.3. Co-localization of heparan sulfate and transthyretin amyloid in the heart affected by cardiomyopathy. (**a**) Myocardial section from a patient with reported cardiomyopathy stained with CR is viewed under polarized light. (**b**) An adjacent section is stained with Alcian blue (specific to GAGs). Arrows in **a** and **b** indicate adjacent locations. CR – Congo red staining. SAB – sulfated Alcian Blue staining. Scale bar – 50 μM. Reprinted from [73].

Extensive studies demonstrated that GAGs, in particular heparin and heparan sulfate, promoted amyloid formation *in vitro* for a variety of amyloidogenic proteins, such as α-synuclein, p25α, and Aβ [75-78]. It should be noted here, that although heparin is synthesized and stored only in mast cells, its structure closely mimics the highly sulfated regions of heparan sulfate [79, 80]. Hence, heparin is often used in *in vitro*

aggregation studies as a suitable model for GAGs [31, 73, 75, 76, 81, 82]. It has been suggested that heparan sulfate is not simply a passive component in amyloid deposits but in fact plays an active role in amyloidogenesis [79]. For example, transgenic mice overexpressing human heparanase, the enzyme which degrades polymeric heparan sulfate into shorter chain length oligosaccharides, in liver and kidney were not susceptible to injections of amyloid protein A fibrils. At the same time, mice in the control group, which did not express the heparanase, developed all symptoms of amyloidosis. Interestingly, those animals that failed to effectively overexpress heparanase remained susceptible to amyloid deposition as well as the wild-type animals [72].

Numerous attempts to identify the mechanism of protein aggregation in the presence of GAGs were made. Nielsen et al. investigated in their work [76] the influence of high molecular weight heparin and its fragments of different length on the aggregation of p25α, the brain-specific protein promoting fibrillization of α-synuclein. They demonstrated that at least ten monosaccharide residue-long heparin chains were necessary to promote p25α aggregation. Moreover, based on isothermal titration calorimetry results, they suggested a model in which the aggregation cascade started by binding of two p25α monomers to one heparin molecule. This core structure served as a template for the subsequent addition of p25α on the heparin molecule, similar to a string of beads.

In another study by Cohlberg et al. [75], fluorescent labeling was used for visualization of heparin localization in mature fibrils of α-synuclein. Amyloid fibrils prepared in the presence of fluorescein-labeled heparin remained fluorescent after repetitive washing steps by hyper- and hypotonic solutions. The authors hypothesized that heparin was intercalated in the amyloid fibril of α-synuclein and argued against the purely catalytic role of heparin in fibril formation.

The stabilization role of GAGs was reported for β2-microglobulin aggregates [83]. GAGs dose-dependently stabilized the β2-microglobulin aggregates preformed at acidic pH in the depolymerization reaction at neutral pH. The extent of protection depended on the degree of GAG sulfation.

The current theory suggests that GAGs act as a "scaffold", inducing or stabilizing amyloidogenic conformations of aggregating proteins by direct association, which then stimulates monomer self-assembly into oligomeric proto-filamentous structures. As multiple filaments arrange into mature fibrils, GAG molecules become incorporated into the fibrils and possibly stabilize inter-protofilament interactions [79].

Motivation of this thesis

The protein folding problem has been in the spotlight of life sciences since formulation of Levinthal's paradox in 1969 [4, 84, 85]. The question how a linear polypeptide chain spontaneously and flawlessly adopts a unique 3D structure with the respective characteristic function and properties has been inspiring researchers in molecular and structural biology and biochemistry for decades and has been the driving force of many discoveries in those fields. The concept of hierarchical folding, or folding funnel that postulates the functional, native state of protein to be at the global minimum of its potential energy landscape seemed to resolve the paradox. The potential energy landscape is encoded by the amino acid sequence [4]. The discoveries of co-translational folding, protein misfolding diseases, and molecular chaperones fit nicely into the framework of folding funnel theory: a nascent polypeptide travels down the potential energy funnel through a series of meta-stable intermediate states by gradually acquiring elements of secondary and tertiary structure and ultimately reaching the unique native structure at the "bottom", unless it is kinetically trapped into some kind of a local minimum. In the latter case, it must either be rescued from the non-native state by chaperones or cleared out from the cell. A failure to do so is often associated with pathology [4].

The discovery of intrinsically disordered proteins on the one hand, and functional amyloids on the other led to a paradigm shift in the protein folding theory. While the former shows that a protein in its native state does not necessarily have a well-defined stable structure, the latter suggests amyloids, which are notorious for being associated with many diseases, to actually be the functional, native state in some proteins. In both cases, it is not clear if the global potential energy minimum is reached by such proteins, and if so – what makes e.g. the amyloid state the global minimum in some cases and the local kinetic trap in the other, especially provided that the amyloid fold is very conservative and seems to be accessible to virtually any protein regardless of amino acid sequence or tertiary structure.

Functional hormone amyloids are remarkable in this context as they are not terminal but intermediate state. The function of hormonal amyloids is temporary storage of hormones within a secretory cell. The very fact that amyloids occur in normal, healthy tissues and organs of a human body and consist of vitally important signaling peptides is astonishing and raises a number of questions:

(i)   What is the structure of functional hormone amyloids?

(ii)   What triggers the aggregation of peptide hormones?

(iii)   What is required to prompt the dissociation of functional hormone amyloids?

(iv)   Are hormone aggregation and dissociation processes spontaneous or do they require additional factors such as catalysts, promoters, stabilizers, etc.?

At present, only experimental finding of amyloid structures inside secretory granules [31] together with the possibility to promote hormone aggregation *in vitro* by adding heparin [31] and some speculative conclusions [34, 37] support the possible functional activity of hormonal amyloids. To ensure proper biological functioning of hormones, hormonal amyloids must be highly dynamic, i.e. be capable of fast assembly and disassembly upon signaling. However, no detailed kinetic characterization of hormone aggregation and disaggregation has been performed so far. Hence, a number of more specific questions need to be addressed in order to understand the nature of functional hormone amyloids:

(v)   What are the differences between hormone aggregates formed under different conditions?

(vi)   Is *in vitro* hormone aggregation indeed reversible?

(vii)   What is the timescale of hormone aggregation and dissociation?

(viii)   What affects the dissociation rate of hormone aggregates?

(ix)   Are GAGs in general, and heparin in particular, essential for hormone aggregation?

Herein, we intent to address the questions above by studying three peptide hormones: corticotropin-releasing factor, somatostatin 14, and β-endorphin. The major goal of this work is to discover the relationship between the structure and dynamic properties of functional hormone amyloids. Among the chosen objects, β-endorphin is the closest to the target, because it is the only peptide hormone for which an atomic model of amyloid fibril structure has been proposed to date. The proposed model allows for hypothesizing a molecular mechanism triggering β-endorphin from amyloid to soluble state, which is tested here experimentally. For the other two peptide hormones, the essential primary steps towards determining the high-resolution structure of their amyloid fibrils including screening of aggregation conditions and morphology characterization *in vitro* are reported here.

Chapter 2

Analytical methods to study protein aggregation

A number of analytical methods is available today for biophysical and biochemical characterization of amyloids. Low- and high-resolution structural methods allow for studying of secondary, tertiary, and quaternary structure of amyloid assemblies [33, 86, 87].

Morphology

Microscopy techniques are the pivotal methods to study biological structures such as cells, their organelles, and macromolecular complexes [88]. High-resolution microscopy has been widely used for morphological characterization of amyloids and their precursors. Moreover, the fibrillar appearance of protein aggregates became a criterion for amyloid identification [33].

Electron microscopy

An image in transmission electron microscopy (TEM) is formed from the electrons transmitted through the electron-transparent specimen [87]. Samples studied by TEM are usually applied onto a metallic grid support coated by a thin, electron-transparent carbon film. Biological macromolecules have nearly the same density as the carbon film, so that unstained samples have a minimal contrast when viewed by TEM. Different techniques can be applied to enhance the contrast. Besides rotary shadowing and cryo-EM, negative staining by uranyl acetate is a commonly used one (**Figure 2.1a**). The contrast enhancement is achieved because uranyl acetate scatters electrons more intensively than macromolecules. The dye covers macromolecules and concentrates in the surface undulations. Thus the TEM image represents a shadow of the real macromolecule, which appears to be a little bigger in size than the real object. In rotary shadowing method, heavy metals are used to cover the specimen, while cryo-EM does not require any staining agents [87]. Negatively stained TEM is widely used to track the aggregation process and characterize individual states of amyloid aggregates from oligomers [89] to mature fibrils [90, 91]. It allows for distinguishing amyloid polymorphs and controlling the predominant structure by variation of fibril growth conditions [9, 90,

92]. TEM has proved to be useful in the studying of mutagenesis effects on the aggregation and fibril morphology [86, 93].
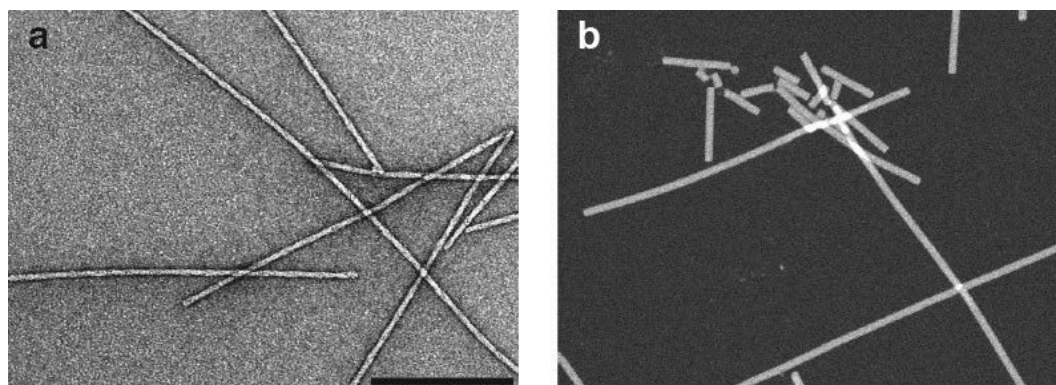
Figure 2.1. Electron micrographs of somatostatin 14 (SS14) fibrils. (**a**) Image of negatively stained SS14 fibrils in TEM. Scale bar – 200 nm. (**b**) Image of unstained SS14 fibrils in STEM.

Scanning transmission electron microscopy (STEM) provides images of unstained samples, which makes it suitable for accurate quantitative mass determination of macromolecular complexes (**Figure 2.1b**). This method was successfully applied in combination with nuclear magnetic resonance (NMR) spectroscopy for structural studies of Aβ polymorphs and provided a body of proof that different fibril morphologies have different underlying molecular structures [90].

Atomic force microscopy

Atomic force microscopy (AFM) provides high-resolution (≤1 nm) images of sample topography. Usually, analyzed samples are adsorbed on atomically flat smooth surfaces, such as mica or gold. A cantilever tip scans the surface of the sample and bends upward upon contact, which is detected by a laser beam focused on the end of the cantilever. The extent of bending is converted to force units by a photodetector. By keeping the force constant while scanning across the surface, the vertical movement of the tip generates the surface contour, which is recorded as the topography map of the sample. AFM has been modified for specific applications and can be used in different modes [87]. For instance, ''tapping mode'' referrers to the oscillation of a stiff cantilever close to the sample. This mode provides good resolution on soft samples and is efficient for investigation of prefibrillar species [94]. Moreover, statistical analysis of high-resolution AFM images in combination with other methods can provide a reconstruction model of the hierarchy of amyloid fibrils assembly [95].

Assembly size and size distribution

Identification of aggregating species and their characterization by size distribution is effectively applied for studying the mechanisms of aggregation. A wide repertoire of methods is available today for such characterization, including electrophoresis in polyacrylamide gel (PAGE) [96], size-exclusion chromatography (SEC) [91, 96], analytical ultracentrifugation [97, 98], dynamic light scattering (DLS) [89, 99], and ion mobility mass spectrometry [100, 101].

Analysis of protein species by PAGE and SEC is technically very simple and inexpensive. PAGE separates molecules by polypeptide charge density, which is usually correlated to the molecular mass of the protein. In SEC, molecules are fractionated based on their hydrodynamic volumes, which reflect molar masses too. However, SEC provides lower resolution than PAGE, and molecular mass estimation can be inaccurate due to high sensitivity of the method to protein conformation (extended vs. globular) [87]. DLS measures temporal fluctuations of the light scattered by solute particles as a function of time. Temporal fluctuations in the intensity of scattered light relate to the rate of Brownian motion, which is correlated to the diffusion coefficient and the radii of particles [87]. DLS has an intrinsic bias for large aggregates because the intensity of scattered light is proportional to the square of particle mass [102]. Analysis of complex aggregation mixtures by DLS is challenging if the shape of the protein is unknown, because the method cannot distinguish oligomers with similar hydrodynamic radii [87].

Tertiary and quaternary structure

Tertiary and quaternary structure of amyloid assemblies is accessible by low-resolution methods such as electron paramagnetic resonance (EPR), hydrogen-deuterium exchange (HDX), limited proteolysis, and by fluorescence spectroscopy.

The physical basics of EPR are similar to NMR, but while NMR measures the signal of atomic nuclei, EPR detects the signal from electrons. Unpaired electrons are usually not found in biological samples. Therefore, EPR measurement requires the introduction of a spin label [87]. EPR spectroscopy is capable of measuring inter- and intramolecular distances in protein aggregates, which can be utilized for structure investigation, as well as for the determination of ordered and less ordered segments within the amyloid fibrils [103].

HDX is a reaction in which labile hydrogen atoms are substituted by deuterium atoms [87, 104-109]. The rate of exchange is a parameter, which is used to distinguish solvent exposed and protected regions of the protein. HDX can be performed on monomeric proteins [110] as well as on oligomers [111] and mature amyloid fibrils [104-106]. The exchange is usually performed upon transferring of the sample into a deuterated solvent. Prior to analysis, the reaction must be quenched, which is achieved by acidification and lowering the temperature of the mixture [107]. The products of exchange process can be monitored either by NMR spectroscopy or by mass spectrometry (MS). Liquid-state NMR analysis of HDX on amyloid fibrils requires fibril dissolution, which is usually achieved by the dilution of the sample in aprotic solvents, such as dimethyl sulfoxide (DMSO) or hexafluoro-2-propanol (HFIP) [105, 112]. Upon substitution of protons to deuterons the corresponding proton signals reduce their intensity or completely disappear from the NMR spectra. Provided that the resolution of acquired spectra is high enough, this approach may yield information for every amino acid residue of the polypeptide [104-106, 108]. For instance, high resolution of HMQC spectra in HDX experiments performed on Aβ amyloid fibrils made a great contribution to the determination of their 3D structure [106]. Although HDX-MS usually cannot provide information regarding the exchange rate of every particular residue, it is capable of distinguishing populations exchanged to a different extent and does not average them out. This advantage was utilized in studying of Aβ fibrils at equilibrium and allowed to identify the natural exchange of monomers between fibrils and solution [113]. Moreover, MS analysis is more sensitive, requires less material and has high potential for automation [107, 112].

Limited proteolysis is a complementary method to HDX. It provides information on structural domains of the protein aggregates, flexible and surface-exposed domains. Common proteases used in this method have either low specificity or very short recognition sequences, to ensure the cleavage in the available sequence. Limited proteolysis is usually coupled with LC-MS, which guarantees low sample consumption and high specificity of identified primary sequences [87].

Fluorescence spectroscopy is another tool for monitoring protein aggregation. Changes in the microenvironment of aromatic amino acid residues (Trp, Tyr, Phe) affect their intrinsic fluorescence, which allows tracking the aggregation *in vitro* [114-116]. In addition, a broad variety of fluorescent dyes available for protein labeling opens the possibility to detect aggregation by fluorescence resonance energy transfer (FRET)

in vitro [117] and *in vivo* [118], or visualize the process of fibril growth by optical super-resolution microscopy techniques [119].

Secondary structure

One of the characteristic features of amyloid is the regular β-sheet structure. To identify a protein aggregate as an amyloid, this secondary structure element must be detected by any biophysical or biochemical method [33].

Spectroscopic methods

Circular dichroism (CD) spectroscopy measures differential absorption of circularly polarized light by chiral molecules as a function of wavelength. CD measurement performed in the far ultraviolet (UV) range (180-250 nm) provides information on the secondary structure of the peptide backbone. Every secondary structure has a fingerprint CD spectrum with characteristic maxima and minima [120]. The phenomenon of protein aggregation accompanied by massive formation of β-sheet structure can be detected by the appearance of an absorption minimum at 215-218 nm in the far-UV CD spectrum [121]. CD is typically used for qualitative determination of the nature of amyloid assemblies and kinetics of conformational transitions taking place during aggregation. Fine details, such as the orientation of β-sheets within monomers (parallel or antiparallel) cannot be determined from CD data. An advantage of CD relative to other methods for determination of secondary structure is its tolerance to a wide range of pH and temperature [87]. For example, low pH compromises the binding of dyes, such as CR and ThT, to amyloid fibrils rendering the detection of β-sheet formation with these dyes difficult at acidic pH [87]. In contrast, CD measurement is not affected by low pH and is effective in detection of secondary structure transitions upon lowering the pH down to two [114, 122].

Infrared spectroscopy (IR) is complementary to CD. It is capable of providing quantitative information for studying secondary protein structure. Absorption bands in IR spectra reflect vibrations of C=O, C-N, and N-H bonds of the peptide backbone, which is used for the determination of the type of secondary structure [87].

Diffraction and scattering methods

In contrast to X-ray crystallography requiring high-quality single crystals, X-ray fiber diffraction is executed on pulverized or lower quality crystalline samples. X-ray

diffraction patterns of almost all amyloid fibrils exhibit meridional reflections at ~4.7 Å. This is an indicator of the β-sheet structure in which β-strands are arranged perpendicular to the fibril axis (cross-β arrangement). Broad equatorial reflections at ~10 Å vary depending on the side-chain composition of the aggregating peptide or protein (**Figure 2.2**).
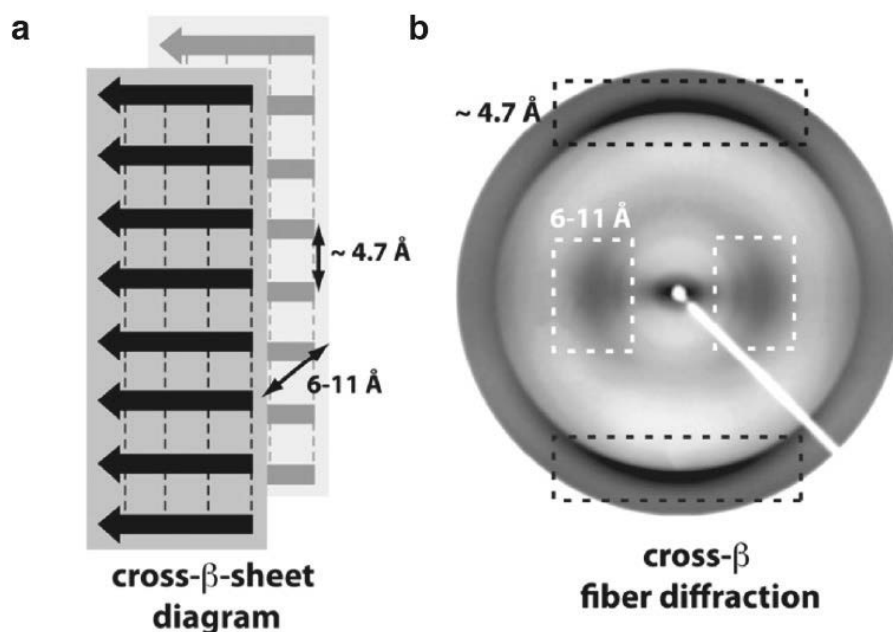
Figure 2.2. Characteristic distances in the amyloid structure can be determined by X-ray fiber diffraction. (**a**) Schematic diagram of the cross-β sheets in a fibril. Dashed lines represent the backbone hydrogen bonds. Double arrows indicate the repetitive spacings that give rise to the characteristic X-ray diffraction pattern. (**b**) A typical fiber diffraction pattern of amyloid aggregates with a meridional reflection at ~ 4.7 Å (black dashed box) and an equatorial reflection at ~ 6-11 Å (white dashed box). Adapted form [8].

Neutron scattering is used, often in combination with X-ray diffraction techniques, to study the structure of amyloid fibrils. Neutrons scattered from nuclei can be used to detect protons, which cannot be detected by X-ray. This helps assigning hydrogen-bond patterns in 3D structures of macromolecules and investigating strand orientation (parallel or antiparallel) in amyloid fibrils [87].

Staining techniques

Detection of amyloids by staining techniques is relatively simple and has been applied in diagnostics [123], *in vitro* [124], and *ex vivo* [73]. The most common dyes for amyloid detection include Congo red (CR) and thioflavin-type dyes (such as thioflavin T, ThT, and thioflavin S, ThS) (**Scheme 2.1**).
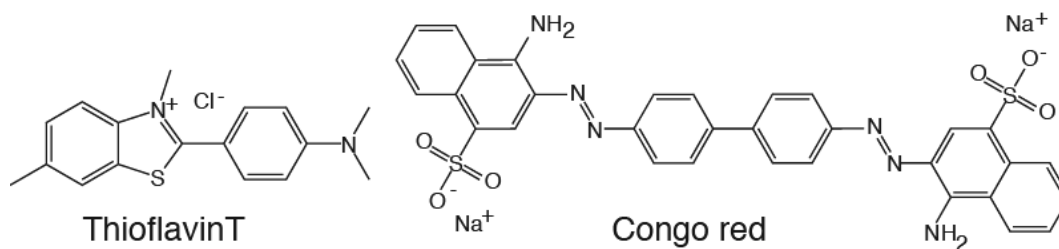
Scheme 2.1. Chemical structure of amyloid-specific dyes, thioflavin T and Congo red.

CR staining is commonly used for the visualization of amyloid in tissue sections [1, 17, 125]. The maximum of CR absorption shifts from 490 to 540 nm upon binding to an amyloid, which enables spectroscopic detection of amyloid formation. Another unique feature of CR is its ability for birefringence. Birefringent substances transmit light polarized in one plane at a faster velocity than that polarized perpendicularly, providing different refractive index in different directions. An incident linearly polarized light wave splits into two orthogonal vectors that have slightly different optical path in a birefringent sample. One passes through the material along the axis with the higher refractive index, or slow axis, and the other runs along the fast axis. When the vectors reach air again, they recombine into one wave, but one vector has been retarded behind the other. Instead of oscillating in only one plane, which is linear polarization, the tip of the combined wave now traces out an ellipse. This elliptical polarization means that some light is in the plane of the crossed analyzer, and can be transmitted, which makes the sample appearance bright against the dark background (**Figure 2.3**). No birefringent effects occur if the low and the fast axes are parallel and perpendicular to the polarized light, because the wave of polarized light does not give two vectors upon entering the sample in this case. CR molecules should be spatially oriented on amyloid fibrils to make the dye birefringent and allow it to produce elliptically polarized light [125-127].
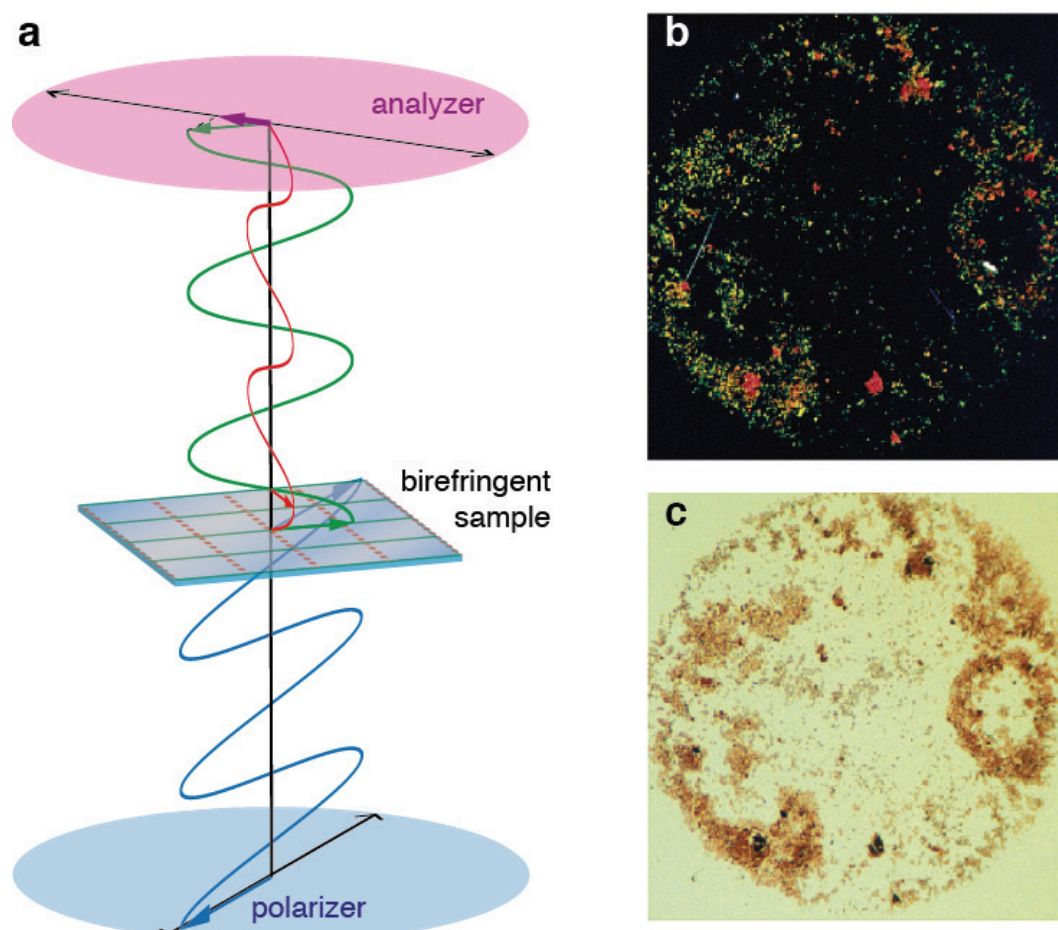
Figure 2.3. The effect of CR birefringence upon binding to amyloid. (**a**) Physical principle of birefringence. Polarized light (blue wave, blue arrows) comes from the polarizer (blue ellipse). Upon entering the birefringent sample, the wave of linear polarized light splits into two vectors passing through slow (high refractive index; shown by red dashed lines) and fast (low refractive index; shown by solid green lines) axes of the sample. At the exit from the sample plane, tips of the two vectors oscillating out of phase (green and red) point elliptical trace (not shown), which corresponds to elliptically polarized light. A fraction of elliptically polarized light (purple arrow) is transmitted at the plane of crossed analyzer (pink ellipse). This leads to bright appearance of birefringent material on the dark background, as shown in **b**. Crossed polarizer and analyzer means that the angle between their axes equals to 90°. (**b**) Aggregates of β2-microglobulin C-terminal fragment viewed under cross-polarized light. (**c**) Aggregates of β2-microglobulin C-terminal fragment viewed in the bright field, i.e. when the axes of polarizer and analyzer are parallel. Images in **b** and **c** are reprinted with permission from [128]. Copyright 2003 American Chemical Society.

The mechanism of CR binding to amyloid fibrils is poorly understood. One hypothesis says that the dye intercalates in between β-strands parallel to the peptide chains and perpendicular to the fibril direction. Alternatively, binding may occur on the fibril surface such that the dye's axis is parallel to the fibril [87, 129]. For instance, it was demonstrated for the HET-$s_{218-289}$ protein that CR interacts with the groove on the fibril surface formed by positively charged amino acid residue side chains. Point mutation disrupting this groove did not change the overall amyloid structure of HET-$s_{218-289}$, which

was confirmed by ssNMR, while the aggregates observed under EM as fibrillar species did not exhibit birefringence upon staining by CR anymore [129].

Application of CR in amyloid formation studies is limited due to its ability to inhibit protein aggregation to a certain extend [130, 131]. Therefore, CR is mainly applied for the detection of already formed aggregates.

ThT is another dye widely used in amyloid aggregation studies. ThT molecules have both polar and nonpolar functional groups (**Scheme 2.1**) and can therefore form micelles in aqueous solutions with the critical micelle concentration (CMC) around 4 μM. ThT binding to β-sheet structures results in fluorescence enhancement relative to unbound ThT [132]. In the free state, the excitation and emission maxima of ThT occur at 342 and 430 nm, respectively. Upon binding to amyloid aggregates, the excitation and emission maxima undergo a bathochromic shift to 442 and 482 nm, respectively [133].

Enhanced ThT fluorescence can be observed by fluorescence microscopy or by fluorescent spectroscopy. The ideal concentration of the dye for spectral measurements and staining is above its CMC [134]. Similar to CR, there is no consistent theory regarding the binding mechanism of ThT to amyloids. Some researchers suggest that ThT binds along β-strands in amyloid fibrils [135]. Others argue that ThT binding is not β-sheet-specific but requires certain spatial orientation of negative charges on the polymer surface [134]. Moreover, the increase of ThT fluorescence in the presence of DNA [136] supports the latter hypothesis. Nevertheless, the pronounced difference in ThT fluorescence between monomeric and amyloid protein states [137] and confirmed minimal influence of ThT on amyloid aggregation kinetics [138, 139] make this dye very attractive for everyday use in amyloid aggregation studies. For example, ThT has been used to study fibril formation for a number of amyloidogenic proteins, including Aβ, insulin, lysozyme, α-synuclein, and β2-microglobulin [94, 137, 140, 141].

The aggregation profile monitored by ThT is typically a sigmoidal curve consisting of three different intervals. The first interval is called the lag-phase, in which β-sheet structures are absent or not abundant enough to afford ThT fluorescence above the baseline level. Next is the exponential growth interval, when the extensive fibril growth leads to nearly exponential increase in ThT fluorescence. Eventually, the plateau phase denoting fibril maturation is observed [33, 87, 140]. Typically, as the fibrils mature, lateral association of the individual filaments partially precludes ThT binding sites, resulting even in lowering of the fluorescence intensity [87].

Unlike ThT, ThS is not a unique chemical – instead, it is a mixture of compounds that results from several consecutive reactions of the primulin molecule (precursor). Binding to amyloid fibrils enhances the emission intensity of ThS several-fold with no change in the excitation or emission spectra [133]. Unfortunately, poor reproducibility of ThS composition and high background fluorescence in solution make this dye unsuitable for quantitative analysis in solution [133].

Recently, a new class of amyloid-specific dyes has become available. Luminescent conjugated probes (LCPs) proved to be effective in amyloid detection [142]. Depending on the protein conformation, different emission spectra of LCP can be observed. The intensity and maximum of LCP fluorescence emission change upon binding to amyloid fibrils. Hence, a specific optical fingerprint can be obtained for the β-sheet-containing amyloid aggregates. Furthermore, the process of fibril formation can be monitored over time by plotting the ratio of emission peak intensities at the wavelengths characteristic to monomer and mature amyloid. The obtained kinetic plots show a lag-phase, followed by a growth phase and a plateau, similar to kinetics detected by CR absorbance or ThT fluorescence [143].

Structure at the level of atomic resolution

At present, there are only two methods of structural biology providing information about structural organization of amyloids at the level of atomic resolution: NMR spectroscopy and X-ray crystallography [86, 87].

NMR spectroscopy

Structure determination by NMR is based on the magnetic properties of atomic nuclei comprising molecules. The nuclei most frequently used in structure determination of biological molecules include ^{1}H, ^{13}C, ^{15}N, and ^{31}P. NMR phenomenon occurs when nuclei with nonzero spin quantum numbers are placed in a magnetic field and subjected to radio-frequency irradiation. This absorbed and re-emitted radiation is recorded as the resonance signals. The resonance signals and their characteristics, such as chemical shift, line width, *J*-coupling, cross-peaks, and nuclear Overhauser effect (NOE), are sensitive to the nuclear environment and can be used for 3D structure determination. Two groups of NMR techniques represented by liquid-state and solid-state NMR (ssNMR) are available for structure determination. Their major difference is highlighted in their names. While liquid-state NMR spectroscopy deals with soluble peptides and small proteins (< 60 kDa),

ssNMR works with insoluble noncrystalline molecular systems, which are not suitable for investigation by liquid-state NMR and X-ray crystallography [87, 144].

Polypeptides and proteins are relatively long polymers comprised of repetitive units, amino acid residues, rendering the interpretation of 1D spectra difficult due to significant overlap of signals. This problem can be overcome by the introduction of additional spectral dimensions, which correlate two or more different experimental parameters. Multidimensional NMR experiments used in structural studies utilize correlations between different features of the same type of nucleus (homonuclear multidimensional NMR) or among different nuclei (heteronuclear multidimensional NMR) [87, 144].

Liquid-state NMR is useful for studying amyloidogenic peptide and protein monomers, but when the monomers aggregate into oligomers, the signals become broader and eventually disappear due to the increase in tumbling time [145], which makes structural investigation of aggregation-prone proteins by liquid-state NMR challenging. High protein concentrations typically used in NMR samples contribute to this issue, too, by promoting aggregation further. Nevertheless, changes in spectroscopic features, such as chemical shift, line width, cross-peaks, and NOE can be used to monitor the transition from monomer to oligomers [145, 146]. 2D NMR spectroscopy is widely used to study protein folding, including the formation of secondary structures and long-range interactions between different regions [147]. NOE signal intensity, J-coupling constants, and chemical shift data are useful for calculating distances and torsion angles of correlated atoms [87, 148, 149]. In summary, only primary aggregating species and early transitions of aggregation can be detected by liquid-state NMR.

Nowadays, ssNMR is the most powerful tool to obtain 3D structure of amyloid fibrils. Implication of ssNMR made structural studies of many amyloidogenic proteins possible. For instance, ssNMR measurements of amyloid aggregates of $A\beta_{1-40}$ [150], transthyretin [151], and fragments of the prion protein HET-s [152] and β2-microglobulin [153] yielded 3D structures. While the determination of the 3D structure is still highly demanding, site-specific secondary structures can be determined from the $^{13}C\alpha$, $^{13}C\beta$ and ^{13}CO chemical shifts quite straightforward [154, 155].

While providing detailed information about the amyloid structure at the atomic level, ssNMR does not see relatively long-distance interactions. Thus the spatial arrangement of filaments within the mature fibril cannot be deduced from ssNMR data [87]. Another, more technical disadvantage of ssNMR spectroscopy is its requirement of

isotopically labeled protein, typically several tens of milligrams [156], which makes this approach for structure determination costly and time-consuming, especially when the sample production method does not easily provide sufficient amounts of protein. Nonetheless, ssNMR incredibly advances structural studies of amyloid aggregates and, in combination with low-resolution structural methods, can deliver new 3D structures [87, 106, 150].

X-ray crystallography

X-ray crystallography examines atomic structures of crystals using diffraction patterns of X-ray radiation directed at homogeneous single crystals in which molecules exist in highly ordered repetitive units [87, 157]. Repetitive patterns within crystal amplify the diffraction signals, which are collected and converted into 3D electron-density map. From these maps positions of atoms are deduced, which in combination with complementary chemical information provide the basis for 3D models of molecular ensembles. The quality of X-ray crystallographic data strongly depend on the regularity of the studied structure.

Although amyloids consist of periodically repeated molecules, presumably in the same conformation, they do not crystallize easily. Amyloid filaments form only partly ordered structures, and the standard methods of crystal structure analysis are therefore not applicable due to the high degree of heterogeneity and large number of overlapping reflections in amyloid samples [87]. However, fibril diffraction can be performed for the analysis of the secondary structure and reveal the characteristic diffraction pattern at 4.7 and 6-11 Å specific to cross β-sheet structure of amyloid [8, 31, 108] (**Figure 2.2**). X-ray crystallography has been mainly used to determine crystal structures of aggregating proteins in their stable non-amyloid state, or fibrillar aggregates comprised of the fragments of amyloidogenic proteins [158, 159]. In several particular cases, amyloidogenic peptides were co-crystallized with small molecules inhibiting aggregation [160, 161] or in antigen-antibody complexes [162, 163].

Investigation of X-ray diffraction patterns of microcrystals formed by short peptide segments of amyloidogenic proteins (e.g. Aβ, myoglobin, lysozyme, β2-microglobulin, etc.) revealed features, which were common for all obtained structures [164]. β-sheets were aligned along the microcrystal (fibril) axis and supported by hydrogen bonding of peptide backbones. Every β-sheet was composed of extended strands perpendicular to the fibril axis. Two sheets contacted tightly via a completely free

of water, dry interface. At this interface, the residue side chains intermeshed with close complementarity, forming a "steric zipper". Layers of "steric zippers" repeated along the fibril axis. However, the relative orientation of individual peptide units, for example, parallel vs. anti-parallel, face-to-face vs. face-to-back, was different in different fibrils, which gave rise to eight distinct classes of "steric zippers". Finally, Sawaya et al. [164] suggested that in fibrils formed by full-length proteins, regions that were not involved in the fibril core formation could even retain native-like conformation on periphery. However, the question to which extend the concept of "steric zippers" can be applicable to the amyloids occurring in nature is still open.

Another X-ray technique, X-ray absorption spectroscopy (XAS), provides information on the local environment and electronic state around heavy atoms in biomolecules. One of the XAS methods called extended X-ray absorption fine structure is particularly useful for studying interactions between an amyloid and metal ions [87, 165]. Many studies report on the potential involvement of transition metal ions in aggregation process [115, 166, 167]. Therefore, this technique may shed the light on the structural aspects of amyloid-metal ion complexes at the level of atomic resolution.

Chapter 3

Exploring the aggregation of corticotropin-releasing factor[1]

Introduction

Corticotropin-releasing factor (CRF), also known as corticotropin-releasing hormone, is a 41 amino acid residue-long polypeptide discovered in 1981 by Vale et al. [168]. This hormone is produced in the brain, hypothalamus, pancreas, stomach, and lymphocytes, but the receptors for CRF were found in a fewer number of tissues [169]. CRF is the major regulator of secretion of ACTH, β-endorphin, and other derivatives of pro-opiomelanocortin (POMC) [168, 170]. CRF is the predominant peptide responsible for the activation of hypothalamo-pituitary-adrenal axis (HPA axis) regulating the stress response. Besides the integration of hormonal cascades in neuroendocrine system (HPA axis), CRF is found to be a key element in autonomic, immunological, and behavioral responses of mammalian organisms to stress. In reproductive system, by lowering the level of luteinizing hormone, high concentrations of CRF inhibit ovulation and disrupt pregnancy, which is also a feedback reaction to stress. On top of that, inappropriate activity of CRF neurons may manifest itself in a number of psychiatric illnesses including affective disorder, anxiety disorders, anorexia, and Alzheimer's disease [169]. Therefore, CRF stands on the top level in hormone hierarchy. It governs diverse hormonal networks in mammalian organisms and coordinates the joint body response to stress [62, 169].

CRF is synthesized from a high-molecular-weight precursor, named prepro-CRF [171]. During its synthesis, intracellular sorting and packaging, this hormone undergoes several steps of co- and post-translational modifications, including specific proteolysis. The first cleavage results in co-translational removal of the signal peptide by a peptidase that is present in all cell types. At a later stage, additional proteolysis occurs at pairs of basic amino acid residues and releases CRF with additional Gly-Lys motif at the C-terminus serving as a template for subsequent amidation [172, 173]. C-terminal amidation of CRF [174] is extremely important for its biological activity [61]. Fully mature peptide is stored in secretory granules until secretion is stimulated by a specific signal [175].

---

[1] ESI-MS analysis was done by Konstantin Barylyuk from the group of Prof. Renato Zenobi (LOC, ETH Zurich, Switzerland).

Romier et al. in 1993 solved the structure of human CRF in solution by ^{1}H NMR [12]. The proposed structure comprised of disordered N-terminal and C-terminal parts and an amphipathic α-helix between residues 6 and 32. Strong correlation between the increased α-helical propensity of the human CRF, as well as its higher affinity to the receptor relative to the ovine CRF [176], and the alanine scan data [61] suggested the responsibility of a central α-helical domain for CRF binding to the receptor. However, NMR data did not allow Romier et al. to propose a unique conformation for the C-terminus [12], which can be presumed from the importance of C-terminal amidation of CRF for its biological activity [61]. Later, crystallographic studies of the CRFR1 receptor in the complex with the CRF$_{22-41}$ fragment as a ligand demonstrated that CRF$_{22-41}$ adopted a continuous α-helical conformation and docked in a hydrophobic core of the extracellular domain of the receptor [13]. Combined together with the solution structure of the full-length peptide, these data demonstrate a high predisposition of CRF to adopt α-helical structures in the free state in solution and when bound to the receptor [12, 13]. The current view of CRF structure suggests that CRF can be divided into two functional parts: residues 4-8 have been found essential for receptor recognition, while residues 9-41 have been identified to be responsible for binding and exertion of action [177].

Optically dense secretory granules storing CRF have been observed in multiple histological studies [178-181]. This high-density packing of CRF has never been associated with a specific peptide fold. Maji et al. [31] reported amyloid formation by CRF for the first time. They described the ability of human, rat, and ovine CRF to form amyloid structures in the presence and absence of heparin, which was confirmed by ThT and Congo red staining, EM, and CD data. The authors suggested that amyloid aggregation of CRF was indeed functional. Amyloid formation allowed for dense packing of CRF stored in secretory granules [31]. Therefore, structural studies of CRF amyloid aggregates are of great interest for structural biology, not to mention biomedical importance. It is very intriguing to identify mechanisms that trigger the reversible change of peptide structure from stable α-helical monomers to compact and rigid β-sheet aggregates and back to functional α-helical monomers [31].

CRF obtained either by chemical synthesis [12, 31, 61, 176] or purification from natural sources [168, 174] was used in the studies described above. Structure elucidation by methods of solid-state and/or liquid-state NMR spectroscopy requires high amounts of isotopically labeled peptide, which can be produced by heterologous expression in *Escherichia coli* [157, 182-184]. At present, there is only one report in the literature

describing the recombinant production of CRF. Castro et al. expressed CRF as a part of preprohormone fused with β-galactosidase. The production according to [172] yielded 2 mg/ml of the chimeric β-galactosidase-prepro-CRF per liter of rich LB medium [172]. The design of this fusion protein did not allow for isolation of individual CRF. Therefore, the reported protocol cannot be utilized directly or with minor optimization for high-yield production of isotopically labeled CRF.

Here we describe the high-efficiency protocol providing 7-9 mg of isotopically labeled CRF of high purity (>99 %) for NMR spectroscopy. In parallel, we take first steps towards understanding the mechanisms responsible for functional amyloid formation by CRF. We employed fluorescence spectroscopy, EM, and optical microscopy for monitoring the aggregation and characterizing the terminal aggregation state of CRF. The results described in this chapter represent essential early steps towards determining the high-resolution 3D structure of CRF in its amyloid state.

Results and discussion

Large-scale production of CRF

The sequence of human CRF was fused to the C-terminus of thioredoxin-6His-tagged chimeric protein (pET32a expression vector) and separated from that by a tobacco etch virus (TEV) protease recognition site (ENLYFQ). Cleavage by the TEV-protease allowed for keeping the native sequence of CRF starting with the serine residue at P1' position. The amino acid sequence of studied human CRF was altered at the C-terminus by adding Gly42 to spatially mimic the naturally amidated Ile41 (CRF-G). This allowed us to simplify the protein production by avoiding the chemical modification and additional purification steps.

The CRF-G-comprising fusion protein was expressed in BL21 Star (DE3) *E. coli* cells in M9 minimal medium and found in the soluble fraction of the cell lysate as well as in the fraction of inclusion bodies. Therefore, both fractions were utilized for subsequent isolation of the target protein (**Figure 3.1**).

The soluble fraction of the cell lysate was purified by affinity chromatography and consequently buffer exchanged to an imidazole-free solution. Obtained after these steps, 75 %-pure fusion protein solution (SDS-PAGE analysis by ImageJ [185], **Figure 3.1a**, lane 5) was enzymatically processed by the TEV-protease at 1:100 enzyme:substrate ratio. The cleavage was complete after three hours (**Figure 3.1a**, lane 6). The precipitate

appearing during the enzymatic treatment of the fusion protein was mainly composed of the thioredoxin protein (**Figure 3.1a**, lane 7). Next, an additional round of affinity chromatography was carried out in order to get rid of the 6His-tagged species, such as thioredoxin-6His, uncut fusion protein, and the TEV-protease. To ensure high purity of recombinant CRF-G for NMR purposes, the second round of Ni-chelate chromatography was followed by reversed-phase high-performance liquid chromatography (RP-HPLC) purification. A typical elution profile is presented in **Figure 3.1c**. The UV absorbance was monitored at 220 and 280 nm. Since CRF-G lacks any tyrosine or tryptophan residues, the chromatographic peak showing absorbance at 220 nm but not at 280 nm was attributed to CRF-G. The identity and purity of the peptide was confirmed by electrospray ionization mass spectrometry (ESI-MS) (**Figure 3.1d**).

The insoluble fraction of the cell lysate was subjected to solubilization in 8 M urea solution followed by Ni-chelate chromatography under denaturing conditions (**Figure 3.1b**). After the affinity chromatography, 95 % purity of the target protein was achieved (SDS-PAGE gel analysis by ImageJ [185]). Urea and imidazole were removed by buffer-exchange to allow for subsequent cleavage of the fusion protein by the TEV-protease. Subsequently, the solution containing the target fusion protein at the concentration of 2.5 mg/ml was subjected to enzymatic cleavage. Enzymatic processing of the fusion protein was nearly 100 % complete (**Figure 3.1b**, lane 6) after three hours of cleavage yielding CRF-G. SDS-PAGE analysis of the precipitate, which occurred during the enzymatic proteolysis, revealed the presence of minor amounts of CRF-G among protein impurities (**Figure 3.1b**, lane 7). The final Ni-chelate chromatography was followed by RP-HPLC (**Figure 3.1c**). The total yield of ^{13}C, ^{15}N-labeled CRF-G was 7-9 mg per liter of minimal medium. Purification of the peptide in rich medium (LB) provided 12-15 mg of the recombinant CRF-G.
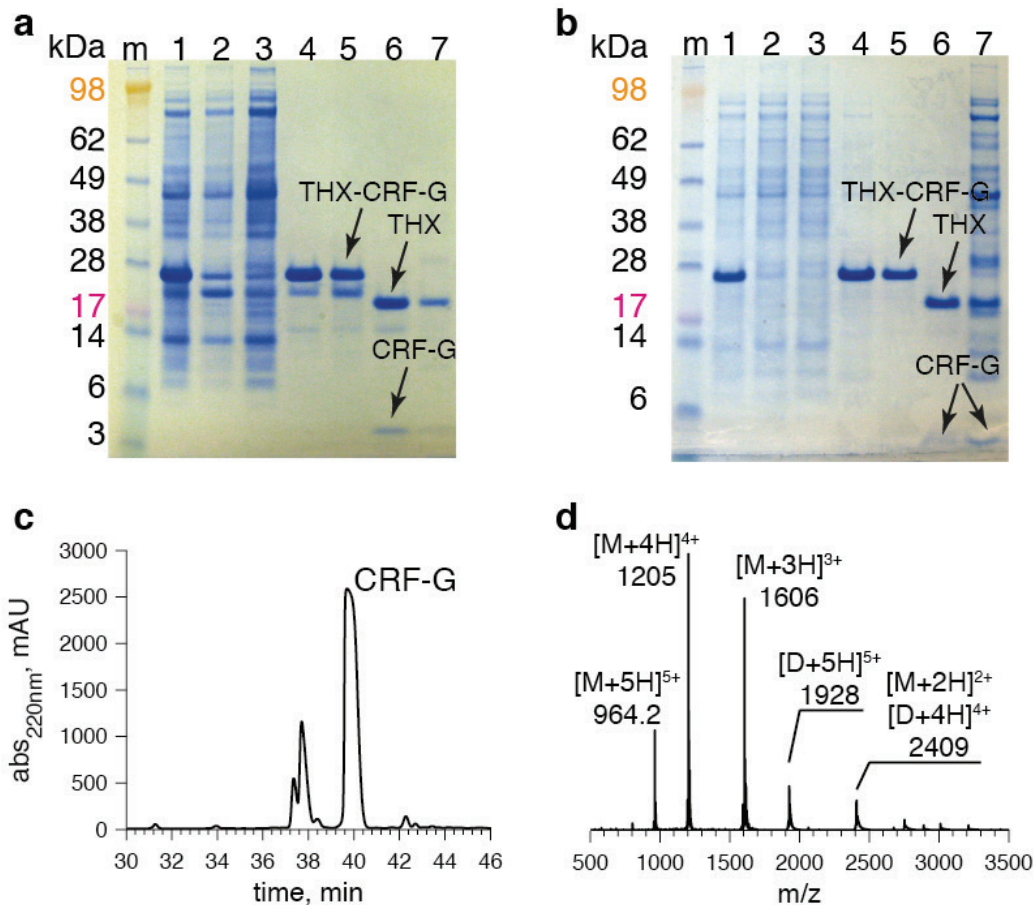
Figure 3.1. Purification of recombinant CRF-G. (**a**) SDS/4-12 % PAGE analysis of CRF-G purification from the soluble fraction of the cell lysate. The gel lanes are marked as follows: m – molecular weight markers with the correspondingly labeled masses in kDa; 1 – soluble protein fraction obtained from the cell lysate; 2, 3 - flow-through from two rounds of loading the protein solution on a HisTrapFF column; 4 – sample eluted from the HisTrapFF column by 300 mM imidazole solution; 5 – sample after buffer exchange to the cleavage buffer; 6 – sample after digestion by the TEV-protease at room temperature for 3 h at 1:100 enzyme:substrate ratio; 7 – precipitate that appeared during cleavage, loaded on the gel at 100-fold increased concentration. Successful cleavage can be determined by the shift of the fusion protein band. (**b**) SDS/4-12 % PAGE analysis of CRF-G purification from the insoluble fraction of the cell lysate. m – molecular weight markers with the correspondingly labeled masses in kDa; 1 – inclusion bodies dissolved in 8 M urea solution; 2, 3 - flow-through from two rounds of loading the protein extract on a HisTrapFF column; 4 – sample eluted from the HisTrapFF column by 300 mM imidazole solution; 5 – sample after buffer exchange to the cleavage buffer; 6 – sample after digestion by the TEV-protease at room temperature during 3 h at 1:100 enzyme:substrate ratio; 7 – precipitate that appeared during cleavage, loaded on the gel at 100-fold increased concentration. (**c**) A typical elution profile of the semi-preparative RP-HPLC of the flow-through solution obtained after the affinity chromatography of the digested THX-CRF-G fusion protein. The intensity axis is shown in optical absorbance units at $\lambda = 220$ nm. (**d**) ESI-MS spectrum of the peak running at 40 min of the RP-HPLC run (labeled as CRF-G in **c**). The mass corresponds exactly to the expected mass of CRF-G. Signals at m/z 964.2, 1205, 1606, 2409 were attributed to 5+, 4+, 3+, and 2+ ions of CRF-G monomer (marked as $[M+5H]^{5+}$, $[M+4H]^{4+}$, $[M+3H]^{3+}$, and $[M+2H]^{2+}$, respectively). Peaks labeled as $[D+5H]^{5+}$, $[D+4H]^{4+}$ with m/z 1928 and 2409 were assigned to 5+ and 4+ ions of unspecific CRF-G dimers appeared due to high peptide concentration.

In addition to mass spectrometry, NMR spectroscopy was used to confirm the identity and purity of the purified recombinant CRF-G. The sequential assignment was obtained from the 3D TROSY-HNCACB [186] spectrum. All backbone amino acid residue resonances were retrieved and assigned (**Figure 3.2**). Only two prolines and the

N-terminal serine did not appear in the 2D [^{15}N,^{1}H]-TROSY spectrum. The sequential assignment obtained from the 3D TROSY-HNCACB [186] spectrum confirmed the correct sequence of CRF-G (data not shown).
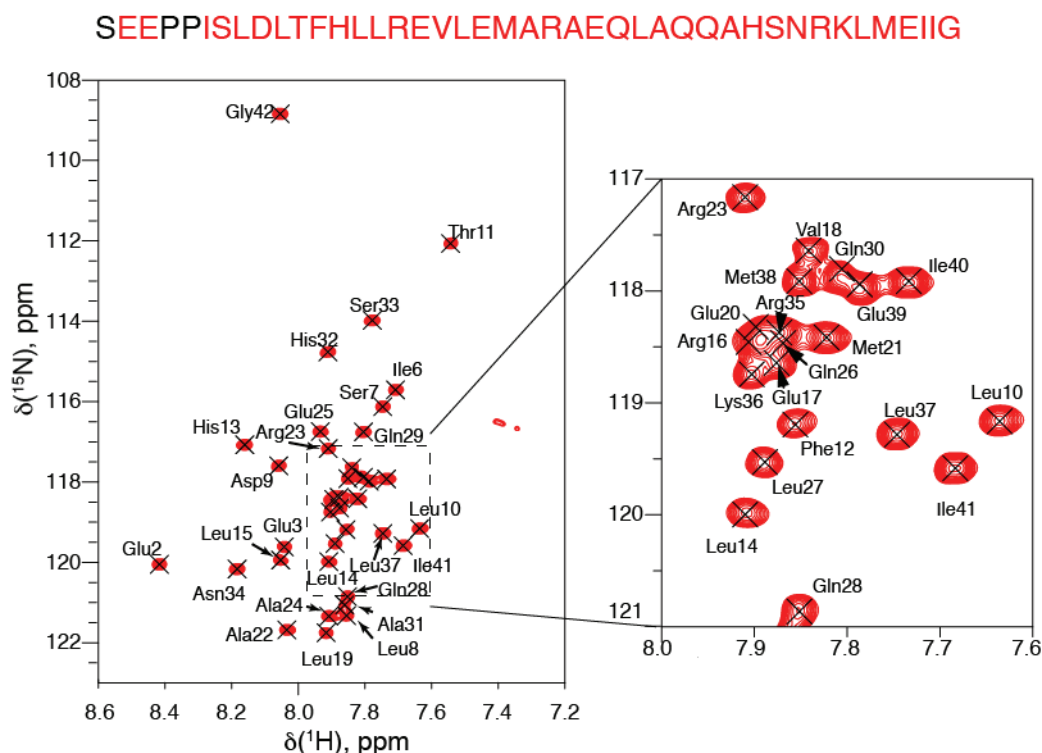
Figure 3.2. 2D [^{15}N, ^{1}H]-TROSY spectrum of ^{15}N, ^{13}C-labeled CRF-G in DMSO. The spectrum was measured at a ^{15}N, ^{13}C-labeled CRF-G concentration of 415 µM in DMSO-D6 containing 0.05 % trifluoroacetic acid-D at 30 °C on a Bruker 700 MHz spectrometer. The individual cross peaks were identified via sequential assignment of triple-resonance spectra. Red (black) coloring of CRF-G amino acid sequence indicates that the corresponding resonance was assigned (not unassigned) in the 2D [^{15}N, ^{1}H]-TROSY spectrum.

The amyloid state of CRF-G

Prediction of amyloidogenic properties of CRF by TANGO and Waltz

The analysis of the primary sequence of CRF by the TANGO algorithm [187] predicts the propensity of residues from 6 to 14 to form a β-strand structure (**Figure 3.3a**). However, this propensity is rather low and does not exceed 15 %. TANGO prediction aims to highlight sequences prone to amyloid aggregation based on the analysis of pathology-related amyloidogenic proteins [187]. Hormone aggregation, in particular CRF-G, is a functional process and it might therefore be not predictable by the TANGO algorithm. Unlike TANGO, Waltz [188] predicts the ability of CRF to undergo amyloid aggregation with a higher score, approximately 80 %, for residues 8-21 and 36-41 at acidic pH (**Figure 3.3b**). The aggregation-prone region becomes shorter (residues 8-15 and 36-41) if the simulation is run for neutral conditions (pH 7.0), although the scoring

remains the same at the level of 80 % (**Figure 3.3c**). At present, the lack of high-resolution structural information does not allow us to judge on the relevance of the Waltz prediction. Low-resolution analytical methods, such as hydrogen-deuterium exchange and limited proteolysis, can be utilized for the identification of structural elements involved in the β-sheet formation.
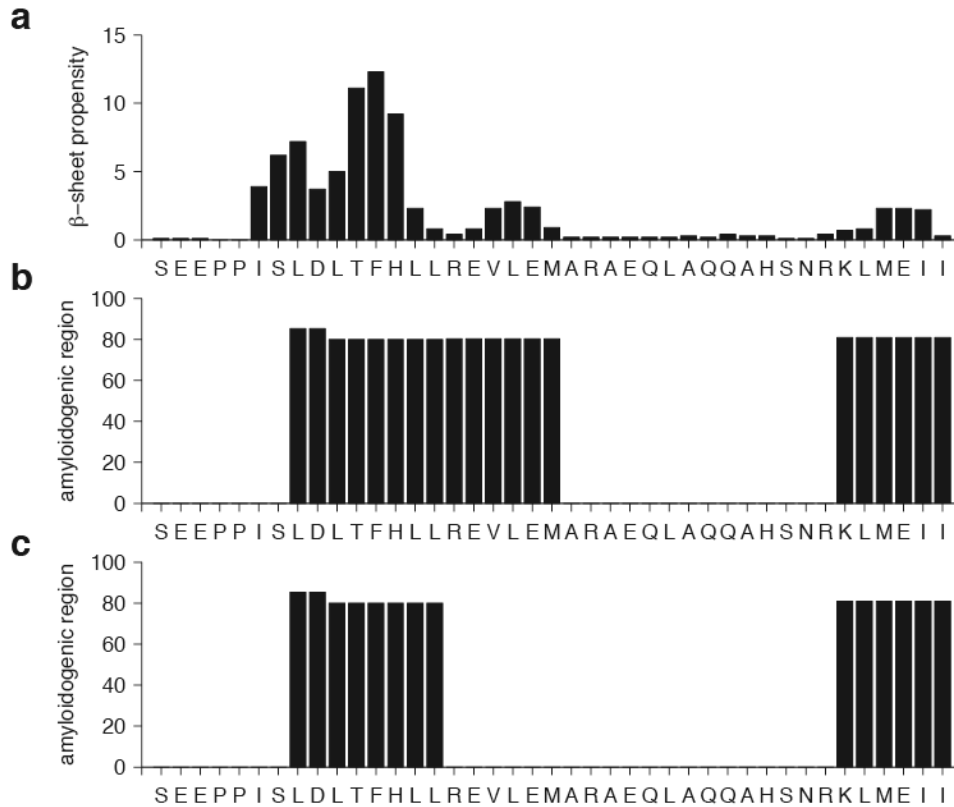
Figure 3.3. Computational prediction of amyloidogenic properties of non-amidated CRF. (**a**) Propensity of monomeric non-amidated CRF to adopt β-sheet structure at +37 ℃, pH 5.5, and ionic strength corresponding to 150 mM NaCl is predicted by TANGO [187]. Waltz [188] prediction of propensity of the non-amidated CRF to form amyloid aggregates at pH 2.6 (**b**) and 7.0 (**c**).

Amyloid formation by CRF-G in vitro

CRF-G aggregates obtained in 10 mM sodium citrate buffer at pH 5.5 containing 5 % mannitol and 2 mg/ml heparin were identified as amyloids based on the fibrillar appearance in EM (**Figure 3.4a**) and other characteristic features of amyloids. For instance, ThT fluorescence increased 16-fold upon binding to CRF-G fibrils (**Figure 3.4b**). Visualization of CR-stained CRF fibrils by polarized light optical microscopy revealed the birefringence effect (**Figure 3.4c-d**).
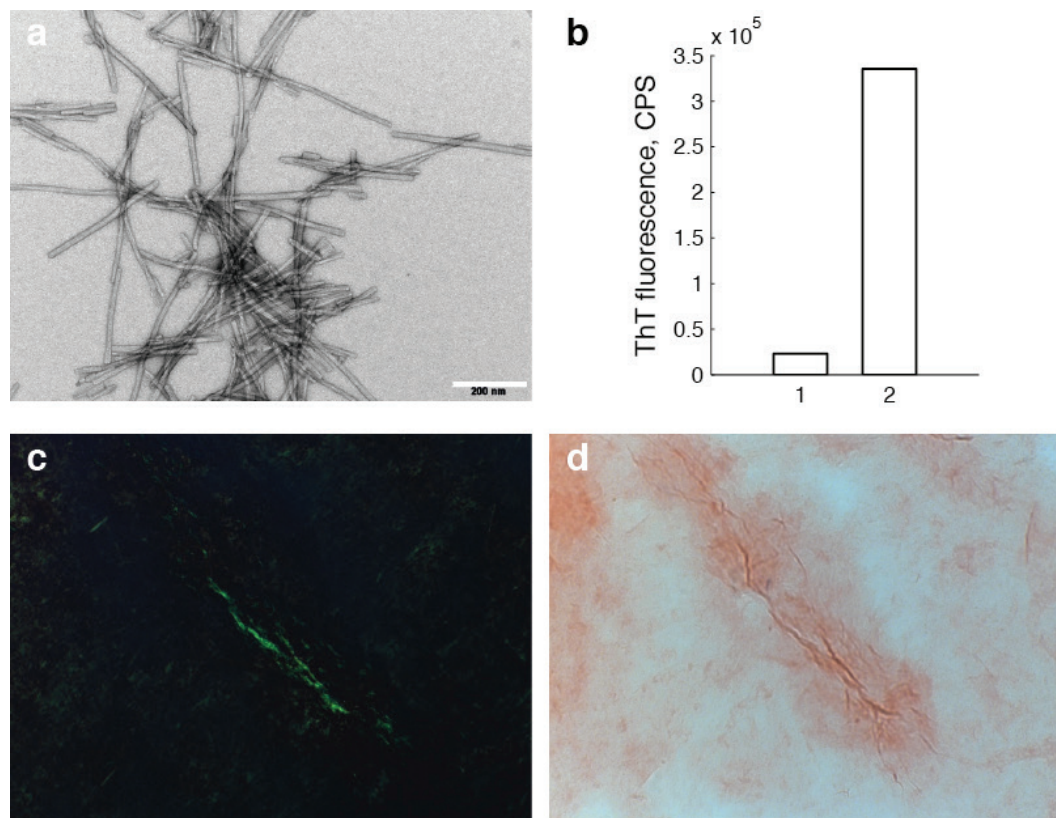
Figure 3.4. Characterization of mature CRF-G fibrils formed at +37 ºC under slight agitation in 10 mM sodium citrate buffer at pH 5.5 in the presence of 5 % mannitol and 2 mg/ml heparin. (**a**) EM micrographs of CRF-G amyloid fibrils. The scale bar is 200 nm. (**b**) ThT fluorescence increases upon binding to CRF-G amyloid fibrils. 1 – fluorescence of ThT in the blank fibrillization buffer. 2 – ThT fluorescence in the presence of CRF-G aggregates. (**c**) Congo red-stained CRF-G aggregates show birefringence in polarized light, 90 º crossed polarizer and analyzer. (**d**) The same as **c** in the bright field. (**c**), (**d**) – original magnification ×630.

Changes in the morphology of CRF-G species upon aggregation at different conditions

Change of the pH happening along the secretory pathway [55] and high abundance of carbohydrates in the ER and GC [68] suggest factors, which are potentially important for the promotion of amyloid formation. In our experiments, we systematically added low-molecular-weight (LMW) compound, mannitol, and a representative of GAGs, heparin, at different pH and examined the visual appearance of CRF-G aggregates by EM (**Figures 3.5-3.7**). The pH of fibrillization buffers was varied from 5.2 to 6.1 values, which are reported for the TGN and secretory granules [55], where functional aggregation of peptides presumably occurs [11, 31, 37].

The analysis of EM images obtained revealed the general ability of heparin to facilitate CRF-G aggregation. In all cases, CRF-G -composed fibrillar aggregates were observed after seven days of incubation in the presence of heparin. Conversely, only amorphous aggregates were detected after seven days in aggregating mixtures in the

absence of heparin. Two types of structures were recognized upon examination of aggregated CRF-G samples in the absence of heparin: octagons with 28-34 nm distance between the opposite sides and amorphous aggregates. With time, they both transformed into regular fibrillar species, which later formed flat ribbons (e.g. **Figure 3.6d, 3.7b**) and flat conglomerates of fibrils (e.g. **Figures 3.5b, 3.7d**).

As it was mentioned before, heparin promoted faster fibrillization. Fibrillar aggregates of CRF-G were detected after seven days of incubation. In general, the fibril population was more homogeneous when heparin was present. The fibrils were isolated and did not form large agglomerates. The detailed analysis of their morphology showed that at lower pH (5.2 and 5.5) CRF-G fibrils featured a periodic twist, unlike the fibrils formed at pH 6.1. The latter ones manifested themselves as short (50-200 nm) flat ribbons (**Figure 3.7f**, **h**). Both twisted fibrils and flat ribbons consisted of thin filaments 5-7 nm in width. Usually, from two to eight filaments could be distinguished in one twisted fibril or ribbon.

Observation of fibrils with distinct morphologies in the EM images is usually attributed to the presence of structural amyloid polymorphs [90, 92]. Therefore, structural characterization of such samples by ssNMR can be very difficult. However, the presence of rather different structural conformers can be an intrinsic property of the system, irrespective of the effort to eliminate polymorphism [189].
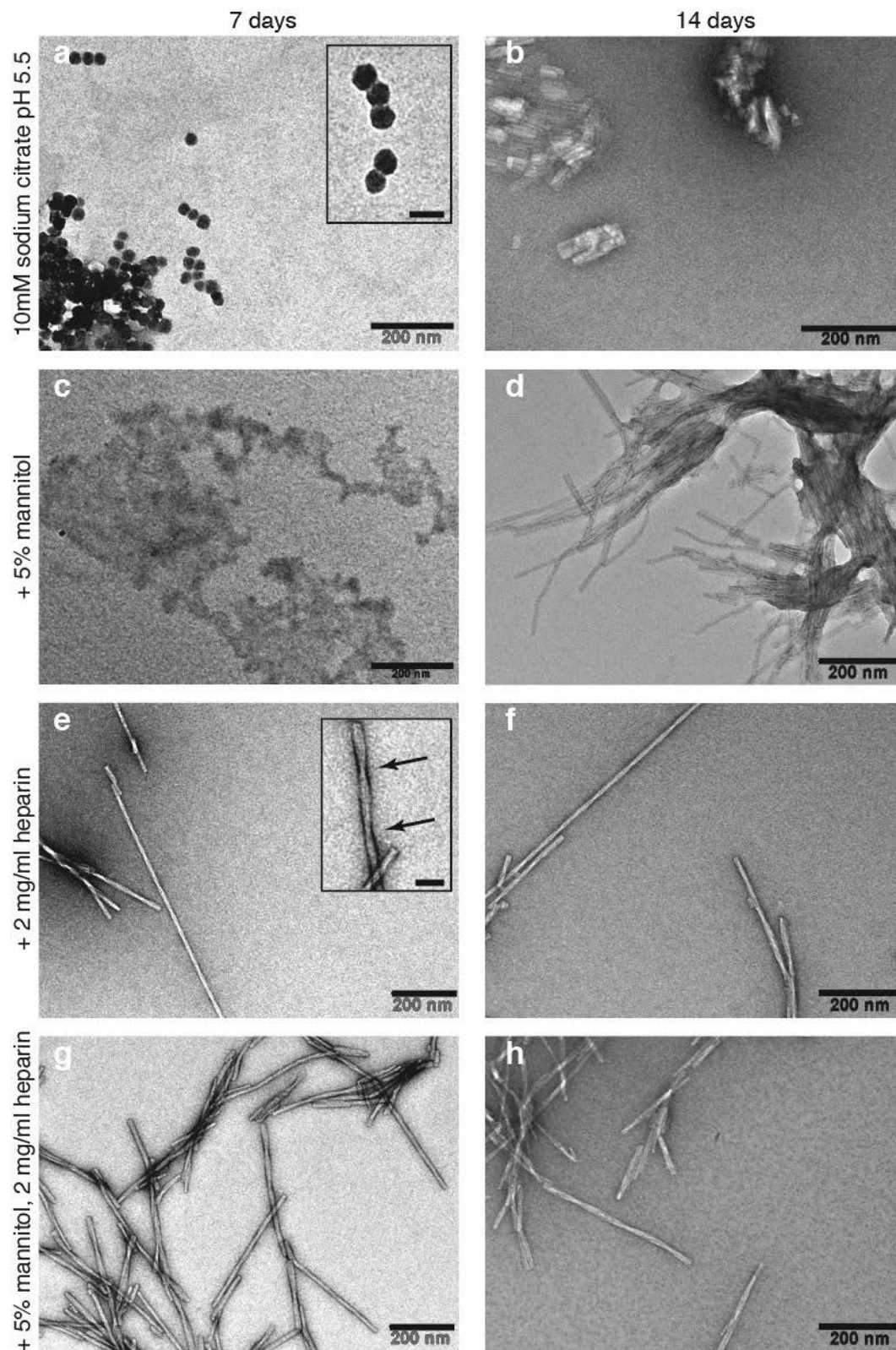
Figure 3.5. EM micrographs of CRF-G aggregates obtained at pH 5.2. (**a**), (**b**) – aggregation in 10 mM sodium citrate buffer; (**c**), (**d**) – aggregation in 10 mM sodium citrate buffer containing 5 % mannitol; (**e**), (**f**) – aggregation in 10 mM sodium citrate buffer containing 2 mg/ml heparin; (**g**), (**h**) – aggregation in 10 mM sodium citrate buffer containing 5 % mannitol and 2 mg/ml heparin. (**a**), (**c**), (**e**), (**g**) – after 7 days of aggregation; (**b**), (**d**), (**f**), (**h**) – after 14 days of aggregation. Insets show enlarged ultrastructure elements mentioned in the text. Arrows indicate fibril twists. Scale bars in all main figures are 200 nm, in all insets – 50 nm.
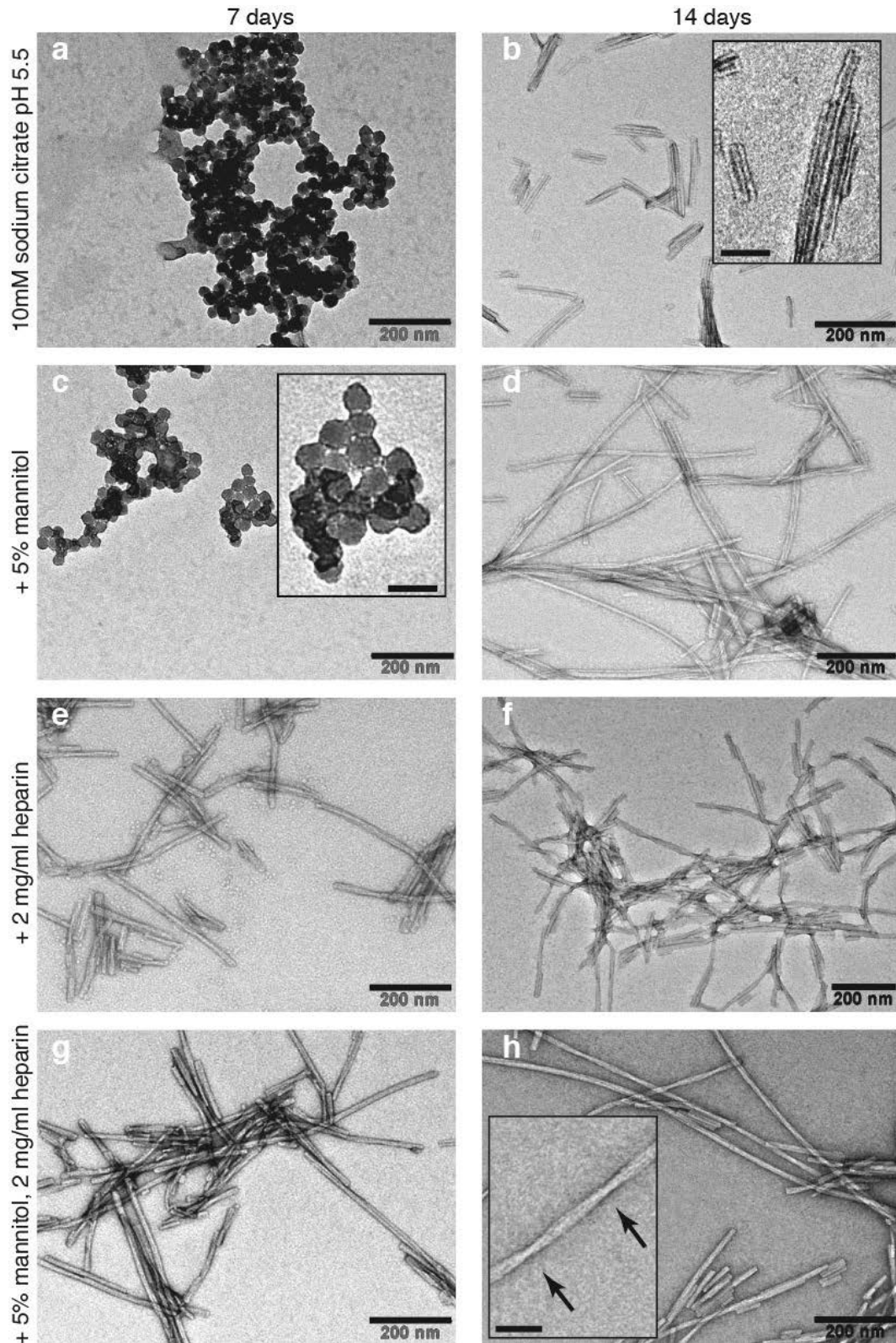
Figure 3.6. EM micrographs of CRF-G aggregates obtained at pH 5.5. (**a**), (**b**) – aggregation in 10 mM sodium citrate buffer; (**c**), (**d**) – aggregation in 10 mM sodium citrate buffer containing 5 % mannitol; (**e**), (**f**) – aggregation in 10 mM sodium citrate buffer containing 2 mg/ml heparin; (**g**), (**h**) – aggregation in 10 mM sodium citrate buffer containing 5 % mannitol and 2 mg/ml heparin. (**a**), (**c**), (**e**), (**g**) – after 7 days of aggregation; (**b**), (**d**), (**f**), (**h**) – after 14 days of aggregation. Insets show enlarged ultrastructure elements mentioned in the text. Arrows indicate fibril twists. Scale bars in all main figures are 200 nm, in all insets – 50 nm.
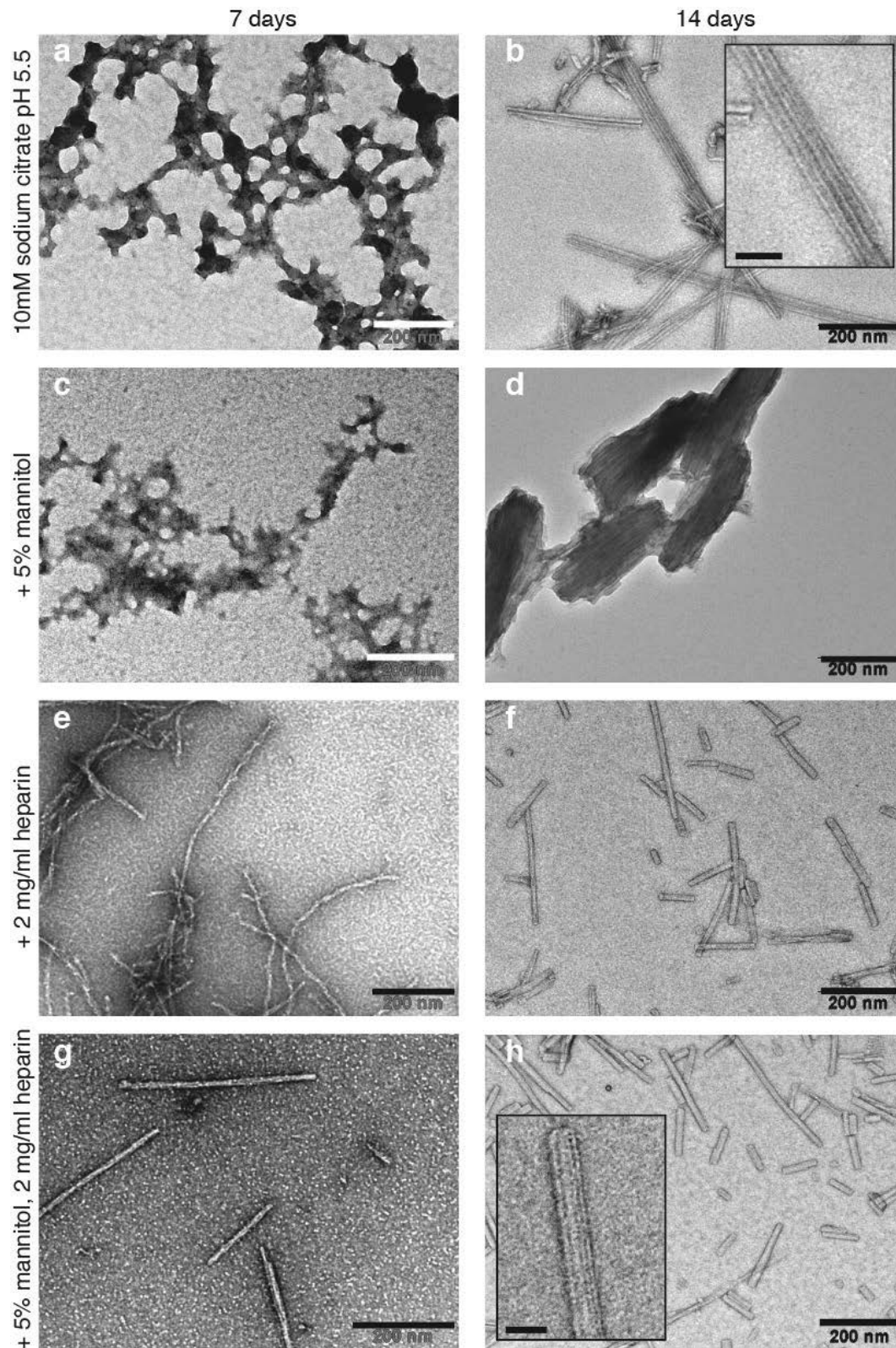
Figure 3.7. EM micrographs of CRF-G aggregates obtained at pH 6.1. (**a**), (**b**) – aggregation in 10 mM sodium citrate buffer; (**c**), (**d**) – aggregation in 10 mM sodium citrate buffer containing 5 % mannitol; (**e**), (**f**) – aggregation in 10 mM sodium citrate buffer containing 2 mg/ml heparin; (**g**), (**h**) – aggregation in 10 mM sodium citrate buffer containing 5 % mannitol and 2 mg/ml heparin. (**a**), (**c**), (**e**), (**g**) – after 7 days of aggregation; (**b**), (**d**), (**f**), (**h**) – after 14 days of aggregation. Insets show enlarged ultrastructure elements mentioned in the text. Scale bars in all main figures are 200 nm, in all insets – 50 nm.

In the absence of heparin, aggregation of CRF-G occurred only after seven days of incubation. Remarkably long fibrillization kinetics can be explained by the difficulty of structural changes, which CRF-G must undergo from stable in solution α-helical conformation to β-sheets composing the amyloid. pH of all buffers used is very close to isoelectric point (pI) of CRF-G, which obviously prompts protein precipitation yielding amorphous aggregates. Interestingly, in all cases studied, amorphous species transform into the ordered amyloid structure with time. CRF-G aggregation can be stimulated by heparin. At the tested pH 5.2, 5.5, and 6.1, the overall peptide charge is estimated at -0.1, -0.7, and -1.4, respectively. Thus, interaction of almost neutral or slightly negatively charged peptide with highly negatively charged heparin should be problematic at these conditions. So, amyloid aggregation of CRF-G in the presence of heparin cannot be explained by the charge-screening effect of heparin. Thus, more complex interactions between the peptide and heparin are likely to be responsible for the CRF-G fibrillization. It can be speculated that heparin acts as a surfactant by preventing chaotic precipitation of CRF-G at the beginning, while later it catalyzes transformation of previously α-helical CRF-G monomer to ordered β-sheets. Such a catalytic activity of heparin is widely known and described in the literature [75, 76, 83]. Heparin is hypothesized to increase the aggregation rate and the extent of fibrillization at the same time. However, the particular mechanism of the catalytic activity of heparin remains unknown.

Maji et al. [31] demonstrated that some peptide hormones could readily form amyloids at provided acidic pH 5.5, while others required the addition of heparin to do so. CRF belongs to the first group: its aggregation does not necessarily require heparin (although heparin facilitates the aggregation process). Interestingly, the two peptide groups could be distinguished based on the pI of peptides. Those peptides that could form amyloid fibrils at acidic conditions without heparin featured on acidic pI. Hormones from the other group had basic pI and aggregated only in the presence of heparin under acidic conditions. This correlation hints that, perhaps, one of the important determinants of peptide aggregation is the ionic state of the peptide at the given conditions. Overall neutral species can easily come close to each other in solution and form agglomerates, while charged species need to be screened by a counter-ion in order to overcome charge repulsions. Interestingly, those agglomerates can evolve into β-sheet amyloid structures in both cases, as it has been demonstrated here for CRF-G.

Conclusions

In the current chapter, we present a strategy for high-efficient heterologous expression of short human peptide hormones, which has been successfully implemented for high-yield production of isotopically labeled CRF-G. Reported expression and purification protocols afforded 7-9 mg and 12-15 mg of CRF-G per one liter of minimal or rich medium, respectively.

Aggregation studies of the α-helical CRF-G polypeptide with predicted low aggregation propensity show that it forms aggregates *in vitro* under the biologically relevant conditions. EM and amyloid-specific staining by ThT and CR dyes allow assigning the amyloid structure to these aggregates. Interestingly, CRF-G was able to adopt the amyloid fold in the presence and absence of heparin and in the range of solution pH from 5.2 to 6.1. Amyloid assemblies formed in the presence of the model GAG heparin featured different morphology compared to heparin-free samples. The early stages of CRF-G aggregation in the absence of heparin were characterized by the appearance of octagonal shapes of 28-34 nm and amorphous aggregates. Irrespective of the fibrillization conditions, mature fibrils demonstrated very similar ultra-structure: they were composed of thin laterally associated filaments 5-7 nm in width. This finding suggests that sugars and GAGs may not be essential for CRF-G aggregation, even though they greatly facilitate this process. Nevertheless, the molecular aspects of peptide-heparin interactions providing need deeper investigation.

The observed correlation of the peptide pI and its ability to aggregate in the absence of heparin hints to the involvement of charge-charge interactions into amyloid aggregation. Perhaps, the initial steps of amyloid aggregation are determined by the overall peptide charge. In contrast, the observed acceleration of CRF-G aggregation by the addition of heparin at acidic pH, where the peptide is nearly neutral or negatively charged, suggests more complex mechanisms of heparin's aggregation inducing activity than just charge-charge interactions.

In the context of functional hormone amyloids, CRF-G represents a unique example, which is capable of reversible structural changes from the stable α-helix to the β-sheet structure and back to the α-helical monomer [31]. Further investigation of mechanisms responsible for such remarkable transformations is of great interest for protein aggregation studies.

Methods

Materials

Tris(hydroxymethyl)aminomethane for molecular biology was provided by BiosolveBV (Valkenswaard, Netherlands). Phenylmethanesulfonyl fluoride (PMSF), isopropyl β-D-1-thiogalactopyranoside (IPTG), and ampicillin were purchased from AppliChem (Darmstadt, Germany). Lysozyme from chicken egg and calcium chloride ($CaCl_2$) were obtained from Fluka production GmbH (Buchs, Switzerland). Glucose, sodium chloride (NaCl), ammonium chloride (NH_4Cl), and ammonium hydroxide (NH_4OH) from Merck KGaA (Darmstadt, Germany) were used in this work. Trifluoroacetic acid (TFA) for HPLC was obtained from Fisher Scientific AG (Loughborough, UK). Fully deuterated dimethyl sulfoxide (DMSO-D6) (D, 99.96 %) and fully deuterated trifluoroacetic acid (TFA-D) (D, 99.5 %) for NMR measurements were from Cambridge Isotope Laboratories (Andover, Massachusetts, USA). All other reagents including labeled substrates ^{13}C-glucose (^{13}C > 99 %) and ^{15}N-ammonium chloride (^{15}N-NH_4Cl) (^{15}N > 98 %) and acetonitrile CHROMASOLV® gradient grade, for HPLC, ≥ 99.9 % were purchased from Sigma-Aldrich (Buchs, Switzerland), unless stated otherwise.

Strains and plasmids

One Shot® Top10 chemically competent *E. coli* cells from Invitrogen (Invitrogen™ by LifeTechnologies™, LuBioScience GmbH, Lucerne, Switzerland) were used as the bacterial host for DNA cloning. For protein expression, *E. coli* One Shot® BL21 Star™ (DE3) strain was provided by Invitrogen, and the pET32a vector was purchased from Novagen (Merck KGaA, Darmstadt, Germany). The recombinant protein contained thioredoxin as a carrier protein with a hexa-histidine tag (6His) followed by the TEV-protease recognition site and CRF sequence (**Supplementary Figure S1**). The DNA coding sequence of CRF-G was engineered and cloned into pET32a plasmid by GeneArt (Burlingame, California, USA). Theoretical molecular weights of the recombinant proteins and molar extinction coefficients were calculated using the ProteinCalculator v3.4 [190].

Expression and purification of recombinant protein

The expression vector pET32a/CRF was used to transform the host *E. coli* One Shot® BL21 Star™ (DE3) strain. Depending on the type of desired isotopic labeling, cells

were precultured in 5 ml of Luria broth (LB) or M9 minimal medium (1 L of M9 medium contains 3 g of D-glucose and 1 g of NH_4Cl) overnight at +37 °C. Cells grew at +37 °C and 120 rpm with 100 mg/L ampicillin. Recombinant gene expression was induced by adding IPTG to 1 mM when the optical density at 600 nm reached 1.2. Expression was performed at +20 °C overnight (16 h). Cells were harvested by centrifugation at 10^4 g (Avanti J-26 XP, Beckman Coulter International S.A., Nyon, Switzerland) at +4 °C for 30 min. 19 g of wet cell pellet was resuspended in 100 ml of the lysis buffer (50 mM Tris-HCl, 100 mM NaCl, 20 mM imidazole, 0.5 mM DTT, pH 8.0), PMSF and lysozyme were added to a final concentration of 1 mM and 0.5 mg/ml, respectively. The lysate was incubated at room temperature with constant stirring for 30 min. Afterwards, cells were disrupted by passing the suspension 3 times through the 110S microfluidizer (Microfluidics, Newton, Massachusetts, USA) at 40 psi. The solution was centrifuged at 2.5×10^4 rpm (rotor 45 Ti, Optima L-90K Ultracentrifuge, Beckman Coulter International S.A., Nyon, Switzerland), +6 °C for 1 h. The supernatant and precipitate were processed further separately.

The soluble fraction of the cell lysate was loaded on a HisTrapFF 5 ml column (GE Healthcare AG, Glattbrugg, Switzerland) by 20 ml increments. The fusion protein was eluted by the elution buffer 1 (50 mM Tris-HCl, 100 mM NaCl, 0.5 mM DTT, 300 mM imidazole, pH 8.0). 70 ml of the protein solution were subjected to buffer exchange on a HiPrep 26/10 desalting column (GE Healthcare AG, Glattbrugg, Switzerland) by 12 ml increments, so that the elution buffer 1 was exchanged to the cleavage buffer (50 mM Tris-HCl, 100 mM NaCl, 0.5 mM DTT, pH 8.0). Next, the fusion protein was treated with the TEV-protease (made in house according to [191]) in a molar ratio of 1:100 at room temperature. After 3 h, the solution was centrifuged at 4×10^3 rpm (Biofuge primo R, Heraeus, Fischer Scientific AG, Reinach, Switzerland) for 15 min at +22 °C. 75 ml of collected supernatant were subjected to another round of affinity chromatography on a HisTrapFF 5 ml column preliminary equilibrated in the lysis buffer. 6His-tagged species were then trapped on the support while the flow-through fraction containing the target peptide was collected. Acetonitrile was added to the peptide solution up to 10 % (vol.) prior to reversed-phase chromatography (RP). The solution was then acidified to pH 2.0 by the addition of TFA to a final concentration of 0.25 % (vol.). The HisTrapFF column was recovered by washing with the elution buffer 1 and

equilibrated again in the lysis buffer. The loading-elution procedure was repeated five times.

The insoluble fraction of the cell lysate was resuspended in 100 ml of the extraction buffer (50 mM Tris-HCl, 8 M urea, 100 mM NaCl, 10 mM imidazole, 0.5 mM DTT, pH 8.0). Extraction of the fusion protein was carried out for 1 h at room temperature under constant stirring. The extract was centrifuged at +22 °C, 4×10^4 rpm (rotor 45 Ti, Optima L-90K Ultracentrifuge) for 1 h. The supernatant was purified on a HisTrapFF 5 ml column by 20 ml increments. The fusion protein was eluted by the elution buffer 2 (50 mM Tris-HCl, 7 M urea, 100 mM NaCl, 0.5 mM DTT, 300 mM imidazole, pH 8.0). 50 ml of the protein solution were subjected to buffer exchange on a HiPrep 26/10 desalting column by 15 ml increments. The elution buffer 2 was therefore exchanged to the cleavage buffer. The subsequent proteolytic cleavage, secondary affinity chromatography followed by peptide preparation for RP-HPLC by the addition of required amounts of acetonitrile and TFA were performed as described above for the purification of CRF from the soluble fraction of the cell lysate.

RP-HPLC

Final purification of CRF was performed on a Discovery BIO Wide Pore C18 column (25 cm x 10 mm, 10 μm; Supelco, Bellefonte, Pennsylvania, USA). The elution was carried out using an acetonitrile gradient (10-40 % buffer B in 37 min, flow rate − 2 ml/min; buffer A - water with 0.1 % TFA, buffer B − acetonitrile with 0.1 % TFA). An Agilent 1200 HPLC (Agilent Technologies (Schweiz) AG, Basel, Switzerland) system equipped with an external manual injector, an automatic fraction collector, and a diode-array detector was used. The elution profile was monitored by UV absorption at 220 and 280 nm. The average injection volume was 15 ml. Fractions absorbing at 220 nm but not at 280 nm were collected, merged, and freeze-dried. The presence and purity of the recombinant protein was confirmed by ESI-MS (Q-TOF Ultima API, Micromass, Manchester, UK).

Protein electrophoresis and concentration measurements

The expression and purification processes were monitored by protein electrophoresis [192] using denaturing NuPAGE® Novex® 4-12 % Bis-Tris Gels (Invitrogen™ by LifeTechnologies™, LuBioScience GmbH, Lucerne, Switzerland) and SeeBlue®Plus2 Pre-Stained Standard from Invitrogen™ according to the manufacturer's

instructions. ImageJ software [185] was used for quantitative analysis of Coomassie-stained [192] SDS-PAGE gel images. The protein concentration was determined by UV spectroscopy (λ_{max} = 280 nm; $\varepsilon_{THX-CRF}$ = 15220 M^{-1} cm^{-1}). Amount of purified CRF was estimated by weighing on Digital Analytical Balance Lab Scale AG204 (Mettler-Toledo Schweiz GmbH, Greifensee, Switzerland), since it does not contain any tryptophan or tyrosine, which makes direct spectrophotometric concentration measurement challenging.

Mass spectrometry

Mass spectra were acquired on a hybrid quadrupole-time-of-flight mass spectrometer Q-TOF Ultima API (Micromass, Manchester, UK) equipped with a Z-spray interface (Waters, Manchester, UK). Ions were generated using an automated chip-based nano-electrospray ion source (NanoMate model 100, Advion BioSciences, Ithaca, NY, USA) at a high voltage of 1.3-1.7 kV applied to the electrospray emitter chip. A backing pressure of 0.5 bar was used to assist the sample flow, and the typical flow rate was approximately 200 nL/min. The ion source was kept at room temperature. Potentials on the ion guides were optimized to ensure efficient ion transmission in the *m/z* range of 100-4000 for the peptide samples or 300-8000 for the protein samples. A single scan time of 1 s was used, and typically 50-100 scans were combined to obtain a representative mass spectrum. Spectra were managed and processed via the MassLynx v. 4.0 software (Waters, Manchester, UK). Multiply-charged peaks in the electrospray spectra were deconvoluted, where necessary, using the MaxEnt 1 tool embedded within the MassLynx software. Mass calibration was performed using CsI clusters. Peptide and protein samples were infused either directly after RP-HPLC or upon desalting, if required, using a ZipTip C18 column (Millipore AG, Zug, Switzerland) according to the procedure described by the manufacturer.

NMR spectroscopy

The peptide used in the NMR experiments was prepared according to the protocol described above. 0.6 mg of lyophilized ^{15}N, ^{13}C-labeled CRF was dissolved in 300 μl DMSO-D6, 0.05 % TFA-D. NMR spectra of the 2D [^{15}N, ^{1}H]-TROSY [193] and 3D TROSY-HNCACB and TROSY-HN(CO)CA [186] were recorded at +30 °C on a Bruker 700 MHz spectrometer equipped with a cryoprobe (Bruker BioSpin AG, Fällanden, Switzerland). The spectra were processed with TopSpin 2.0 software (Bruker BioSpin AG, Fällanden, Switzerland) and assigned using the CCPN software package

[194]. Sequential connectivities were established by the 3D TROSY-HNCACB experiment following the established procedures [186].

Protein aggregation

CRF was dissolved in the fibrillization buffer (e.g. 10 mM sodium citrate, 5 % w/v D-mannitol, pH 5.5) at 2 mg/ml concentration, unless otherwise stated. Aggregation was set up in low-retention 1.5 ml test tubes (Vaudaux-Eppendorf AG, Schönenbuch/Basel, Switzerland) in the EchoTherm RT11 rotating mixer (Torrey Pines Scientific, Inc., Carlsbad, USA) at a rotation speed of approximately 30 rpm inside +37 ℃ incubator. 250 mg of heparin (heparin sodium salt, sc-203075, Santa Cruz Biotechnology, Inc., Heidelberg, Germany) were dissolved in 2.5 ml of double-deionized water in the presence of 0.05 % (w/v) sodium azide (AppliChem, AXON LAB AG, Baden-Dättwil, Switzerland) to prepare a heparin stock solution. One part of the heparin stock solution was added to 50 parts of CRF dissolved in the fibrillization buffer to initialize fibrillization. Afterwards sodium azide was added up to a concentration of 0.05 % to the peptide solution. Sample tubes were sealed by PARAFILM® M (Sigma-Aldrich Chemie GmbH, Buchs, Switzerland) and placed for fibrillization.

Transmission electron microscopy

5 µl samples of CRF fibrils were deposited for 1 min on carbon-coated copper grids previously glow-discharged (Electron Microscopy Sciences, Hatfield, Pennsylvania). The grids were then blotted, washed twice in drops of double-distilled water and negatively stained for 15 s with filtered 2 % (w/v) uranyl acetate (Sigma-Aldrich Chemie GmbH, Buchs, Switzerland). Images were acquired with the FEI Morgagni 268 electron microscope (FEI Company, Eindhoven, Netherlands) operated at 100 kV. Electron micrographs were recorded on a 1376 by 1032 pixel charge-coupled device camera (Veleta, Olympus soft imaging solutions GmbH, Münster, Germany).

Thioflavin T staining

The fibril-containing solution was diluted 60-fold by the fibrillization buffer (20 µM final protein concentration) and mixed with 1 mM thioflavin T (ThT) aqueous solution yielding 20 µM ThT in the sample. Fluorescence spectra were recorded on FluoroMax®-4 spectrofluorometer controlled by FluorEssence™ software (Horiba Jobin Yvon GmbH, Munich, Germany). The excitation wavelength was 440 nm and the spectra were acquired in the range of 460-550 nm utilizing 3 nm slits for excitation and emission.

Congo red staining

The CR staining protocol of the kit HT-60 (Sigma-Aldrich Chemie GmbH, Buchs, Switzerland) was used with minor modifications. Briefly, CRF aggregates (prepared in 10 mM sodium citrate, pH 5.5, 5 % D-mannitol, 2 mg/ml heparin) were dried on poly-L-lysine coated glass slide (Poly-Prep slides, Sigma-Aldrich Chemie GmbH, Buchs, Switzerland). 4 % formaldehyde solution was used for sample fixation for 10 min. Next, the sample was rinsed three times in deionized water, dried and stained for one minute with Mayer's hematoxylin (Sigma-Aldrich Chemie GmbH, Buchs, Switzerland). After washing for 1 min with tap water and 3 times with deionized water, the sample was placed in filtered alkaline NaCl solution for 20 min followed by incubation in filtered alkaline CR staining solution. The slide was washed twice with 95 % ethanol and twice with 100 % ethanol. The sample was cleaned in xylene and mounted with a drop of Dako Fluorescence Mounting Medium (Dako, Schweiz AG, Baar, Switzerland). The sample was studied using PALM-Microdissection and Widefield Microscope Zeiss Axiovert 200M (Carl Zeiss Microscopy GmbH, Göttingen, Germany). Images were acquired by Zeiss AxioCam camera in AxioVision software (Carl Zeiss Microscopy GmbH, Göttingen, Germany).

Chapter 4

Heterologous expression of somatostatin 14[1]

Introduction

Somatostatin 14 (SS14) is an essential peptide hormone produced in neurons of the hypothalamus and in some peripheral organs, such as the endocrine part of pancreas, gut, adrenals, and kidney [195]. This hormone is 14 amino acid residues long and has a disulfide bridge between residues Cys3 and Cys14. SS14 is classified as an inhibitory hormone because it suppresses the release of growth hormone, thyroid-stimulating hormone, and corticotropin-releasing factor by the pituitary gland [195]. Besides neurohormonal functioning, SS14 can act as a neurotransmitter by directly activating cortical neurons [196], and as a neuromodulator by inhibiting the generation of the respiratory rhythms [196-198]. Recently, a high interest in SS14 and its analogues emerged due to their potential application in the treatment of hormone-secreting pituitary tumors [197]. The solution structure of SS14 and its analogues has been a subject of deep investigation during the last forty years [199-202]. Nonetheless, no 3D structure of SS14 in complex with one of its receptors has been determined yet.

It has been discussed previously (**Chapter 1**) that SS14, as some other peptide hormones, is stored in secretory granules in an amyloid-like state [31]. In order to get a detailed understanding of the apparent pluripotent activities of hormone amyloids, the knowledge of their 3D structures becomes of a great importance. However, no 3D structure of a functional hormone amyloid has been determined to date.

Multi-dimensional solid-state NMR spectroscopy is a method of choice for determining 3D structures of amyloid fibrils at the level of atomic resolution. Solving a structure by solid-state NMR requires several ^{13}C- and/or ^{15}N-labeled peptide samples of 10-20 mg each [156, 157]. Large-scale production of isotopically labeled peptides by chemical synthesis is very expensive. Therefore, heterologous expression in *Escherichia coli* was chosen as a method for the production of isotopically labeled SS14.

The general strategy for recombinant synthesis of short peptides usually utilizes expression of a fusion construct containing a carrier protein and affinity tags along with the target peptide to prevent degradation of the peptide and facilitating the purification procedure [172, 203-205]. The target peptide is subsequently excised from the fusion construct with a sequence-specific protease that can be chosen from a wide repertoire of well-characterized enzymes [204]. The uniform isotopic labeling is accomplished via metabolic incorporation of the required isotopes by host cells during the expression of the recombinant gene. This imposes another restriction on the protocol of synthesis: the host cell culture must grow in the presence of a single source of carbon and nitrogen, i.e. in a minimal medium [206]. Such a strategy has successfully been implemented for the synthesis of proteins and small peptides [182, 184, 207-209]. Several studies reported a protocol for recombinant synthesis of SS14 in *E. coli* [210-212], which was the first example of its kind [211]. In the work of Notani et al. [210], SS14 was expressed with somatomedin C (Phe23-Glu46) and human interferon-γ (Cys1-Leu59) as fusion partners yielding 13 mg of fusion protein per liter of *E. coli* culture grown in a rich medium. The authors [210] did not intend to transfer the expression system to the minimal medium.

In the present work, an efficient method for the high-yield production of recombinant SS14 allowing for uniform metabolic ^{13}C and ^{15}N-labeling of the peptide for heteronuclear NMR spectroscopy is developed. The optimization of several important parameters, including the expression vector, temperature and duration of the expression, and the induction method, was carried out in order to maximize the yield of recombinant SS14. The target product isolation and purification procedure is another subject of optimization. Finally, the proper disulfide bond should be introduced into synthetic SS14 molecules.

The present work also demonstrates that following the standard procedures does not necessarily guarantee success, even though the general methodology of recombinant protein expression and purification is very well developed and considered as a routine nowadays. To name only a few examples, point mutations and amino acid misincorporation [213] or frameshift [214-216] occurring during protein translation can lead to the production of a protein with an incorrect primary sequence, promoter deletions can end up in a leaky expression or growth of only non-producers [217]. In other words, the synthesis of recombinant protein can be still challenging, as it is demonstrated here for the case of SS14.

Results and discussion

Selection of the expression vector

With the introduction of recombinant DNA technologies a few decades ago, a new area in biology began, and concomitantly significant progress has been achieved in this field [157, 218, 219]. For instance, the synthesis of recombinant genes, as well as the nucleic acid restriction enzymes and expression vectors are commercially available products that significantly simplify the access of researchers to large amounts of desired recombinant proteins [220]. These products and services allow a high level of optimization and ensure a very high rate of success, and in most cases they give reliable results. However, as it is shown below, the biology of a host organism may interfere with the predicted action of the recombinant DNA leading to abortive or erroneous synthesis of the target protein [214-216, 221-226].

At the beginning of our work, we chose very common expression systems and recombinant DNA design. The synthetic gene of SS14 was cloned into the commercially available expression vectors pET32a and pMAL-c5X and expressed in *E. coli* BL21 Star™ (DE3) producing strain. SS14 sequence was therefore fused to the two carrier proteins: maltose-binding protein, MBP (pMAL-c5X) or thioredoxin (pET32a) (**Figure 4.1**). These proteins are often used for both small- and large-scale production of recombinant peptides [182, 204, 227]. Thioredoxin and MBP fusion proteins were found in inclusion bodies despite their postulated property to stabilize fusion proteins in a soluble fraction [203, 204]. The recovery of the MBP-SS14 hybrid protein from the inclusion bodies was inefficient, since the fusion protein precipitated during buffer exchange (**Figure 4.2**). In contrast, the thioredoxin-SS14 fusion protein could be easily recovered from inclusion bodies in the case of the pET32a-based expression system. We therefore opted for the pET32a plasmid for the expression of the fusion protein containing thioredoxin with the 6His-tag placed between thioredoxin and the tobacco etch virus protease recognition site (TEVrs) followed by the SS14 sequence (**Figure 4.1**). Cleavage by the TEV-protease was selected because it permits a native sequence for SS14 with the starting alanine residue at P1' position. Furthermore, the TEV-protease can be easily produced in-house in sufficient amounts [191, 228, 229].
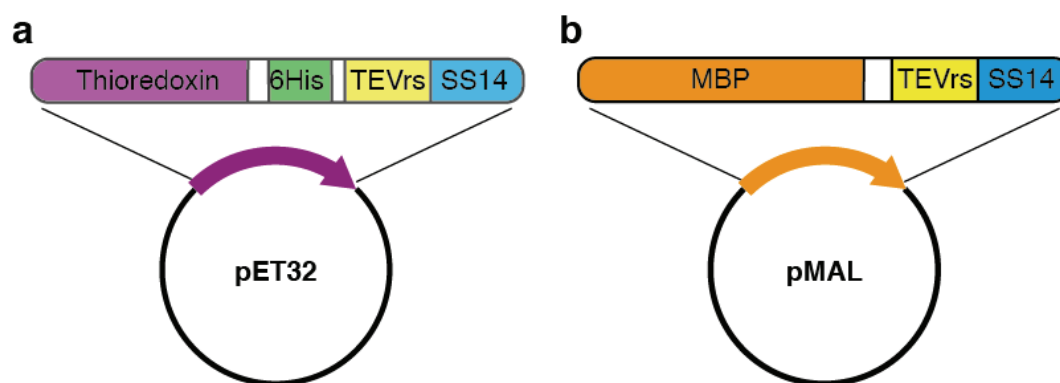
Figure 4.1. Genetic constructs designed and tested for SS14 expression. (**a**) SS14 expression system based on pET32 vector. (**b**) SS14 expression system based on pMAL vector. 6His – hexa-histidine tag; MBP – maltose binding protein; TEVrs – tobacco etch virus protease recognition site.
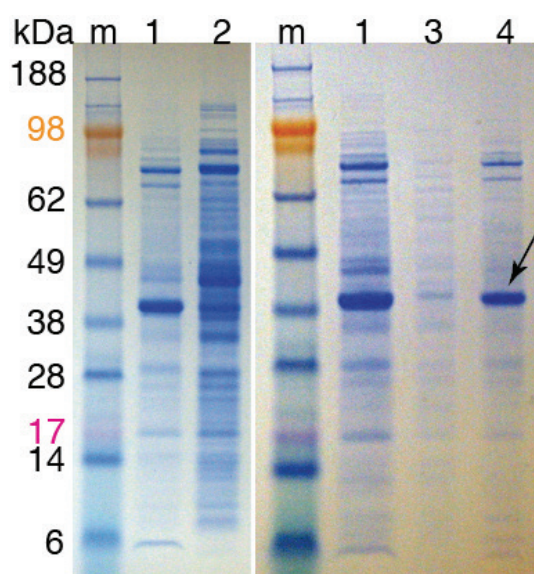
Figure 4.2. SDS-PAGE analysis of expression and purification of the MBP-SS14 fusion protein in *E. coli* (SDS/4-12 % PAGE). The gel lanes are marked as follows: m – molecular weight standards with the correspondingly labeled mass in kDa, 1 – inclusion bodies dissolved in 8 M urea solution, 2 – soluble protein fraction obtained from the cell lysate, 3 – soluble protein fraction recovered from dialysis, 4 – protein precipitate formed during dialysis. The arrow points to the fusion protein band. The gel was stained with 0.2 % Coomassie blue staining solution [192].

Analysis of the expression reveals a stop codon read-through

The host cells transformed with the pET32a/THX-SS14 expression vector exhibited overexpression of two polypeptides, with one running at approximately 20 kDa in SDS-PAGE and another heavier by approximately 5 kDa (**Figure 4.3**, lane 2). The 20 kDa band was attributed to the target construct (MW_{theor} = 20137.69 Da). Surprisingly, both overexpressed proteins were co-purified during Ni-chelate chromatography. The longer expression product constituted approximately 30-35 % of the isolated protein fraction, as revealed by the analysis of gel images by ImageJ software [185] (**Figure 4.3**, lane 2). Both polypeptides were digested by the TEV-protease yielding one identical cleavage product with the molecular weight of approximately 18 kDa (**Figure 4.3**, lane 8), which was assigned to the N-terminal thioredoxin-6His fragment of the fusion construct. Subsequent RP-HPLC separation of the peptide mixture obtained after the

enzymatic digestion allowed us to isolate a fraction containing the target peptide with a molecular weight of 1638.73 ± 0.07 Da, as measured by ESI-MS, which is consistent with the theoretical mass of SS14 ($MW_{theor} = 1638.7323$ Da). A complimentary ESI-MS/MS analysis resulted in successful identification of the SS14 sequence.
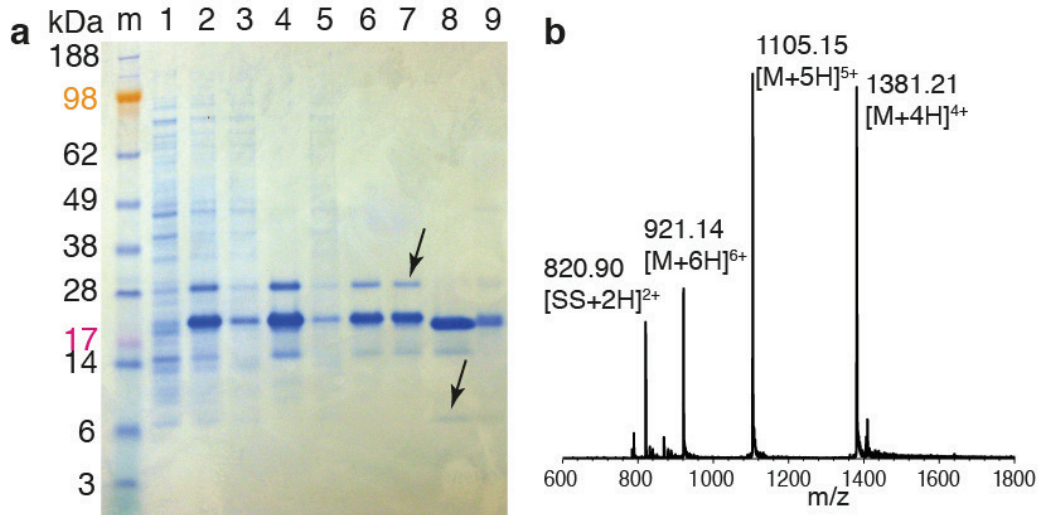
Figure 4.3. Analysis of expression and purification of the THX-SS14 fusion protein. (**a**) SDS/(4-12 %) PAGE analysis of expression and purification of the THX-SS14 fusion protein: m – molecular weight standards with the correspondingly labeled mass in kDa; 1 – soluble protein fraction obtained from the cell lysate; 2 – inclusion bodies dissolved in 8 M urea solution; 3, 5 – flow-through fraction from a HisTrapFF column; 4, 6 – sample eluted from a HisTrapFF column with the buffer containing 300 mM imidazole; 7 – sample solution after buffer exchange to the cleavage buffer; 8 – sample after digestion with the TEV-protease at room temperature during 2 h at 1:100 enzyme:substrate ratio (SS14 is not visible due to too small molecular size); 9 – precipitate that appeared during cleavage, loaded on the gel at 100-fold increased concentration. Arrows indicate contaminating protein and peptide at 25 and 5.5 kDa, respectively. (**b**) High-resolution ESI mass spectrum of the RP-HPLC isolated products of the TEV-protease digest. Plotted x values are mass to charge ratios (*m/z*). The peak at *m/z* 820.90 was attributed to the doubly charged protonated ion of SS14 (marked as $[SS+2H]^{2+}$); signals at *m/z* 921.14, 1105.15, 1381.21 were attributed to 6+, 5+, 4+ ions of the long peptide (marked as $[M+6H]^{6+}$, $[M+5H]^{5+}$, $[M+4H]^{4+}$, respectively) with the measured molecular weight of 5520.84 ± 0.09 Da.

However, ESI-MS analysis revealed that the SS14-containing fraction was significantly contaminated with an unknown peptide having a molecular weight of 5520.84 ± 0.09 Da (**Figure 4.3b**). Therefore, the initial expression and purification procedure had to be re-evaluated in order to improve the purity and yield of SS14. In particular, we had to understand the origin and identity of the contaminating polypeptide.

The protein mixture subjected to the TEV-protease treatment contained only two major components, namely the target fusion protein (20 kDa) and the unknown 25 kDa polypeptide. This unknown 25 kDa protein appeared to comprise the thioredoxin-6His fragment, as suggested from the SDS-PAGE analysis of the TEV-protease treated sample (**Figure 4.3a**, lane 8). Hence, the 5.5 kDa peptide may result from the proteolysis of the latter. It was hypothesized that the 25 kDa polypeptide and the 5.5 kDa peptide appearing

after the TEV-protease cleavage originated from an erroneous translation of the target gene by the host cells, most probably due to some putative reading through the stop codon. We then focused our further efforts on inhibiting the 25 kDa polypeptide expression.

Stop codon optimization

A stop codon read-through problem was described previously for the production of human interferon-α2b in *E. coli* LE 392 transformed with the pAG 11-3 expression vector [224]. In that study, the replacement of the natural stop signal TGA with TAA yielded the correct recombinant protein. Thus, the TGA codon was substituted with the stronger TAA one in the SS14 fusion construct (**Figure 4.4**). Unfortunately, this replacement did not have a significant effect on the amount of the read-through product (**Figure 4.4a**, lane 2): the ratio of the correct product to the read-through product was estimated to be approximately 65:35 % (ImageJ [185]).
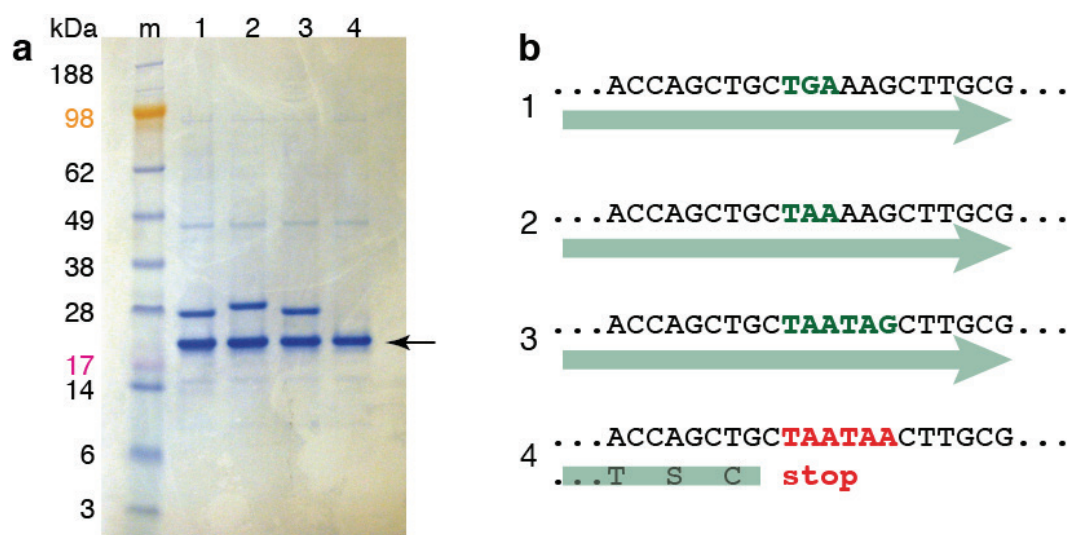
Figure 4.4. The efficiency of translation termination with different stop codon variants used in the expression vector for THX-SS14. (**a**) SDS/(4-12 %) PAGE analysis of the expression products: m – molecular weight standards with the corresponding masses in kDa labeled; lanes 1-4 reveal the products of THX-SS14 expression carried out with different variants of the stop codon sequence (shown schematically in **b**) purified on a HisTrapFF column. Variants 1-3 yielded an elongated product along with the target polypeptide (marked with the arrow in a) due to inefficient termination of translation by the stop codon. The stop codon variant 4 efficiently terminated the protein translation and yielded the correct THX-SS14 product. (**b**) Schematic representation of the stop codon region in the sequence of THX-SS14 expression vector. The DNA sequence is given in letters. The stop codon is highlighted in green or red (1-3 and 4, respectively). The translated polypeptide is shown by the green arrows. The numbers correspond to the numbers of lanes in **a**.

It is known from the literature that the nucleotide positioned downstream from the stop codon plays an important role in efficient translation termination [230]. For instance, the highest efficiency in modulation of termination was shown for the uridine nucleotide.

To test this in the SS14 expression system, the triplet following the stop codon was replaced by TAG or TAA yielding TAATAG and TAATAA sequences (**Figure 4.4b**, examples 3 and 4). In the case of the TAATAA sequence, only the target fusion protein was obtained, without the read-through product (**Figure 4.4a**, lane 4). The identity of the synthesized fusion protein as well as the purified SS14 was confirmed by ESI-MS. This vector coding the thioredoxin-SS14 fusion protein with the TAATAA sequence in the stop-codon region was used for the large-scale protein production.

Identification of 25 kDa and 5.5 kDa polypeptides

Even though the introduction of TAATAA sequence resolved the read-through issue, the following analysis was carried out in order to identify the contaminative polypeptide. The protein fraction isolated on a Ni-NTA Sepharose column was subjected to SDS-PAGE. The gel band running at approximately 25 kDa was cut out from the gel and treated by trypsin. The products of enzymatic degradation were analyzed by MALDI-MS/MS. The search of protein sequences was done by MASCOT MS/MS Ions Search tool [231]. The thioredoxin/transketolase fusion protein (synthetic construct) was identified with the highest score. Furthermore, the Edman degradation [232] of the contaminative 5.5 kDa peptide showed that the first 7 residues from its N-terminus are identical to respective residues of SS14. The occurrence of the elongated byproduct containing thioredoxin sequence, 6His-tag, TEVrs, and at least the N-terminal part of SS14 might be attributed to a stop codon read-through, which was observed in some cases in *E. coli* [224].

However, a simple stop codon read-through by misincorporation of a tryptophan instead of termination [224] would result in a polypeptide with a 6His-tag at its C-terminus (**Figure 4.5**). Yet, no retention of the cleaved 5.5 kDa peptide on Ni-NTA Sepharose was observed (data not shown). This apparent contradiction suggested the occurrence of a frame shift in the SS14 sequence in the region between Phe7 (based on the results from the Edman degradation) and the stop codon. A potential ±2 frameshift would yield a stop codon at position +53 after the designed stop codon resulting in a polypeptide with molecular weight at around 3.5 kDa. In contrast, a ±1 frame shift would possibly yield the 5.5 kDa peptide because of a stop codon positioned +107 nucleotides downstream from the original stop codon. Indeed, the ESI-MS/MS analysis of the 5.5 kDa peptide confirmed this hypothesis (**Figure 4.6, Supplementary Table S4.1**). The frameshift leading to the expression of the 25 kDa polypeptide was found to occur

directly after Phe7. Thus, both N-terminal peptide sequencing by the Edman degradation and ESI-MS/MS confirmed the identity of seven N-terminal residues (AGCKNFF) in the 5.5 kDa peptide and SS14. The downstream sequence (GKPLPAAES) determined by MS/MS was however different in the long peptide (**Figure 4.7**). Thus, the combination of DNA sequence analysis, N-terminal peptide sequencing by the Edman degradation, exact mass measurements by ESI-MS, and peptide sequence analysis by ESI-MS/MS allowed us to unambiguously identify the co-expressed long polypeptide and demonstrated that a +1 frameshift during translation is responsible for its occurrence.

```
ATGAGCGATAAAATTATTCACCTGACTGACGACAGTTTTGACACGGATGTACTCAAAGCG
 M   S   D   K   I   I   H   L   T   D   D   S   F   D   T   D   V   L   K   A
GACGGGGCGATCCTCGTCGATTTCTGGGCAGAGTGGTGCGGTCCGTGCAAAATGATCGCC
 D   G   A   I   L   V   D   F   W   A   E   W   C   G   P   C   K   M   I   A
CCGATTCTGGATGAAATCGCTGACGAATATCAGGGCAAACTGACCGTTGCAAAACTGAAC
 P   I   L   D   E   I   A   D   E   Y   Q   G   K   L   T   V   A   K   L   N
ATCGATCAAAACCCTGGCACTGCGCCGAAATATGGCATCCGTGGTATCCCGACTCTGCTG
 I   D   Q   N   P   G   T   A   P   K   Y   G   I   R   G   I   P   T   L   L
CTGTTCAAAAACGGTGAAGTGGCGGCAACCAAAGTGGGTGCACTGTCTAAAGGTCAGTTG
 L   F   K   N   G   E   V   A   A   T   K   V   G   A   L   S   K   G   Q   L
AAAGAGTTCCTCGACGCTAACCTGGCCGGTTCTGGTTCTGGCCATATGCACCATCATCAT
 K   E   F   L   D   A   N   L   A   G   S   G   S   G   H   M   H   H   H   H
CATCATTCTTCTGGTCTGGTGCCACGCGGTTCTGGTATGAAAGAAACCGCTGCTGCTAAA
 H   H   S   S   G   L   V   P   R   G   S   G   M   K   E   T   A   A   A   K
TTCGAACGCCAGCACATGGACAGCCCAGATCTGGGTACCGACGACGACGACAAGGCCATG
 F   E   R   Q   H   M   D   S   P   D   L   G   T   D   D   D   D   K   A   M
GCTGATATCGGATCCGAAAACCTGTATTTTCAGGCAGGCTGCAAAAATTTTTTTTGGAAA
 A   D   I   G   S   E   N   L   Y   F   Q   A   G   C   K   N   F   F   W   K
ACCTTTACCAGCTGCTGAAAGCTTGCGGCCGCACTCGAGCACCACCACCACCACCACTGA
 T   F   T   S   C   *   K   L   A   A   A   L   E   H   H   H   H   H   H   *
GATCCGGCTGCTAACAAAGCCCG
 D   P   A   A   N   K   A   R
```

Figure 4.5. Original nucleotide and amino acid sequence of the THX-SS14 fusion protein. The displayed sequence contains also a segment of the downstream plasmid sequence. The 6His-tag is highlighted in green; the TEV-protease recognition site is highlighted in purple, and the sequence of SS14 is in yellow. The region, which was changed during stop codon optimization, is highlighted in orange; an arrow indicates the length of nucleotide sequence, which is important for the termination of protein translation. Shown DNA sequence was confirmed by DNA sequencing.

NH₂–AGCKNFFGKPLPAAESLRPHSSTTTTTTTEIRLLTKPERKLSWLLPPLSNN–OH
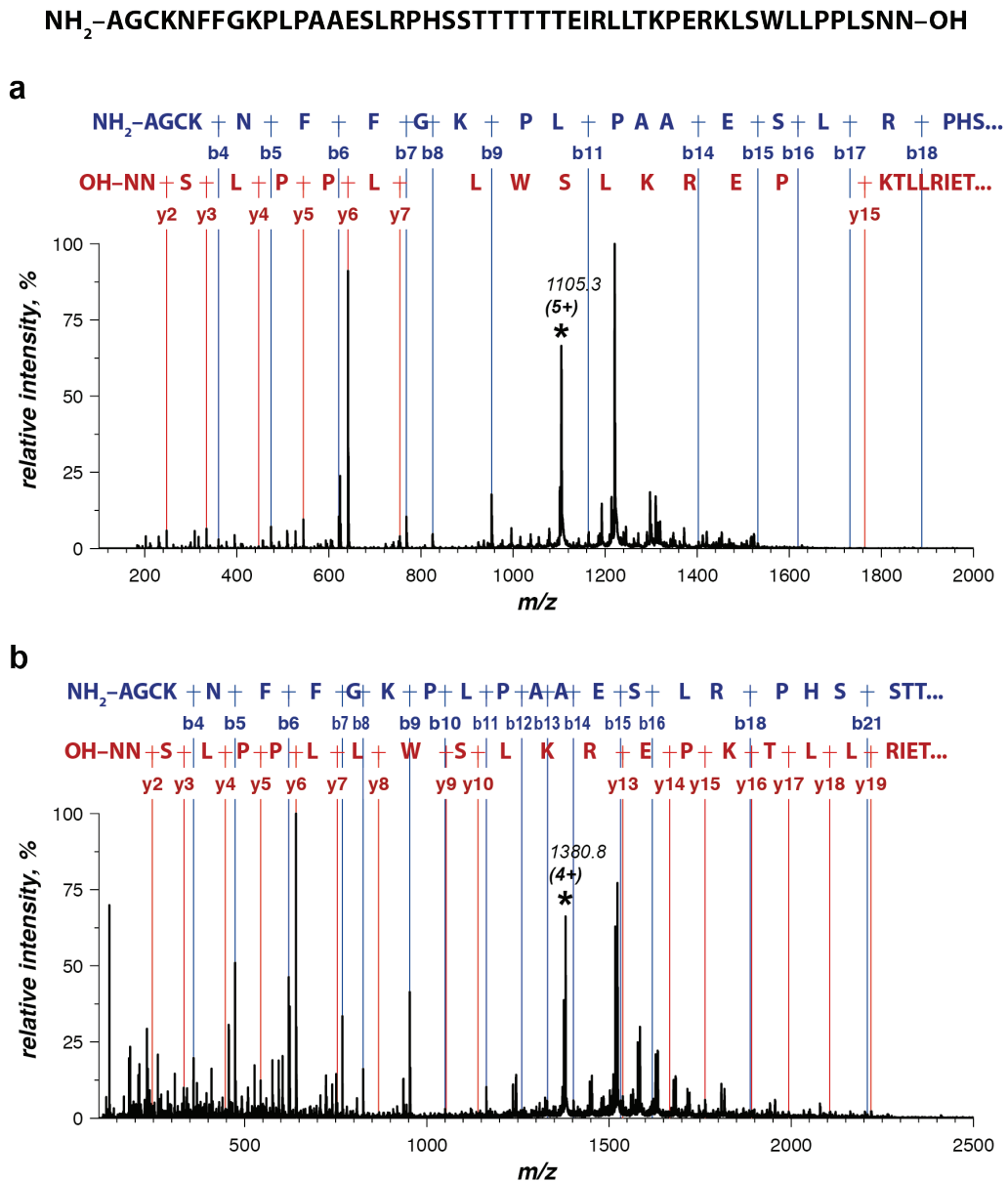
Figure 4.6. Identification of 5.5 kDa polypeptide by ESI-MS/MS. The precursor ion (marked with asterisk) was isolated by the quadrupole of Q-TOF mass spectrometer and subjected to collision-induced dissociation (CID) in the passive hexapole collision cell filled with argon. A collision energy offset of 20-30 V was applied prior to collision cell to increase the precursor ion kinetic energy and induce CID by amide bond cleavages. The m/z ratios of fragment ions were analyzed by the TOF. Each mass spectrum was produced by combining 100 individual scans (scan time 1 s) and smoothing the data using the moving average algorithm (window width 7 data points). The fragment ion peaks were assigned by matching the fragment masses theoretically generated for the sequence shown on top of the figure (the mass tolerance threshold was set to 50 ppm). Only singly charged ions of the b- and y-series fragments are shown. (**a**) MS/MS analysis of 1105.3[5+] ion reveals 18 residue-long N-terminal and 15 residue-long C-terminal sequence tags. (**b**) MS/MS analysis of 1380.8[4+] ion confirms 21 residue-long N-terminal and 19 residue-long C-terminal sequence tags.

```
GCAGGCTGCAAAAATTTTTTTTGGAAAACCTTTACCAGCTGCTGAAAGCTTGCGG
 A   G   C   K   N   F   F   G   K   P   L   P   A   A   E   S   L   R
CCGCACTCGAGCACCACCACCACCACCACTGAGATCCGGCTGCTAACAAAGCCC
 P   H   S   S   T   T   T   T   T   T   E   I   R   L   L   T   K   P
GAAAGGAAGCTGAGTTGGCTGCTGCCACCGCTGAGCAATAACTAGCATAACCCC
 E   R   K   L   S   W   L   L   P   P   L   S   N   N   *
TTGGGGCCTCTAAACGGGTGTCTTGAGGGGTGTCTTGAGGGGTTTTTTG
                        T7 terminator
```

Figure 4.7. Summary of ESI-MS/MS identification of the 5.5 kDa polypeptide. The displayed nucleotide sequence is compiled of the result of plasmid sequencing with T7 terminator as a primer and the pET-32a vector map provided by the manufacturer (Novagen) [233]. S-shaped sign indicates the point of conjunction of the two parts. N-terminal tag sequenced by ESI-MS/MS is highlighted in blue; C-terminal tag sequenced by ESI-MS/MS is highlighted in green. The region where the frameshift occurred is indicated by double-head arrow. Black line indicates T7 terminator sequence [233].

In summary, there is a frameshift directly after Phe7, which results in synthesis of the long side product. The stop codon and downstream sequence optimization effectively suppresses the expression of the unwanted 25 kDa polypeptide and thus the frameshift. However, the nature of this phenomenon remains unknown. It can be speculated that the mRNA segment around the codon of Phe7 has a tendency to form a secondary structure with downstream sequence regions including the stop codon, which leads to the frameshift. The optimization of the downstream stop codon sequence may suppress the upstream frameshift by breaking or altering the putative secondary structure. However, the details of organization of such secondary structure element, as well as the mechanisms responsible for the frameshift occurrence and suppression remain unknown.

Large-scale expression in minimal medium for stable isotope labeling

The ultimate goal of this study was to develop a method for the large-scale production of uniformly ^{13}C- and ^{15}N-labeled SS14 for NMR spectroscopy [183, 234]. A factor of 2-4 lower yield is usually obtained in the minimal medium (M9) when compared with rich media (such as LB) [183, 234]. Moreover, a relatively low yield of 330 μg SS14 per liter of rich LB medium was previously reported [210], further highlighting potential difficulties in obtaining high yields of SS14 in a minimal medium.

In order to optimize the expression of SS14 in M9 minimal medium, the effect of temperature, induction time point, and duration of expression was studied. First, the bacterial growth curve was measured in order to find the optimal induction point (**Figure 4.8**) [228]. The OD_{600} values of 1.4-1.6 corresponding to the middle of exponential phase were found to be optimal for induction [228], despite the fact that the value of 0.5-0.8 is recommended and most frequently used for pET plasmids and

BL21(DE3) cells [235, 236]. The protein yield obtained after the induction at optical densities 0.8 was approximately 30 % lower than that in the case of induction at $OD_{600} = 1.6$. No significant difference in the yield of the fusion protein was observed when the expression was done at +37 °C for 6-8 h or at +20 °C for 16-18 h. In both cases, the fusion protein of interest was found in the insoluble fraction. Expression at +20 °C for 16-18 h was chosen for practical reasons.
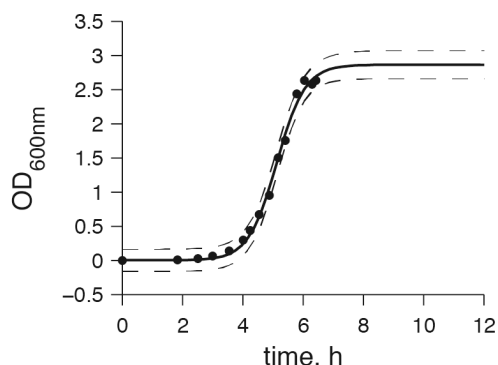
Figure 4.8. *E. coli* cell culture growth curve. The *E. coli* BL21* (DE3) cell culture growth in M9 medium was monitored by measuring the optical density at λ = 600 nm. The bacterial cells were transformed by the THX-SS14 expression vector (pET32a plasmid). Dots represent experimental data; solid line corresponds to the line of best fit derived from the logistic model [237]; dashed lines show the 95 % confidence interval for new observations.

Somatostatin purification

Since the thioredoxin-SS14 fusion protein was deposited in inclusion bodies, we chose denaturing conditions for its recovery. The cells were harvested and lysed following by centrifugation of the cell lysate. The insoluble fraction was subjected to consecutive solubilization in 8 M urea solution and Ni-chelate chromatography (**Figure 4.9**). At this stage, 95 % purity (SDS-PAGE gel analysis by ImageJ [185]) of the target protein was obtained. Urea and imidazole were removed by a buffer-exchange step to allow for subsequent cleavage of the fusion protein by the TEV-protease. 45 ml of the target fusion protein solution at the concentration of 1.3 mg/ml were subjected to enzymatic cleavage. Enzymatic processing of the fusion protein was nearly 100 %-complete (**Figure 4.9**, lane 6) yielding the reduced SS14 after 2 h of cleavage (ImageJ [185]). Some protein precipitation was observed during the enzymatic proteolysis. SDS-PAGE analysis of precipitate revealed the presence of N-terminal thioredoxin-containing part of the fusion protein and the TEV-protease (**Figure 4.9**, lane 7). Finally, further trapping of the N-terminal fragment as well as the recombinant His-tagged TEV-protease was achieved in another round of Ni-chelate chromatography (**Figure 4.9**).
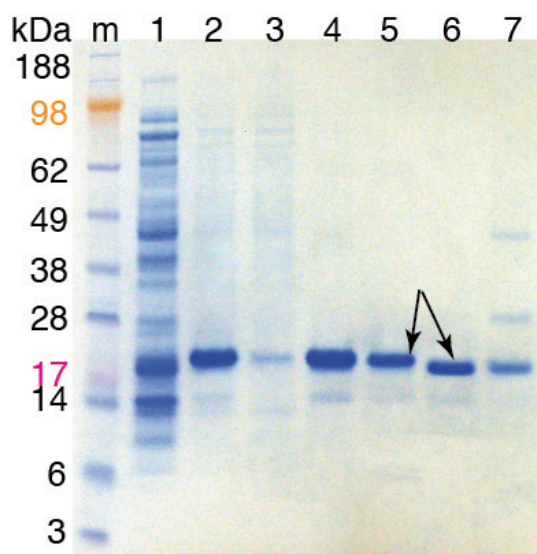
Figure 4.9. SDS-PAGE analysis of expression and purification of the THX-SS14 fusion protein in *E. coli* (SDS/4-12 % PAGE). The gel lanes are marked as follows: m – molecular weight standards with the corresponding masses in kDa labeled; 1 – soluble protein fraction obtained from the cell lysate; 2 – inclusion bodies dissolved in 8 M urea solution; 3 – flow-through of a solution applied to a HisTrapFF column; 4 – sample eluted from a HisTrapFF column by elution solution containing 300 mM imidazole; 5 – sample after buffer exchange to the cleavage buffer; 6 – sample after digestion by the TEV-protease at room temperature during 2 h at 1:100 enzyme:substrate ratio; 7 – precipitate that appeared during cleavage, loaded on the gel at 100-fold increased concentration. SS14 is not visible due to small molecular size. Successful cleavage can be determined by the slight shift of the fusion protein band (pointed by arrows).

NMR spectroscopy is very sensitive to sample impurities. To satisfy the high purity requirement, we utilized a semi-preparative RP-HPLC on the final step of SS14 purification. A typical elution profile (**Figure 4.10a**) featured several peaks, as monitored by the absorption at 280 nm, with one dominant peak eluting at 33 min. ESI-MS analysis confirmed that this major fraction contained pure reduced SS14 (**Figure 4.10b**). The obtained yield of reduced SS14 was 1.7 mg per liter of minimal medium.
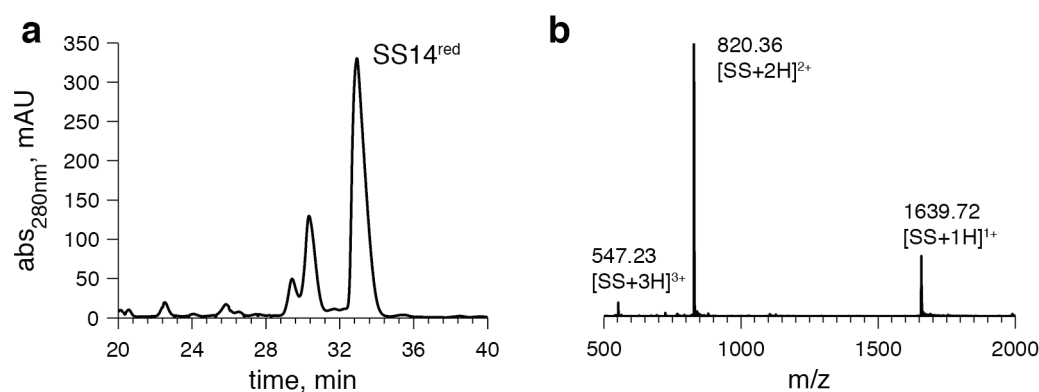
Figure 4.10. Isolation and identification of reduced SS14 using RP-HPLC. (**a**) A typical elution profile of the semi-preparative RP-HPLC of the flow-through solution obtained after the second Ni-chelate chromatography. Optical absorbance at $\lambda = 280$ nm was monitored. (**b**) ESI-MS spectrum of the peak running at 33 min of RP-HPLC (labeled as SS14^{red} in **a**). The mass corresponds exactly to the expected mass of reduced SS14. Notations as in **Figure 4.3b**.

Cyclization of reduced SS14

The formation of a disulfide bond is often a crucial step in peptide and protein production [238, 239]. Several oxidation procedures were tested in order to choose the most efficient and robust one. The first procedure was oxidation in Tris-HCl buffer

(50 mM Tris-HCl, pH 8.0) under constant stirring, as previously proposed by Notani et al. [205] and Rivier et al. [210, 240]. Slightly basic pH was necessary to deprotonate the SH-group of cysteines (pK$_a$ 8.1) to facilitate the formation of the disulfide bridge. The protein concentration in the reaction mixture was kept low (50-100 μg/ml) to minimize potential intermolecular bond formation. The oxidative cyclization was accomplished in 24-30 h, and longer incubation times did not yield more target product (data not shown). The products were separated by RP-HPLC followed by ESI-MS analysis, which determined the mass shift of -2 Da expected for the oxidized SS14 (1636.69 Da) relative to the reduced SS14 (1638.72 Da). The relative abundances of the correctly oxidized SS14, reduced SS14, and cross-linked oligomers were approximately 20 %, 15 %, and 20 %, respectively. At the very end of the elution profile, disulfide-linked multimers were eluted constituting the remaining 45 % of the eluted species (**Figure 4.11**, dashed line). Next, we tried to facilitate the oxidation procedure by performing the reaction under constant airflow. However, deep oxidation of cysteine residues to sulfones and sulfoxides decreased the yield of SS14 even further. Thus, the strategy of SS14 oxidation with dioxygen dissolved in Tris-HCl buffer was generally of low efficiency.

In an alternative method [238, 241], the oxidative cyclization of SS14 was performed by solution of potassium ferricyanide K$_3$[Fe(CN)$_6$]. The opposite strategies for intramolecular disulfide bond formation were suggested by Rivier et al. [238] and Chen et al. [241]. While Chen et al. [241] described the dropwise addition of the peptide to the K$_3$[Fe(CN)$_6$] solution, the oxidant was titrated into the dilute peptide solution in the work of Rivier et al. [238]. In both cases the intramolecular disulfide bond formation was favored by following the high dilution principle. In the present work, we compared both methods and found that the addition of the oxidant to the peptide was more efficient. This method proved to be efficient for SS14 providing a yield of 88 % (**Table 4.1**). The alternative method yielded only 70 % recovery of the target peptide, because SS14 was lost due to precipitation. Presumably, the diffusion of peptide added dropwise was not fast enough to ensure high dilution prior to intermolecular disulfide bridge formation yielding cross-linked multimers of SS14.
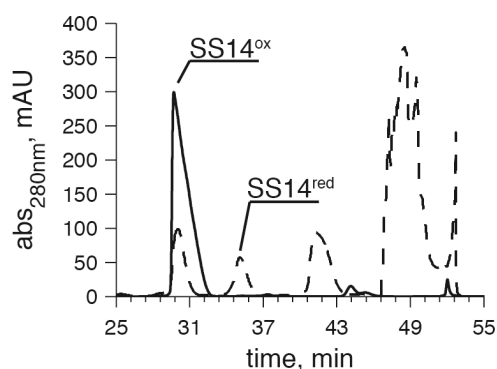
Figure 4.11. Comparison of SS14 cyclization procedures. RP-HPLC elution profiles of the products of SS14 oxidation by dioxygen dissolved in Tris-HCl buffer at pH 8.0 (dashed line) or with $K_3[Fe(CN)_6]$ in 100 mM ammonium acetate buffer at pH 6.8 (solid line). SS14^{ox} and SS14^{red} indicate the peaks of cyclized SS14 and linear SS14, respectively, which was confirmed by subsequent ESI-MS. The retention time of reduced SS14 is longer than that in **Figure 4.10** because of the greater injection volume.

The final yield of the cyclic SS14 amounted to 1.5 mg per one liter of the minimal medium, which was a factor of four higher than in the previously reported experiments using LB medium [210]. This corresponds to 32 % conversion of the fusion protein to the final product (**Table 4.1**).

Table 4.1

Purification of ^{13}C, ^{15}N-labeled SS14

Purification step	Volume (ml)	Total protein (mg)	Purity (%)	Recovery/efficiency (%)
Inclusion bodies extract	25	n/a	28^a	n/a
Purification on HisTrapFF	36	65	95^a	n/a
Buffer exchange	45	62	95^a	95
Enzymatic cleavage	45	n/a	95^a	>99
Secondary purification on HisTrapFF	67.5	2.6	66^b	58
RP-HPLC	54	1.7	>99^b	65
RP-HPLC after oxidation reaction	22	1.5	>99^b	88

n/a – was not determined

^{a} – determined by analysis of Coomassie stained [192] SDS-PAGE gels by ImageJ software [185]

^{b} – determined by RP-HPLC analysis

The efficiency of transition from the previous to the current purification step is reported in the column Recovery/Efficiency.

^{13}C/^{15}N enrichment and heteronuclear NMR spectroscopy

Highly ^{13}C- and ^{15}N-enriched samples are required for high-performance heteronuclear NMR spectroscopy. The degree of ^{13}C and ^{15}N metabolic incorporation is only limited by the level of enrichment of the substrates utilized in a cell-culturing medium. High-resolution mass spectra of uniformly labeled SS14 were measured in order to analyze the achieved ^{13}C- and ^{15}N-enrichment level upon overexpression in minimal medium with ^{13}C glucose as the single carbon source and ^{15}NH$_4$Cl as the only nitrogen

source. The experimental isotopic pattern was compared to the theoretical distribution. A 99 % enrichment of SS14 with ^{13}C and ^{15}N was found (**Supplementary Figure S2**), which corresponds to the enrichment level of the used carbon and nitrogen source compounds and indicates 100 % efficiency of incorporation.

In addition to the mass spectrometric data, NMR spectroscopy can provide insights into the purity and conformation of purified SS14. All backbone amino acid residue resonances were retrieved and assigned, as demonstrated by **Figure 4.12** showing a 2D [^{15}N,^{1}H]-TROSY spectrum [193]. The sequential assignment obtained from the 3D TROSY-HNCACB [186] spectrum confirmed the correct sequence of SS14 (data not shown).
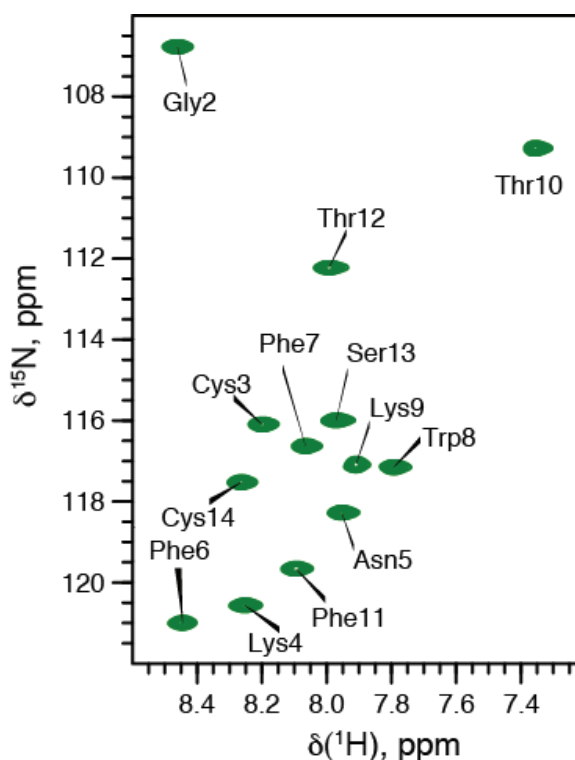
Figure 4.12. 2D [^{15}N, ^{1}H]-TROSY spectrum of ^{15}N, ^{13}C-labeled SS14 in DMSO. The spectrum was measured for the 700 µM solution of ^{15}N, ^{13}C-labeled SS14 in DMSO-D6, containing 0.02 % TFA-D at 30 °C on a Bruker 700 MHz spectrometer. The individual cross peaks were identified via sequential assignment of triple resonance spectra.

Conclusions

In the present work, a method for high-efficient heterologous expression of recombinant human SS14 is reported. Careful selection of the expression system and optimization of the synthetic gene ensured stable synthesis of the target protein in high abundance and allowed for the relatively simple transition from low- to large-scale

synthesis. The optimized conditions for the expression provided the high yield of the recombinant SS14 even in M9 minimal medium. The final yield of cyclic SS14 amounted to 1.5 mg per one liter of minimal medium, corresponding to 32 % conversion of the fusion protein to the final product. The method is suitable for uniform labeling of SS14 by metabolic incorporation of ^{13}C and ^{15}N up to the highest possible degree of stable isotope enrichment, which delivers high-quality samples for NMR studies.

Our study also demonstrates that the biology of the host organism may interfere with recombinant gene expression and can lead to an unexpected result. Here, we showed that the frameshift occurring during translation resulted in co-expression of a longer polypeptide along with the target product. The presence of this side product decreased the yield of the SS14-containing fusion protein expression and complicated the purification of SS14. DNA sequencing combined with amino acid sequencing by the Edman degradation and high-resolution mass spectrometry allowed for the identification of the side product and the frameshift site. Interestingly, the optimization of the stop codon region of the recombinant gene resulted in a complete suppression of the side product synthesis, even though the frameshift occurred in a remote site upstream of the stop codon in the original DNA construct.

Methods

Materials

Tris(hydroxymethyl)aminomethane for molecular biology was provided by BiosolveBV (Valkenswaard, Netherlands). Phenylmethanesulfonyl fluoride (PMSF), isopropyl β-D-1-thiogalactopyranoside (IPTG), and ampicillin were purchased from AppliChem (Darmstadt, Germany). Lysozyme from chicken egg, calcium chloride $(CaCl_2)$, and potassium hexacyanoferrate (III) $(K_3[Fe(CN)_6])$ were obtained from Fluka production GmbH (Buchs, Switzerland). Glucose, sodium chloride (NaCl), ammonium chloride (NH_4Cl), and ammonium hydroxide (NH_4OH), ammonium acetate for analysis from Merck KGaA (Darmstadt, Germany) were used in this work. Trifluoroacetic acid (TFA) for HPLC was obtained from Fisher Scientific AG (Loughborough, UK). Fully deuterated dimethyl sulfoxide (DMSO-D6) (D, 99.96 %) and fully deuterated trifluoroacetic acid (TFA-D) (D, 99.5 %) for NMR measurements were from Cambridge Isotope Laboratories (Andover, Massachusetts, USA). All other reagents including labeled substrates ^{13}C-glucose (^{13}C > 99 %) and ^{15}N-ammonium chloride (^{15}N-NH_4Cl)

(^{15}N > 98 %) and acetonitrile CHROMASOLV® gradient grade, for HPLC, ≥ 99.9 % were purchased from Sigma-Aldrich (Buchs, Switzerland), unless stated otherwise.

Strains and plasmids

One Shot® Top10 chemically competent *E. coli* cells from Invitrogen (Invitrogen™ by LifeTechnologies™, LuBioScience GmbH, Lucerne, Switzerland) were used as the bacterial host for DNA cloning. For protein expression, *E. coli* One Shot® BL21 Star™ (DE3) strain was obtained from Invitrogen and the T7 plasmids pET32a and pMAL-c5X were purchased from Novagen (Merck KGaA, Darmstadt, Germany) and New England BioLabs, Inc. (Beverly, Massachusetts, USA), respectively. The oligonucleotides listed in **Table 4.2** were purchased from Microsynth AG (Balgach, Switzerland). DpnI endonuclease from New England BioLabs, Inc. (Bioconcept, Allschwil, Switzerland) and Pfusion DNA Polymerase from Finnzymes part of Thermo Fisher Scientific (Espoo, Finland) were used in this work. The DNA coding sequence of somatostatin was engineered and cloned into pET32a and pMAL-c5X plasmids by GeneArt (Burlingame, California, USA). The recombinant proteins contained SS14 fused at its N-terminus to carrier proteins: (*i*) thioredoxin with a hexa-histidine tag (6His) and a TEV-protease recognition site (pET32a vector) (**Figure 4.1a** and **4.5**) or (*ii*) maltose-binding protein followed by a flexible spacer containing 6His tag and the TEV-protease cleavage site (pMAL-c5X vector) (**Figure 4.1b**). Theoretical molecular weights of the recombinant proteins and molar extinction coefficients were calculated by ProteinCalculator v3.4 [190].

Point mutations

Point mutations were introduced in the stop codon region of pET32a/SS14 expression vector by PCR using the primers listed in **Table 4.2**. PCR reactions were performed using Phusion DNA Polymerase (1U), 0.5 μM of each primer (forward and reverse), 5xPhusion HF Buffer, and 0.2 mM dNTPs. The following PCR parameters were used: denaturation at +98 °C for 5 s, annealing at +62 °C for 25 s, and extension at +72 °C for 2.5 min (the cycle was repeated 30 times). The removal of the template vector was performed by DpnI endonuclease according to the protocol of the enzyme manufacturer, New England BioLabs, Inc. (Bioconcept, Allschwil, Switzerland) Incorporation of the desired nucleotides was verified by DNA sequencing.

Table 4.2

Primers used to introduce point mutations in the stop codon region of the recombinant gene coding THX-SS14

Termination signal	Primers*
TAA	Fw 5'-ACCTTTACCAGCTGC<u>TAA</u>AAGCTTGCGGCCGC-3' Rv 5'-GCGGCCGCAAGCTT<u>TTA</u>GCAGCTGGTAAAGGT-3'
TAATAG	Fw 5'-AAACCTTTACCAGCTGC<u>TAATAG</u>CTTGCGGCCGC-3' Rv 5'-GCGGCCGCAAG<u>CTATTA</u>GCAGCTGGTAAAGGTTT-3'
TAATAA	Fw 5'-ACCTTTACCAGCTGC<u>TAATAA</u>GCTTGCGGCCGC-3' Rv 5'-GCGGCCGCAAGC<u>TTATTA</u>GCAGCTGGTAAAGGT-3'

* Fw – the DNA sequence of forward primer; Rv – the DNA sequence of reverse primer.

Expression and purification of recombinant protein

The plasmids obtained from GeneArt were used to transform the host *E. coli* One Shot® BL21 Star™ (DE3) strain (Invitrogen™ by LifeTechnologies™, LuBioScience GmbH, Lucerne, Switzerland). Cells were precultured in 5 ml of M9 minimal medium overnight at +37 °C. 1 L of M9 medium containing 3 g of $^{13}C_6$-D-glucose and 1 g of $^{15}NH_4Cl$ was inoculated with the starting culture. Cells grew at +37 °C and 120 rpm with 100 mg/L ampicillin. Recombinant gene expression was induced by adding IPTG to 1 mM when the optical density at 600 nm reached 1.4. Expression was performed at +20 °C overnight (16 h). Cells were harvested by centrifugation at 10^4 g (Avanti J-26 XP, Beckman Coulter International S.A., Nyon, Switzerland) at +4 °C for 30 min. 4.5 g of wet cell pellet was resuspended in 25 ml of lysis buffer (50 mM Tris-HCl, 150 mM NaCl, 1 mM DTT, pH 7.0), PMSF and lysozyme were added to a final concentration of 1 mM and 0.5 mg/ml, respectively. The lysate was incubated at room temperature under constant stirring for 30 min. Afterwards, cells were further disrupted by passing the suspension several times through the 110S microfluidizer (Microfluidics, Newton, Massachusetts, USA) at 40 psi. The solution was centrifuged at 2.5×10^4 rpm (rotor 45 Ti, Optima L-90K Ultracentrifuge, Beckman Coulter International S.A., Nyon, Switzerland), +6 °C for 1 h. The precipitate was resuspended in 25 ml of extraction buffer (50 mM Tris-HCl, 8 M urea, 150 mM NaCl, 10 mM imidazole, 1 mM DTT, pH 7.5). Extraction of the fusion protein was carried out for 16 h at room temperature. The extract was centrifuged at +22 °C, 4×10^4 rpm (rotor 45 Ti, Optima L-90K Ultracentrifuge) for 1 h. The supernatant was purified on a HisTrapFF 5 ml column (GE Healthcare AG, Glattbrugg, Switzerland) by 7-ml increments. The fusion protein was eluted by elution

buffer 1 (50 mM Tris-HCl, 7 M urea, 150 mM NaCl, 1 mM DTT, 300 mM imidazole, pH 7.5). 36 ml of the protein solution were subjected to buffer exchange on a HiPrep 26/10 desalting column (GE Healthcare AG, Glattbrugg, Switzerland) by 12 ml increments. Elution buffer 1 was exchanged to the cleavage buffer (50 mM Tris-HCl, 150 mM NaCl, 1 mM DTT, pH 7.5). Next, the fusion protein was treated with the TEV-protease (made in house according to [191]) in a molar ratio of 1:100 at room temperature. After 2 h, the solution was centrifuged at 4×10^3 rpm (Biofuge primo R, Heraeus, Fischer Scientific AG, Reinach, Switzerland) for 15 min at +22 °C. 45 ml of collected supernatant were subjected to another round of affinity chromatography on a HisTrapFF 5 ml column preliminary equilibrated in the lysis buffer containing 20 mM imidazole. 6His-tagged species were then trapped on the support while the flow-through peptide-containing fraction was collected. Acetonitrile was added to the peptide solution up to 5 % (vol.) prior to reversed-phase chromatography (RP). Then the solution was acidified to pH 2.0 by the addition of TFA to a final concentration of 0.3 % (vol.). The HisTrapFF column was recovered by washing with the elution buffer 2 (50 mM Tris-HCl, 150 mM NaCl, 1 mM DTT, 300 mM imidazole, pH 7.0) and equilibrated again in the lysis buffer with 20 mM imidazole. The loading-elution procedure was repeated three times.

RP-HPLC of peptide products

Reduced and oxidized forms of SS14 were purified on a Discovery BIO Wide Pore C18 column (25 cm x 10 mm, 10 μm; Supelco, Bellefonte, Pennsylvania, USA). The elution was carried out using an acetonitrile gradient (17-27 % buffer B in 6 min, followed by 27-36.8 % buffer B in 36 min; flow rate – 2 ml/min; buffer A - water with 0.1 % TFA, buffer B – acetonitrile with 0.1 % TFA). An Agilent 1200 HPLC system (Agilent Technologies (Schweiz) AG, Basel, Switzerland) equipped with an external manual injector, an automatic fraction collector, and a diode-array detector was used. The elution profile was monitored by UV absorption at 220 and 280 nm. Some fractions were subjected to ESI-MS. Fractions containing either reduced or oxidized SS14 were collected, combined accordingly, and freeze-dried.

Oxidation of SS14

Lyophilized SS14 was dissolved at 7 μM concentration in 100 mM ammonium acetate solution pH 6.8. A filtered solution of 50 mM $K_3[Fe(CN)_6]$ was added dropwise to

the peptide solution until the solution color turned to light yellow. The reaction was performed under nitrogen flow and constant stirring. The pH was maintained at 6.8. At the end of the reaction, the pH was decreased to 2.0 by addition of TFA. Acetonitrile was added up to 5 % (vol.). The final purification step to obtain oxidized SS14 was carried out by RP-HPLC, following the protocol described above (*RP-HPLC of peptide products*). The presence and purity of the recombinant protein at different stages was monitored by ESI-MS (Q-TOF Ultima API, Micromass, Manchester, UK). Fractions containing cyclic SS14 were merged and lyophilized.

Mass spectrometry

Mass spectra were acquired on a hybrid quadrupole-time-of-flight mass spectrometer Q-TOF Ultima API (Micromass, Manchester, UK) equipped with a Z-spray interface (Waters, Manchester, UK). Ions were generated using an automated chip-based nano-electrospray ion source (NanoMate model 100, Advion BioSciences, Ithaca, NY, USA) at a high voltage of 1.3-1.7 kV applied to the electrospray emitter chip. A backing pressure of 0.5 bar was used to assist the sample flow, and the typical flow rate was approximately 200 nL/min. The ion source was kept at room temperature. Potentials on the ion guides were optimized to ensure efficient ion transmission in the *m/z* range of 100-4000 for the peptide samples or 300-8000 for the protein samples. A single scan time of 1 s was used, and typically 50-100 scans were combined to obtain a representative mass spectrum. Spectra were managed and processed via the MassLynx v. 4.0 software (Waters, Manchester, UK). Multiply-charged peaks in the electrospray spectra were deconvoluted, where necessary, using the MaxEnt 1 tool embedded within the MassLynx software. Mass calibration was performed using CsI clusters. Peptide and protein samples were infused either directly after RP-HPLC or upon desalting, if required, using a ZipTip C18 column (Millipore AG, Zug, Switzerland) according to the procedure described by the manufacturer.

Tryptic digestion

The gel band of the protein of interest was cut into small pieces, washed twice with 100 μl of 100 mM NH_4HCO_3 solution in 50 % acetonitrile, and then washed with 50 μl of acetonitrile. All three supernatants were discarded. The cleavage was done overnight at +37 °C in 20 μl of buffer (10 mM Tris-HCl, 2 mM $CaCl_2$, pH 8.2) with 0.1 μg of trypsin (proteomics grade, BioReagent, Sigma-Aldrich). The supernatant was

removed and the gel pieces were extracted twice with 100 µl of 0.1 % TFA in 50 % acetonitrile. All three supernatants were combined and dried. Samples were dissolved in 20 µl of 0.1 % TFA. The samples were desalted by using a ZipTip C18 column and mixed 1:1 with the matrix solution (5 mg/ml α-cyano-4-hydroxycinnamic acid (HCCA) in 0.1 % TFA, 50 % acetonitrile). The resulting sample was then used for MALDI-MS/MS analysis.

Edman degradation, protein electrophoresis and concentration measurements

The Edman degradation was performed as described elsewhere [232]. The expression and purification processes were monitored by protein electrophoresis [192] using denaturing NuPAGE® Novex® 4-12% Bis-Tris Gels (Invitrogen™ by LifeTechnologies™, LuBioScience GmbH, Lucerne, Switzerland) and SeeBlue® Pre-Stained Standard from Invitrogen™ according to the manufacturer's instructions. ImageJ software [185] was used for quantitative analysis of Coomassie-stained [192] SDS-PAGE gel images. The protein concentration was determined by UV spectroscopy (280 nm; $\varepsilon_{\text{THX-SS14}} = 20910 \text{ M}^{-1} \text{ cm}^{-1}$, $\varepsilon_{\text{SS14 linear}} = 5690 \text{ M}^{-1} \text{ cm}^{-1}$, $\varepsilon_{\text{SS14 cyclic}} = 5810 \text{ M}^{-1} \text{ cm}^{-1}$).

NMR spectroscopy

The peptide used in the NMR experiments was prepared according to the protocol suggested in this manuscript. 0.4 mg of lyophilized cyclic ^{15}N, ^{13}C-labeled SS14 was dissolved in 300 µl DMSO-D6, 0.02 % TFA-D. NMR spectra of the 2D [^{15}N, ^{1}H]-TROSY [193] and 3D TROSY-HNCACB [186] were recorded at +30 °C on a Bruker 700 MHz spectrometer equipped with a cryoprobe. The spectra were processed with TopSpin 2.0 (Bruker BioSpin AG, Fällanden, Switzerland) software and assigned using the CCPN software package [194]. Sequential connectivities were established by the 3D TROSY-HNCACB experiment following established procedures [186].

Chapter 5

Towards a high-resolution structure of the amyloid state of somatostatin 14[1]

Introduction

The structure and activities of SS14 have been under deep investigation since the hormone was identified in 1973 [242]. SS14 is involved in a very wide hormonal network as an inhibitor of many regulatory cascades [195]. As many other hormones, SS14 is synthesized as part of a larger precursor molecule, which is promptly processed into mature forms. Although converting enzymes are present along the whole secretory pathway (from the ER via the GC to secretory granules) the enzymatic cleavage of prosomatostatin is strongly associated with secretory granules [243, 244]. Among six known polypeptides originated from prosomatostatin only two, namely somatostatin 14 and somatostatin 28 (SS14 with elongated N-terminus), interact with classical somatostatin receptors and induce the respective response [245].

SS14 is one of the shortest human peptide hormones. It possesses a disulfide bridge, which imposes limitations on the possible conformation of SS14 in solution. The pioneering CD spectroscopy-based structural study of this peptide revealed that SS14 has a stable structure in aqueous solution: a hairpin loop consisting of two anti-parallel β-strands with hydrophobic domain at one end and a hydrophilic domain at the other end [202]. The laser Raman spectroscopy study by Han et al. also revealed the stable β-hairpin loop conformation of SS14 in aqueous solution [14]. On the other hand, liquid-state ^{1}H-NMR spectroscopy indicated conformational flexibility of SS14 in DMSO [200]. Finally, Hallenga et al. suggested based on liquid-state ^{1}H-NMR data that the native SS14 exists in aqueous solution in equilibrium between several low-energy flexible conformations featuring a β-turn structure between Trp8 and Thr12 [15]. Remarkably, the conformation of SS14 in DMSO differed from that in water [200]. Thus, even though there is no consensus on the solution-phase conformation of SS14 reached, SS14 very likely adopts the stable β-hairpin loop structure in solution. The potential existence of the

---

naturally preformed β-hairpin loop conformation in solution prompts a suggestion that SS14 can undergo the transition from a monomeric β-sheet to a stack of β-sheets, i.e. forms amyloid fibrils. This was however not observed when SS14 was initially tested for fibril formation propensity among other 20 neuropeptides [34]. Only the linear, i.e. reduced and non-functional form of SS14 could form fibrils in 2 % (w/v) NaCl solution at a peptide concentration of 5 mg/ml. Long fibrillar structures of 5-7 nm in width were observed by EM (**Figure 5.1a**). Nevertheless, the cyclic form of SS14 also did not remain monomeric under the same conditions, but formed so-called non-fibrillar amorphous aggregates instead (**Figure 5.1b**) [34].
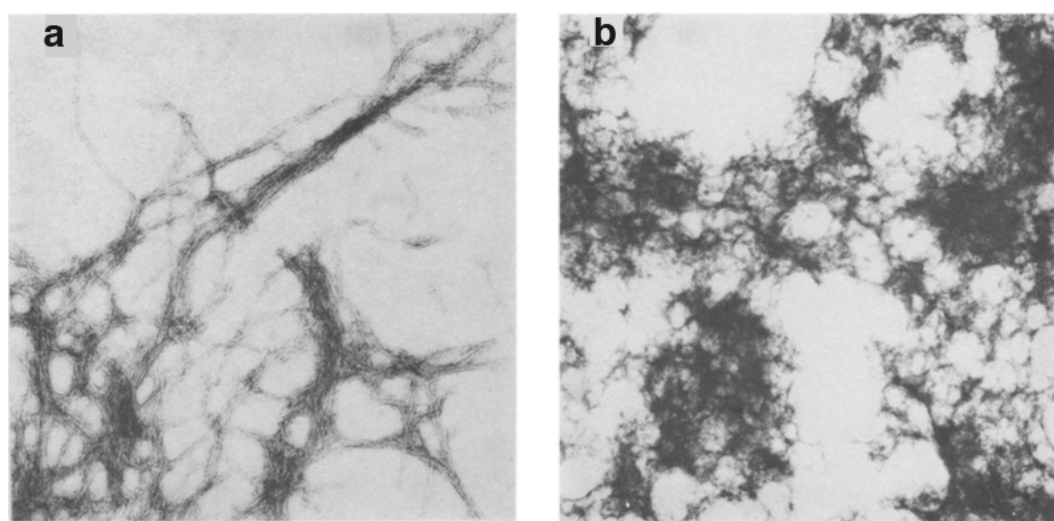
Figure 5.1. Electron micrographs of SS14 aggregates. (**a**) Linear SS14 forms fibrillar structure. Magnification 9×10^5. (**b**) Cyclic SS14 demonstrates non-fibrillar amorphous aggregates. Magnification 10^6. Reproduced from [34].

Later studies demonstrated the ability of the oxidized functional form of SS14 to form fibrillar structures, too [246, 247]. Aggregation of cyclic SS14 at very high concentrations led to amyloid fibril formation. For instance, van Grondelle et al. [246] let SS14 aggregate at a concentration of 30-100 mg/ml and obtained fibrils characterized as amyloid by EM, Congo red staining, and X-ray scattering. Detailed structural studies by vibrational spectroscopy (ATR-FTIR and Raman scattering) and cryo-EM allowed for proposing the model of SS14 packing into amyloid fibrils (**Figure 5.2**) [247]. It was suggested that laterally aggregated SS14 monomers in β-hairpin conformation arranged into protofibrils featuring antiparallel β-sheets. In turn, mature amyloid fibrils were built of these elementary units, protofibrils. This model provides an insight into the molecular organization of SS14 fibrils but does not yield structural details at the level of atomic resolution because it is based on the data of low spatial resolution. However, it can

complement the data of other high-resolution methods and help to generate the atomic model of the SS14 amyloid.
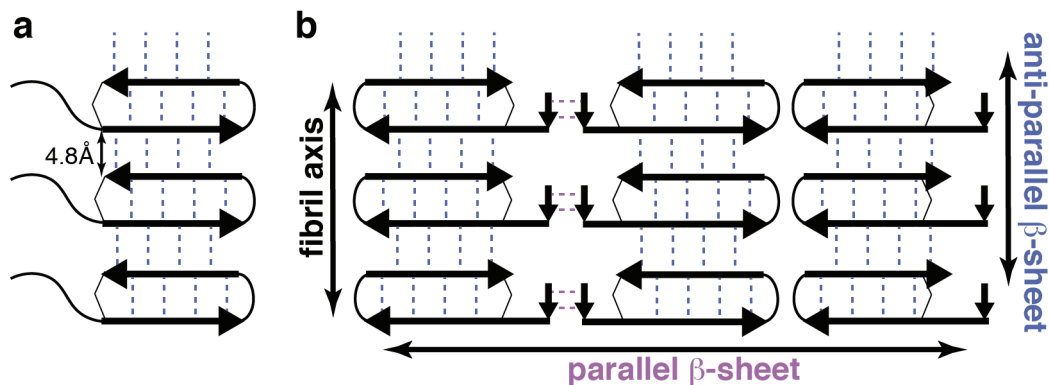
Figure 5.2. Hypothesized scheme of SS14 fibrils organization. (**a**) β-hairpin conformation of SS14 in the protofibril. (**b**) Packing of protofibrils into the mature amyloid fibril. Dashed lines represent hydrogen bonds. Adapted from [247].

Maji et al. [31] performed studies of SS14 aggregation in a more biologically relevant context than van Grondelle et al. [246, 247]. They used 5 % D-mannitol solution at pH 5.5 containing heparin to mimic the secretory granule environment, taking into account the decrease in pH along the secretory pathway [41, 55] and high abundance of carbohydrates in the ER and GC [68]. SS14 formed amyloid fibrils at 2 mg/ml concentration under the conditions used by Maji et al. [31]. The work of Maji et al. [31] emphasized the potentially highly important role of the secretory granule environment and their constituents, such as sugars and GAGs, in hormone aggregation. However, no insight into the structure of SS14 amyloid or molecular mechanisms of aggregation was provided.

The controversy of results described above is remarkable. Despite the structure of SS14 is a preformed β-hairpin rigidified by the intramolecular disulfide bond, the hormone did not readily aggregate into amyloid fibrils, unless its concentration was increased to an immensely high level [246, 247]. That said, the presence of heparin and mannitol, which are suspected to co-localize with SS14 in secretory granules, afforded SS14 amyloid fibrils at lower peptide concentration [31]. Further investigations of the factors that influence SS14 aggregation and the structure of SS14 amyloid fibrils are therefore necessary to understand the molecular mechanisms of SS14 functional amyloid formation.

In parallel, we investigated the amyloid state of SS14 by fluorescence, electron, and optical microscopy. The results described in this chapter represent early steps towards determining the high-resolution 3D structure of the SS14 amyloid.

Results and discussion

Morphological transitions during SS14 aggregation

Previous studies of amyloid formation by SS14 were done mainly in pure water and saline solution [34, 246, 247]. Although biological aspect of aggregation was taken into account by Maji et al. [31], the study did not aim to solve the molecular mechanisms of hormonal amyloid formation as well as the 3D structure of the functional hormone amyloid.

Our first step towards understanding of the molecular mechanisms of hormonal amyloid aggregation was the characterization of morphological changes upon SS14 aggregation. We visualized SS14 aggregates at different time points by EM (**Figure 5.3**). Fibril formation was facilitated by agitation (30 rpm) at higher temperature. This result was in agreement with observations for other aggregation-prone proteins, such as lysozyme [248] and insulin [249], which aggregated upon vigorous agitation while remained intact at quiescent conditions. Amorphous aggregates observed after 30 min incubation of SS14 in aggregation buffer in the presence of heparin (**Figure 5.3a**, **d**) appeared to be very similar to non-fibrillar aggregates found for cyclic SS14 by Oakley et al. [34] (**Figure 5.1b**). With time, SS14 developed fibrillar structures in both cases, with and without agitation.

The morphology of intermediate aggregates obtained under slight agitation was however different from that under quiescent conditions. Narrow ribbons observed at early stages of aggregation under agitation transformed into tight twisted fibers. The periodicity of twists decreased from 75-100 nm to 15-30 nm (**Figure 5.3b-c**). Aggregation under quiescent conditions was slower. After 3 days of aggregation, round-shape structures replaced amorphous aggregates. Interestingly, the shape of SS14 aggregates appeared to be pretty regular and well defined. SS14 formed octagons with the distance of 32-38 nm between two opposite sides (**Figure 5.3e**). Later on, mature SS14 fibrils arose, but they were different from the ones formed under agitation (**Figure 5.3c**, **f**). The majority of quiescent fibril population was represented by rather short, 40-80 nm, and thin, 5-7 nm, fibrils (**Figure 5.3f**, indicated by arrows). Periodical twists were not anymore the

characteristic feature of these fibrils – the aggregates appeared as rod-like structures instead. Longer incubation of the peptide either under agitation or under quiescent conditions did not yield fibrils of any new morphology.
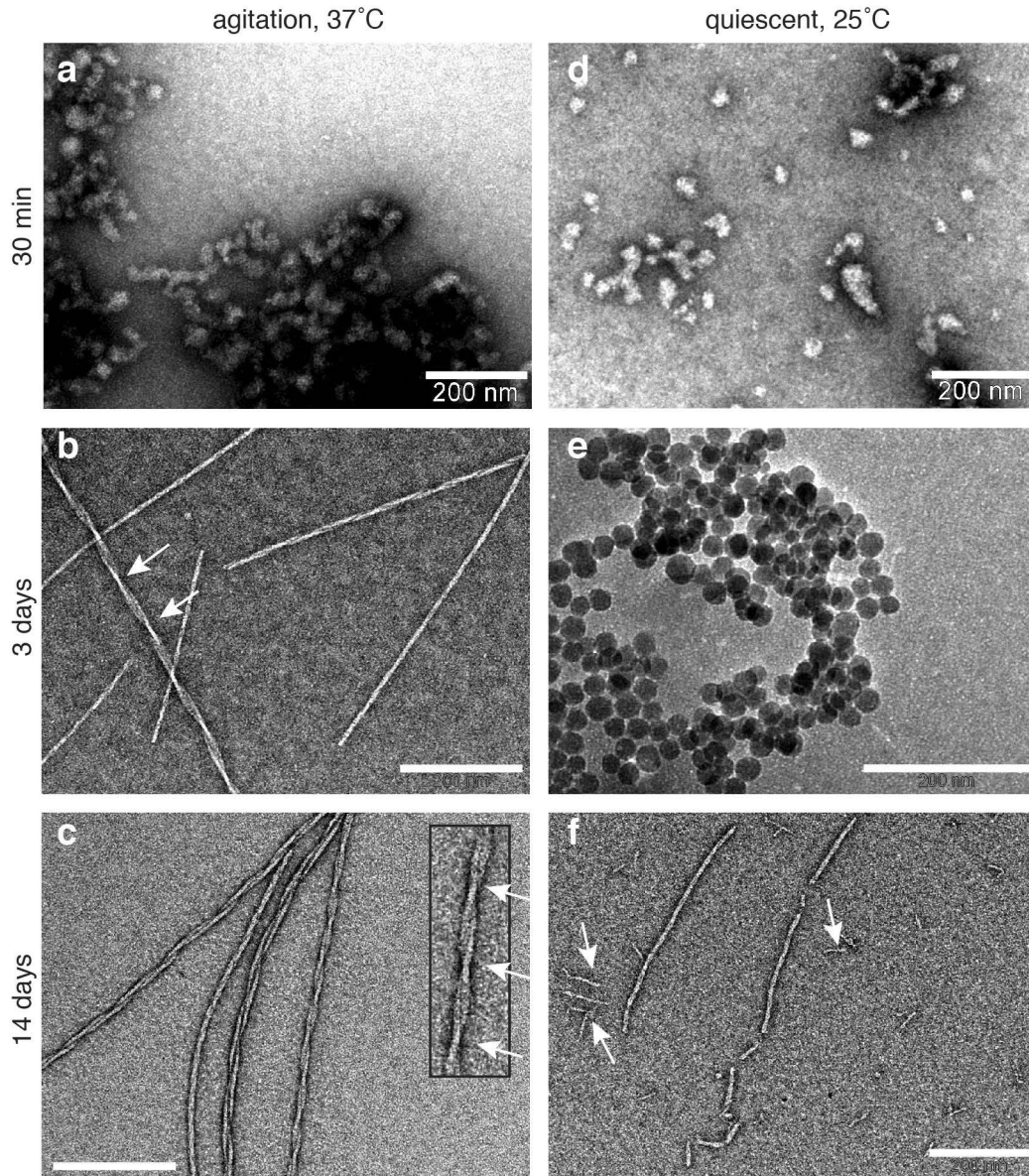
Figure 5.3. Electron micrographs of SS14 aggregates at different time points of aggregation under slight agitation (30 rpm) at +37 ºC (**a-c**) or at room temperature under quiescent conditions (**d-f**). Time points: (**a**), (**d**) – 30 min of aggregation; (**b**), (**e**) – 3 days of aggregation; (**c**), (**f**) – 14 days of aggregation. Arrows in panel **b** and in the inset in panel **c** showing a fibril at higher magnification point to fibril twists. Arrows in **f** indicate thin and short fibrils representing the majority of observed SS14 fibrils formed under quiescent condition. Scale bars – 200 nm.

The terminal state of SS14 aggregates obtained at +37 ºC under slight agitation was confirmed to be an amyloid based on the following characteristics. (*i*) The structures observed by EM (**Figure 5.4a**) had fibrillar morphology, with a diameter of 5-18 nm. Their length varied from 30 nm to 2-3 μm. Twisting along the fibril axis had an apparent

periodicity of 15-30 nm. (*ii*) The aggregates bound amyloid-specific dies [33, 87], such as ThT and CR (**Figure 5.4b-d**). ThT fluorescence increased 6-fold upon interaction with SS14 fibrils. Birefringence effect was observed for CR-stained SS14 fibrillar material deposited on a poly-lysine glass slide under a polarized light microscope upon crossing the polarizer and analyzer at 90 º angle (**Figure 5.4c**).

Interestingly, it was not possible to deposit SS14 fibrils on regular glass slides. This phenomenon can be explained by the presence of heparin in the sample. Heparin is a highly hydrophilic polymer carrying multiple negative charges [76], which likely prevented the adhesion of SS14-heparin aggregates on the negatively charged glass surface [250]. Alkaline treatment of the sample during the staining procedure [76] increased the density of negative charges on the glass surface even further, which contributed to the inhibition of fibrils binding to the glass [87, 250]. Instead, ionic interactions between poly-lysine coating and negative charges of heparin allowed for tight binding of the protein sample to the surface. This suggests that heparin is tightly associated with the SS14 amyloid fibrils, if not an integral structural element of these aggregates.
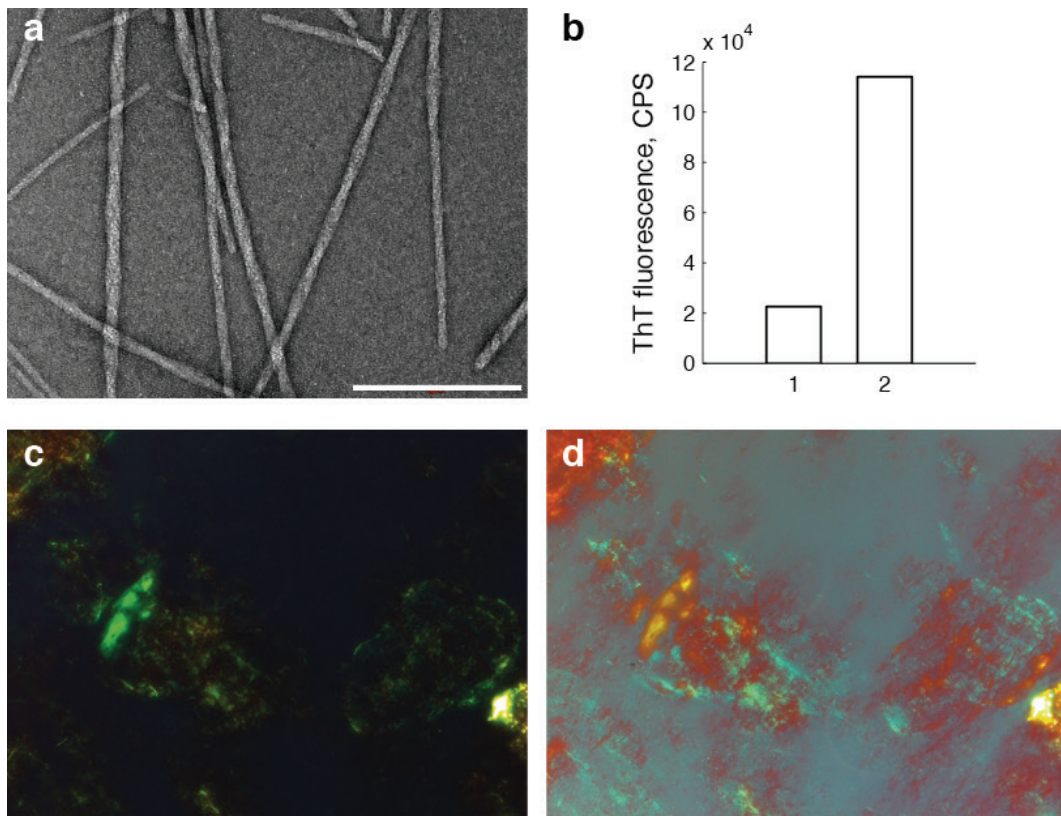
Figure 5.4. Characterization of mature SS14 fibrils obtained after 14 days of incubation under slight agitation at +37 ℃. (**a**) EM micrographs of SS14 amyloid fibrils. The scale bar is 200 nm. (**b**) ThT fluorescence increases upon binding to SS14 amyloid fibrils. 1 – fluorescence of ThT in the blank aggregation buffer. 2 – ThT fluorescence in the presence of SS14 aggregates. (**c**) CR-stained SS14 aggregates show birefringence in polarized light with the analyzer orthogonal to the polarizer. (**d**) Colors in **c** change upon slight uncrossing of the polarizer and analyzer, which is a characteristic feature of the amyloid structure, too [125]. (**c**), (**d**) – original magnification 630.

Insights into the 3D structure of SS14 amyloid fibrils formed in the presence of heparin

Raman spectroscopy of mature SS14 fibrils prepared in the presence of heparin revealed co-localization of the peptide and heparin (**Figure 5.5**). The ratio between heparin and SS14 was found to be one elementary disaccharide of heparin to 9.5 molecules of SS14. In other words, approximately 4 % of heparin added to the reaction remained bound to amyloid fibrils after washing. Unfortunately, this method does not provide structural details about SS14-heparin interactions. Moreover, it was not possible to distinguish between specific and unspecific interactions of the peptide and heparin.
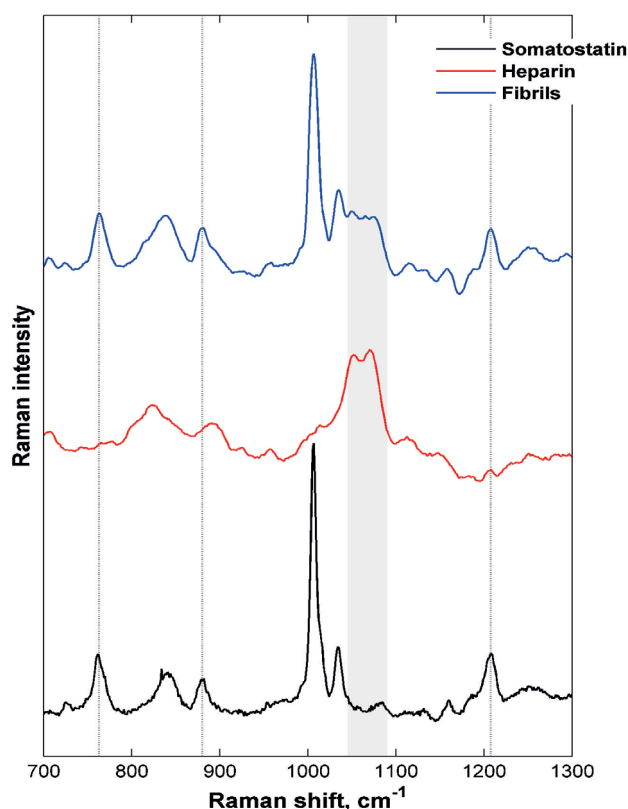
Figure 5.5. Analysis of the composition of SS14 amyloid fibrils prepared in the presence of heparin. Overlaid Raman spectra of SS14 peptide (black), heparin (red), and dried SS14 fibrils prepared in the presence of heparin (blue).

Solid-state NMR spectroscopy is the main tool in structure elucidation of amyloid fibrils [9, 86, 87, 153, 156, 251, 252]. The assignment of the fingerprint 2D [^{13}C, ^{13}C] DARR spectrum [253] (**Figure 5.6**) revealed the complexity of the studied system. Although SS14 is 14 amino acid residues long, the number of peaks found in the spectrum was greater than expected. Careful assignment estimated the presence of at least three polymorphs in the same SS14 sample (**Figure 5.6b**). High structural variability was found at the C-terminal part of SS14. By contrast, the N-terminus (Ala1-Cys3) and the loop region (Trp8-Phe11) adopted a single stable conformation, while β-strands (Lys4-Phe7 and Thr12-Cys14) existed as two alternative configurations. The ratio between polymorphic stretches (Lys4-Phe7 and Thr12-Cys14) was constant among different ssNMR samples and equaled to one. Based on this observation, we can speculate that the structural polymorphism of SS14 fibrils observed in the ssNMR spectra is an intrinsic property of the system. The nature of this polymorphism could be based the simplest building block of SS14 aggregates might be composed of two structurally unequal

monomers, and only such asymmetric spatial arrangement can lead to amyloid formation. Very similar observation was reported for the Sup35 prion protein fragment [189]. Amyloid fibrils of Sup35 are characterized by the presence of three structurally different conformers reproducibly detected at the constant ratio by ssNMR irrespective of the extensive modulation of fibrillization conditions.

Statistical analysis of chemical shifts of Cα, Cβ, and carbonyl C (C') obtained for a variety of proteins provides a simple technique for the prediction of secondary structure elements [254]. It has been demonstrated that deviation of measured chemical shifts from chemical shifts characteristic for a random coil can provide reliable information regarding the secondary structure of the protein of interest. Successive negative difference for at least three amino acid residues for Cα and C' and positive numbers for Cβ suggest a β-strand structure. The opposite, high positive values for Cα and C' differences and negative for Cβ for at least four amino acid residues, indicate the high probability of α-helix secondary structure [154, 254, 255]. The analysis of chemical shift differences for all molecular systems described above (**Figure 5.7a**) does not provide unambiguous identification of β-strands in SS14 molecule. A quick look on the ΔδCα-ΔδCβ plot suggests the presence of two β-strands: Ala1-Lys4 and Thr12-Cys14 (**Figure 5.7b**). The ΔδC' plot (**Figure 5.7c**) does not completely agree with it. The most prominent differences correspond to Asn5 and Cys14, which extend first β-strand to Ala1-Asn5 and breaks down the second strand. However, the chemical shift of the carbonyl C of Cys14 can be affected by the fact that it is a terminal carbonyl group and not necessarily involved in a β-sheet formation, therefore, the difference with random coil chemical shift can be interpreted structure wise. In summary, the C-terminal part of SS14 looks more prominent to β-strand structure, while chemical shifts of the central part of the peptide balance around values characteristic for random coil, which is difficult to interpret. The C-terminus of SS14 is likely involved in β-sheet formation, however, the discrepancy between ΔδCα-ΔδCβ and ΔδC' plots does not allow for unambiguous interpretation of the secondary structure based on the analysis of secondary chemical shifts.

Interestingly, the analysis of Cα and Cβ secondary chemical shifts of SS14 in solution indicates the presence of β-strand structure at the N-terminus (Gly2-Asn5), while the middle part and C-terminus of SS14 do not differ significantly from a random coil conformation (**Figure 5.7d**). The comparison of chemical shifts of SS14 in solution and in the amyloid fibrils reveals that the N-terminal β-strand appears in both states, while the

C-terminal residues become involved in another β-strand only in the case of amyloid (**Supplementary Figure S3**).
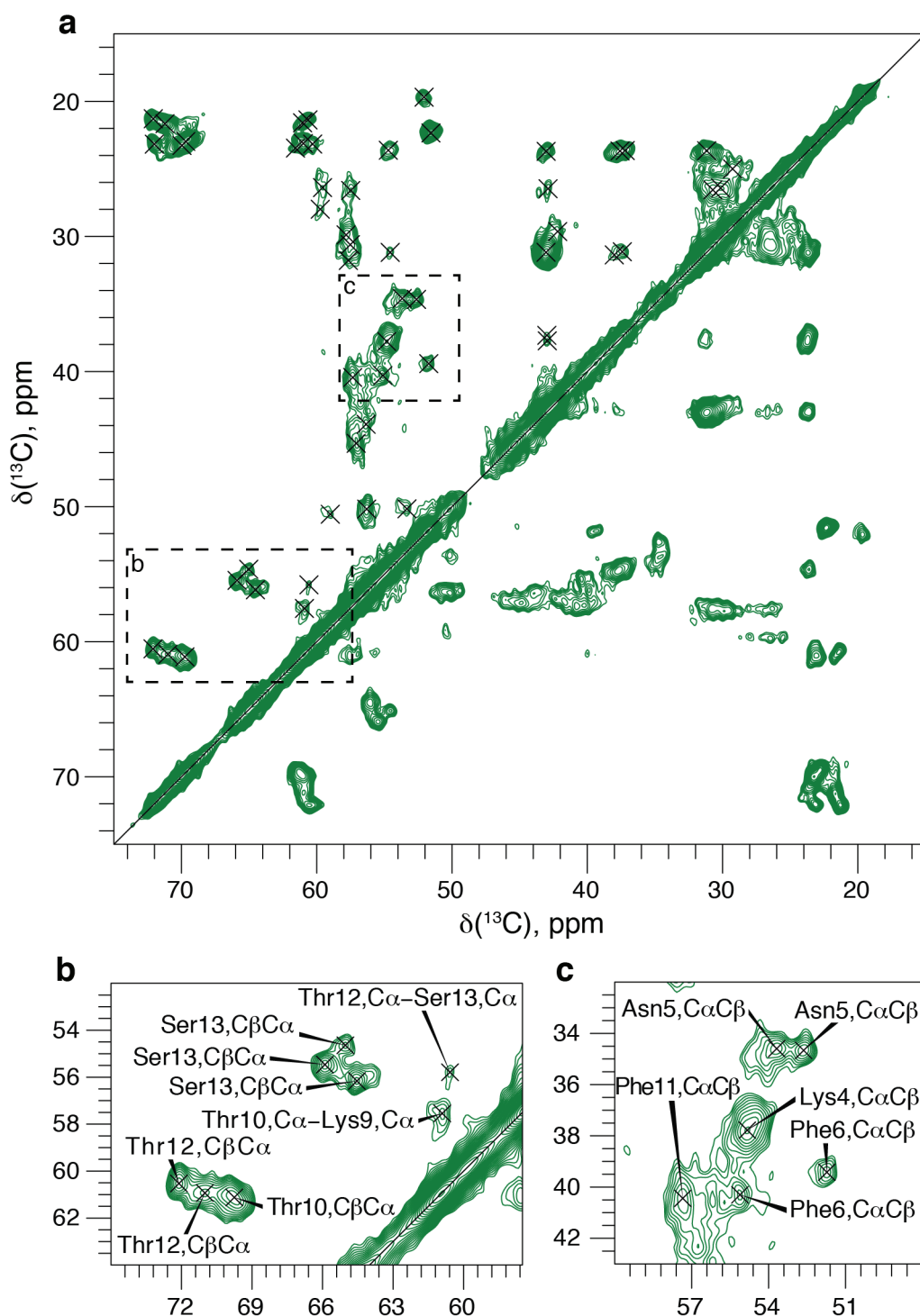
Figure 5.6. 20ms 2D DARR spectrum of ^{13}C, ^{15}N-labeled SS14 amyloid fibrils. (**a**) Aliphatic region of the DARR spectrum. Crosses indicate picked peaks, which were sequentially assigned according to the established strategy [256]. Black dashed boxes highlight insets shown in **b** and **c**. (**b**) Selected region of the DARR spectrum shows the presence of polymorphism of Thr12 and Ser13 residues. (**c**) Selected region of the DARR spectrum shows the polymorphism of Asn5 and Phe6 residues.
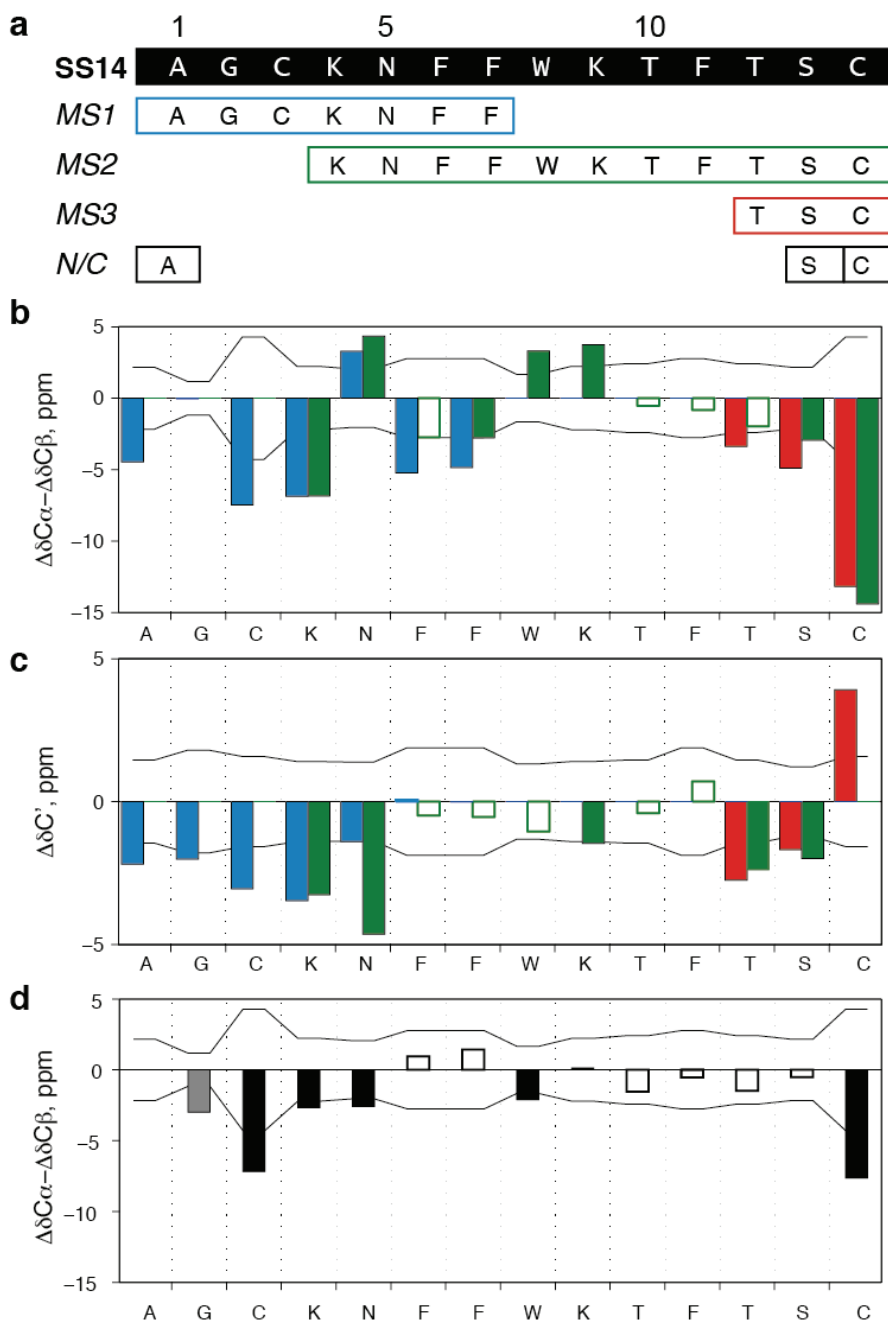
Figure 5.7. Schematic representation of SS14 amyloid polymorphism revealed by ssNMR. (**a**) MS (1-3) – molecular systems with distinct intramolecular interactions determined by ssNMR. Stretches represent sequentially assigned sets of connections in 3D ssNMR spectra. Additional peaks seen in the DARR spectrum with unidentified intramolecular connections in 3D spectra are shown by short stretches (Ala1, Ser13) and marked by N/C (no connection). One peak is identified as Thr amino acid residue, which appears only in the 3D NCA spectrum. It lacks any intramolecular connections in 3D spectra. It has the same Cα, Cβ chemical shifts as Thr12 in the 3D NCA spectrum, but different chemical shift in the N-dimension. Moreover, it shows the contact to Ser13 in the 250 ms PDSD spectrum. Therefore, this peak is referred to the third identified Thr12. (**b**), (**c**) Secondary chemical shift analysis of SS14 fibrils. Molecular systems are color-coded: the sequentially assigned stretch is shown in the same color as the corresponding differences in chemical shifts in **b** and **c**: MS1 – blue, MS2 – green; MS3 - red. Secondary chemical shifts outstanding from the confidence interval are filled by the respective color. Black polygonal line demonstrates confidence intervals of random coil chemical shifts of a respective amino acid residue [257]. (**d**) Secondary chemical shift analysis of SS14 in solution. Secondary chemical shifts outstanding from the confidence interval are filled by the black color. Black polygonal line demonstrates confidence intervals of random coil chemical shifts [257]. Gly is shown in grey, because only Cα chemical shift has been analyzed.

Despite the apparent simplicity of SS14 dictated by its short primary sequence and conformational restrictions imposed by the presence of the intramolecular disulfide bond, determining the structure of functional SS14 amyloid fibrils turned out to be not straightforward. A large number of distinct conformations and, hence, possible intra- and intermolecular interactions render the structure elucidation difficult. Therefore, more fibrillization procedures should be tested in order to either confirm the hypothesis of two conformers essential for amyloid formation or find the condition yielding more homogeneous sample. Different environmental parameters can be adjusted in these tests, including ionic strength, the composition of fibrillization buffer, temperature, and agitation rate [189]. Finally, seeded fibrillization may help to saturate the sample with a certain polymorph [90].

Prediction of amyloidogenic properties of SS14 by TANGO and Waltz

The analysis of primary sequence of SS14 by the TANGO algorithm [187] predicts the propensity of residues from 4 to 12 to form a β-sheet (**Figure 5.8**). This prediction is in agreement with the previously proposed solution model of SS14 [202]. The algorithm cannot however predict the amyloid formation by SS14. The parameter representing the β-sheet aggregation propensity, i.e. ability to form amyloid, calculated to be zero for SS14 sequence. This can be explained by the fact that TANGO was developed based on the data set obtained from the analysis of pathology-associated protein aggregation [187], while SS14 aggregation is functional and must be reversible. Thus, the features of SS14 primary sequence responsible for functional aggregation may be not recognizable by the TANGO algorithm.

The alternative aggregation prediction tool, Waltz [188], recognizes the ability of SS14 to form amyloid aggregates with very high sensitivity, but it does not shed light on the structure and mechanisms of formation of these aggregates. The Waltz tool is developed based on the library of sequences of functional amyloids [188], and it is therefore expected to be better suited for the analysis of functional amyloids. However, almost the whole SS14 sequence is assigned to be equally aggregation-prone, which renders the prediction difficult to interpret.
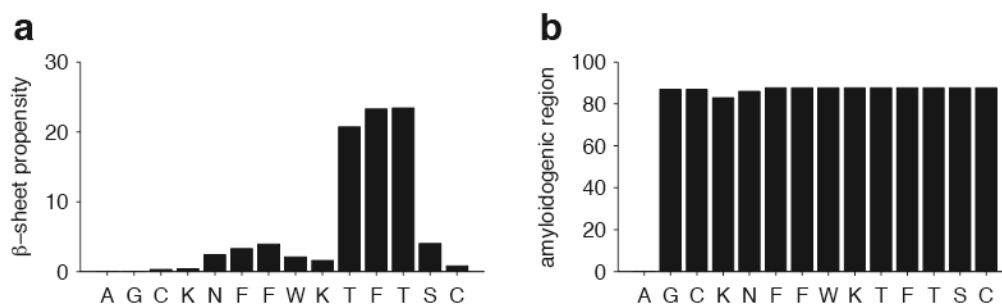
Figure 5.8. Computational prediction of amyloidogenic properties of SS14 by the TANGO algorithm [187] (**a**) and the Waltz tool [188] (**b**). (**a**) Propensity of monomeric SS14 to adopt β-stranded structure at +37 ℃, pH 5.5, and ionic strength corresponding to 150 mM NaCl predicted by TANGO. (**b**) Propensity of SS14 to form amyloid aggregates predicted by Waltz. The cyclic nature of the peptide was not taken into account in both cases.

Exceptional stability of SS14 amyloid fibrils formed in the presence of heparin

Only the monomeric form of SS14 is considered to be functional [64]. Thus, SS14 amyloid aggregates must dissociate upon release from the secretory granules to the blood. Preliminary examination of stability of SS14 fibrils formed in the presence of heparin revealed that they were stable upon 10-fold dilution into 20 mM sodium phosphate buffer at pH 7.4 (**Figure 5.9**). This finding is very similar to another observation discussed in **Chapter 6**, where we demonstrated that phosphate promotes and stabilizes functional β-endorphin amyloid.
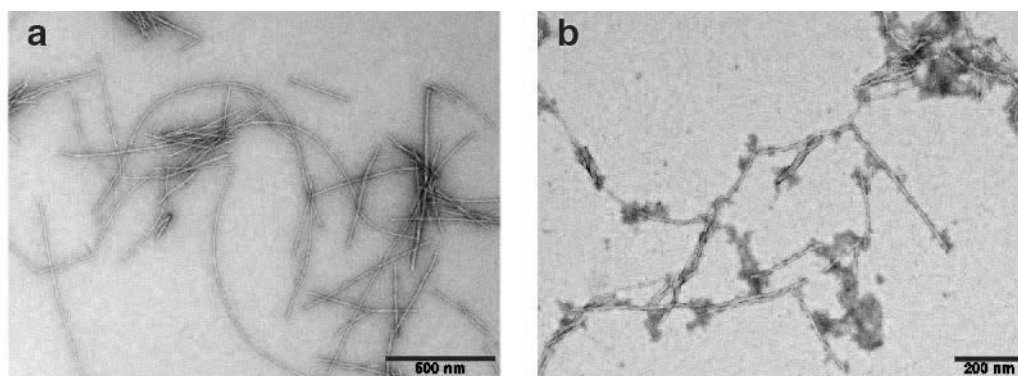
Figure 5.9. Electron micrographs of SS14 fibrils formed in the presence of heparin. (**a**) SS14 fibrils before the dissociation assay. Scale bar - 500 nm. (**b**) SS14 fibrils after 24 h incubation in 20 mM sodium phosphate buffer (pH 7.4) at 10-fold dilution. Scale bar - 200 nm.

Facing high stability of SS14 fibrils, we attempted to probe their resistance to different mixtures of organic solvent, which are usually used to dissolve amyloid fibrils in HDX experiments [104-106, 108, 110, 112, 113, 258]. Surprisingly, SS14 amyloid aggregates formed in the presence of heparin demonstrated striking stability in many cases. Among five tested solvent compositions, only pure DMSO with 0.1 % TFA could

disrupt the amyloid structure of SS14 (**Figure 5.10a**) leaving only a minor fraction of fibrillar aggregates (data not shown). Other solvent compositions did not influence the fibril morphology significantly. The majority of examined aggregates retained their fibrillar appearance (representative EM images are shown in **Figure 5.10**).
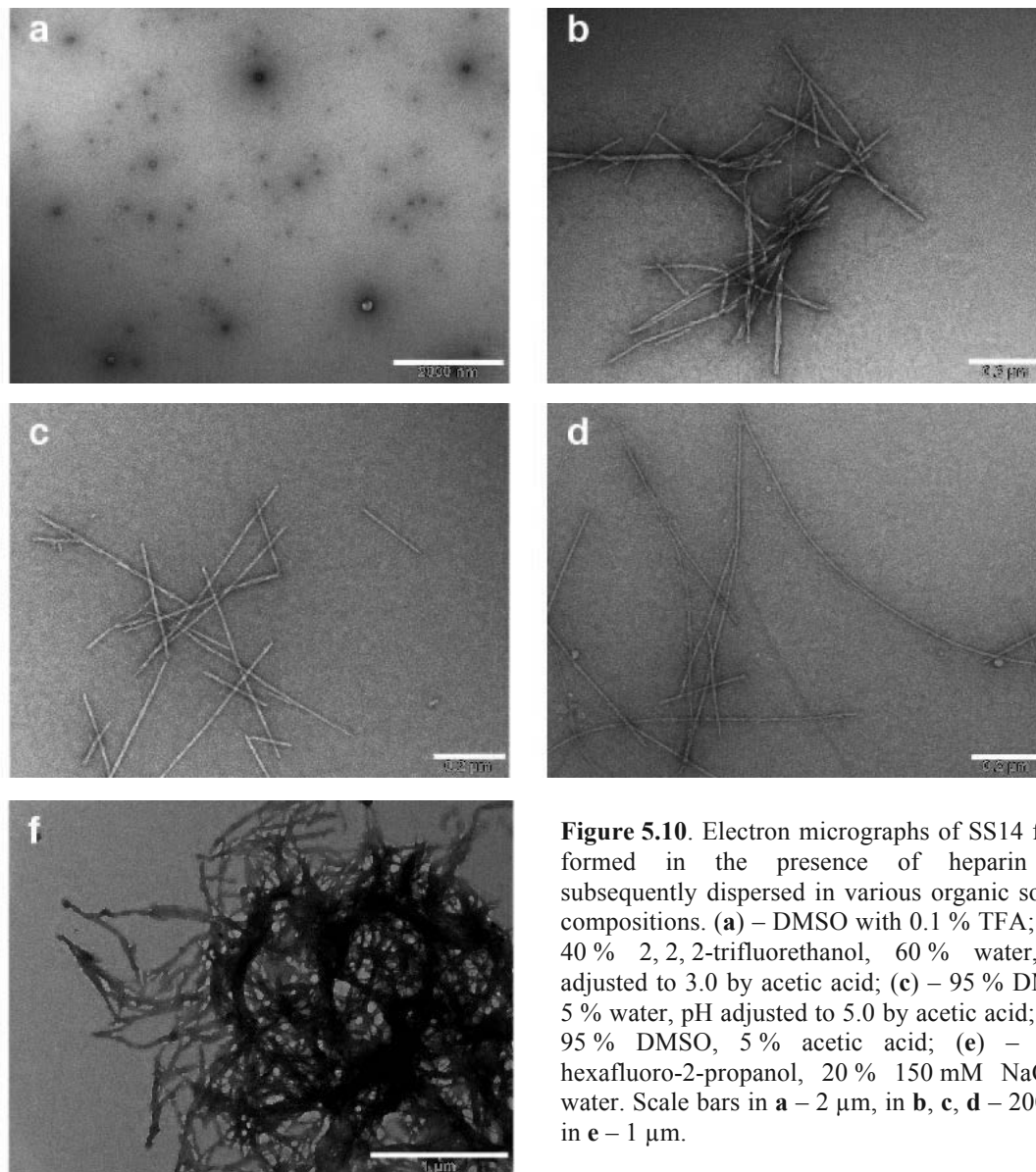
Figure 5.10. Electron micrographs of SS14 fibrils formed in the presence of heparin and subsequently dispersed in various organic solvent compositions. (**a**) – DMSO with 0.1 % TFA; (**b**) – 40 % 2, 2, 2-trifluorethanol, 60 % water, pH adjusted to 3.0 by acetic acid; (**c**) – 95 % DMSO, 5 % water, pH adjusted to 5.0 by acetic acid; (**d**) – 95 % DMSO, 5 % acetic acid; (**e**) – 80 % hexafluoro-2-propanol, 20 % 150 mM NaCl in water. Scale bars in **a** – 2 μm, in **b**, **c**, **d** – 200 nm, in **e** – 1 μm.

Similar to β-endorphin (**Chapter 6**), SS14 fibrils formed in the presence of heparin display extreme cohesion. On the contrary, SS14 amyloids must be highly dynamic structures capable of rapid disassembly *in vivo* to ensure functional signaling. Reversibility of hormone aggregation is believed – although not by everyone [259] – to be an intrinsic property of peptide hormones [31]. This controversy raises doubts about the biological relevance of SS14 amyloids obtained and described here. It is therefore extremely important to find physiologically relevant conditions of SS14 fibrillization

affording the dynamic amyloid structure capable of dissociation, which is of true interest for structural and cell biology, physiology, and medicine.

Conclusions

This chapter describes early steps towards determining a high-resolution structure of functional SS14 amyloid fibrils. Fibrillar morphology revealed by EM, binding of ThT and CR allowed for assigning the amyloid structure to the mature SS14 aggregates. Preliminary ssNMR spectroscopy data demonstrated the complexity of the system. Almost equal abundances of polymorphs reproducibly found in several measured samples suggested the possible structural asymmetry of elementary subunits of SS14 amyloids. The necessity for a relatively short cyclic peptide to adapt several specific conformations in order to form asymmetric building blocks in sufficient amounts may also explain why SS14 aggregation proceeded for several days through a number of morphologically distinct intermediate stages.

Alternatively, the discovered SS14 amyloid polymorphism may be due to non-optimal aggregation conditions. There are several experimental evidences that indirectly suggest poor relevance of the aggregation conditions used to the situation *in vivo*. The aggregation kinetics observed *in vitro* was quite slow. The morphology of aggregation intermediates was different depending on the experimental conditions, i.e. the system may be sensitive to the environment. Finally, the SS14 fibrils produced in the presence of heparin appear to be exceptionally stable and resistant to dissociation upon washing with water, dilution in PBS, and even when treated with various organic solvents. Moreover, data obtained by Raman spectroscopy suggest tight interaction between heparin and SS14 within the amyloid fibril. The latter two findings indicate that heparin may actually be an integral structural component of the fibrils, rather than simply promote and catalyze the aggregation process.

Further screening and optimization of aggregation conditions are therefore necessary to understand the mechanism of functional SS14 amyloid formation and determine its structure. Complementary methods to study amyloids, such as hydrogen-deuterium exchange, fluorescence microscopy, and limited proteolysis may assist ssNMR spectroscopy-based structure elucidation and provide insights into the mechanism and pathways of aggregation.

Methods

Protein aggregation

SS14 was dissolved in the fibrillization buffer (10 mM sodium citrate, 5 % w/v D-mannitol, pH 5.5) at 2 mg/ml concentration. Aggregation was set up in low-retention 1.5 ml test tubes (Vaudaux-Eppendorf AG, Schönenbuch/Basel, Switzerland) in the EchoTherm RT11 rotating mixer (Torrey Pines Scientific, Inc., Carlsbad, USA) at a rotation speed of approximately 30 rpm inside an incubator thermostated at +37 ℃ (slight agitation, +37 ℃ condition, **Figure 5.3a-c**). Alternatively, test tubes with aggregation reaction were kept at room temperature quiescent (quiescent, +25 ℃ condition, **Figure 5.3d-f**). A heparin stock solution was prepared by dissolving 250 mg of heparin (heparin sodium salt, sc-203075, Santa Cruz Biotechnology, Inc., Heidelberg, Germany) in 2.5 ml of double-deionized water containing 0.05 % (w/v) sodium azide (AppliChem, AXON LAB AG, Baden-Dättwil, Switzerland). One part of heparin stock solution was added to 50 parts of SS14 dissolved in the fibrillization buffer to initiate fibrillization. Afterwards, sodium azide was added up to a concentration of 0.05 % to the peptide solution. Sample tubes were sealed by PARAFILM® M (Sigma-Aldrich Chemie GmbH, Buchs, Switzerland) and placed for fibrillization. 5 µl aliquots were taken out for analysis when necessary.

Transmission electron microscopy

5 µl samples of SS14 fibrils were deposited for 1 min on previously glow-discharged carbon-coated copper grids (Electron Microscopy Sciences, Hatfield, Pennsylvania). The grids were then blotted, washed twice in drops of double-distilled water and negatively stained for 15 s with filtered 2 % (w/v) uranyl acetate (Sigma-Aldrich Chemie GmbH, Buchs, Switzerland). Images were acquired with the FEI Morgagni 268 electron microscope (FEI Company, Eindhoven, Netherlands) operated at 100 kV. Electron micrographs were recorded on a 1376 by 1032 pixel charge-coupled device camera (Veleta, Olympus soft imaging solutions GmbH, Münster, Germany).

Thioflavin T staining

The fibril-containing solution was diluted 60-fold by fibrillization buffer (20 µM final protein concentration) and mixed with 1 mM thioflavin T (ThT) solution prepared in water yielding 20 µM ThT in the sample. Fluorescence spectra were recorded on FluoroMax®-4 spectrofluorometer controlled by FluorEssence™ software (Horiba Jobin

Yvon GmbH, Munich, Germany). The excitation wavelength was set to 440 nm, and the spectra were acquired in the range of 460-550 nm utilizing 3 nm slits for excitation and emission.

Congo red staining

The Congo red staining protocol of the kit HT-60 (Sigma-Aldrich Chemie GmbH, Buchs, Switzerland) with minor modifications was used. Briefly, protein aggregates were dried on poly-L-lysine coated glass slide (Poly-Prep slides, Sigma-Aldrich Chemie GmbH, Buchs, Switzerland). 4 % formaldehyde solution was used for sample fixation for 10 min. Next, the sample was rinsed three times in deionized water, dried and stained for one minute with Mayer's hematoxylin (Sigma-Aldrich Chemie GmbH, Buchs, Switzerland). After washing for 1 min with tap water and 3 times with deionized water, the sample was placed in filtered alkaline NaCl solution for 20 min followed by incubation in filtered alkaline Congo red staining solution. The slide was washed twice with 95 % ethanol and twice with 100 % ethanol. The sample was cleaned in xylene and mounted with a drop of Dako Fluorescence Mounting Medium (Dako Schweiz AG, Baar, Switzerland). The sample was studied using PALM-Microdissection and Widefield Microscope Zeiss Axiovert 200M (Carl Zeiss Microscopy GmbH, Göttingen, Germany). Images were acquired by Zeiss AxioCam camera in AxioVision software (Carl Zeiss Microscopy GmbH, Göttingen, Germany).

Raman spectroscopy

An upright Raman microscope (NTEGRA Spectra, NT-MDT, Russia) was employed for Raman microscopy and AFM measurements. The system was equipped with an upright confocal laser microscope, an atomic force microscope (AFM), a white-light video microscope for rough observation and alignment of the sample, a photomultiplier tube (PMT) detector for confocal imaging, and a Raman spectrograph equipped with a charge-coupled device (CCD). It allowed simultaneous AFM and optical measurements on exactly the same part of transparent and opaque samples. All optical measurements were performed using a 100×long working-distance objective with a numerical aperture (NA) of 0.7 for both excitation and collection of the backscattered light from the sample. Two lasers, a red HeNe (632.8 nm, 5 mW at the sample) provided by Laser Drive, Inc. and a green DPSS (532 nm, 3-4 mW at the sample) provided by Changchun New Industries (CNI) Optoelectronics Tech. Co., Ltd. were used for Raman

spectroscopy. An area of 5×5 µm (256×256 pixels) was scanned by AFM in tapping mode with a speed of 1 line per second. AdvancedTEC cantilevers (NANOSENSORS, Switzerland) with resonance frequencies in the 210-490 kHz range and force constants of 12-110 N m-1 were used.

50 µl of SS14 fibrils were washed in double-deionized water twice according to the following procedure. Fibrils were centrifuged at $2.5×10^4$ g and a temperature of +22 ºC for 15 min (Microcentrifuge 5417R, Vaudaux-Eppendorf AG, Schönenbuch/Basel, Switzerland). The pellet was resuspended in 50 µl of double-deionized water, extensively pipetted and centrifuged again. 20 µl of washed fibrils were dried on the microscope slide with cut edges (Menzel-Gläser, Gerhard Menzel GmbH, Braunschweig, Germany) for 2 h. A green DPSS laser (532 nm, 3-4 mW at the sample) was used for Raman spectroscopy of SS14 fibrils as well as of lyophilized heparin and SS14 monomer. Three to five spectra were accumulated for 600 s of total time each. Standard procedures for spike and fluorescent background corrections were applied [260]. The final spectra were smoothed by Savitzky-Golay filtering [261].

Dissociation test in phosphate buffer

50 µl of SS14 fibrils formed as described above were centrifuged at $2.5×10^4$ g and +21 ºC for 40 min (Microcentrifuge 5417R, Vaudaux-Eppendorf AG, Schönenbuch/Basel, Switzerland). The supernatant was discarded, and the pellet was subsequently resuspended in 20 mM sodium phosphate buffer at pH 7.4 and incubated for 24 h with slight agitation.

Dissolution of SS14 fibrils in organic solvents

5 µl of SS14 fibrils formed in the presence of heparin were centrifuged at $2.5×10^4$ g and +15 ºC temperature for 15 min (Microcentrifuge 5417R, Vaudaux-Eppendorf AG, Schönenbuch/Basel, Switzerland). The pellet was resuspended in 30 µl of organic mixture, extensively pipetted for 1 min and loaded on an EM grid for analysis. Organic mixtures used in this assay were the following: (a) – DMSO with 0.1 % TFA; (b) – 40 % 2, 2, 2-trifluorethanol, 60 % double-deionized water, adjusted to pH 3.0 by addition of acetic acid; (c) – 95 % DMSO, 5 % double-deionized water, adjusted to pH 5.0 by addition of acetic acid; (d) – 95 % DMSO, 5 % acetic acid; (e) – 80 % hexafluoro-2-propanol, 20 % 150 mM NaCl in double-deionized water.

Probing the role of Glu8 residue in functional β-endorphin aggregation[1]

Introduction

The discovery of brain receptors specifically recognizing morphine and its natural or synthesized derivatives suggested the existence of endogenous opiate ligands [262]. In 1975, two pentapeptides with morphinomimetic properties were isolated form the brain: methionine-enkephalin and leucine-enkephalin. A few months later, Li and Chung [263] isolated from camel pituitary glands a peptide comprising of 31 amino acid residues with N-terminal residues identical to the methionine-enkephalin sequence. This peptide was named β-endorphin – by combining two words "endogenous morphine" describing its activity [264]. Notably, the sequence of β-endorphin corresponded to the C-terminal fragment of another neuropeptide, β-lipotropin, which had been known before. However, β-endorphin did not display the same activity, as β-lipotropin [263]. The overlap of primary sequences of β-endorphin and β-lipotropin supported the revolutionary at that time hypothesis of the existence of hormonal precursor molecules [265]. Later, in 1977, the common precursor molecule of β-endorphin and β-lipotropin was discovered, which is known now as pro-opiomelanocortin (POMC) [262]. The maturation of POMC in the adenohypophysis leads to the production of pro-ACTH and β-lipotropin, which are further processed by cell-specific proprotein convertases to shorter active peptide hormones (**Figure 6.1**) [266, 267].

Structural studies of β-endorphin in aqueous solution by ^{1}H-NMR spectroscopy identified a random-coil conformation [16], which agreed with the previous CD measurements [268]. Functional tests of β-endorphin fragments and analogs suggested the presence of two receptor-binding sites at the N- and C-termini. They were shown to bind to different types of opioid receptors. The N-terminal fragment seemed to be

[1] All ssNMR spectra presented in this chapter were measured by Julia Gath from the group of Prof. Beat Meier (LPC, ETH Zurich, Switzerland). The assignment of the spectra and structure calculations of the wild-type β-endorphin fibrils prepared in 10 mM ammonium acetate buffer at pH 5.5 containing 200 mM NaCl and 2 mg/ml heparin were performed by Carolin Seuring and Julia Gath under the supervision of Prof. Roland Riek (LPC, ETH Zurich, Switzerland), Prof. Beat Meier, and Prof. Anja Böckmann (IBCP, CNRS/Université de Lyon, France). Raman spectroscopy and ESI-MS analysis were done in the group of Prof. Renato Zenobi (LOC, ETH Zurich, Switzerland) by Roman Balabin and Konstantin Barylyuk, respectively. Aβ amyloid fibrils were produced by Marielle Wälti from the group of Prof. Roland Riek.

necessary in all cases for functional signal transduction. Interestingly, the simultaneous injection of β-endorphin$_{6\text{-}31}$ fragment with the full-length peptide inhibited the analgesic effect of the latter [269].
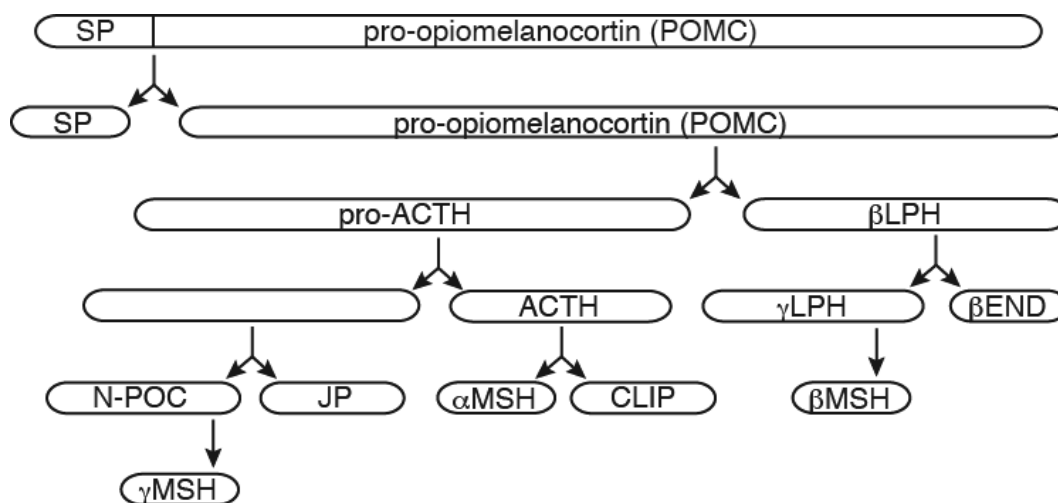
Figure 6.1. Enzymatic processing of POMC. SP – signal peptide, βLPH – β-lipotropin, γLPH – γ-lipotropin, βEND - β-endorphin, N-POC – pro-opiomelanocortin N-terminal glycopeptide, JP – joining peptide, CLIP – corticotropin-like intermediate lobe peptide, α/β/γMSH – α-, β-, γ-melanotropin, respectively [266, 267].

Functions of endomorphines, and β-endorphin in particular, are numerous. They are involved in many hormonal networks [262]. That said, the most prominent activity of endogenous morphines is pain control. Enkephalinergic neurons inhibit the transmission of neural impulses and the release of pain-inducing neuromediators in synapses [262]. However, overproduction of β-endorphin can have a negative effect though. For example, high level of β-endorphin in patients with silent myocardial ischemia decreases the sensitivity to pain during a heart attack, which can lead to fatal consequences [270, 271]. The decrease in cerebral β-endorphin concentration in mothers at the time of childbirth is vital for inducing maternal behavior. It has been shown that administration of morphine blocks the onset of maternal behavior [272]. β-endorphin is unique among the other endomorphines because it is considered to be involved in the learning process. The synthesis of β-endorphin in the brain takes several hours, whereas depletion due to an exercise involving the memory takes less than six minutes [262, 273]. β-endorphin is found in many areas of the brain and can behave as a modulator, hormone, and mediator [262]. Therefore, the field of β-endorphin action appears to be enormously diverse.

As can be seen from **Figure 6.1** and the associated discussion, the synthesis and maturation of β-endorphin is a long multistage process that takes quite a long time to complete. On the other hand, the role of β-endorphin in signaling and brain activity

regulation is vitally important. Thus, an intracellular depot of β-endorphin must exist to ensure the availability of sufficient amount of the hormone when it is necessary to transduce the signal. Indeed, β-endorphin has been found in the secretory granules inside of AtT20 cell line and rat pituitary corticotropes by immunogold staining [274]. This finding agrees with the hypothesis of functional aggregation of peptide hormones [31, 34, 37]. Dense packing of the secretory granule content allows to store large amounts of bioactive peptides and release them at once to ensure a quicker response to a stimuli than protein synthesis rates would provide [8, 11]. The density of hormone packing is in turn provided by the adoption of the compact amyloid fold [8]. Interestingly, processing of the β-endorphin precursor, POMC, starts in the TGN, but mainly occurs in secretory granules, which contain all necessary enzymes and co-factors [274]. However, packing of the immature hormone into secretory granules does not contradict the hypothesis of functional hormone aggregation, because self-association of the long precursor does not necessarily prevent it from further processing into smaller peptides [275].

Maji et al. [31] experimentally demonstrated for the first time the amyloid nature of β-endorphin stored in secretory granules. In their study, they probed the content of secretory granules purified from AtT20 cell line and rat pituitaries by amyloid-specific tests including ThT binding, CR staining, and X-ray fiber diffraction. In experiments *in vitro*, β-endorphin assembled into amyloid fibrils under the conditions intended to mimic the secretory granule environment. More specifically, the buffer's pH was kept at 5.5, mannitol and heparin were added to simulate the high abundance of carbohydrates in this cellular compartment. That said, this work lacked sufficient evidence that would unambiguously demonstrate rapid and reversible switching between the amyloid and the soluble state of peptide hormones. Reversible aggregation of peptide hormones is an essential prerequisite of hormone storage and release, which distinguishes hormone aggregates among other functional amyloids. Furthermore, no insight into the molecular mechanism of reversible hormone aggregation was provided.

The classic molecular biology approach to elucidate molecular mechanisms responsible for biological phenomena is to determine a high-resolution 3D structure of the active biomolecules and establish the underlying structure-activity relationships. In the case of amyloid fibrils, ssNMR spectroscopy is recognized as the method of choice for the 3D structure determination. Structural study of β-endorphin fibrils by ssNMR represents the first attempt to reveal mechanisms of specific hormone aggregation [276, 277].

The structural model of β-endorphin amyloid fibrils formed in the presence of heparin has been proposed recently based on the ssNMR data supported by MPL measurements [276, 277] (**Figure 6.2**). β-endorphin fibrils are characterized by a triangular core comprising of three β-strands (**Figure 6.2a**): Phe4-Ser10 ($β_1$), Leu14-Lys19 ($β_2$), Ala21-Lys24 ($β_3$). The core is composed of polar (Thr6, Glu8, Ser10, Thr16) and hydrophobic residues (Phe4, Leu14, Phe18, Ala21, Ile23, Ala26). **Figure 6.2b** shows that $β_1$ strand of a given molecule is located in the same plane as $β_2$ and $β_3$ strands of the adjacent molecule. I.e. β-strands feature staggered orientation along the fibril axis [276].
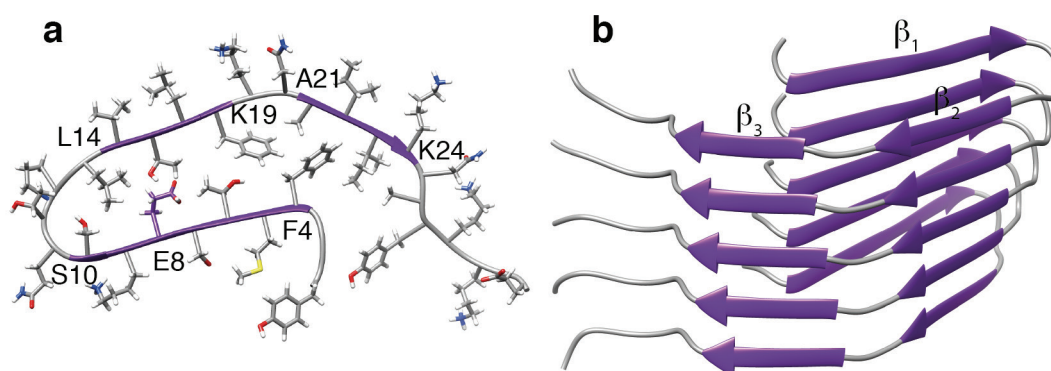
Figure 6.2. Structural model of β-endorphin amyloid fibrils [276]. (**a**) Top view of an individual β-endorphin molecule. Peptide backbone is shown as a ribbon, amino acid residue side chains are shown as sticks. Some amino acid residues are marked (see text for details). (**b**) Ribbon diagram showing a stack of five β-endorphin molecules staggered in the amyloid fibril. Individual β-strands are marked as $β_1$, $β_2$, and $β_3$.

One interesting and unusual feature of the proposed structural model of β-endorphin amyloid fibril is that the side chain of Glu8 residue faces into the fibril core (**Figure 6.2a**) [276]. Generally, charged groups are extremely rare inside a protein core due to a large energetic penalty [278]. In this case, the observed chemical shift of Cδ atom is relatively low and has therefore been attributed to the protonated form of glutamic acid [279]. The theoretical pKa value of the carboxyl group of Glu side chain is 4.15 [280], which means that only 4 % of glutamate residues are protonated at pH 5.5 [276]. However, the microenvironment may affect the apparent pKa value of the γ-carboxyl group of Glu8 [281] favoring the protonated state. Moreover, the sequestering of β-endorphin with protonated Glu8 into the amyloid fibril may shift the equilibrium of the protonation/deprotonation reaction according to Le Chatelier's principle towards protonation of new monomers. Therefore, it was hypothesized that the dynamic β-endorphin assembly and disassembly may be controlled by the ionic state of the Glu8 side chain and may follow the next scenario *in vivo*: (*i*) Protonation of Glu8 occurring at

acidic pH in the TGN neutralizes its charge and allows β-endorphin to adapt the conformation favorable for aggregation, with Glu8 buried inside. (*ii*) Molecules of β-endorphin come close enough to aggregate and form the amyloid. The peptide is stored in secretory granules until the cell receives a stimulus for hormone secretion. (*iii*) Upon signaling, secretory granules release their contents into the blood (pH 7.35-7.45) [282]. (*iv*) The glutamate residue buried into the fibril core becomes deprotonated at neutral pH and internal charge repulsion blasts the fibril into the functional monomeric β-endorphin molecules (**Figure 6.3**). A similar mechanism has been reported for the Glu-rich repeat domain of the Pmel17 protein. The amyloid aggregates formed by the repeat domain at pH 5.0 dissolve upon pH increase to 6.5 [283].
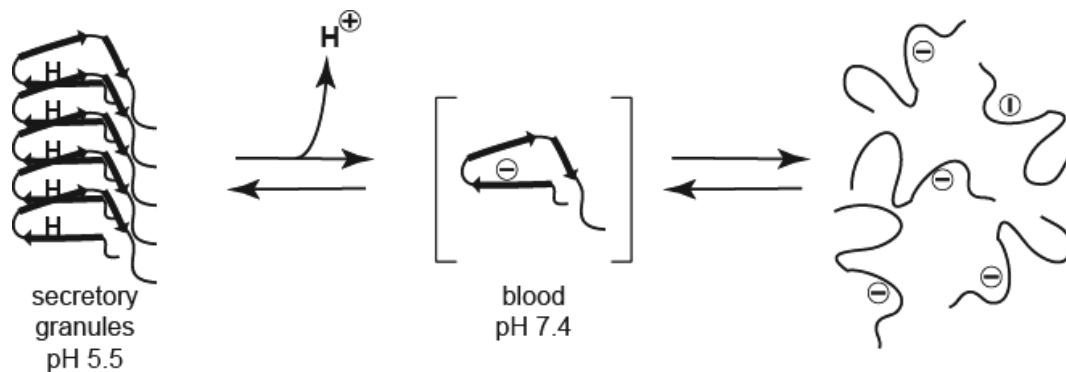
Figure 6.3. Hypothetical mechanism of pH-induced dissociation of the functional β-endorphin amyloid. The peptide is stored in secretory granules at acidic conditions. Glu8 is protonated and buried in the fibril core. Upon secretory granule release to the blood, the pH of the environment shifts from 5.5 to 7.4. This pH change leads to deprotonation of Glu8 side chain and destabilization of the β-endorphin amyloid, which translates into rapid fibril dissociation.

The alignment of β-endorphin amino acid sequences from different species shows that Glu8 is a part of the conservative N-terminal region. It has been found substituted by another residue, glutamine, only in one species (*Acipencer transmontanus*). Interestingly, chemically synthesized the E8Q variant of human β-endorphin demonstrated three-fold increase of analgesic activity, while the potency of the E31G variant (replacement of the second glutamate in the β-endorphin sequence) appeared to be unaffected [284]. In combination with some previous data, the authors concluded that Glu8 plays an important role in the receptor binding and activation [284]. Perhaps, the high degree of amino acid sequence conservation in this region may be also exploited in controlling the functional aggregation of β-endorphin by involving Glu8.

Herein, we test the hypothesis of the key role of Glu8 ionic state for controlling functional β-endorphin aggregation and dissociation. We employ an interdisciplinary

approach combining various biophysical, biochemical, and molecular biology methods to probe the structure-activity relationships emerging from the structural model of β-endorphin amyloid fibril proposed by Gath [276]. In addition, we developed a new method for high-yield production of recombinant β-endorphin in order to satisfy the demand for large sample amounts.

Results and discussion

Expression and purification of β-endorphin

Heterologous expression is the best strategy for obtaining milligrams of isotopically labeled β-endorphin for structural investigation by NMR spectroscopy [157]. The very first reported protocol for expression and purification of recombinant β-endorphin proposed expression of the fusion protein consisting of β-galactosidase followed by β-melanotropin and β-endorphin sequence [285]. The naturally occurring Lys-Arg dipeptide between β-melanotropin and β-endorphin was used as the cleavage site recognized by trypsin. Since there are three lysine residues within β-endorphin sequence, lysine side chains were protected by treating the hybrid protein with citraconic anhydride, while arginine residues remained accessible to cleavage by trypsin. After the enzymatic cleavage, (2,3)-methylmaleyl protecting groups were removed by acid, and the target peptide was purified by glass extraction. The estimated yield of β-endorphin amounted to one milligram per liter of the cell culture [285] – too low for aggregation experiments and NMR-based structural studies.

Another purification protocol yielding 3-5 mg of ^{13}C, ^{15}N-labeled β-endorphin has recently been developed in the group of Prof. R. Riek at ETH Zurich [277]. The recombinant gene construct comprises human β-endorphin sequence fused to the C-terminus of the thioredoxin-6His-tagged chimeric protein (pET32a expression vector) via a linker containing a tobacco etch virus (TEV) protease recognition site (ENLYFQ). The cleavage by the TEV-protease allows for keeping the native sequence of β-endorphin starting with the tyrosine residue at P1' position. The recombinant gene design is similar to that described for CRF and SS14 in **Chapter 3** and **Chapter 4** of this thesis. Herein, we report a significant improvement of the recombinant β-endorphin yield achieved by extensive optimization of protein expression, as well as isolation and purification steps.

The fusion protein was expressed in BL21 Star (DE3) *E. coli* cell culture in M9-minimal medium. Harvested cells were lysed and centrifuged to separate the soluble

protein fraction of the cell lysate and inclusion bodies. The target product was found in the soluble fraction of the cell lysate as well as in the fraction of inclusion bodies at comparable amounts. Therefore, the target protein was pulled down from both fractions. The supernatant was purified by Ni-chelate chromatography and consequently buffer-exchanged to get rid of imidazole affording 80 % pure fusion protein (analysis of SDS-PAGE gels by ImageJ [185], **Figure 6.4a**, lanes 3-4). The insoluble fraction of the cell lysate was solubilized in 8 M urea solution and subjected to Ni-chelate chromatography affording 95 % purity of the target protein (SDS-PAGE analysis by ImageJ [185], **Figure 6.4b**, lanes 4-5). Urea and imidazole were removed by a buffer exchange step to allow for subsequent cleavage of the fusion protein by the TEV-protease. The fusion protein was enzymatically processed by the TEV-protease at 1:100 enzyme:substrate ratio. The cleavage was complete in 16 h (**Figure 6.4a**, lane 5, **Figure 6.4b**, lane 6). The unwanted products of proteolysis (thioredoxin-6His, uncut full fusion protein, and the TEV-protease – all containing 6His-tag) were removed by the second round of Ni-chelate chromatography. Finally, RP-HPLC purification was employed to provide high purity of recombinant β-endorphin. The typical elution profile is shown in **Figure 6.4c**. The identity of the peptide was confirmed by ESI-MS (**Figure 6.4d**). Fractions containing the target peptide were collected, merged, and freeze-dried. The total yield of ^{13}C, ^{15}N-labeled β-endorphin amounted to 10-12 mg per liter of M9-based minimal medium or to 22-24 mg per liter of rich LB medium.
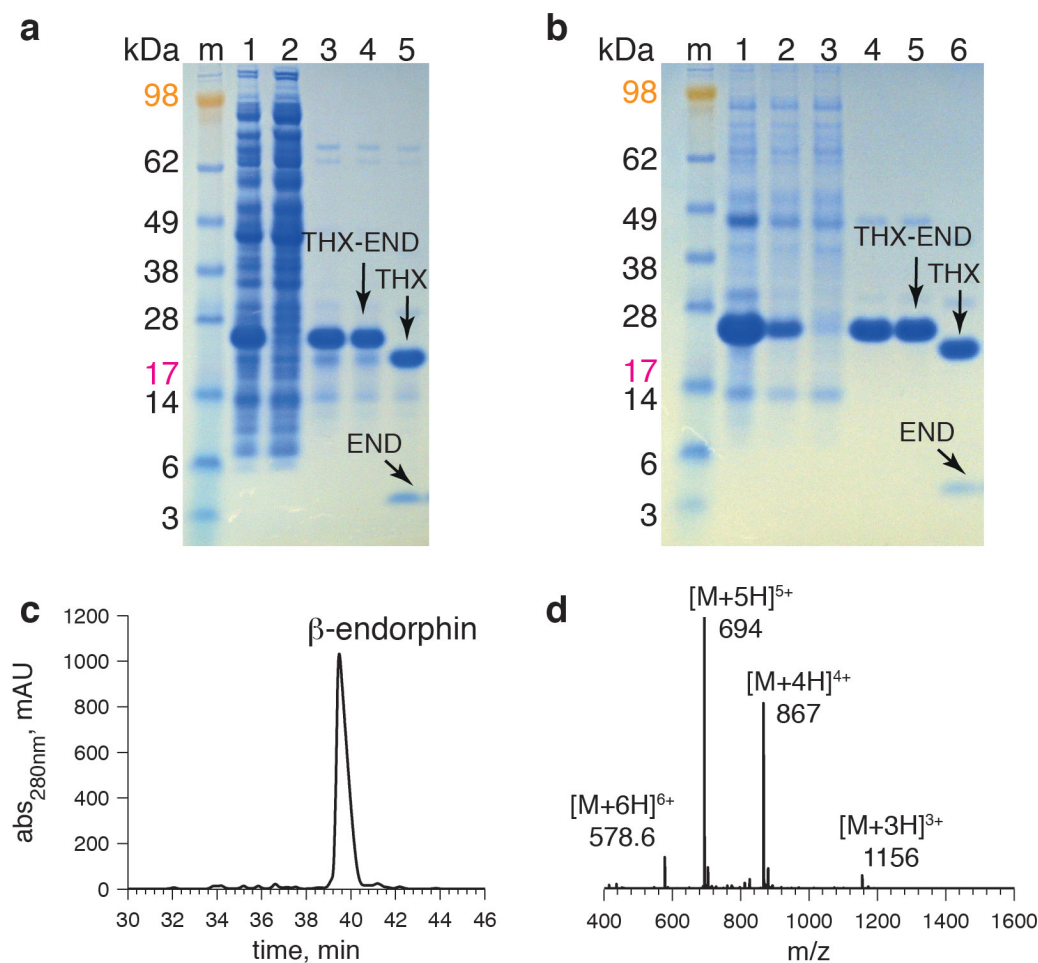
Figure 6.4. Purification of recombinant β-endorphin. (**a**) SDS/4-12 % PAGE analysis of β-endorphin purification from the soluble fraction of the cell lysate. The gel lanes are marked as follows: m – molecular weight markers with the corresponding masses labeled in kDa; 1 – soluble protein fraction obtained from the cell lysate; 2 - flow-through of the protein solution applied to a HisTrapFF column; 3 – sample eluted from the HisTrapFF column by 300 mM imidazole solution; 4 – sample after buffer exchange to the cleavage buffer; 5 – sample after digestion by the TEV-protease at room temperature during 16 h at 1:100 enzyme:substrate ratio. Successful cleavage can be determined by the shift of the fusion protein band. THX-END – full-length fusion protein; THX – part of the fusion protein without the sequence of β-endorphin, END – β-endorphin. (**b**) SDS/4-12 % PAGE analysis of β-endorphin purification from inclusion bodies. m – molecular weight markers with the corresponding masses labeled in kDa; 1 – inclusion bodies dissolved in 8 M urea solution; 2, 3 - flow-through of two repetitive loadings of the protein extract on a HisTrapFF column; 4 – sample eluted from the HisTrapFF column by 300 mM imidazole solution; 5 – sample after buffer exchange to the cleavage buffer; 6 – sample after digestion by the TEV-protease at room temperature during 16 h at 1:100 enzyme:substrate ratio. (**c**) A typical elution profile of the semi-preparative RP-HPLC of the flow-through solution obtained after the affinity chromatography of the digested THX-END fusion protein. The intensity axis is shown in the optical absorbance units at λ = 280 nm. (**d**) ESI-MS spectrum of the peak running at 39.5 min of RP-HPLC labeled with β-endorphin in **c**. The mass corresponds exactly to the expected mass of β-endorphin. Signals at *m/z* 578.6, 694, 867, 1156 were attributed to 6+, 5+, 4+, and 3+ ions of β-endorphin (marked as $[M+6H]^{6+}$, $[M+5H]^{5+}$, $[M+4H]^{4+}$, and $[M+3H]^{3+}$, respectively).

Figure 6.5 shows the assigned 2D $[^{15}N, {}^{1}H]$-HMQC spectrum of 500 μM ^{13}C, ^{15}N-labeled β-endorphin. A complete backbone assignment (except for Pro13) was done according to conventional strategies (utilizing 3D HN(CO)CA, HNCACB, and

HN(COCA)NH-NOESY spectra) [144], which also confirmed the primary sequence identity of β-endorphin.
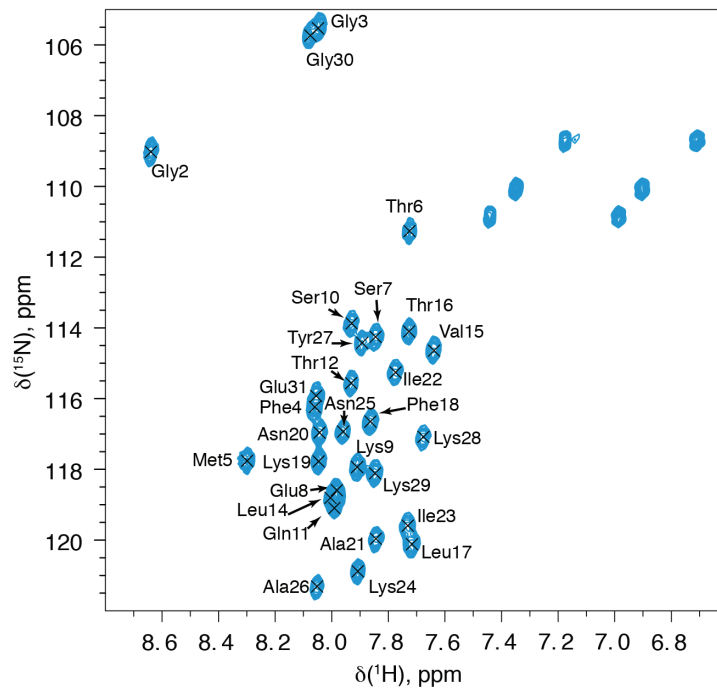
Figure 6.5. 2D [^{15}N, ^{1}H]-HMQC spectrum of ^{15}N, ^{13}C-labeled β-endorphin in DMSO. The spectrum was measured for the 500 μM solution of ^{15}N, ^{13}C-labeled β-endorphin in DMSO-D6, containing 0.02 % TFA-D at 30 °C on a Bruker 700 MHz spectrometer. The individual cross peaks were identified via sequential assignment of triple-resonance spectra.

Exploring the relationship between amyloid fibril structure and functional aggregation of β-endorphin

As described above, the high-resolution 3D structure of β-endorphin amyloid fibrils obtained at pH 5.5 in the presence of heparin allowed us to propose a hypothetical mechanism responsible for reversible hormone aggregation. According to our working hypothesis, the ionic state of the key Glu8 residue is responsible for pH-dependent triggering between the amyloid and the soluble state of β-endorphin [276]. The protonation of γ-carboxylic group of Glu8 at acidic pH, relevant to the secretory granule environment, allows the peptide to adapt a specific aggregation-prone conformation and ultimately form amyloid fibrils. Conversely, neutral pH relevant to the extracellular environment facilitates the deprotonation of Glu8 side chain and triggers the fibril dissociation upon secretion. Therefore, the aggregation of β-endorphin is not expected at neutral pH.

To test our hypothesis, we prepared β-endorphin samples of typical composition for hormone aggregation (10 mM ammonium acetate, 200 mM NaCl, 2 mg/ml heparin), the pH was adjusted to 7.4 instead of 5.5. Conversely to our expectations, the peptide was

capable of aggregation under these conditions. Moreover, the aggregates obtained bound ThT and increased its fluorescence (data not shown). We examined the morphology of these aggregates by TEM. The morphology of β-endorphin fibrils formed at pH 7.4 was quite similar to that of amyloid fibrils obtained at pH 5.5. The fibrils appeared as very long ribbons comprising of several filaments of 5-7 nm diameter each, providing the total width of the fibril of approximately 15-40 nm (**Figure 6.6**). Thus, β-endorphin aggregates produced at neutral pH were, likewise, identified as amyloids.
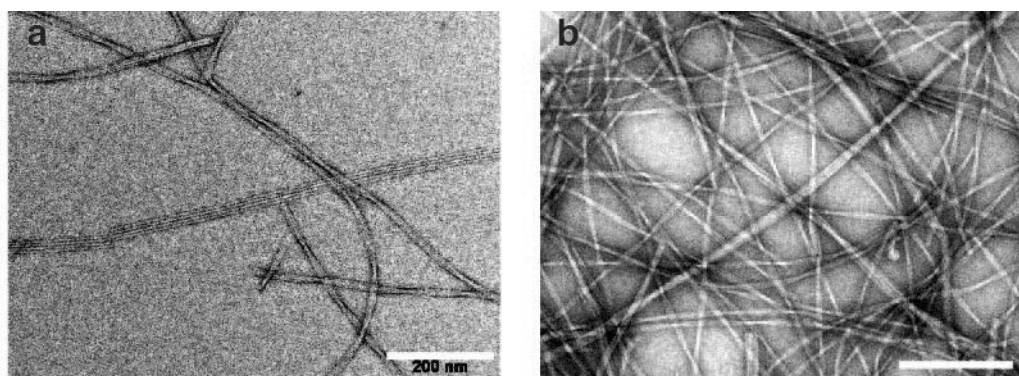
Figure 6.6. Electron micrographs of β-endorphin amyloid fibrils formed in 10 mM ammonium acetate buffer containing 200 mM NaCl and 2 mg/ml heparin at pH 5.5 (**a**) and 7.4 (**b**). Scale bars – 200 nm.

Moreover, ^{13}C-^{13}C DARR spectra [253] of ^{13}C, ^{15}N-labeled β-endorphin fibrils formed at acidic and neutral pH were similar as well (**Figure 6.7**). Only minor changes referring to slightly more pronounced presence of β-endorphin polymorphism were noticed at pH 7.4. Thus, the ssNMR data suggest that the structure of β-endorphin amyloid fibrils obtained in these two cases was very similar, if not identical. Remarkably, Glu8 γ-carboxylic group was protonated in the case of fibrils obtained at neutral pH as evidenced by the Cδ chemical shift. Perhaps, the aggregation mixture environment facilitated the Glu8 side chain protonation efficiently enough to promote aggregation of β-endorphin even at neutral pH. Various factors, such as the sequestering of aggregates from solution or the shift of Glu8 protonation equilibrium due to unusual molecular surrounding could contribute to this process. Indeed, the aggregation buffer components were specifically selected by Maji et al. [31] and further optimized by Seuring [277] with the intention to promote aggregation in β-endorphin. In this particular case, however, the highly optimized buffer composition might obscure the molecular mechanism allowing for reversible hormone aggregation.
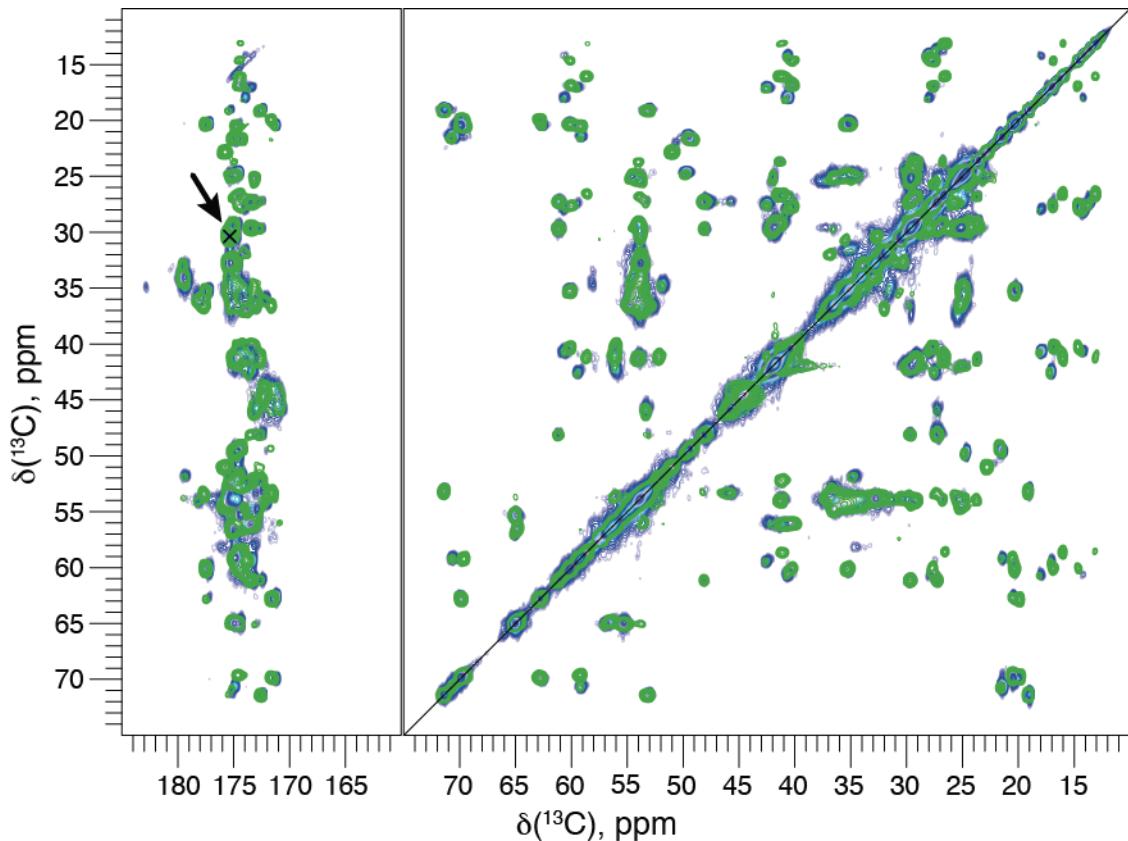
Figure 6.7. 20 ms DARR spectra of β-endorphin amyloid fibrils formed in 10 mM ammonium acetate, 200 mM NaCl buffer at pH 5.5 (blue) and 7.4 (green), in the presence of 2 mg/ml heparin. The arrow highlights the Glu8 CδCβ cross-peak. The Cδ chemical shift of 175.3 ppm indicates the protonated state of the Glu8 γ-carboxyl group.

If Glu8 indeed plays a key role in controlling the formation of functional β-endorphin amyloid, then point mutations of this residue should affect this process. To test this idea, a series of mutants (E8Q, E8L, E8K, E8R) was produced with the intention to perturb or even disrupt β-endorphin amyloidogenesis. While the charge loss in E8Q and E8L mutants was supposed to lock the amyloid state of β-endorphin, the positive charge of E8R and E8K mutants was expected to prevent the amyloid formation. Surprisingly, all mutants aggregated under a broad range of experimental conditions (buffer composition, pH) (**Supplementary Table S3**), as well as the wild-type (WT) variant.

The subsequently measured ^{13}C-^{13}C DARR spectra of fibrils formed by the mutants revealed that the E8R mutation resulted in a dramatic change of the fibril structure (**Figure 6.8**). Despite the unexpected ability of the E8R β-endorphin to form amyloid aggregates, it could not adopt the same 3D structure as WT β-endorphin. The long bulky side chain of arginine could not be incorporated into the fibril core due to steric limitations and due to the positive charge of the guanidinium group, which could

not be compensated by any other residue involved in the fibril core formation. Thus, differently looking ^{13}C-^{13}C DARR spectra of E8R β-endorphin fibrils clearly indicate the distinct amyloid structure developed by the mutant. The E8K mutation was considered to have similar effect on the structure of β-endorphin fibrils. Due to the structural difference between WT and E8R β-endorphin fibrils revealed by ssNMR, there was no rationale to study E8R and E8K fibrils further.
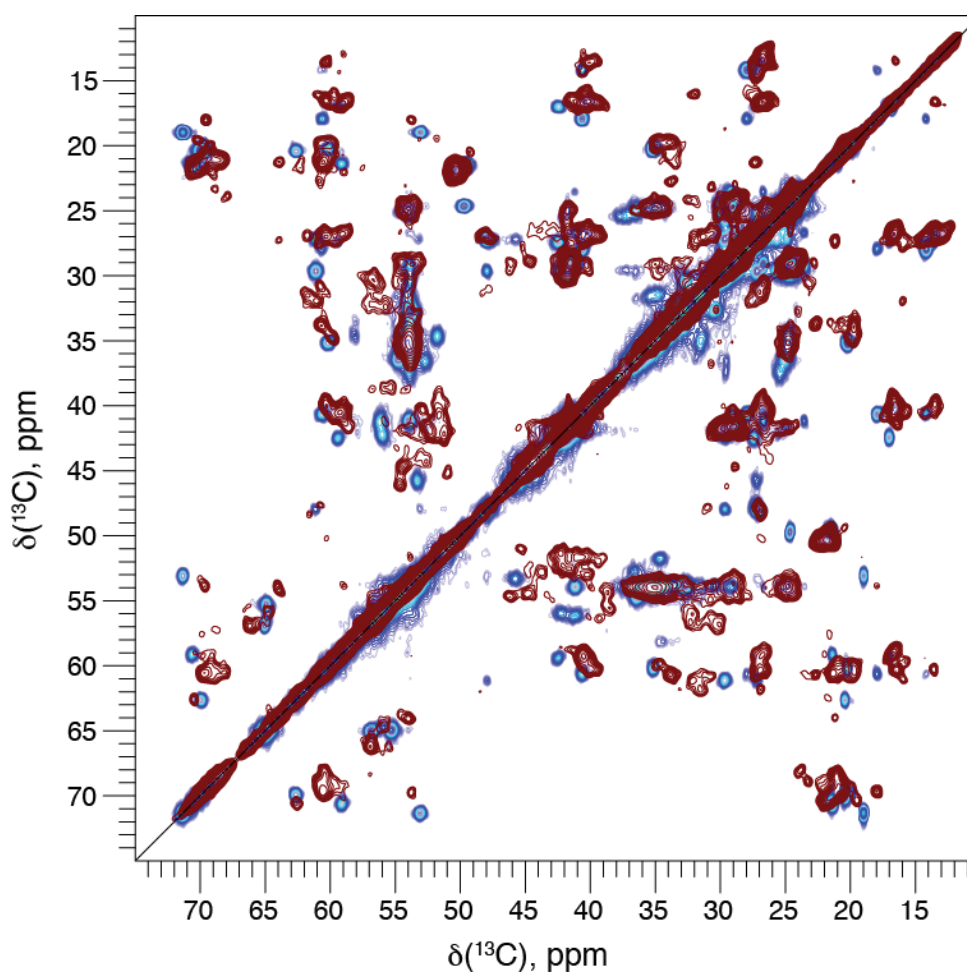
Figure 6.8. 20 ms DARR spectra of amyloid fibrils formed by ^{13}C, ^{15}N-labeled E8R (maroon) and WT (blue) β-endorphin in 10 mM ammonium acetate buffer at pH 5.5 containing 200 mM NaCl and 2 mg/ml heparin.

In turn, the E8Q mutation introduced only minimal disturbances in the amyloid structure (**Figure 6.9**). E8Q spectral differences were limited to the peaks assigned to the residues in the beginning of β$_2$ strand (Leu14, Val15, Thr16, Leu17) facing the Gln8 side chain in the fibril core (**Figure 6.2a**). Perturbations noticed in the DARR spectrum of the E8Q mutant indirectly confirm the proposed structure of β-endorphin amyloid fibrils. Only the residues spatially close to the mutation point experienced changes in molecular microenvironment, which was reflected by the spectral changes.
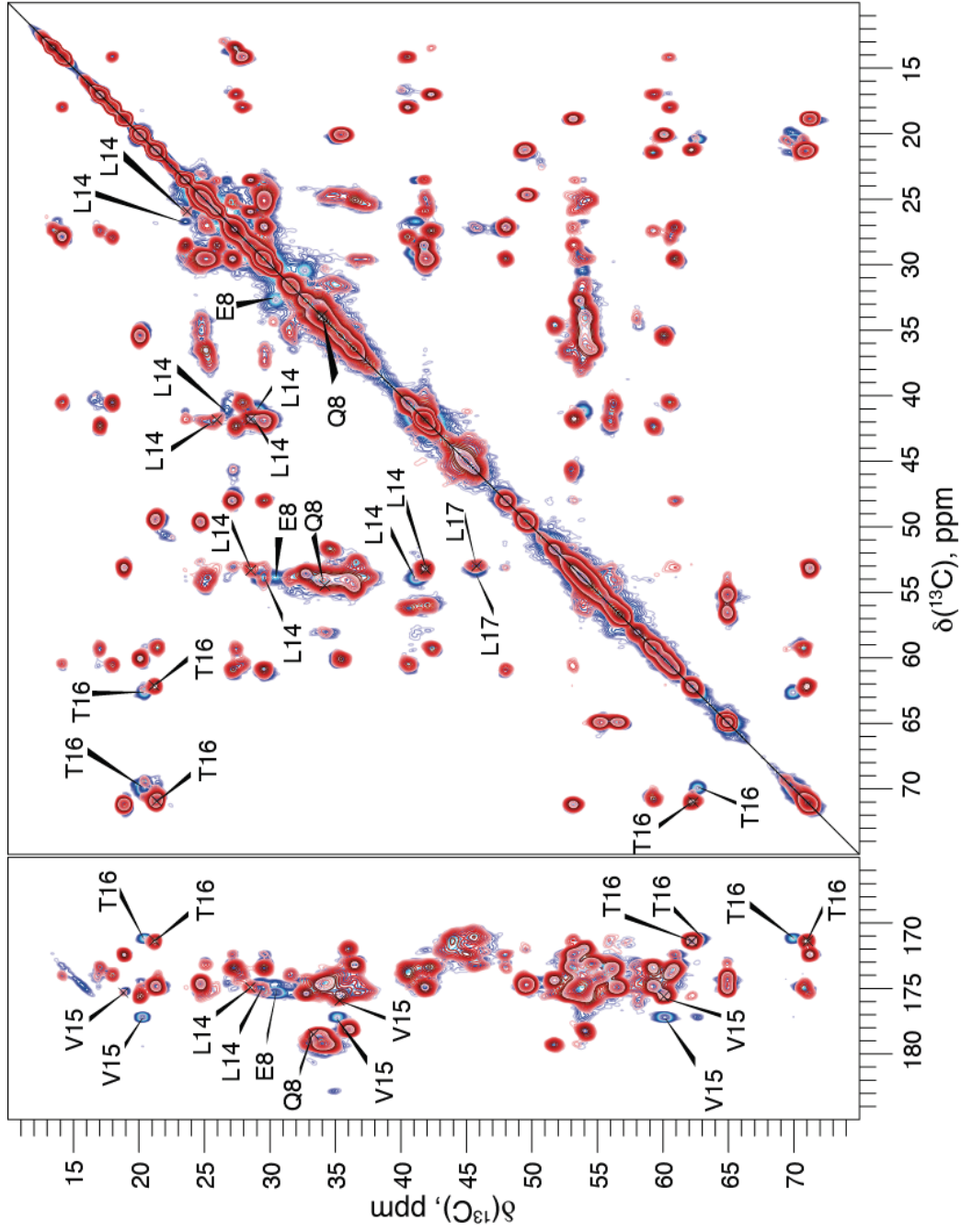
Figure 6.9. 20 ms DARR spectra of amyloid fibrils formed by ^{13}C, ^{15}N-labeled E8Q (red) and WT (blue) β-endorphin in 10 mM ammonium acetate, 200 mM NaCl, 2 mg/ml heparin (pH 5.5).

In the proposed hypothetical mechanism of β-endorphin functional aggregation, the protonation of Glu8 γ-carboxylic group is considered the rate-limiting factor. Indeed, a typical aggregation process consists of the initial buildup of the so-called amyloid seeds, which are subsequently elongated by addition of monomers. Both stages are expected to slow down if a major fraction of β-endorphin monomers contains ionized Glu8 side chain. Thus, despite the structural similarity of the terminal aggregation states of WT and E8Q β-endorphin, the fibril association and dissociation rates should be different. Presumably, E8Q β-endorphin should form fibrils faster because of bypassing the protonation of Glu8. At the same time, fibrils formed by E8Q β-endorphin are expected either to be more stable under the dissociation conditions or demonstrate slower dissociation rates.

We monitored the aggregation kinetics of β-endorphin variants by measuring the ThT fluorescence intensity over time. The WT and E8Q samples were incubated in 10 mM ammonium acetate buffer at pH 5.5 containing 200 mM NaCl and 2 mg/ml heparin at +37 ºC. Aliquots were taken at different time intervals and mixed with ThT, and the fluorescence intensity at $\lambda_{max} = 482$ nm was measured. Surprisingly, the comparison of aggregation kinetics of WT and E8Q β-endorphin revealed no significant difference between the two samples (**Figure 6.10**). ThT fluorescence significantly increased within first hours and remained at the same level in both cases. A possible explanation to this observation can be that the protonation of Glu8 side chain in WT β-endorphin is not the rate-limiting step. Perhaps, the amount of the peptide molecules with protonated Glu8 γ-carboxylic group is already high enough to afford sufficient number of seeds, which can in turn have a strong template effect on the structure and ionic state of newly added monomers and facilitate fibril growth. Alternatively, a possible effect of the aggregation buffer components on the Glu8 side chain protonation equilibrium cannot be excluded.
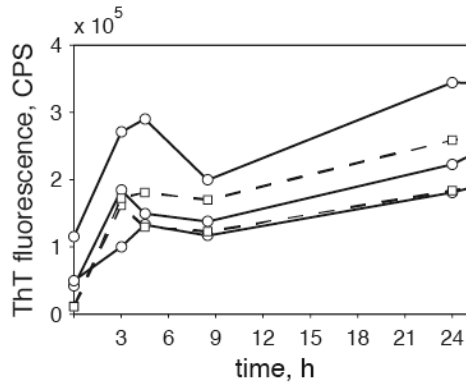
Figure 6.10. Aggregation of WT (circles, solid lines) and E8Q (squares, dashed lines) β-endorphin monitored by ThT fluorescence. Circles and squares represent individual measurements at different time points. Lines are given to guide the eye. Three independent replicates are shown for the WT peptide and two for the E8Q mutant. The data are baseline-subtracted.

The only aspect of the proposed hypothesis yet remained to be tested was the fibril dissociation triggering by pH-driven Glu8 side chain deprotonation. The E8Q mutation was expected to disrupt this mechanism and therefore lock β-endorphin in the amyloid state. Release of secretory granule content occurs *in vivo* upon dilution of the material into the blood. Hence, several parameters of the local environment, such as pH and salt content, change. Maji et al. reported the dissociation of some functional hormone amyloids *in vitro* upon dialysis against 10 mM Tris-HCl buffer at pH 7.4 [31], even though the observed rates were too slow to be biologically relevant. Here, aliquots of fibrils formed by WT and E8Q β-endorphin were centrifuged and the pellets obtained were diluted 20-fold with the same dissociation buffer (10 mM Tris-HCl buffer at pH 7.4 [31]) directly in order to induce amyloid disassembly (**Supplementary Figure S4**). Samples taken from the dissociation mixtures at different time points were examined by the ThT binding assay. In parallel, the appearance of monomeric β-endorphin was probed by UV absorbance and Tyr fluorescence measurements. The separation of monomeric and fibrillar β-endorphin was achieved by ultracentrifugation. Contrary to our expectations, not only did dissolution tests show no difference in the dissociation rates of WT and E8Q β-endorphin, but also the dissociation was not detected at all within 24 h (**Figure 6.11**). ThT fluorescence remained at the same high level ($\sim 0.8\text{-}1.0\times10^6$ cps and $\sim 5.0\text{-}6.0\times10^6$ cps for the WT and E8Q, respectively; blank fluorescence intensity was at the level of approximately 1.2×10^4 cps) during the whole time of experiment, as well as Tyr fluorescence stayed at the initial low level.
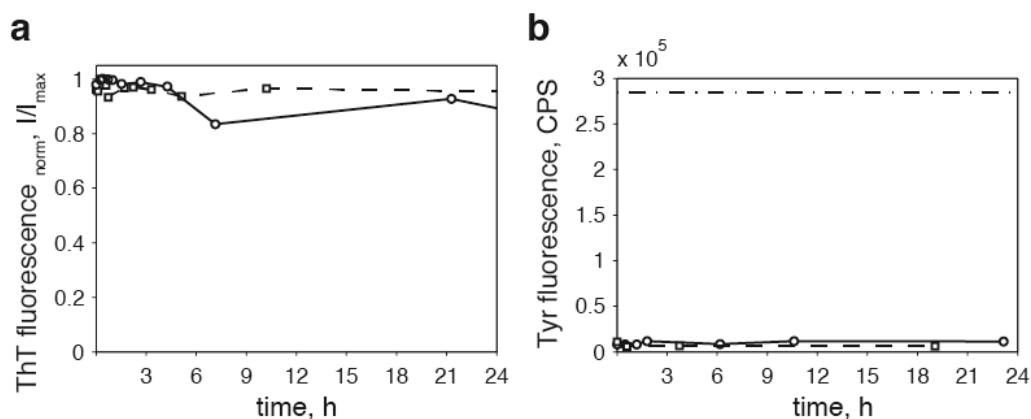
Figure 6.11. Dissociation assay carried out on amyloid fibrils formed by WT (circles, solid lines) and E8Q (squares, dashed lines) β-endorphin. (**a**) Presence of amyloid fibrils in the dissociation mixture monitored by ThT binding. Plotted are fluorescence intensities measured at $\lambda^{em} = 482$ nm upon excitation at $\lambda_{max} = 440$ nm and normalized to the maximum value after baseline subtraction. (**b**) Detection of monomeric β-endorphin in the supernatant of the dissociation mixture probed by intrinsic Tyr fluorescence. The dash-and-dot line indicates the level of Tyr fluorescence expected if 100 % fibrils dissociated. Circles and squares represent individual measurements at different time points. Lines are given to guide the eye.

The obtained results drastically disagree with the proposed hypothesis of the key role of Glu8 for triggering the dissociation of β-endorphin amyloid fibrils. Moreover, the fact that β-endorphin fibrils did not demonstrate dynamic behavior dramatically contradicts the concept of functional hormone amyloids. What could be the reason for such unexpectedly high stability of β-endorphin amyloid in the dissociation assay? First, the dissociation conditions modeled *in vitro*, such as the buffer composition, the dilution factor, and the mixing rate, could be non-optimal. For instance, the 20-fold dilution factor was rather low compared to theoretically possible 10^3-10^4 dilutions occurring *in vivo*. Second, the length of amyloid fibrils obtained *in vitro* (several micrometers; **Figure 6.6a**) significantly exceeded the diameter of secretory granules (100-400 nm) [38, 39, 286]. The core of thick and long β-endorphin fibrils produced *in vitro* could be poorly accessible for solvent, so that the majority of peptide units deeply buried within fibrils could not sense and react in reasonable time to the change of pH, dilution, and other environmental factors. Finally, the fibrils could be stabilized by some other molecules that were present in the environment during either aggregation or dissociation. We focused our further efforts to systematically test these possibilities.

Probing the stability of β-endorphin amyloid fibrils

To understand the contribution of the fibril length and the dilution factor to the observed β-endorphin fibril stability in the dissociation assay, the dissociation experiments were repeated with some parameters altered. The fibrils were shortened by

sonication, which is typically applied for the production of short fibril fragments – the so-called seeds [90, 287]. Length of the obtained β-endorphin fibrils varied from 50 to 500 nm, which is closer to the characteristic size of secretory granules. The examination of fibril morphology by EM did not reveal noticeable changes in comparison to the conventional fibril samples besides the shortened length of fibrils. The observed fibrils demonstrated the same ribbon-like morphology and were composed of several protofilaments 5-7 nm in width. Total width of ribbons varied from 15 to approximately 50 nm depending on the number of associated filaments (**Figure 6.12a**). The short fibrils were subjected to the dissociation assay upon 1000-fold dilution, as described above (**Figure 6.12b**). Despite several-fold decrease in fibrils length, they remained resistant to dissociation, which was reflected by more or less persistent ThT binding. We also softened the sample preparation procedure by omitting the ultracentrifugation step, which might infringe the structure of aggregates and crumple them, and thereby significantly slowing down the dissociation rate. This did not affect amyloid stability as well. In both cases, ThT fluorescence intensity fluctuated at more or less same high levels (**Figure 6.12b**). Thus, we could conclude that the fibril length was not a primary factor responsible for the stability of β-endorphin amyloid.
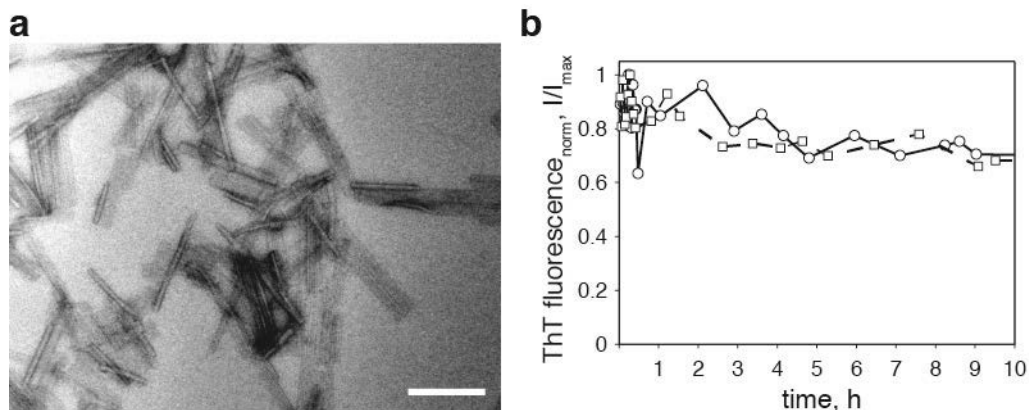
Figure 6.12. Effect of sonication on morphology and stability of β-endorphin fibrils. (**a**) Electron micrograph of sonicated β-endorphin fibrils. Scale bar – 200 nm. (**b**) Monitoring of β-endorphin fibril stability in the dissociation buffer by ThT fluorescence. Amyloid fibrils were harvested by ultracentrifugation (circles, solid lines) or alternatively transferred directly from the aggregation mixture to the dissociation buffer in order to avoid fibril compression due to centrifugation (squares, dashed lines). Plotted are fluorescence intensities measured at $\lambda^{em} = 482$ nm upon excitation at $\lambda_{max} = 440$ nm and normalized to the maximum value after baseline subtraction. The absolute fluorescence intensity was at the level of approximately $(1.1\pm0.2)\times10^5$ cps. Circles and squares represent individual measurements at different time points. Lines are given to guide the eye.

If there is a threshold peptide concentration, analogous to a critical micelle concentration, above which amyloid fibrils are always present, then dilution of

β-endorphin fibrils below this level can facilitate their disassembly. We gradually diluted the fibril samples with the dissociation buffer up to a factor of 10^4 and monitored the ThT fluorescence intensity over time. Further dilution was not considered due to approaching the detection limit of ThT binding assay. In parallel, the behavior of Aβ amyloid fibrils was monitored under the same conditions in order to exclude possible artifacts related to the sensitivity of ThT binding assay at low peptide concentrations. As it was expected, Aβ fibrils were permanently ThT-positive irrespective of the applied dilution: within three-day interval ThT fluorescence remained at high level. The same was observed for β-endorphin amyloids (**Figure 6.13**). Hence, we could rule out the dilution as a dominant factor governing the β-endorphin fibril dissociation.
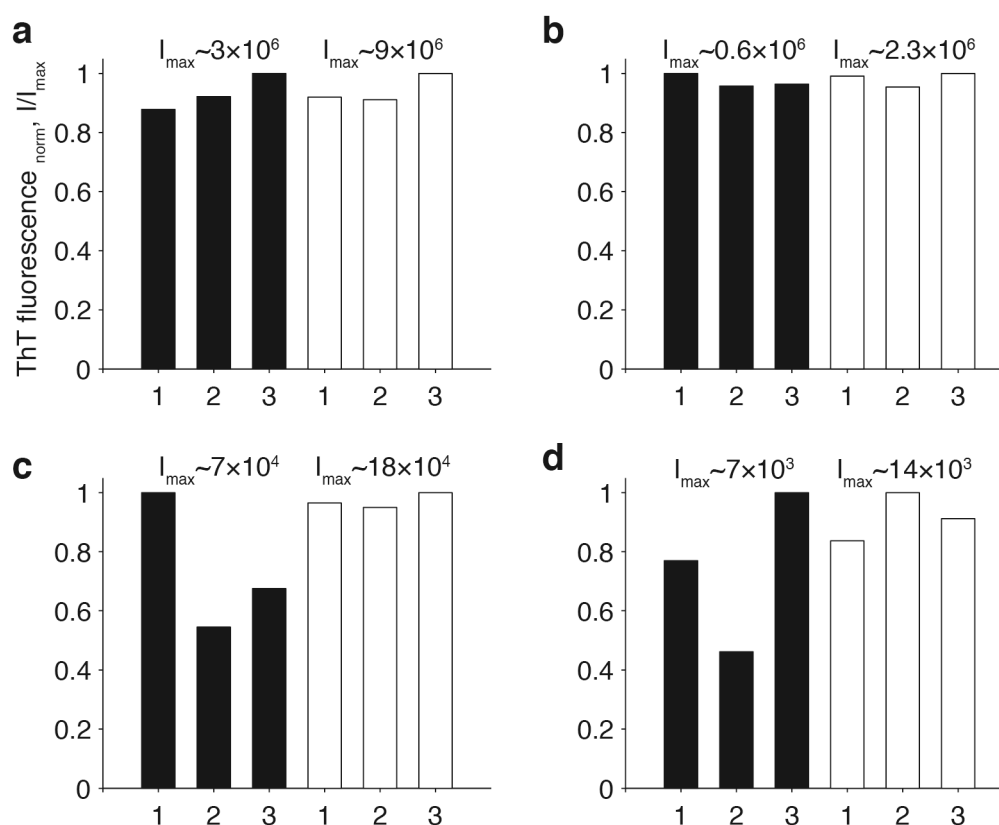
Figure 6.13. Probing the stability of Aβ (black bars) and β-endorphin (white bars) amyloid fibrils at high dilution monitored by ThT fluorescence assay. Samples were taken at the beginning of the assay (1), after three hours (2), and after three days (3). Dilution factors applied in the experiment were the following: 20 (**a**), 10^2 (**b**), 10^3 (**c**), and 10^4 (**d**).

The only factor that could explain the resistance of β-endorphin amyloid fibrils to dissociation could be some component of the aggregation or dissociation buffer that interacted with the peptide and arrested it in the aggregated state. The most probable candidate to this role seemed to be heparin. Indeed, the ability of heparin to promote

protein aggregation and stabilize amyloid fibrils has been widely recognized [75, 83]. Maji et al. demonstrated in their work that the addition of heparin promoted the aggregation in 35 peptide hormone out of 42 tested, and in 23 cases the aggregation was observed only when heparin was added. Finally, some results discussed in **Chapter 5** of this thesis indirectly speak for high stability of amyloid fibrils obtained from SS14 in the presence of heparin. Perhaps, heparin molecules could provide a polymer scaffold for peptides within amyloid fibrils or alternatively wrap around the fibrils. In both cases, heparin chains would serve as non-covalent "cross-linkers", thereby holding the peptide molecules together and protecting the fibrils from dissociation.

In support of tight β-endorphin-heparin interactions, Raman spectroscopy revealed their co-localization in the fibrils even after washing (**Figure 6.14**). The ratio between heparin and β-endorphin was found to be three sulfate groups, which corresponded to one elementary disaccharide of heparin, to 1.2 molecules of the peptide. Therefore, approximately 30 % of heparin added to the fibrillization mixture remained bound to amyloid fibrils after washing. However, it was not possible to identify the specificity of peptide-heparin interaction.
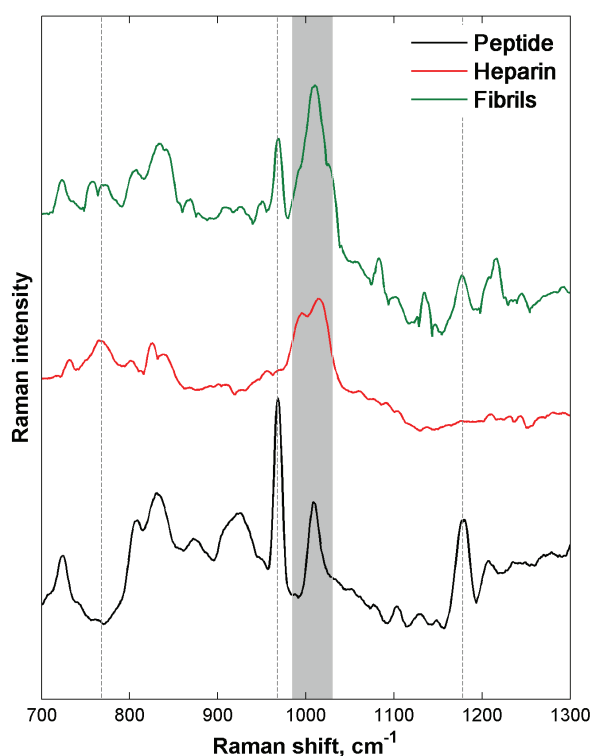
Figure 6.14. Raman spectroscopy-based analysis of the composition of β-endorphin amyloid fibrils prepared in the presence of heparin. Raman spectra of β-endorphin peptide, heparin, and dried β-endorphin fibrils prepared in the presence of heparin are shown as black, red, and green curves, respectively. The grey band highlights the characteristic peaks originated from sulfate groups of heparin.

The co-localization of β-endorphin and heparin within amyloid fibrils revealed by Raman spectroscopy indicated the possible role of heparin in fibril stability. It was however impossible to find out whether heparin intercalated into fibrils or interacted with the fibril surface. In the latter case, heparin molecules could be exposed to the solvent. Thus, the disruption of the heparin scaffold by a hydrolytic enzyme could destabilize β-endorphin fibrils resulting in fibril dissociation. To test this assumption, calcium-depended glycosidase, heparinase I, which cleaves the heparin molecule at D-glucosamine-L-iduronic acid bond, was applied to β-endorphin fibrils formed in the presence of heparin. The control experiment was performed by the addition of $CaCl_2$ to β-endorphin fibrils alone, without the enzyme, in order to exclude the influence of Ca^{2+} on ThT fluorescence. ThT fluorescence significantly dropped (from ~7.0-9.0×10^6 cps to ~1.0-3.0×10^6 cps) in both experiments – upon addition of the heparinase I and $CaCl_2$ or $CaCl_2$ alone – and remained further unchanged. Thus, the decrease in fluorescence intensity was attributed to the effect of Ca^{2+} ions on ThT fluorescence and not to fibril dissociation (**Figure 6.15**). The stability of β-endorphin fibrils observed in this experiment could have different reasons. For example, the specific cleavage sites were not accessible to the enzyme, the produced oligosaccharide species were long enough to protect β-endorphin fibrils from disassembly, etc. Nevertheless, the inability of heparinase I to promote the dissociation of heparin-induced fibrils indirectly indicated tight association between heparin and β-endorphin within amyloid fibrils.
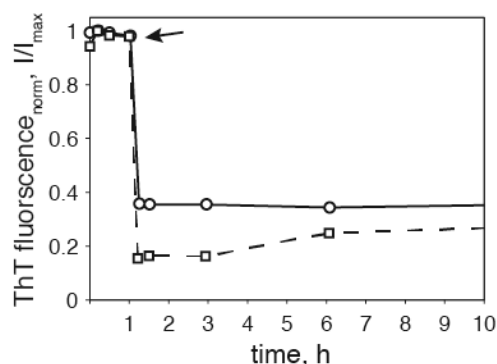
Figure 6.15. Fluorescence of ThT bound to β-endorphin fibrils in the dissociation buffer monitored before and after adding heparinase I. The arrow indicates the moment of heparinase I and $CaCl_2$ addition. In the experiment, heparinase I and $CaCl_2$ were added to the fibrils (circles, solid lines). As a control, $CaCl_2$ was added to β-endorphin fibrils alone (squares, dashed lines). Plotted are fluorescence intensities measured at $\lambda^{em} = 482$ nm upon excitation at $\lambda_{max} = 440$ nm and normalized to the maximum value after baseline subtraction. Circles and squares represent individual measurements at different time points. Lines are given to guide the eye.

Conclusions

Herein, we have applied a combination of biophysical, biochemical, and molecular biology methods to probe the molecular mechanism of β-endorphin functional aggregation. The working hypothesis has been generated based on the structural model

derived from ssNMR spectroscopy and MPL data. The protonation state of Glu8 residue γ-carboxylic group has been identified as a potential trigger of pH-dependent β-endorphin aggregation and dissociation. Our experimental results contradict to the proposed hypothesis. (*i*) β-endorphin aggregated equally well at both acidic and neutral pH. (*ii*) ssNMR revealed no significant structural difference between the hormone amyloid fibrils obtained in either case. (*iii*) Point mutagenesis of Glu8 to neutral (E8Q, E8L) or positively charged (E8K, E8R) amino acids yielded mutants which aggregated in the broad range of experimental conditions. As found by ssNMR, the E8R mutant adopted a different conformation in the fibrils compared to the WT peptide, while the E8Q variant displayed only minimal perturbation in the orientation of residues directly contacting the E/Q. (*iv*) The rates of aggregation of the WT and E8Q β-endorphin monitored by ThT-binding assay have been almost equal. (*v*) No dissociation of the WT or E8Q β-endorphin fibrils has been found in the dissociation assay.

The pronounced stability of β-endorphin amyloid fibrils observed in our experiments questions the functional nature of these amyloids. No correlation between the stability of β-endorphin fibrils under the conditions of dissociation assay and the length of fibrils or the dilution factor has been found. We have discovered a tight association between the peptide and heparin within fibrils by Raman spectroscopy, which has been supported further by the resistance of fibrils to dissociation upon treatment with heparinase I. We therefore propose heparin to be responsible for stabilizing the β-endorphin amyloid fibrils. The exact mechanism of this stabilizing effect is however unknown and requires further investigation. Nonetheless, our data question the applicability of heparin as amyloid aggregation promoter in the case of peptide hormones.

Alongside this, we have significantly improved the strategy for recombinant β-endorphin expression and purification. The described approach provides 3 to 5-fold higher yields of the target product. The achieved gain of β-endorphin amount allows us to concentrate on structural and functional studies rather than on repetitive time-consuming protein production.

Methods

Materials

Tris(hydroxymethyl)aminomethane for molecular biology was provided by BiosolveBV (Valkenswaard, Netherlands). Phenylmethanesulfonyl fluoride (PMSF),

isopropyl β-D-1-thiogalactopyranoside (IPTG), and ampicillin were purchased from AppliChem (Darmstadt, Germany). Lysozyme from chicken egg and calcium chloride (CaCl$_2$) were obtained from Fluka production GmbH (Buchs, Switzerland). Glucose, sodium chloride (NaCl), ammonium chloride (NH$_4$Cl), ammonium acetate (CH$_3$COONH$_4$) for analysis and ammonium hydroxide (NH$_4$OH) from Merck KGaA (Darmstadt, Germany) were used in this work. Trifluoroacetic acid (TFA) for HPLC was obtained from Fisher Scientific AG (Loughborough, UK). Fully deuterated dimethyl sulfoxide (DMSO-D6) (D, 99.96 %) and fully deuterated trifluoroacetic acid (TFA-D) (D, 99.5 %) for NMR measurements were from Cambridge Isotope Laboratories (Andover, Massachusetts, USA). All other reagents including labeled substrates ^{13}C-glucose (^{13}C > 99 %) and ^{15}N-ammonium chloride (^{15}N-NH$_4$Cl) (^{15}N > 98 %) and acetonitrile CHROMASOLV® gradient grade, for HPLC, ≥ 99.9 % were purchased from Sigma-Aldrich (Buchs, Switzerland), unless stated otherwise.

Strains and plasmids

One Shot® Top10 chemically competent *E. coli* cells from Invitrogen (Invitrogen™ by LifeTechnologies™, LuBioScience GmbH, Lucerne, Switzerland) were used as the bacterial host for DNA cloning. For protein expression, *E. coli* One Shot® BL21 Star™ (DE3) strain was obtained from Invitrogen and the pET32a vector was purchased from Novagen (Merck KGaA, Darmstadt, Germany). The recombinant protein contained thioredoxin as a carrier protein with the C-terminal hexa-histidine tag (6His) followed by the TEV-protease recognition site and β-endorphin sequence (**Supplementary Figure S5**). Theoretical molecular weights of the recombinant protein and molar extinction coefficients were calculated using the ProteinCalculator v3.4 [190].

Point mutations

Point mutations E8Q, E8L, E8K, and E8R were introduced in the β-endorphin sequence by PCR using Phusion High-Fidelity PCR kit from Thermo Scientific (Fischer Scientific-Switzerland, Wohlen, Switzerland). Mutagenic oligonucleotides used are listed in **Table 6.1**. pET32a/β-endorphin expression vector was used as a template (except E8L mutation, see **Table 6.2**). PCR reactions were performed using 1U of the Phusion DNA Polymerase, 0.5 μM of each primer (forward and reverse), 5xPhusion HF Buffer, and 0.2 mM dNTPs. The parameters utilized to perform PCR can be found in **Table 6.2**. The removal of template vector was performed by DpnI endonuclease

according to the protocol of manufacturer, New England BioLabs, Inc. (Bioconcept, Allschwil, Switzerland). Incorporation of the desired nucleotides was verified by DNA sequencing.

Table 6.1

Primers used to introduce point mutations in the β-endorphin sequence

Mutation	Primers*
E8Q	Fw 5' – TATGGTGGCTTTATGACCAGC<u>CAG</u>AAAAGCCAGACACCG – 3' Rv 5' – CGGTGTCTGGCTTTT<u>CTG</u>GCTGGTCATAAAGCCACCATA – 3'
E8L	Fw 5' – GGTGGCTTTATGACCAGC<u>CTG</u>AAAAGCCAGACACCG – 3' Rv 5' – CGGTGTCTGGCTTTT<u>CAG</u>GCTGGTCATAAAGCCACC – 3'
E8K	Fw 5' – GTGGCTTTATGACCAGC<u>AAA</u>AAAAGCCAGACACCG – 3' Rv 5' – CGGTGTCTGGCTTTT<u>TTT</u>GCTGGTCATAAAGCCAC – 3'
E8R	Fw 5' – GCTTTATGACCAGC<u>AGA</u>AAAAGCCAGACACCGCT – 3' Rv 5' – AGCGGTGTCTGGCTTTT<u>TCT</u>GCTGGTCATAAAGC – 3'

* Fw – the DNA sequence of forward primer; Rv – the DNA sequence of reverse primer.

Table 6.2

Cycling parameters to introduce point mutations in the β-endorphin sequence by PCR[a]

Mutation	Denaturation	Annealing	Extension	Template
E8Q	98 °C for 5 s	65 °C for 30 s	72 °C for 3 min	WT
E8L	98 °C for 5 s	69 °C for 30 s	72 °C for 3 min	E8Q
E8K[b]	98 °C for 5 s	72 °C for 30 s	72 °C for 2.5 min	WT
E8R[c]	98 °C for 5 s	69 °C for 30 s	72 °C for 3 min	WT

[a] – The number of cycle runs was 30-35.
[b] – reaction was performed in the presence of 8 % DMSO.
[c] – reaction was performed in the presence of 4 % DMSO.

Expression and purification of recombinant protein

pET32a/β-endorphin WT or mutant plasmids were used to transform the host *E. coli* One Shot® BL21 Star™ (DE3) strain. Depending on the type of needed isotopic labeling, cells were precultured in 5 ml of Luria broth (LB) or M9 minimal medium (1 L of M9 medium contains 3 g of D-glucose and 1 g of NH_4Cl) overnight at +37 °C. Cells grew at +37 °C and 120 rpm with 100 mg/L ampicillin. Recombinant gene expression was induced by adding IPTG to 1 mM when the optical density at 600 nm reached 1.0. Expression was performed at +20 °C overnight (16 h). Cells were harvested by centrifugation at 10^5 g (Avanti J-26 XP centrifuge from Beckman Coulter International S.A., Nyon, Switzerland) at +4 °C for 30 min. 8.6 g of wet cell pellet was resuspended in

50 ml of lysis buffer (50 mM Tris-HCl, 150 mM NaCl, 20 mM imidazole, 1 mM DTT, pH 8.0), PMSF and lysozyme were added to a final concentration of 1 mM and 0.5 mg/ml, respectively. The lysate was incubated at room temperature with constant stirring for one hour. Afterwards, cells were further disrupted by passing the suspension three times through the 110S microfluidizer (Microfluidics, Newton, Massachusetts, USA) at 40 psi. The solution was centrifuged at 2.5×10^4 rpm (rotor 45 Ti, Optima L-90K Ultracentrifuge, Beckman Coulter International S.A., Nyon, Switzerland), +6 °C for one hour. The supernatant and precipitate were purified separately.

The soluble fraction of the cell lysate was loaded on a HisTrapFF 5 ml column (GE Healthcare AG, Glattbrugg, Switzerland) by 7 ml increments. The fusion protein was eluted by elution buffer 1 (50 mM Tris-HCl, 150 mM NaCl, 0.5 mM DTT, 300 mM imidazole, pH 8.0). 72 ml of the protein solution were subjected to buffer exchange on a HiPrep 26/10 desalting column (GE Healthcare AG, Glattbrugg, Switzerland) by 12 ml increments. Elution buffer 1 was exchanged to the cleavage buffer (50 mM Tris-HCl, 150 mM NaCl, 0.5 mM DTT, pH 8.0). Next, the fusion protein was treated with the TEV-protease (made in house according to [191]) in a molar ratio of 1:100 at room temperature. After 16 h, 98 ml of enzymatically processed fusion protein was filtered through 0.2-µm syringe filter (Filtropur S, SARSTEDT AG & Co., Germany) and subjected to another round of affinity chromatography on a HisTrapFF 5 ml column preliminary equilibrated in the lysis buffer. 6His-tagged species were then trapped on the support, while the flow-through peptide-containing fraction was collected. Acetonitrile was added to the peptide solution up to 5 % (initial vol.) prior to RP-HPLC. Then the solution was acidified to pH 2.0 by the addition of TFA to a final concentration of 0.25 % (vol.). The HisTrapFF column was recovered by washing with the elution buffer 1 and equilibrated again in the lysis buffer. The loading-elution procedure was repeated eight times. Before applying the sample to RP-HPLC, the solution was centrifuged at 4×10^3 rpm (Biofuge primo R, Heraeus, Fischer Scientific AG, Reinach, Switzerland) for 15 min at +22 °C and the supernatant was subsequently filtered through 0.2-µm Filtropur S filter in order to remove the protein precipitate that occurred upon addition of TFA.

The insoluble fraction of the cell lysate was resuspended in 50 ml of extraction buffer (50 mM Tris-HCl, 8 M urea, 150 mM NaCl, 10 mM imidazole, 1 mM DTT, pH 8.0). Extraction of the fusion protein was carried out for one hour at room temperature under constant stirring. The extract was centrifuged at +22 °C, 4×10^4 rpm (rotor 45 Ti,

Optima L-90K Ultracentrifuge) for 1.5 hour. The supernatant was purified on a HisTrapFF 5 ml column by 5-ml increments. The fusion protein was eluted by elution buffer 2 (50 mM Tris-HCl, 7 M urea, 150 mM NaCl, 0.5 mM DTT, 300 mM imidazole, pH 8.0). The flow-through contained the target fusion protein and was therefore re-loaded on the HisTrapFF 5 ml column five times by 25 ml. 110 ml of the protein solution obtained were subjected to buffer exchange on a HiPrep 26/10 desalting column by 12-13 ml increments. Elution buffer 2 was exchanged to the cleavage buffer. The following steps (treatment with the TEV-protease, secondary Ni-chelate chromatography) were carried out in exactly the same way as described above for the case of soluble protein fraction.

Final purification of β-endorphin was performed on a Discovery BIO Wide Pore C18 column (25 cm x 10 mm, 10 μm; Supelco, Bellefonte, Pennsylvania, USA). The elution was carried out using an acetonitrile gradient (12-45 % buffer B in 30 min, flow rate – 2 ml/min; buffer A - water with 0.1 % TFA, buffer B – acetonitrile with 0.1 % TFA). An Agilent 1200 HPLC system (Agilent Technologies (Schweiz) AG, Basel, Switzerland) equipped with an external manual injector, an automatic fraction collector, and a diode-array detector was used. The elution profile was monitored by UV absorption at 220 and 280 nm. Average injection volume was 15 ml. Fractions containing β-endorphin were collected, merged, and freeze-dried. 2 and 4 mg aliquots of lyophilized peptide were stored at -25 ºC until use. The identity and purity of the recombinant peptide was monitored by ESI-MS (Q-TOF Ultima API, Micromass, Manchester, UK).

Protein electrophoresis and concentration measurements

The expression and purification processes were monitored by protein electrophoresis [192] using denaturing NuPAGE® Novex® 4-12% Bis-Tris Gels (Invitrogen™ by LifeTechnologies™, LuBioScience GmbH, Lucerne, Switzerland) and SeeBlue® Pre-Stained Standard from Invitrogen™ according to the manufacturer's instructions. ImageJ software [185] was used for quantitative analysis of Coomassie-stained [192] SDS-PAGE gel images. The protein concentration was determined by UV spectroscopy (λ_{max} = 280 nm; $\varepsilon_{THX-\beta-endorphin}$ = 17900 M^{-1} cm^{-1}, $\varepsilon_{\beta-endorphin}$ = 2560 M^{-1} cm^{-1}).

Mass spectrometry

Mass spectra were acquired on a hybrid quadrupole-time-of-flight mass spectrometer Q-TOF Ultima API (Micromass, Manchester, UK) equipped with a Z-spray

interface (Waters, Manchester, UK). Ions were generated using an automated chip-based nano-electrospray ion source (NanoMate model 100, Advion BioSciences, Ithaca, NY, USA) at a high voltage of 1.3-1.7 kV applied to the electrospray emitter chip. A backing pressure of 0.5 bar was used to assist the sample flow, and the typical flow rate was approximately 200 nL/min. The ion source was kept at room temperature. Potentials on the ion guides were optimized to ensure efficient ion transmission in the *m/z* range of 100-4000 for the peptide samples or 300-8000 for the protein samples. A single scan time of 1 s was used, and typically 50-100 scans were combined to obtain a representative mass spectrum. Spectra were managed and processed via the MassLynx v. 4.0 software (Waters, Manchester, UK). Multiply-charged peaks in the electrospray spectra were deconvoluted, where necessary, using the MaxEnt 1 tool embedded within the MassLynx software. Mass calibration was performed using CsI clusters. Peptide and protein samples were infused either directly after RP-HPLC or upon desalting, if required, using a ZipTip C18 column (Millipore AG, Zug, Switzerland) according to the procedure described by the manufacturer.

Liquid-state NMR spectroscopy

The peptide used in NMR experiments was prepared according to the protocol described by Seuring [277]. 0.9 mg of lyophilized ^{15}N, ^{13}C-labeled β-endorphin was dissolved in 500 μl DMSO-D6, 0.02 % TFA-D. NMR spectra of the 2D [^{15}N, ^{1}H]-HMQC and 3D HN(CO)CA, HNCACB, and HN(COCA)NH were recorded at 30 °C on a Bruker 700 MHz spectrometer equipped with a cryoprobe. The spectra were processed with TopSpin 2.0 software (Bruker BioSpin AG, Fällanden, Switzerland) and assigned using the CCPN software package [194]. Sequential connectivities were established by using the data of 3D NMR experiments following conventional strategies [144].

Preparation of fibrils for ssNMR measurements and dissociation assays

β-endorphin was dissolved in the fibrillization buffer (10 mM ammonium acetate, 200 mM NaCl, 2 mg/ml heparin, pH 5.5) at 2 mg/ml concentration. Aggregation was set up in low-retention 1.5 ml test tubes (Vaudaux-Eppendorf AG, Schönenbuch/Basel, Switzerland) in the EchoTherm RT11 rotating mixer (Torrey Pines Scientific, Inc., Carlsbad, USA) at a rotation speed of approximately 30 rpm inside an incubator thermostated at +37 ºC. A heparin stock solution was prepared by dissolving 250 mg of heparin (heparin sodium salt, sc-203075, Santa Cruz Biotechnology, Inc., Heidelberg,

Germany) in 2.5 ml of double-deionized water containing 0.05 % (w/v) sodium azide (AppliChem, AXON LAB AG, Baden-Dättwil, Switzerland). One part of the heparin stock solution was added to 50 parts of β-endorphin dissolved in the fibrillization buffer to initiate fibrillization. Afterwards, sodium azide was added up to a concentration of 0.05 % to the peptide solution. Sample tubes were sealed by PARAFILM® M (Sigma-Aldrich Chemie GmbH, Buchs, Switzerland) and placed for fibrillization. Aliquots were taken out for analysis when necessary. For dissociation assays, fibrils were taken after 3-5 days of incubation.

Transmission electron microscopy

5 μl samples of β-endorphin fibrils were deposited for 1 min on previously glow-discharged carbon-coated copper grid (Electron Microscopy Sciences, Hatfield, Pennsylvania). The grid was then blotted, washed twice in drops of double-distilled water and negatively stained for 15 s with filtered 2 % (w/v) uranyl acetate (Sigma-Aldrich Chemie GmbH, Buchs, Switzerland). Images were acquired with the FEI Morgagni 268 electron microscope (FEI Company, Eindhoven, Netherlands) operated at 100 kV. Electron micrographs were recorded on a 1376 by 1032 pixel charge-coupled device camera (Veleta, Olympus soft imaging solutions GmbH, Münster, Germany).

Raman spectroscopy

An upright Raman microscope (NTEGRA Spectra, NT-MDT, Russia) was employed for Raman microscopy and AFM measurements. The system was equipped with an upright confocal laser microscope, an atomic force microscope (AFM), a white-light video microscope for rough observation and alignment of the sample, a photomultiplier tube (PMT) detector for confocal imaging, and a Raman spectrograph equipped with a charge-coupled device (CCD). It allowed simultaneous AFM and optical measurements on exactly the same part of transparent and opaque samples. All optical measurements were performed using a 100×long working-distance objective with a numerical aperture (NA) of 0.7 for both excitation and collection of the backscattered light from the sample. Two lasers, a red HeNe (632.8 nm, 5 mW at the sample) provided by Laser Drive, Inc. and a green DPSS (532 nm, 3-4 mW at the sample) provided by Changchun New Industries (CNI) Optoelectronics Tech. Co., Ltd. were used for Raman spectroscopy. An area of 5×5 μm (256×256 pixels) was scanned by AFM in tapping mode with a speed of 1 line per second. AdvancedTEC cantilevers (NANOSENSORS,

Switzerland) with resonance frequencies in the 210-490 kHz range and force constants of 12-110 Nxm^{-1} were used.

50 µl of β-endorphin fibrils prepared in 10 mM ammonium acetate buffer at pH 5.5 with 200 mM NaCl and 2 mg/ml heparin were washed in double-deionized water twice according to the following procedure. Fibrils were centrifuged at 2.5×10^4 g and a temperature of +22 ºC for 15 min (Microcentrifuge 5417R, Vaudaux-Eppendorf AG, Schönenbuch/Basel, Switzerland). The pellet was resuspended in 50 µl of double-deionized water, extensively pipetted and centrifuged again. 20 µl of washed fibrils were dried on the microscope slide with cut edges (Menzel-Gläser, Gerhard Menzel GmbH, Braunschweig, Germany) for 2 h. A red HeNe laser (632.8 nm, 5 mW at the sample) was used for Raman spectroscopy of dried β-endorphin fibrils. Three to seven spectra were accumulated for 600 s of total time each. Standard procedures for spike and fluorescent background corrections were applied [260]. The final spectra were smoothed by Savitzky-Golay filtering [261]. The same approach was used to measure Raman spectra of lyophilized heparin and monomeric β-endorphin.

Dissociation assay

200 µl of amyloid fibrils formed by β-endorphin (WT, E8Q, E8L, E8K, E8R variants) in 10 mM ammonium acetate at pH 5.5 containing 200 mM NaCl and 2 mg/ml heparin were centrifuged for 30 min at 28 psi in the Airfuge® Air-Driven centrifuge (Beckman Coulter International S.A., Nyon, Switzerland). Aβ aggregates preformed in 20 mM sodium phosphate buffer at pH 7.4 containing 25 mM sodium chloride were used as a control in some experiments. The pellets obtained were resuspended in 200 µl of 10 mM Tris-HCl buffer at pH 7.4 and subsequently diluted to 4 ml with Tris-HCl buffer, pH 7.4 in 5-ml glass bottles closed by polypropylene caps. The dissociation mixture was kept at room temperature under constant stirring at 250 rpm on a magnetic stirrer plate. Samples were taken at different time points either for ThT binding or for Tyr fluorescence measurements. The samples taken for ThT binding measurements were represented by 150 µl of the dissociation mixture, which were directly mixed with 1 µl of 1.5 mM ThT solution. ThT fluorescence spectra were recorded on FluoroMax®-4 spectrofluorometer controlled by FluorEssence™ software (Horiba Jobin Yvon GmbH, Munich, Germany). Excitation wavelength was 440 nm and spectra were acquired in the range of 460-550 nm utilizing 3 nm slits for excitation and emission. To monitor the appearance of soluble β-endorphin, 150 µl of the dissociation mixture were centrifuged

for 30 min at 28 psi in the Airfuge® Air-Driven centrifuge. The supernatant was used to measure intrinsic Tyr fluorescence. Tyr fluorescence spectra were recorded on FluoroMax®-4 spectrofluorometer. Excitation wavelength was 275 nm and spectra were acquired in the range of 290-500 nm utilizing 3 nm slits for excitation and emission. Next, the UV absorbance of the examined solution was recorded on the UV-Vis spectrophotometer V-650 (JASCO Labor und Datentechnik GmbH, Gross-Umstadt, Germany) in the range of 240-340 nm.

Single-point measurements of ThT binding

To monitor the aggregation of WT and E8Q β-endorphin in 10 mM ammonium acetate buffer at pH 5.5 containing 200 mM NaCl and 2 mg/ml heparin, 5 µl aliquots were taken from the aggregation mixture, diluted by 245 µl of the fibrillization buffer without heparin and stained by 1.5 µl of 0.7 mM ThT solution. The spectra were recorded on FluoroMax®-4 spectrofluorometer in the range of 460-550 nm with excitation at 440 nm and 3 nm slits for excitation and emission.

Shortening of β-endorphin fibrils by the ultra-sound treatment

200 µl of preformed β-endorphin fibrils were sonicated on ice by Sonopuls HD2070 sonicator with a MS 73 tip (Bandelin, Berlin, Germany). Four cycles of sonication were applied. One cycle comprised of 10 s sonication and 10 s rest at 50 % power. The result of fibril shortening was controlled by EM.

Solid-state NMR spectroscopy

All ^{13}C-^{13}C DARR spectra of WT, E8Q, and E8R β-endorphin fibrils obtained in 10 mM ammonium acetate buffer at pH 5.5 containing 200 mM NaCl and 2 mg/ml heparin were recorded on a Bruker Avance spectrometer operating at a static magnetic field of 14.1 T. A Bruker 3.2 mm triple resonance probe was used. The spinning speed was set to 13 kHz and the sample temperature was held between +5 ºC and +10 ºC during the measurement. 90 kHz to 100 kHz SPINAL proton decoupling [288] was applied in all dimensions during acquisition. All spectra were processed using Topspin 2.1 (Bruker BioSpin AG, Fällanden, Switzerland), using a shifted cosine squared window function and zero-filling to the next power of two in all dimensions. Automated baseline correction was applied in the direct dimension. The spectra were analyzed using the CCPN software package [194]. Further acquisition and processing details are given in **Supplementary Table S4**.

Data analysis

Data analysis of secondary chemical shifts, all aggregation and dissociation assays was done in the commercial software MATLAB 8.0, The MathWorks Inc., Natick, Massachusetts, USA. In the dissociation assay, the baseline fluorescence of the 20 μM ThT solution in 10 mM Tris-HCl buffer at pH 7.4 was subtracted from all the data. The baseline-subtracted data were then normalized to the maximum fluorescence intensity value in the series.

Chapter 7

Dynamic assembly and disassembly of functional β-endorphin amyloid fibrils[1]

Introduction

As described in **Chapter 6**, the β-endorphin amyloid fibrils produced in the presence of heparin exhibited a pronounced resistance to dissociation. The reversibility of hormone aggregation is a key property of these functional amyloids and is absolutely necessary for functional signal transduction *in vivo*. The findings reported in **Chapter 6** have questioned the biological relevance of the fibrils formed in the presence of heparin, as well as the use of heparin as a universal aggregation promoter.

The pronounced efficiency of heparin in promoting amyloid aggregation is widely recognized [31, 66, 73, 75, 76, 82, 83, 289-291]. For instance, the addition of heparin to the aggregation mixture could enforce the amyloidogenesis in 35 peptide hormones including β-endorphin [31, 291]. However, it is actually not obvious if this compound universally displays this activity *in vivo*. In fact, secretory granules filled with heparin were found only in mast cells, whose major function is secretion of heparin to blood [68]. Thus, the need to search for biologically relevant conditions for hormone aggregation clearly arises. Identifying the difference between intra- and extracellular environment may hint to the factors that control the functional aggregation of hormones in the cell and the dissociation of these amyloid aggregates upon secretion.

Environmental changes occurring in the secretory pathway take place along with hormone maturation and its packing into secretory granules [41, 54, 56-58]. Analysis of biological fluids has demonstrated asymmetric distribution of mono- and polyvalent ions. For example, multiply charged anions are quite abundant in the cell, while monovalent anions and cations are plentiful in the blood and interstitial fluid (**Figure 7.1**). The level of phosphate is one of the highest in the cell and corresponds to 60 mM, while bicarbonate is the major buffering system in the blood [292]. The high concentration of phosphate is partly provided by different hexose-phosphates present in the GC, in particular mannose-6-phosphate serving as the sorting signal of lysosomal proteins [36].

---

[1] All ssNMR spectra presented in this chapter were measured by Julia Gath from the group of Prof. Beat Meier (LPC, ETH Zurich, Switzerland).

Obviously, one of the possible factors that may be involved in dynamic assembly and disassembly of hormonal amyloids is the change of major salt ions. Another potentially important factor is the change of pH from 5.5 in the secretory granules to 7.4 in the blood.
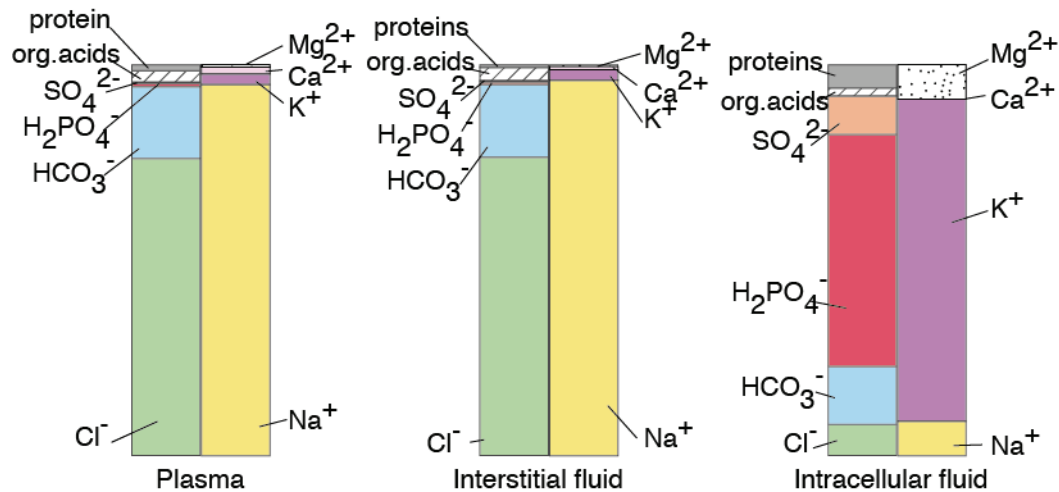
Figure 7.1. Distribution of ions in biological liquids [292].

It is also important to note here that the release of the secretory granule content occurs almost instantly via the so-called degranulation pathway. Briefly, secretory tissue cells are surrounded by the fenestrated capillaries. These capillaries are characterized by pores in endothelial cells (60-80 nm in diameter), which permit the diffusion of proteins and small molecules [293]. The specific anatomy of these capillaries allows for direct passage of hormonal dense granules from secretory vesicles into a capillary bore (**Figure 7.2**) [292, 294]. Thus, a relatively high dilution of the secretory granule content occurs upon secretion and is expected to be another driving force of hormone amyloid dissociation.
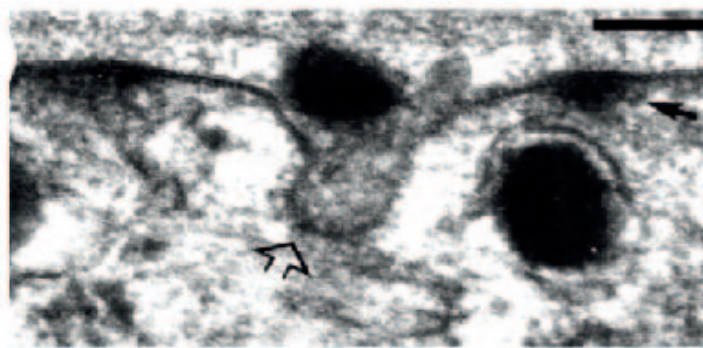
Figure 7.2. Exocytosis of secretory granules. The transparent arrow points to the granule core release. Black arrows indicate the dense secretory granule cores. Scale bar – 100 nm. Reprinted from [286].

The possible influence of carbohydrates on specific protein aggregation during sorting in the GC cannot be neglected. Different sugars are highly abundant in the ER and GC, which are the main location of carbohydrate synthesis in mammalian cells [36]. The influence of carbohydrates on amyloidogenic proteins has been extensively studied. High-molecular-weight GAGs, such as heparin and heparan sulfate, as well as simple monosaccharides, e.g., glucose, fructose, and mannose, have been investigated in the context of pathological aggregation of Aβ, α-synuclein, immunoglobulin light chains, and insulin [75, 76, 79, 83, 295-298]. The variety of obtained results differs from stimulation of faster fibril formation to pronounced reduction of amyloid aggregation. The major conclusion of all these experiments has been summarized by Fung et al. [297]. The less mobile sugars are expected to form more stable hydrogen bonds and increase native stability of a protein. Conversely, more mobile sugars will withdraw water from a fibril and therefore promote amyloid formation. However, little is known to date about the influence of low-molecular-weight carbohydrates on dynamic assembly and disassembly of functional hormone amyloids.

In the present chapter, we explore the influence of the factors identified above on the structure and properties of β-endorphin aggregates in order to reveal the mechanism of reversible functional hormone aggregation.

Results and discussion

Multivalent anions promote reversible β-endorphin aggregation

The discovered stability of heparin-induced β-endorphin fibrils in the dissociation assay compelled us to search for heparin-free conditions to promote β-endorphin amyloid aggregation. During the broad screening of fibrillization conditions, multiply charged anions were identified as effective promoters of β-endorphin aggregation (**Supplementary Table S3**). The salt-promoted aggregates were identified as amyloid fibrils based on fibrillar morphology revealed by EM (**Figure 7.3**) and the ability to bind ThT and increase its fluorescence. Moreover, the fibrils obtained in buffers containing multivalent anions, such as phosphate, sulfate, citrate, and maleate, sheared common appearance in EM. Remarkably, salts of monoprotic acids, such as ammonium acetate or Tris-HCl, did not promote β-endorphin aggregation. Thus, 10 mM Tris-HCl buffer at pH 7.4 was chosen for the fibril dissociation assay.

The main feature distinguishing the "salt-type" fibrils from the heparin-induced ones (see **Figure 6.6**) was their tendency for clustering, lateral association of individual fibrils resulting in emergence of fibril bundles of a thickness ≥100 nm (**Figure 7.3**). The tendency of salt-type fibrils to cluster can be attributed to neutralization of the peptide charged groups by counter-anions. The isoelectric point (pI) of β-endorphin equals to approximately 9.8, i.e. the peptide is positively charged at acidic and neutral pH. The anions form salt pairs with the positively charged groups of β-endorphin exposed to solvent and effectively neutralize them, thereby suppressing the Coulomb repulsion between peptide monomers and fibrils, so that large peptide aggregates can ultimately agglomerate. In turn, heparin is a polyanion and the stoichiometry of heparin binding to β-endorphin fibrils was measured as 3 sulfate groups per 1.2 peptide molecule, which should suffice to suppress the electrostatic charge of fibrils as well. Nonetheless, heparin is a highly sulfated irregular polymer, i.e. the exact number of sulfate groups bearing negative charges brought to fibrils by heparin is difficult to estimate and can actually be non-stoichiometric, which may result in charge disbalance and cause Coulomb repulsion. Moreover, the nature of heparin-peptide interaction seems to be more complex than simple ion pairing, as demonstrated in **Chapter 3** for the case of CRF. Eventually, heparin somehow maintains β-endorphin amyloid fibrils isolated and prevents their agglomeration.
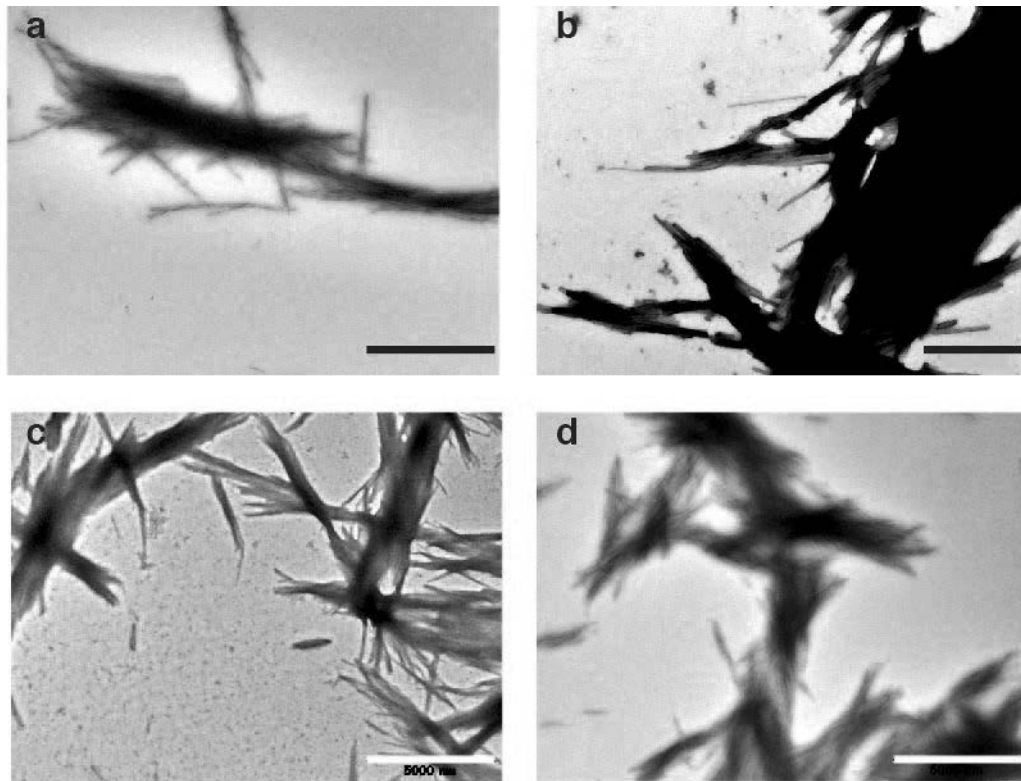
Figure 7.3. Electron micrographs of β-endorphin fibrils promoted by sulfate (**a**), phosphate (**b**), citrate (**c**), maleate (**d**). Scale bars in **a**, **c**, **d** – 5 μm, in **b** – 1 μm.

β-endorphin fibrils formed in the presence of polyvalent anions, such as sulfate, phosphate, and a combination of phosphate and citrate, were compared in the dissociation assay with the heparin-induced fibrils. Fibril samples were centrifuged at 10^5 g. Pellets were subsequently diluted 20-fold into 10 mM Tris-HCl buffer at pH 7.4 mimicking the blood environment and left under stirring at room temperature. Aliquots were taken from dissociation mixtures at different time points and mixed with the ThT dye for fluorescence measurements. Other aliquots were subjected to ultracentrifugation and the obtained supernatants were directly used for measurements of Tyr fluorescence and UV absorbance. All salt-induced amyloid fibrils of β-endorphin demonstrated pronounced ThT fluorescence decay from ~1.6×10^6 cps to ~9.0×10^4 cps with apparently exponential kinetics, indicating the disappearance of the amyloid from the bulk phase of solution. Fibril disassembly occurred on a relatively short time scale with the estimated decay constant (time when fluorescence intensity is reduced to $1/e$ its initial value) of two hours or less (**Figure 7.4a**). Heparin-induced β-endorphin fibrils instead demonstrated consistently high ThT fluorescence intensity of approximately 9.6×10^6 cps over time. In addition, monitoring of Tyr fluorescence revealed rapid buildup of the signal intensity in the samples obtained from dissociation mixtures of salt-induced fibrils. This indicated

that monomeric β-endorphin was released from the salt-promoted fibrils. EM examination of the salt- and heparin-induced fibrils before and after the 24-h dissociation assay revealed disappearance of the fibrillar material from samples of salt-promoted aggregates, while fibrils could be easily found in specimens of heparin-induced fibrils.
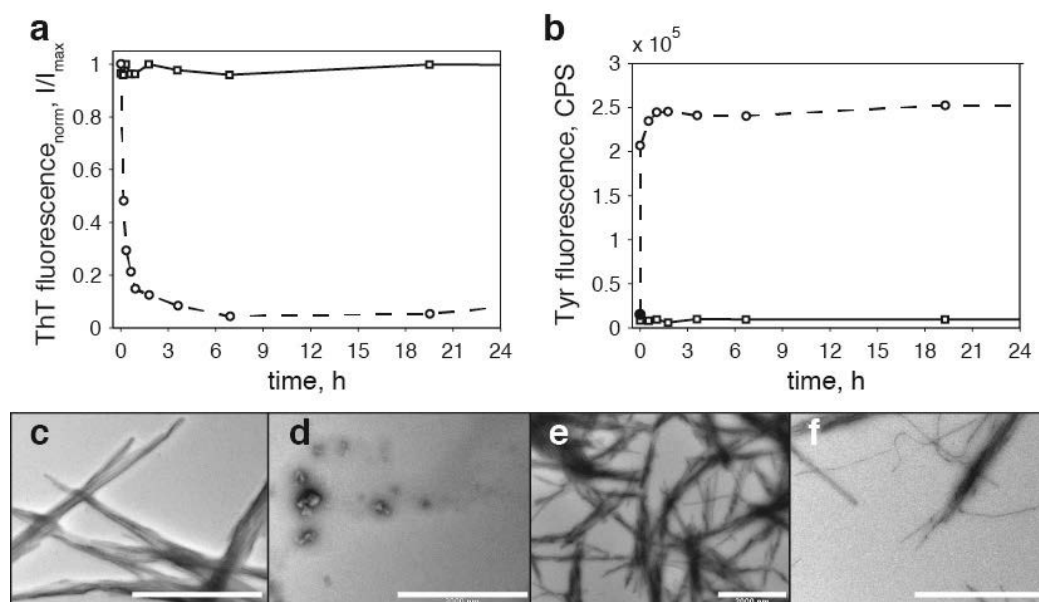
Figure 7.4. Fibril dissociation assay carried out for β-endorphin fibrils formed in PBS (circles, dashed lines) and those in the presence of heparin (squares, solid lines) (**a**) ThT fluorescence intensity over time. ThT fluorescence decay observed for the fibrils formed in PBS indicates their dissociation. In contrary, β-endorphin fibrils formed in the presence of heparin demonstrate consistently high ThT fluorescence, which has been interpreted as their resistance to dissociation. Plotted are fluorescence intensities measured at $\lambda^{em} = 482$ nm upon excitation at $\lambda_{max} = 440$ nm and normalized to the maximum value after baseline subtraction. (**b**) Detection of monomeric β-endorphin in the supernatant of dissociation mixtures is probed by intrinsic Tyr fluorescence. The rapid increase of Tyr fluorescence in the samples of fibrils formed in PBS indicates the appearance of monomeric β-endorphin, while steadily low signals found for the samples of heparin-induced fibrils suggest no release of the peptide monomers. Circles and squares represent individual measurements at different time points. The filled circle represents the extrapolated initial level of Tyr fluorescence in the sample of β-endorphin fibrils formed in PBS. Lines are given to guide the eye. (**c-f**) Electron micrographs of β-endorphin fibrils formed in PBS (**c**) and in the presence of heparin (**e**) before the dissociation and 24 h after the beginning of the assay (respectively **d** and **f**). Scale bars – 2 μm

Solid-state NMR spectroscopy data suggest pronounced structural differences between the salt-promoted and heparin-induced β-endorphin amyloid fibrils

The findings described above represent the very first unambiguous demonstration of the reversibility of functional hormone aggregation. Numerous experimental evidences coming from several orthogonal methods consistently demonstrated rapid disassembly of β-endorphin amyloid fibrils, whose aggregation was promoted by salts of polyprotic acids. In contrast, the heparin-induced amyloid fibrils were stable under the conditions of the dissociation assay on the timescale of experiments. The question arises: what allows the salt-promoted aggregation of β-endorphin to be reversible. To address this question,

we applied ssNMR spectroscopy to probe the structure of salt-promoted fibrils and compare it to the structural model of heparin-induced β-endorphin amyloid fibril described earlier.

Uniformly ^{13}C, ^{15}N-labeled β-endorphin fibrils were produced in 50 mM sodium phosphate, 2 mM sodium citrate buffer at pH 6.0, which is further referred to as CP buffer. Comparison of ^{13}C-^{13}C DARR spectra of ^{13}C, ^{15}N-labeled heparin-induced β-endorphin fibrils formed in ammonium acetate buffer at pH 5.5 [276, 277] and the salt-promoted ones formed in CP buffer at pH 6.0 revealed significant differences in the spectra (**Figure 7.5, Supplementary Figure S6**). All peaks in the spectrum of fibrils obtained in CP buffer appeared at new positions, which made it impossible to match the spectrum of heparin-induced fibrils by a simple translation of peaks. A new sequential assignment was required in order to identify structural changes at the level of individual amino acid residues. While the amino acid sequence of β-endorphin contains two serines and three threonines, the number of peaks found in the spectral regions specific for serine and threonine was greater than two and three, respectively, indicating the presence of amyloid polymorphism (**Figure 7.5b, Supplementary Figures S7-S10**). Comparison of peak intensities suggested that the polymorphs were present in almost equal amounts. More importantly, the sequential assignment of ^{13}C-^{13}C DARR spectrum of the β-endorphin fibrils obtained in CP buffer revealed that the carboxyl group of Glu8 was deprotonated, as reflected by the high chemical shift of Cδ atom of 182.5 ppm (compare to 175.3 ppm in the case of heparin-induced fibrils). Interestingly, fibril polymorphism noticed for Ser and Thr residues involved Glu8, too. As can be seen in **Figure 7.5c**, four peaks in the DARR spectrum were assigned to CδCβ of Glu8 and all of them were attributed to a deprotonated γ-carboxyl group of the side chain.
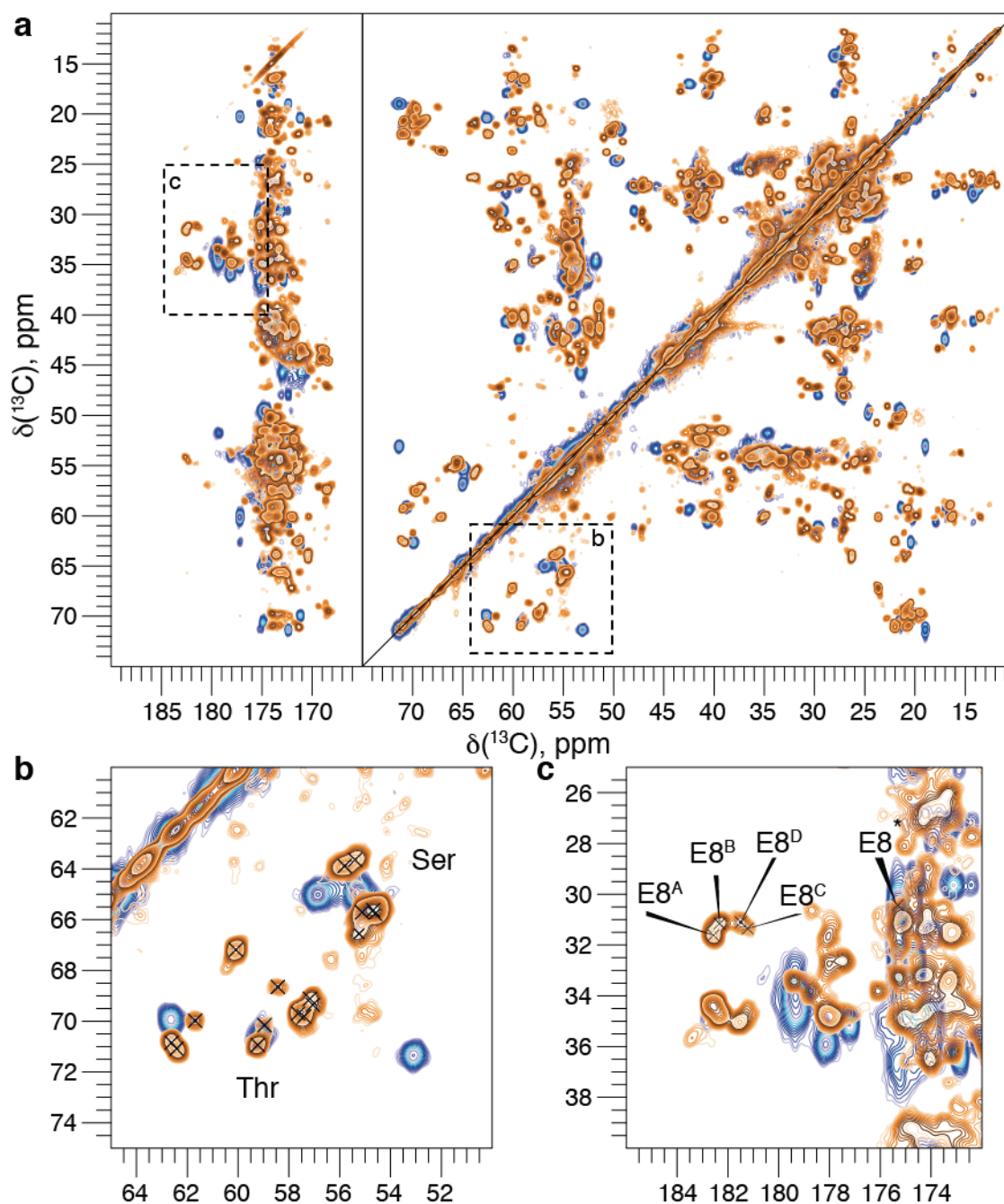
Figure 7.5. 20 ms DARR spectra of amyloid fibrils formed by ^{13}C, ^{15}N-labeled WT β-endorphin in ammonium acetate buffer at pH 5.5 with 200 mM NaCl and 2 mg/ml of heparin (blue) and in CP buffer at pH 6.0 (orange). (**a**) Combination of the aliphatic and carbonyl regions of the DARR spectra. Dashed boxes indicate areas zoomed in in **b** and **c**. (**b**) Selected region of the DARR spectra shows two peaks corresponding to CαCβ of Ser and three – to CαCβ of Thr in the sample of heparin-promoted fibrils (blue), while a great number of peaks appears in the spectrum of salt-induced fibrils. Crosses indicate peaks in the spectrum of salt-promoted fibrils. (**c**) Selected region of the DARR spectra shows CδCβ peaks of Glu8. E8[A], E8[B], E8[C], E8[D] correspond to four polymorphic forms of Glu8 in the salt-induced fibrils. E8* indicates the CδCβ peak of Glu8 observed in the spectra of β-endorphin fibrils aggregated with heparin.

Several polymorphs were clearly demonstrated by the 20 ms DARR spectrum of β-endorphin fibrils prepared in CP buffer. Because of the presence of the structural polymorphism the sequential assignment of ssNMR spectra – an essential step in

determining the high-resolution 3D structure – was difficult. It was speculated whether the polymorphism was due to a possible variation of the fibril structure induced by different anions present in CP buffer. An attempt was made to isolate these polymorphs by utilizing citrate and phosphate salts separately or slightly varying the fibrillization conditions. Three more ^{13}C, ^{15}N-labeled β-endorphin samples were prepared for ssNMR measurements: (*1*) fibrils prepared in 14 mM sodium citrate buffer at pH 6.0, (*2*) fibrils formed in 55 mM sodium phosphate buffer at pH 6.0, (*3*) fibrils obtained in 50 mM sodium phosphate with 2 mM sodium citrate at pH 5.5. Concentrations of individual components were adjusted in order to keep the ionic strength similar between the samples. In general, all three DARR spectra were highly similar to the spectrum of fibrils formed in CP buffer at pH 6.0 (**Supplementary Figures S11-S13**) suggesting a general ability of multivalent ions to promote the structural polymorphism of β-endorphin amyloid fibrils. Several peaks were absent in the spectra of samples prepared in individual salts. Interestingly, these absent peaks could not be attributed to the effect of a particular salt, because they disappeared simultaneously from the spectrum of sample *1* and *2*. Some of them were absent in the spectrum of sample *3*, too. Thus, the attempt to enrich a certain β-endorphin amyloid polymorph by varying the composition of fibrillization buffer or its pH was not successful. It was therefore impossible to determine the high-resolution 3D structure of the salt-promoted β-endorphin amyloid fibrils and compare it to that of heparin-induced fibrils at the atomic level of detail.

The ssNMR spectroscopy data measured can nevertheless be used to obtain some information about the structure of the salt-promoted β-endorphin amyloid fibrils in order to reveal the structural basis of the differences in behavior of the salt-promoted and heparin-induced fibrils. For instance, secondary structure prediction can be done by comparing the measured chemical shifts of backbone carbon atoms to the well-know values of random-coil conformation [254, 257]. If the difference, which is often referred to as the secondary chemical shift, is positive for at least four residues or negative for at least three residues in a row, this is interpreted as an α-helix or a β-strand, respectively. Secondary chemical shifts of Cβ and Cα atoms are considered to be a more reliable criteria for prediction of β-strand structure than that of C'. It is highly recommended to take into account the standard deviations of chemical-shift distribution, because it plays an important role in the evaluation of the structure identification reliability [257].

^{13}C-^{13}C DARR spectrum of ^{13}C, ^{15}N-labeled β-endorphin fibrils obtained in CP buffer at pH 6.0 was assigned utilizing conventional strategy [256]. The assignment

resulted in the identification of three major polymorphs, namely chain A, B, and C. The most complete assignment was obtained for the chain B spanning from Tyr1 to Tyr27. Chain C instead represented a combination of polypeptide stretches, which could not be sequentially connected either to chain A or to B. Moreover, some residues, such as Thr6, Ser7, Glu8, Thr12, Pro13, Ala21, Ile22, appeared in the spectra at least four times and formed stretches, which also could not be associated with major polymorphs.

All backbone resonances of chains A, B, and C were taken for secondary chemical shift calculations in order to characterize the secondary structure of β-endorphin fibrils formed in CP buffer and compare it to the proposed structure of heparin-induced fibrils. The difference of secondary chemical shifts of Cα and Cβ atoms was used instead of separated values, because it allowed to eliminate possible referencing offsets [276]. Calculated differences were plotted against the amino acid sequence of β-endorphin and compared with tabulated standard deviations [257]. The prediction was considered reliable, if the difference between the experimentally measured chemical shift and the chemical shift reported for a random coil exceeded the standard deviation. Only reliable deviations from random coil were taken for structure predictions. Analysis of secondary chemical shifts revealed that salt-promoted β-endorphin fibrils differed in structural organization form the heparin-induced fibrils (**Figure 7.6**). Surprisingly, all three chains of salt-promoted fibrils demonstrated different distribution of secondary structure elements. Chain A was characterized by two β-strands: a long stretch Gly3-Ser10 and a short one Ala21-Ile23. Chain B had three fragments reliably predicted as β-strands: Thr6-Thr12, Leu17-Ala21, and Ans25-Tyr27. Chain C combined from different stretches also demonstrated two fragments forming β-strands: Gly3-Met5 and Ser10-Pro13. None of the peptide fragments was identified in all three polymorphs as a β-strand, although some amino acid residues were involved in β-strands in several, if not all, cases. I.e., only partial overlap of β-strands between chains A, B, and C on the one hand, and the heparin-induced fibrils on the other was found. Overall, the prediction of secondary structure by the analysis of secondary chemical shifts suggests structural difference between the salt-promoted and heparin-induced β-endorphin amyloid fibrils.
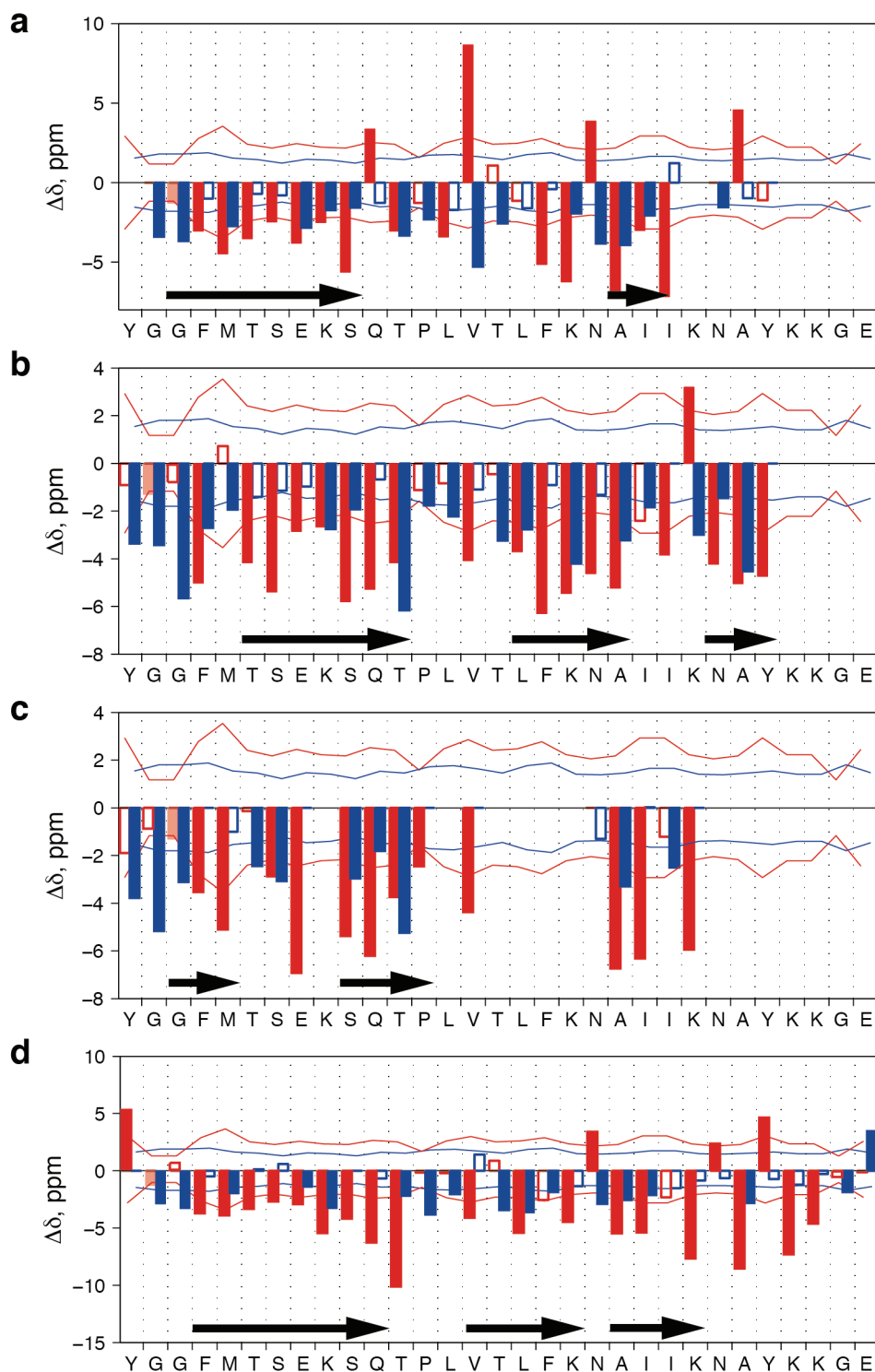
Figure 7.6. Analysis of secondary chemical shifts of β-endorphin fibrils. (**a**), (**b**), (**c**) Secondary chemical shifts plotted for chains A, B, and C, respectively, of β-endorphin fibrils obtained in CP buffer at pH 6.0. Note that the sequential assignment is tentative. (**d**) Secondary chemical shifts plotted for β-endorphin fibrils formed in ammonium acetate buffer at pH 5.5 in the presence of heparin. The position of β-strands is adapted from [276, 277]. Blue bars represent secondary chemical shifts of C′ atoms; red bars represent the difference in secondary chemical shifts of Cα and Cβ atoms. Only secondary chemical shifts of Cα atoms are shown for Gly residues. The bars showing secondary chemical shifts exceeding the confidence interval are filled by the respective color. Red and blue lines are the confidence interval boundaries of CαCβ and C′, respectively [257]. Arrows indicate the predicted β-strands.

Similar to the case of SS14, the computational analysis of β-endorphin amino acid sequence with TANGO [187] and Waltz [188] algorithms was not inline with the ssNMR data. The TANGO algorithm failed to recognize amyloidogenic properties of β-endorphin. The maximum scoring corresponding to the Val15-Leu17 stretch did not exceed 10 % (**Figure 7.7a**). Waltz, predicted the ability of β-endorphin to undergo the amyloid aggregation with much higher score, approximately 80 %, for residues 14-31 at acidic and neutral pH (**Figure 7.7b**). However, both predictions were not in line with the determined structure of heparin-induced β-endorphin amyloid [276, 277], neither were they in line with the assignment of secondary structure in the salt-promoted fibrils performed here based on the analysis of secondary chemical shifts.

Figure 7.7. Computational prediction of amyloidogenic properties of β-endorphin. (**a**) The propensity of monomeric β-endorphin to adopt β-strand conformation at +37 ℃, pH 5.5, and the ionic strength corresponding to 150 mM NaCl predicted by the TANGO algorithm [187]. (**b**) The propensity of β-endorphin to form amyloid aggregates predicted by Waltz [188].

Despite no high-resolution 3D structure of salt-promoted fibrils could be determined at this stage, the significant spectral difference found by comparing ssNMR spectra of the salt-promoted and heparin-induced fibrils suggested remarkable difference in the atomic structure of fibrils obtained under different conditions. Even at this coarse level, we could hypothesize that the position of β-strands, the orientation of side chains, intra- and intermolecular contacts in salt-promoted fibrils were dramatically different from those found in the heparin-induced amyloid [276, 277]. For instance, Glu8 residue appeared to be no longer protonated and, perhaps, exposed to a solvent. If so, Glu8 can no longer play a key role in triggering fibril assembly or dissociation, and no effect on the

dissociation kinetics shall be expected if point mutations introduced at this position. To test this hypothesis, we studied the fibrils formed by WT β-endorphin and E8Q and E8L variants in CP buffer at pH 5.5 in the dissociation assay (**Figure 7.8**). The observed ThT fluorescence decay by approximately two orders of magnitude did not show significant difference in dissociation rates between WT β-endorphin and E8Q and E8L mutants.
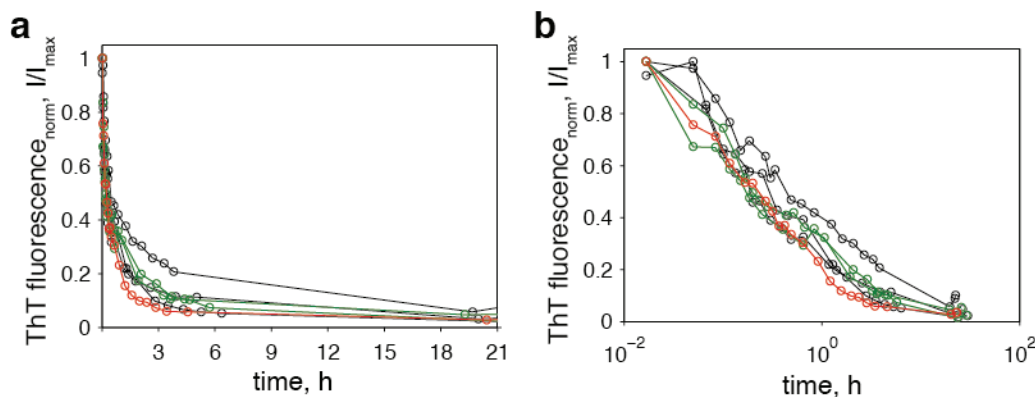
Figure 7.8. Dissociation of β-endorphin amyloid fibrils monitored by ThT fluorescence. (**a**) ThT fluorescence in the dissociation mixtures of WT (black), E8Q (green), and E8L (red) β-endorphin fibrils formed in CP buffer. (**b**) The same data as in **a** shown in a semi-logarithmic plot. Circles represent individual measurements at different time points. Lines connect individual data series measured independently. Plotted are fluorescence intensities measured at $\lambda^{em} = 482$ nm upon excitation at $\lambda_{max} = 440$ nm and normalized to the maximum value after baseline subtraction. Lines are given to guide the eye.

The modification of β-endorphin fibrillization protocol (implementation of multivalent anions instead of heparin as aggregation promoter) yielded dynamic amyloid fibrils capable of assembly and disassembly on a relatively short time scale, in contrast to very stable heparin-induced fibrils. It was however unclear what exactly was responsible for the difference in fibril structure and behavior. On the one hand, two alternative amyloid folds could exist for β-endorphin: one functional and another one resistant to dissociation. Heparin or salt ions could select for alternative peptide conformation and favor the formation of the respective type of amyloid. Alternatively, the incorporation of salt anions into fibril could force less densely packed amyloid structure that could readily dissociate upon the change of conditions. In the latter case, the presence of salt anions and heparin in the aggregation solution could potentially yield β-endorphin amyloid featuring the structure of "heparin-type" fibrils as well as the dynamic nature of the "salt-type" fibrils.

We prepared a sample of ^{13}C, ^{15}N-labeled β-endorphin fibrils in CP buffer at pH 6.0 containing 2 mg/ml heparin and examined it by ssNMR. Remarkably, ^{13}C-^{13}C DARR spectrum of these fibrils was very similar to the one of the canonical heparin-

induced β-endorphin fibrils (**Figure 7.9**). In particular, the characteristic chemical shift of Cδ indicated the protonation of Glu8 γ-carboxylic group. The fact, that the DARR spectra of β-endorphin fibrils, which were formed in the presence of heparin but in different buffers resemble each other, suggested the dominating role of heparin in the promotion of β-endorphin aggregation to a non-functional, stable amyloid.
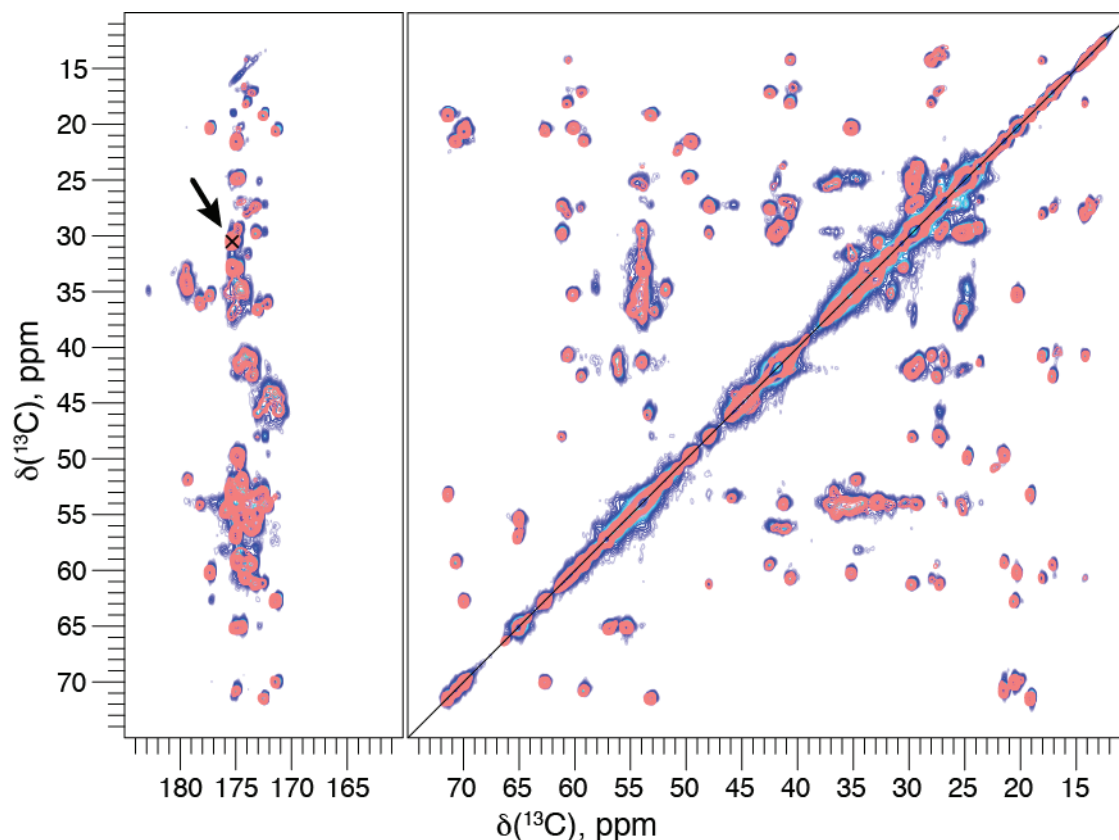
Figure 7.9. 20 ms DARR spectra of amyloid fibrils formed by ^{13}C, ^{15}N-labeled WT β-endorphin in 10 mM ammonium acetate buffer at pH 5.5 containing 200 mM NaCl and 2 mg/ml heparin (blue) and in CP buffer at pH 6.0 containing 2 mg/ml heparin (pink).

In summary, the results obtained here strongly suggest the pronounced stabilization effect of heparin on β-endorphin amyloid fibrils, which is attributed to the ability of heparin to induce a specific structure in the peptide. This effect outcompetes the other factors such as the solution pH and the buffer composition, the fibril length or the dilution factor (see **Chapter 6** for details). The mechanism of this effect is unclear. Our findings question the applicability of heparin as a model GAG for hormone aggregation studies and challenge the biological relevance of heparin-induced amyloids. On the other hand, various carbohydrates are abundant in the cellular compartments where functional hormone aggregation takes place, and their potential influence on this process cannot be overlooked.

The salt-promoted aggregation of β-endorphin yielded truly dynamic amyloids capable of dissociation on a relatively short time scale. Further investigations are needed to elucidate the molecular mechanisms that allow for reversible aggregation. The fact that various salts of polyprotic acids promoted the formation of β-endorphin aggregates behaving almost identically in the dissociation assay suggests that the effect of salt was rather non-specific. Most likely, the presence of salts resulted in neutralization of the peptide ionic groups by counter-ions and suppressed the electrostatic repulsion between the monomers allowing them to aggregate. Hence, the rate of β-endorphin aggregation shall depend on the ionic strength of solution and on the peptide ionic state. We focused our further efforts on exploring the two aspects discussed above.

pH dependence of β-endorphin aggregation

To further explore the mechanism of β-endorphin aggregation, the influence of pH on β-endorphin aggregation was studied. CP buffer was used for fibrillization as a system, which allows for working in the wide range of pH (2.6-7.6) [299] conveniently covering the normal biological pH values, such as pH 5.5 in secretory granules [55], 7.4 in the blood [282], as well as the intermediate values along the secretory pathway [55]. Salts composing this buffer are present in every cell, they are not artificial for a biological system [36]. Moreover, inorganic phosphate has been identified among other low-molecular weight constituents of secretory granules [41]. In our experiments, the aggregation buffer consisted of 50 mM sodium phosphate and 2 mM sodium citrate salts. Peptide aggregation was monitored in parallel by two complementary methods: ThT fluorescence and light absorption at 600 nm, which was used as a measure of turbidity [140]. The experiment was performed in the 96-well plate format, which allowed for simultaneous test of several experimental conditions in the same plate. Tested pH values were varied from 5.0 to 8.0 by 0.5 pH unit steps (**Figure 7.10**, **Supplementary Figures S14-S15**).
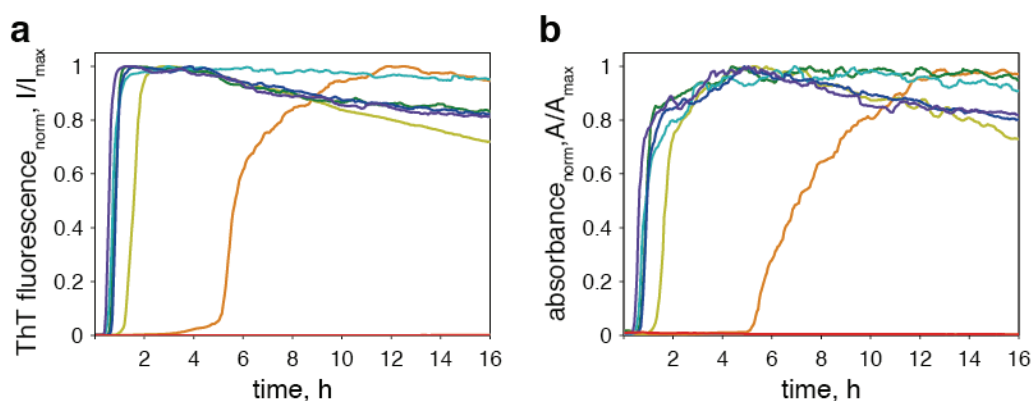
Figure 7.10. Aggregation of β-endorphin in 50 mM sodium phosphate, 2 mM sodium citrate buffer at different pH. (**a**) Aggregation of β-endorphin tracked by ThT fluorescence. The fluorescence intensity plotted is baseline-subtracted and normalized to the maximum value in the series. (**b**) Aggregation of β-endorphin tracked by absorbance measurements at 600 nm. The absorbance plotted is baseline-subtracted and normalized to the maximum value in the series. pH 5.5 – orange, 6.0 – yellow, 6.5 – green, 7.0 – cyan, 7.5 – blue, 8.0 – purple.

β-endorphin aggregated into fibrillar structures binding the ThT dye in the wide pH range (**Figure 7.10a**). β-endorphin aggregation was reproducibly detected starting from pH 5.5 and above. The lag-phase of the aggregation curve became shorter as the solution pH approached the value of β-endorphin pI = 9.6. Notably, the rate of aggregation in the exponential phase of fibril growth did not vary significantly with pH. The dramatic increase in the steepness of the exponential phase appeared between pH 5.5 and 6.0 and remained the same above pH 6.0. Curves representing the turbidity of aggregation mixtures followed the same trend as ThT fluorescence curves (**Figure 7.10b**). The apparent similarity of aggregation curves measured at pH 6.0-8.0 and their difference with those measured at pH 5.5 could be explained by the charge state of β-endorphin. According to theoretical calculations, the titration curve of β-endorphin is rather flat in the pH interval between 6.0 and 8.0, predicting the peptide charge of approximately +3. At pH 5.5, it has an inflection point where the charge increases steeply from +3 to higher values. Therefore, the peptide charge at pH 5.5 can be characterized as a metastable state, which can be highly sensitive to different factors (temperature, peptide concentration, etc.). The increasing probability of having the peptide charge above +3 below pH 6.0 decreased the fibril assembly rate at pH 5.5. Moreover, the distinct step in front of the exponential phase suggested the necessity to accumulate a certain amount of early-state aggregates in order to prompt the exponential growth of fibrils. The aggregation was not observed at pH 5.0 during the same 16-hour interval: the ThT fluorescence intensity remained at the same low level as the background signal. Apparently, the peptide charge at pH 5.0 was high enough to completely prevent the

association of peptide molecules due to electrostatic repulsion. Hypothetically, the presence of higher salt concentrations could neutralize peptide charges and allow aggregation even at lower pH.

Investigation of β-endorphin aggregation dependence on the phosphate concentration revealed that 1 mM concentration of sodium phosphate added to 10 mM Tris-HCl buffer at pH 7.4 was already sufficient to promote amyloid formation, while no fibrils were found within 24 h when phosphate was substituted with 150 mM NaCl (**Supplementary Table S3**). This difference cannot be simply attributed to the difference of solution ionic strength, which was actually greater in the latter case. The salts of multiprotic acids exhibit a greater impact on β-endorphin aggregation compared to those of monoprotic acids. The fibrils obtained in 10 mM Tris-HCl buffer at pH 7.4 containing 10 mM sodium phosphate were tested in the fibril dissociation assay by transferring them into 10 mM Tris-HCl buffer at pH 7.4 either directly, so that a final phosphate concentration was equal to 0.5 mM, or after complete removal of phosphate by ultracentrifugation. The buffer compositions in this experiment were chosen to isolate phosphate-specific effects. Phosphate at 0.5 mM concentration notably slowed down the disassembly process – almost by a factor of 20 (**Figure 7.11**).
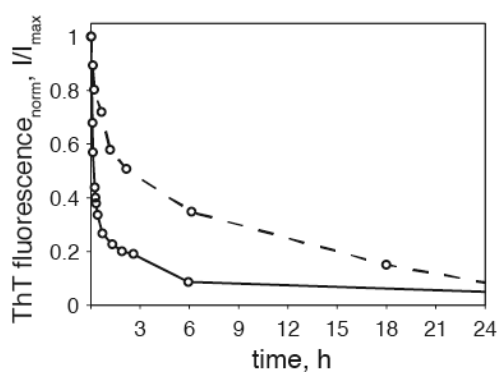
Figure 7.11. Monitoring of β-endorphin fibril dissociation by ThT fluorescence. The fibrils were prepared in 10 mM Tris-HCl buffer at pH 7.4 containing 10 mM sodium phosphate. The dissociation was performed in 10 mM Tris-HCl buffer at pH 7.4 (solid line) or in the same buffer containing additionally 0.5 mM sodium phosphate (dashed line). Circles represent individual measurements at different time points. Plotted are fluorescence intensities measured at $\lambda^{em} = 482$ nm upon excitation at $\lambda_{max} = 440$ nm and normalized to the maximum value after baseline subtraction. Lines are given to guide the eye.

Amyloid fibrils obtained at different pH shared very similar morphology visualized by EM (**Figure 7.12**). Several-micrometer-long fibrils appeared as flat ribbons composed of many (from 5 to 10 and more) thin filaments 5-7 nm in diameter. These ribbons had a tendency to cluster together forming large bundles of fibrils. Narrow twisted fibrils, which were characteristic for heparin-induced β-endorphin amyloids (see **Figure 6.6**), were found rarely in these cases.
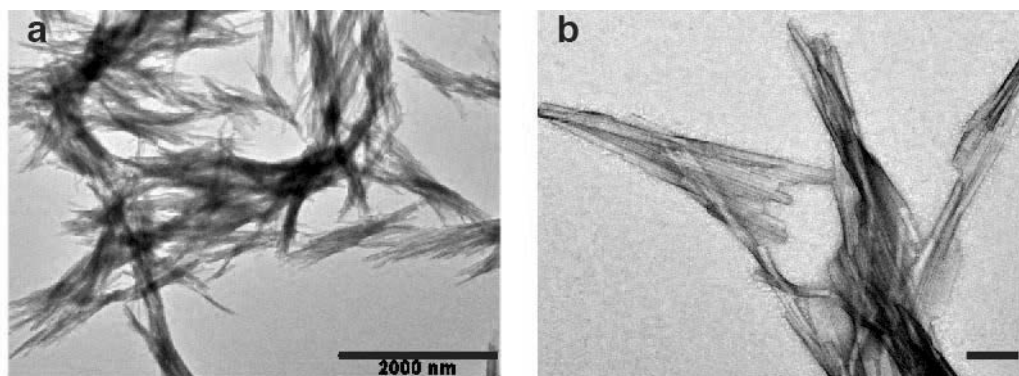
Figure 7.12. Electron micrographs of typical β-endorphin fibrils formed in 50 mM sodium phosphate, 2 mM sodium citrate buffer at different magnification. Scale bar – 2 μm in **a,** 200 nm in **b.**

We measured the aggregation kinetics of β-endorphin in CP buffer containing 2 mg/ml heparin at different pH and compared it to the results obtained for heparin-free samples and found them to be strikingly different. The trend of ThT fluorescence intensity over time indicated the absence of lag-phase at the beginning of β-endorphin aggregation in the presence of heparin (**Figure 7.13**, **Supplementary Figures S16-S17**). All aggregation curves started already at a high level of fluorescence intensity and grew further approximately by a factor of two in quite a short time in all tested cases (pH 5.0-8.0). Then ThT signal followed a different route in each case: it dropped back to the initial values within 2 and 4 h at pH 5.0 and 5.5, respectively, slowly increased at pH 6.0, or doubled at pH 6.5-8.0 within 4 h (**Figure 7.13a**). On top of that, the absorbance measurements showed unexpected results. Independently of the buffer at pH, absorbance at 600 nm increased very fast in the first 10-20 minutes and went back to the background level 2 to 16 h later depending on the solution pH. Interestingly, time required for reaching the noise level of absorbance agreed with time needed for ThT fluorescence change from initial jump to the final plateau (**Figure 7.13b**).
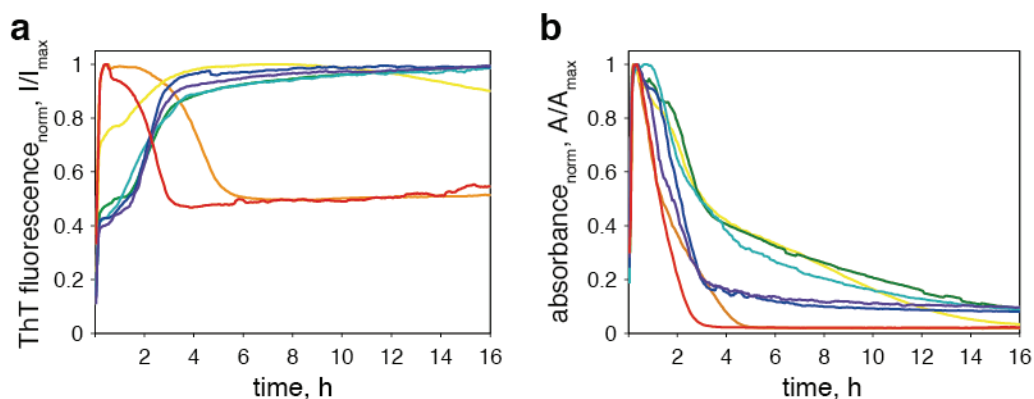
Figure 7.13. Aggregation of β-endorphin in 50 mM sodium phosphate, 2 mM sodium citrate at different pH in the presence of heparin. (**a**) Aggregation of β-endorphin monitored by ThT fluorescence. The fluorescence intensity plotted is baseline-subtracted and normalized to the maximum value in the series. (**b**) Aggregation of β-endorphin tracked by absorbance measurements at 600 nm. The absorbance plotted is baseline-subtracted and normalized to the maximum value in the series. pH 5.0 – red, 5.5 – orange, 6.0 – yellow, 6.5 – green, 7.0 – light blue, 7.5 – dark blue, 8.0 – purple.

The observed biphasic character of β-endorphin aggregation in the presence of heparin represented an interesting phenomenon. Notably, heparin by itself did not increase ThT fluorescence, which was confirmed in a blank experiment (buffer with added heparin and ThT; data not shown). However, its presence in peptide-containing samples promoted immediate increase of fluorescence. This property of heparin to increase ThT fluorescence at the moment of addition to peptide solutions, was described previously in the aggregation studies of kisspeptin 10, a neurohormone that regulates reproductive behavior and gonadotropin secretion [82]. Nielsen et al. suggested that primary associates of kisspeptin 10 and heparin molecules could serve as seeds for secondary nucleation of aggregation [82]. However, these associates did not transform into mature fibrils by themselves. In the case of β-endorphin, a similar phenomenon could explain the apparent lag-phase between the initial burst and the subsequent increase or decrease in ThT fluorescence intensity before reaching the plateau. Conversely to kisspeptin 10, such amorphous seeds of β-endorphin seem to be capable of transforming into mature fibrils at later stages of the aggregation process. Whether the ThT fluorescence intensity increased or decreased upon conversion of seeds into fibrils can be simply explained by the fact that ThT binds to the amyloid structure weaker at acidic pH [133]. The results of tracking the course of β-endorphin aggregation in CP buffer containing heparin by absorbance measurements indirectly support our speculations. The initial burst of absorbance can be attributed to the accumulation of the hypothetical amorphous seeds that efficiently scattered light. The long mature heparin-induced β-endorphin fibrils in turn could form a gel that was transparent to light with the

wavelength $\lambda = 600$ nm, which has been observed for some other amyloidogenic peptides and proteins [32, 300]. Investigation of the samples at final stages of aggregation by EM demonstrated the presence of thin regular wire-like fibrils (data not shown). Visual examination of the samples revealed the presence of transparent jelly-like substance.

In summary, a clear dependence of β-endorphin salt-promoted aggregation on the solution pH supports the proposed hypothesis of peptide charge neutralization by counter-anions as the driving force of aggregation. Conversely, the absence of β-endorphin aggregation dependence on the solution pH in the presence of heparin supports our hypothesis of the determinant role of heparin in promoting the hormone aggregation to a stable distinct amyloid type.

Impact of carbohydrates on β-endorphin aggregation

In the present work, a number of sugars were tested in order to determine their ability to promote β-endorphin aggregation and stabilize its fibrils in the dissociation assay. Analyzed compounds were represented by neutral linear mannitol[1] and cyclic d-glucose, negatively charged glucuronic acid and positively charged glucosamine, amphiphilic glucosamine-6-sulfate, and complex heparin disaccharide I-S bearing three sulfate groups (**Scheme 7.1**).
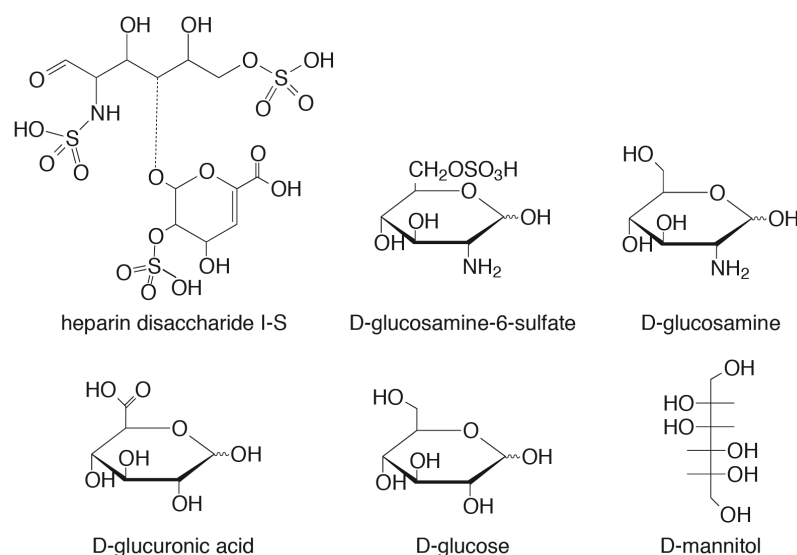
Scheme 7.1. Structures of low-molecular-weight carbohydrates used to promote aggregation of β-endorphin.

---

[1] Although mannitol is not a carbohydrate but polyol it was nevertheless considered here in the same context.

All tested carbohydrates were able to promote β-endorphin fibril assembly in 10 mM ammonium acetate, 200 mM NaCl buffer at pH 5.5, which does not induce β-endorphin aggregation by itself (**Supplementary Table S3**). Similar to salt-induced fibrils, morphology of aggregates formed in the presence of low-molecular-weight (LMW) carbohydrates was characterized by flat ribbons clustering together. Individual filaments forming these ribbons were 5-7 nm in diameter. The bundles composed of multiple fibrils were several micrometers in length (**Figure 7.14**).
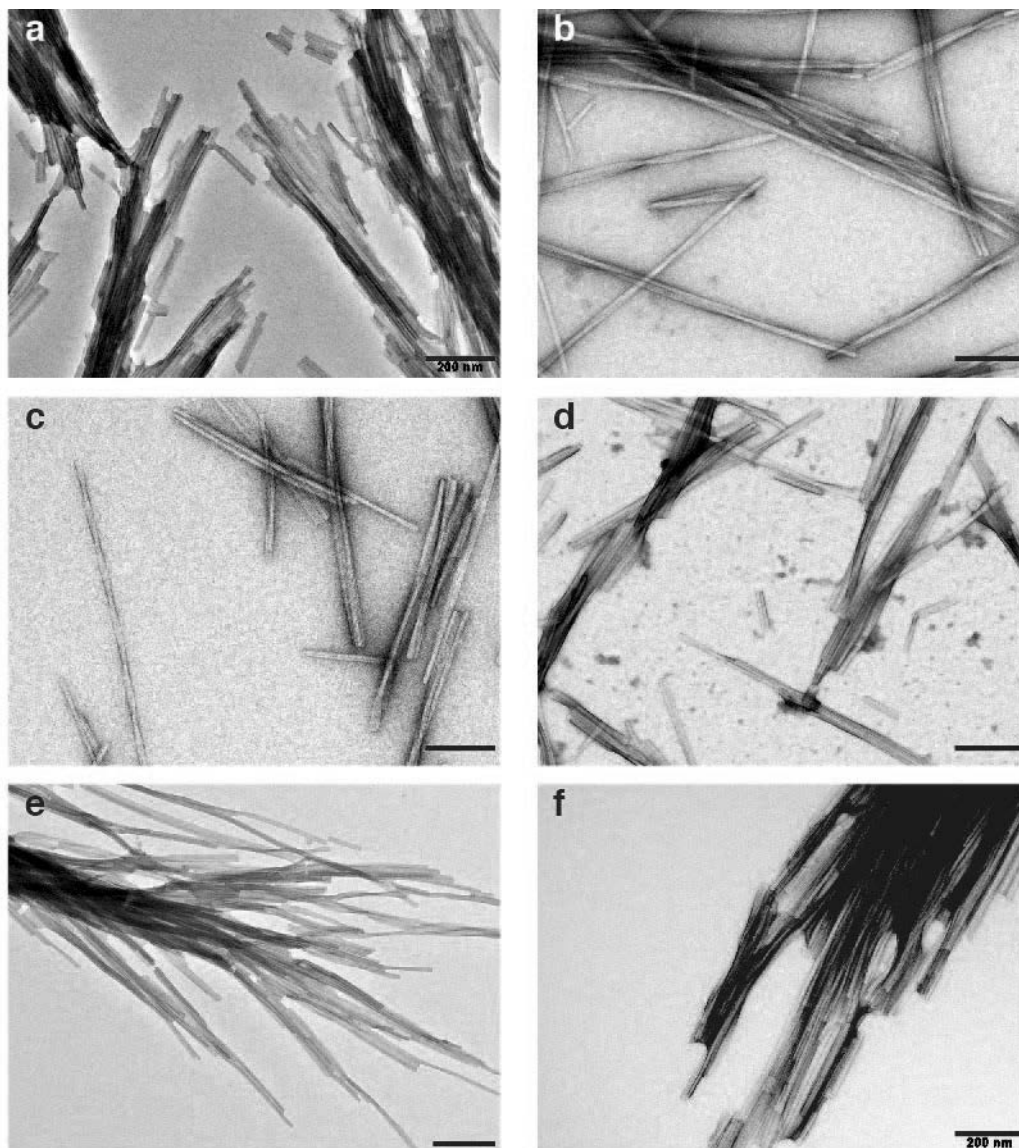
Figure 7.14. Electron micrographs of β-endorphin amyloid fibrils obtained in the presence of various LMW carbohydrates. Fibrils were formed in CP buffer at pH 6.0 alone (**a**) or in the presence of low-molecular-weight carbohydrates: mannitol (**b**), glucose (**c**), glucosamine (**d**), glucosamine-6-sulfate (**e**), heparin disaccharide I-S (**f**). Scale bars – 200 nm.

Aggregation kinetics of β-endorphin tracked by ThT fluorescence and absorbance measurements in the presence of different carbohydrates did not deviate from that

observed for fibrillization in CP buffer alone (**Figure 7.15**). The lag-phase, exponential growth, and plateau were highly similar between samples in the presence and absence of added sugars.
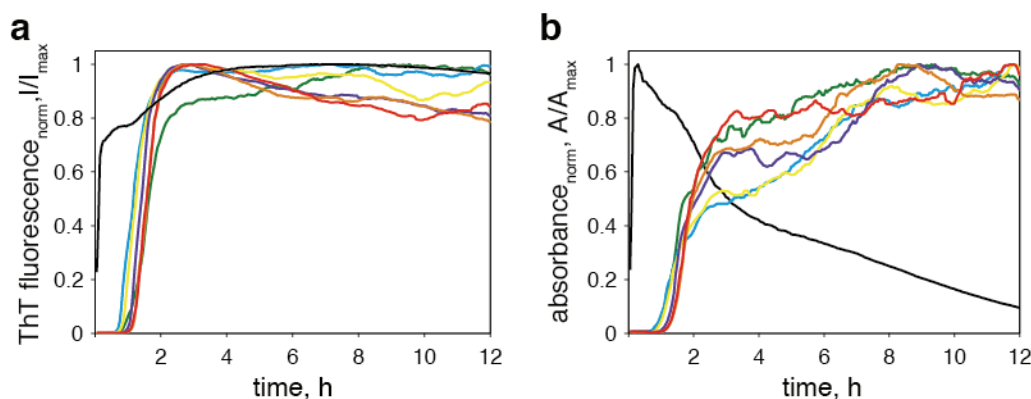
Figure 7.15. Aggregation kinetics of β-endorphin in CP buffer at pH 6.0 (red) alone or in the presence of different carbohydrates: heparin disaccharide I-S (green), glucosamine-6-sulfate (blue), glucosamine (yellow), glucose (purple), mannitol (orange), heparin (black). (**a**) Aggregation of β-endorphin tracked by ThT fluorescence. (**b**) Aggregation of β-endorphin tracked by absorbance measurements at $\lambda = 600$ nm. Plotted are values that were baseline-subtracted and normalized to the maximum value in the series.

Interestingly, all tested sugars were capable of inducing β-endorphin aggregation *in vitro* in 10 mM ammonium acetate buffer at pH 5.5 containing 200 mM NaCl, while the incubation of peptide in the buffer alone did not promote amyloid formation. (**Supplementary Table S3**). At the same time, none of the sugars affected the aggregation kinetics in CP buffer at pH 6.0 (**Figure 7.15**). Similar observations were reported for the aggregation of glucagon, a peptide hormone rising blood glucose level, which aggregated *in vitro* at both extremely acidic and alkaline conditions [301]. Addition of polyols (mannitol, glucose, sucrose, etc.) did not affect significantly the duration of lag-phase, neither did it affect the rate of glucagon aggregation at pH 2.5 [295]. However, it is not known whether low-molecular-weight carbohydrates could promote glucagon aggregation at neutral pH.

Comparison of ^{13}C-^{13}C 20 ms DARR spectra of the β-endorphin fibrils formed in the presence of heparin disaccharide I-S and glucosamine-6-sulfate revealed high similarity with the spectrum obtained for the fibrils obtained in CP buffer alone (**Supplementary Figures S18**-**S19**). Moreover, the fingerprint DARR spectra of the ^{13}C, ^{15}N-labeled β-endorphin amyloid fibrils formed in the presence of heparin disaccharide I-S in ammonium acetate and CP buffers significantly overlapped (**Supplementary Figure S20**). Thus, the sulfated LMW carbohydrates did not have the

same impact on the structure of β-endorphin amyloid fibrils as heparin, even though they resembled the chemical structure of heparin to a certain degree.

We expected no stabilization of β-endorphin amyloid fibrils by the tested low-molecular-weigh sugars, because the structures of fibrils produced in CP buffer in the presence or absence of the sugars were very similar, if not equal. On the other hand, the structure of fibrils produced in the presence of the sugars was quite different from that of heparin-induced fibrils. To test this assumption, we assayed the dissociation kinetics exhibited by different types of fibrils. The off-line dissociation assay described earlier was modified in order to gain better time resolution and automate the measurement process. Aliquots of fibrillar material obtained after β-endorphin fibrillization in CP buffer alone and in the presence of either low-molecular-weight carbohydrates or heparin were centrifuged at 25×10^3 g. The pellets were resuspended at 100-fold dilution in a fluorescence cuvette filled with 10 mM Tris-HCl buffer at pH 7.4 containing 10 µM ThT dye. ThT fluorescence of constantly stirred sample was automatically recorded at 482 nm upon excitation at 440 nm every two minutes for three hours. All measured dissociation curves demonstrated similar decay, while heparin-induced fibrils exhibited high stability (**Figure 7.16**).
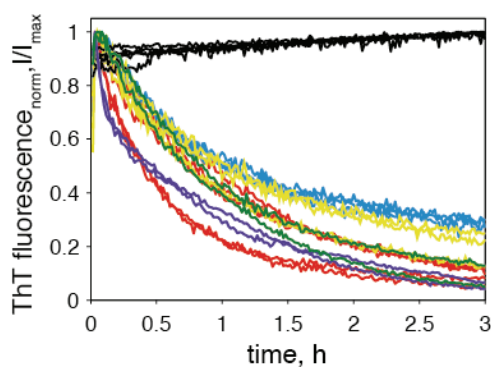
Figure 7.16. Dissociation of β-endorphin amyloid fibrils formed in CP buffer at pH 6.0 (red) and in the presence of different carbohydrates: heparin disaccharide I-S (green), glucosamine-6-sulfate (blue), glucosamine (yellow), mannitol (purple), or heparin (black). Every curve represents a single experiment. The ThT fluorescence intensity values are baseline-subtracted and normalized to the maximum value in the series.

Detection of β-endorphin monomers appearance by Tyr fluorescence, which was previously used in the off-line dissociation assay, was obscured in this case due to the presence of ThT in the sample. Therefore, after the dissociation experiment had been finished the analyzed sample was centrifuged at 10^5 g, the supernatant was subsequently filtered through a 0.2-µm syringe filter, and the obtained filtrate was analyzed by RP-HPLC. Notably, the supernatants obtained after centrifugation of heparin-containing samples could not pass the filter, i.e. the filters were completely blocked. This indicated the presence of large heparin-peptide aggregates, which did not pellet down during the

ultracentrifugation and subsequently clogged the 0.2-µm filters. In all other cases, the supernatants obtained after dissociation of β-endorphin fibrils were filtered and monomer was successfully detected by RP-HPLC (data not shown). Additionally, dissociation mixtures were examined by EM. Aliquots were taken at the beginning and at the end of the dissociation experiments. As demonstrated in **Figure 7.17** and **Figure 7.18,** fibrillar structures and their bundles were seen in the samples obtained at the starting point, whereas amorphous aggregates or isolated fibrils were rarely detected at the end of the dissociation assay, with the exception of heparin-induced fibrils (**Figure 7.17e-f**).
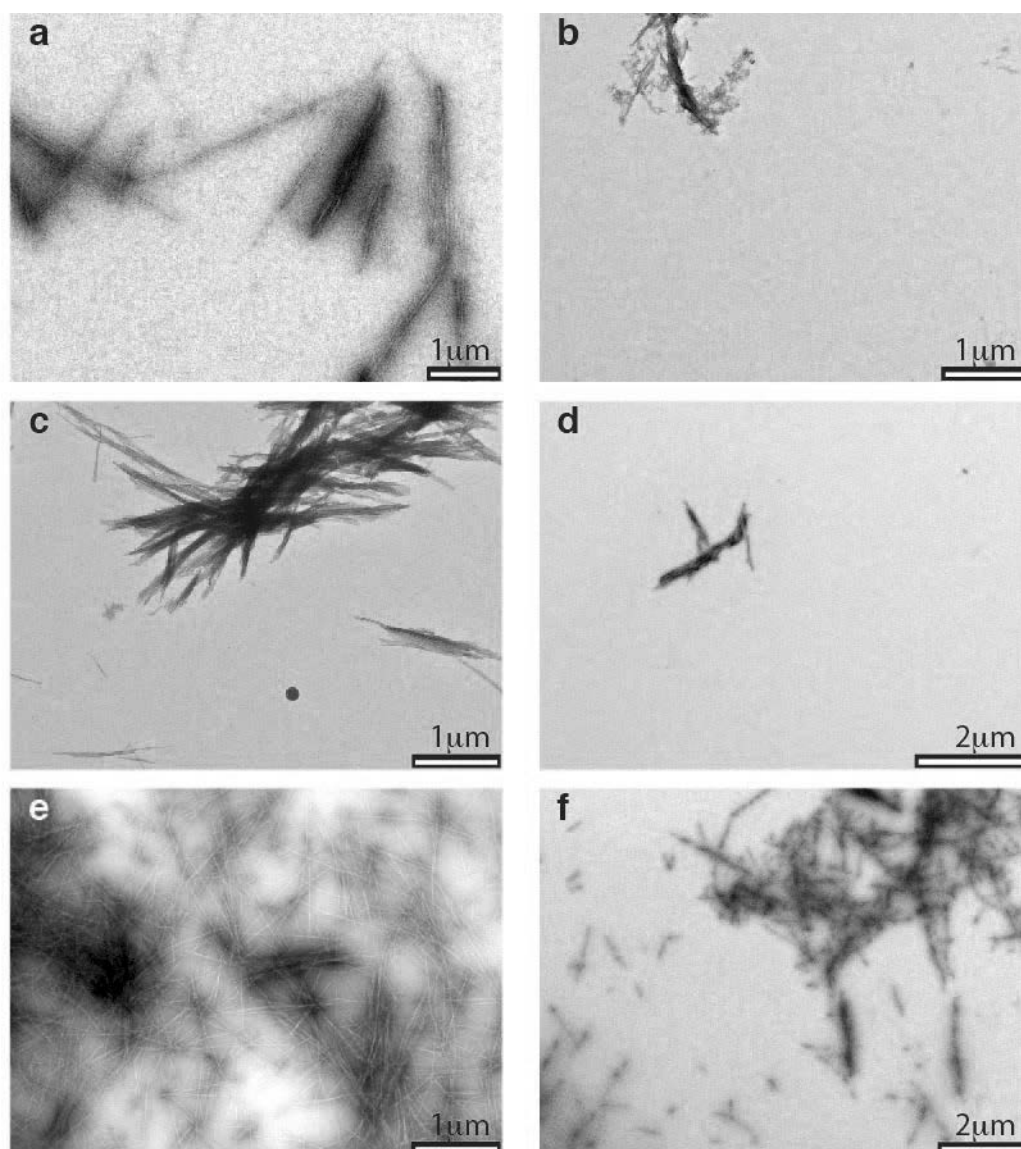
Figure 7.17. Electron micrographs of β-endorphin amyloid fibrils at the beginning (**a**), (**c**), (**e**) and after three hours of dissociation (**b**), (**d**), (**f**). Tested fibrils were formed in CP buffer at pH 6.0 in the presence of glucosamine-6-sulfate (**a**), (**b**), heparin disaccharide I-S (**c**), (**d**), and heparin (**e**), (**f**).
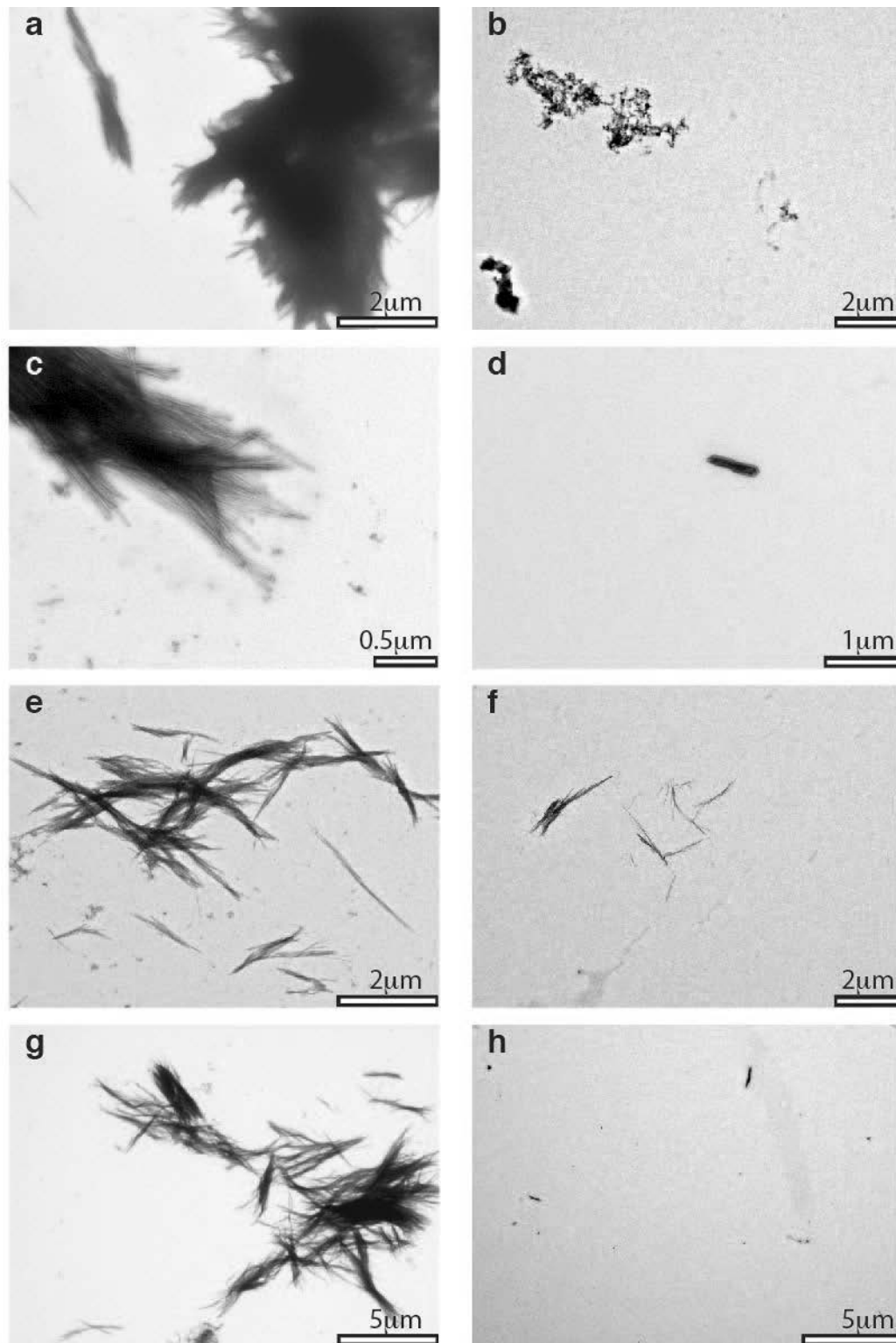
Figure 7.18. Electron micrographs of β-endorphin amyloid fibrils at the beginning (**a**), (**c**), (**e**), (**g**) and after three hours of dissociation (**b**), (**d**), (**f**), (**h**). Tested fibrils were formed in CP buffer at pH 6.0 alone (**a**), (**b**) and in the presence of mannitol (**c**), (**d**), glucose (**e**), (**f**), and glucosamine (**g**), (**h**).

All these data combined indicate the secondary role of sugars in β-endorphin aggregation. They could assist the aggregation under conditions, which normally did not promote aggregation (e.g., in 10 mM ammonium acetate pH 5.5 containing 200 mM

NaCl), but had no impact on the structure of fibrils, as revealed by ssNMR and EM data, neither did they have any influence on the aggregation and dissociation kinetics, as demonstrated by the respective assays.

Conclusions

Herein, we have investigated by a combination of ssNMR spectroscopy, EM, and kinetic assays the structure-activity relationships in several types of β-endorphin amyloid fibrils. The dynamic assembly and disassembly of a functional hormone amyloid has been unambiguously demonstrated experimentally for the first time. Several orthogonal methods have provided convergent evidences of β-endorphin functional aggregation and dissociation. The rates of aggregation and dissociation observed in this study were relatively high and in a reasonable agreement with the kinetics expected *in vivo*.

We have discovered that various factors including salts of polyprotic acids, neutral and ionic LMW carbohydrates, and heparin can promote β-endorphin aggregation. We suggest that neutralization of the peptide charges by counter-anions is responsible for spontaneous aggregation. The efficiency of electrostatic shielding by various anions is however unequal: the anions of polyprotic acids such as phosphate, sulfate, or citrate promoted β-endorphin aggregation already when present at low-millimolar concentrations, while the anions of monoprotic acids such as chloride or acetate were not efficient at physiological concentrations. LMW carbohydrates can assist the peptide aggregation, but do not have any significant impact on fibril structure, stability, and dynamics. In contrast, heparin exhibits a strikingly different effect on β-endorphin aggregation: it induces a stable, non-functional structure in the hormone amyloids and arrests the peptide in the amyloid state. Our findings question the applicability of heparin as a model GAG in hormone aggregation studies.

Further studies are necessary to reveal the exact molecular mechanism allowing β-endorphin to aggregate reversibly in the presence of salt. A high-resolution 3D structure of salt-promoted β-endorphin amyloid fibril can provide an insight into the molecular basis of dynamic triggering between the amyloid and soluble state under different conditions.

Methods

Preparation of fibrils for ssNMR measurements and dissociation assays

β-endorphin was dissolved in CP buffer at pH 6.0 prepared in accordance with **Table 7.1** (or another buffer listed in **Supplementary Table S3**) at 2 mg/ml concentration. Recombinant β-endorphin was produced as described in **Chapter 6**. In the studies of phosphate anions influence on the dissociation rate of β-endorphin fibrils, β-endorphin amyloids were formed in 10 mM Tris-HCl pH 7.4 in the presence of 10 mM sodium phosphate. Preparation of LMW carbohydrates and heparin stocks is described in "*Aggregation kinetics measured in 96-well plate format*" section below. The required carbohydrate was added to the peptide solution to provide 2 mg/ml final concentration. Afterwards, sodium azide (AppliChem, AXON LAB AG, Baden-Dättwil, Switzerland) was added up to 0.05 %. Sample tubes were sealed by PARAFILM® M (Sigma-Aldrich Chemie GmbH, Buchs, Switzerland) and placed for fibrillization. Aggregation was set up in low-retention 1.5 ml test tubes (Vaudaux-Eppendorf AG, Schönenbuch/Basel, Switzerland) in the EchoTherm RT11 rotating mixer (Torrey Pines Scientific, Inc., Carlsbad, USA) at a rotation speed of approximately 30 rpm inside an incubator at +37 ºC. Aliquots were taken out for analysis when necessary. For dissociation assays fibrils were taken after 3-5 days of incubation.

Transmission electron microscopy

5 μl samples of β-endorphin fibrils were deposited for 1 min on previously glow-discharged carbon-coated copper grid (Electron Microscopy Sciences, Hatfield, Pennsylvania). The grid was then blotted, washed twice in drops of double-distilled water and negatively stained for 15 s with filtered 2 % (w/v) uranyl acetate (Sigma-Aldrich Chemie GmbH, Buchs, Switzerland). Images were acquired with FEI Morgagni 268 electron microscope (FEI Company, Eindhoven, Netherlands) operated at 100 kV. Electron micrographs were recorded on a 1376 by 1032 pixel charge-coupled device camera (Veleta, Olympus soft imaging solutions GmbH, Münster, Germany).

Aggregation kinetics measured in 96-well plate

The ThT dye from Sigma (St. Louis, Missouri, USA) was dissolved in double-deionized water and filtered through a 0.2-μm Filtropur S filter (SARSTEDT AG & Co., Germany). Its concentration was determined by UV absorbance ($\varepsilon_{412nm} = 36000$ $M^{-1}cm^{-1}$). Stocks at 1.5 mM concentration were prepared and stored at -25 ºC until use. Stocks of

200 mM dibasic sodium phosphate and 200 mM monobasic sodium phosphate (Sigma-Aldrich Chemie GmbH, Buchs, Switzerland), 1 M citric acid (Merck KGaA, Darmstadt, Germany), 1 M sodium citrate tribasic (Sigma-Aldrich Chemie GmbH, Steinheim, Germany) were prepared fresh before each experimental series. Aliquots of monomeric β-endorphin were dissolved in CP buffer. The required pH of the buffer was achieved by preparation in accordance with empirically established recipe listed in **Table 7.1**.

Table 7.1

Preparation of 50 mM sodium phosphate, 2 mM sodium citrate buffer* at different pH

pH	200 mM Na_2HPO_4, ml	200 mM NaH_2PO_4, ml	1 M citric acid, µl	1 M sodium citrate, µl
5.0	0.4	4.6	40	-
5.5	0.4	4.6	25	15
6.0	0.615	4.385	5	35
6.5	1.4	3.6	-	40
7.0	3.05	1.95	-	40
7.5	4.1	0.9	-	40
8.0	4.735	0.265	-	40

* – obtained 5 ml of salt mixture was diluted up to 20 ml by double-deionized water.

Stocks of sugars were prepared by dissolution of a sugar in double-deionized water at 100 mg/ml concentration. The following carbohydrates were used in the present study: D-mannitol and D-(+)-glucosamine hydrochloride, ≥ 99 %, D-glucosamine 6-sulfate, ≥ 99 %, heparin disaccharide I-S sodium salt (Sigma-Aldrich Chemie GmbH, Buchs, Switzerland), D-glucuronic acid, 98 %, D(+)-glucose, ACS reagent, anhydrous (Acros Organics, Fisher Scientific AG, Wohlen, Switzerland). Heparin stock solution was prepared by dissolving 250 mg of heparin (heparin sodium salt, sc-203075, Santa Cruz Biotechnology, Inc., Heidelberg, Germany) in 2.5 ml of double-deionized water containing 0.05 % (w/v) sodium azide (AppliChem, AXON LAB AG, Baden-Dättwil, Switzerland). Stock solutions of carbohydrates were stored at +4 ºC.

Aggregation assay at different pH

Deionized water was distributed around the sample wells by 200 µl. 2 ml of CP buffer were mixed with 20 µl of 1.5 mM ThT stock and loaded by 180 µl in the non-binding, clear bottom, black 96-well plate (cat. no. 655906, from Greiner Bio-One, Stonehouse, UK). Two 2 mg peptide aliquots were dissolved in CP buffer. 10 µl of

1.5 mM ThT stock solution was added to every 1 ml of peptide solution, mixed and distributed in the 96-well plate by 180 µl. Heparin stock was added by 3.6 µl to 5 wells containing only the buffer, and subsequently, to 5 wells containing the peptide solution. Therefore, each condition was present on a plate in 5 replica. The measurement was repeated at least twice for each condition independently in two different plates. The 96-well plate was sealed by AMPLiseal™, Transparent Microplate Sealer (made in USA pn 676040 from Greiner Bio-One, Frickenhausen, Germany). Fluorescence measurements were performed with an Enspire 2300 Multilabel Plate Reader (PerkinElmer, Schwerzenbach, Switzerland). The temperature was set to +37 and +41 °C for the lower and upper heaters, respectively, to prevent condensation. The intensity of ThT emission at 485 nm was measured every 3 min in bottom excitation/emission mode at a fixed focal height of 3 mm. Excitation was at 450 nm, with 50 flashes. The absorbance at 600 nm was measured with 20 flashes. Fluorescence and absorbance signals were collected at 5 different spots on the XY-plane and averaged. One fluorescence measurement, one absorbance measurement and shaking for 55 s at 500 rpm in orbital mode after each measurement comprised one cycle. One cycle was repeated 480 times. 25 wells were measured in each experiment.

Aggregation assay at pH 6.0 with LMW carbohydrates

Experiments were performed similar to the described above, in the section "*Aggregation assay at different pH*". To dissolve β-endorphin aliquots, CP buffer was prepared at pH 6.0. For every LMW carbohydrate, experiment was repeated twice. In one plate, aggregation of β-endorphin in the presence of one carbohydrate was compared with aggregation in CP buffer alone.

Dissociation kinetics measured in the Fluoromax®-4 spectrofluorometer

30 µl of amyloid fibrils formed by β-endorphin in CP buffer at pH 6.0 alone or in the presence of D-mannitol, D-(+)-glucosamine hydrochloride, ≥ 99 %, heparin disaccharide I-S sodium salt, or heparin were centrifuged at 2.5×10^4 g and a temperature of +22 ºC for 15 min (Microcentrifuge 5417R, Vaudaux-Eppendorf AG, Schönenbuch/Basel, Switzerland). The pellet was resuspended in 30 µl of 10 mM Tris-HCl buffer at pH 7.4 and transferred to 2.95 ml Tris-HCl buffer (pH 7.4) premixed with 20 µl of 1.5 mM ThT stock solution in the fluorescent cuvette 111-QS (Hellma® Analytics, Hellma Schweiz AG, Zumikon, Switzerland) and closed with the cuvette lid. 180 point measurements of ThT fluorescence were recorded every 2 min on

FluoroMax®-4 spectrofluorometer controlled by FluorEssence™ software (Horiba Jobin Yvon GmbH, Munich, Germany). Excitation wavelength was 440 nm and the emission — 482 nm, slits were set for 3 nm. Dissociation mixture was under constant stirring at maximum rate provided by the FluoroMax®-4 instrument. The measurement cell was at +37 ℃ controlled by the temperature bath (Compatible control CC3, Huber, Faust, Schaffhausen, Switzerland). Between measurements, cuvette was extensively washed by deionized water and isopropanol. The cuvette was stored in 5 % (v/v) solution of deconex® 11 UNIVERSAL from Borer Lab (Dr. Grogg Chemie AG, Srettlen-Deisswil, Switzerland) at room temperature.

Analytical RP-HPLC

To analyze the release of β-endorphin monomer during the dissociation assay performed in the Fluoromax®-4, the following procedure was carried out. The dissociation mixture from the fluorescent cuvette was centrifuged for 30 min at 28 psi in the Airfuge® Air-Driven centrifuge (Beckman Coulter International S.A., Nyon, Switzerland). The supernatant was filtered through 0.2-μm syringe filters with PVDF membrane (cat. no. 6779-0402, Whatman, GE Healthcare Europe GmbH, Glattbrugg, Switzerland). Acetonitrile and TFA were added to 2.8 ml of the filtrate up to 5 and 0.25 % respectively. Qualitative analysis of the presence soluble β-endorphin was performed on a Discovery BIO Wide Pore C18 column (15 cm x 4.6 mm, 5 μm; Supelco, Bellefonte, Pennsylvania, USA). The elution was carried out using an acetonitrile gradient started at the 4th min of sample loading (12-45 % buffer B in 6 min, flow rate – 1 ml/min; buffer A - water with 0.1 % TFA, buffer B – acetonitrile with 0.1 % TFA). An Agilent 1200 HPLC system (Agilent Technologies (Schweiz) AG, Basel, Switzerland) equipped with an external manual injector, an automatic fraction collector, and a diode-array detector was used. The elution profile was monitored by UV absorption at 220 and 280 nm. The peak corresponding to β-endorphin was eluted at 11.4 min. The identity of β-endorphin was confirmed by ESI-MS (Q-TOF Ultima API, Micromass, Manchester, UK).

Dissociation kinetics measured in the "off-line" regime

200 μl of amyloid fibrils formed by β-endorphin (WT, E8Q, E8L variants) in 10 mM ammonium acetate pH 5.5 containing 200 mM NaCl and 2 mg/ml heparin were centrifuged for 30 min at 28 psi in the Airfuge® Air-Driven centrifuge. Obtained pellets

were resuspended in 200 μl of 10 mM Tris-HCl buffer (pH 7.4) and subsequently diluted to 4 ml Tris-HCl buffer (pH 7.4) in 5 ml glass bottles closed by polypropylene caps. The dissociation mixture was kept at room temperature under constant stirring at 250 rpm on a magnetic stirrer plate. At different time points, samples were taken either for ThT binding or for Tyr fluorescence measurements. 150 μl of the dissociation mixture were taken for ThT binding measurements. They were directly mixed with 1 μl of 1.5 mM ThT solution. ThT fluorescence spectra were recorded on FluoroMax®-4 spectrofluorometer. Excitation wavelength was 440 nm and spectra were acquired in the range of 460-550 nm utilizing 3 nm slits for excitation and emission. To monitor the appearance of soluble β-endorphin 150 μl of the dissociation mixture were centrifuged for 30 min at 28 psi in the Airfuge® Air-Driven centrifuge. The supernatant was used to measure intrinsic Tyr fluorescence. Tyr fluorescence spectra were recorded on FluoroMax®-4 spectrofluorometer. Excitation wavelength was 275 nm and spectra were acquired in the range of 290-500 nm utilizing 3 nm slits for excitation and emission. Next, the UV absorbance of the examined solution was recorded on the UV-Vis spectrophotometer V-650 (JASCO Labor und Datentechnik GmbH, Gross-Umstadt, Germany) in the range of 240-340 nm.

Solid-state NMR spectroscopy

All ^{13}C-^{13}C DARR spectra of β-endorphin fibrils obtained in CP buffer at pH 6.0 were recorded on a Bruker Avance spectrometer operating at a static magnetic field of 14.1 T. A Bruker 3.2 mm triple resonance probe was used. The spinning speed was set to 13 kHz and the sample temperature was held between +5 °C and +10 °C during the measurement. 90 kHz to 100 kHz SPINAL proton decoupling [288] was applied in all dimensions during acquisition. The ^{13}C-^{13}C DARR spectrum of amyloid fibrils formed by β-endorphin in 10 mM ammonium acetate buffer at pH 5.5 containing 200 mM NaCl and 2 mg/ml heparin was recorded at 20.0 T static magnetic field and the spinning speed of 17 kHz. All spectra used for the sequential assignment (3D NCACB, 3D NCOCA, 3D CANCO and 3D NCACO, 80 ms ^{13}C-^{13}C DARR, 2D NCO, 2D NCA) of β-endorphin fibrils formed in CP buffer at pH 6.0 were recorded at 20.0 T static magnetic field and a spinning speed of 17 kHz. All spectra were processed using Topspin 2.1 (Bruker BioSpin AG, Fällanden, Switzerland), using a shifted cosine squared window function and zero-filling to the next power of two in all dimensions. Automated baseline correction was applied in the direct dimension. The spectra were analyzed using the

CCPN software package [194]. Further acquisition and processing details are given in **Supplementary Table S4** and **Supplementary Table S5**. The assignment of ^{13}C-^{13}C DARR spectrum of WT β-endorphin fibrils formed in CP buffer at pH 6.0 was sequentially obtained by following established procedures [256].

Data analysis

Data analysis of secondary chemical shifts, all aggregation and dissociation assays was done in the commercial software MATLAB 8.0, The MathWorks Inc., Natick, Massachusetts, USA. In the dissociation and aggregation assays, the baseline fluorescence of the ThT dye in the respective buffer was subtracted from the experimental data. The baseline-subtracted data were then normalized to the maximum fluorescence intensity value in the series.

.

Chapter 8

Conclusions and outlook

This thesis intended to study the functional hormone aggregation and reveal the molecular mechanism underlying this phenomenon. The study focused on three particular hormones: corticotropin-releasing factor (CRF), somatostatin 14 (SS14), and β-endorphin. A highly interdisciplinary approach combining various biophysical, biochemical, and molecular biology methods was chosen to comprehensively characterize the aggregation and dissociation of these hormones, as well as the structure and properties of their amyloid fibrils. Although all experiments were done *in vitro*, a strong emphasis on the biological relevance of findings was made. To satisfy the demand for large sample amounts, an efficient strategy for high-yield production of the recombinant peptides has been developed and optimized in each case. Even though recombinant protein synthesis in bacterial cell culture is considered routing nowadays, it sometimes requires significant efforts, as the case of SS14 demonstrated.

The properties and mechanisms of biological phenomena are generally explained through revealing the structure-activity relationships in the subject. Hence, significant efforts are usually aimed for structure elucidation. In the case of hormone amyloids, ssNMR spectroscopy is considered the method of choice for the determination of their high-resolution 3D structure. This study is no exception in this context. While only preliminary steps towards the high-resolution 3D structure have been taken in the cases of CRF and SS14, the study of β-endorphin has benefited from the availability of the first structural model and could therefore advance much further.

As this study clearly demonstrated, heparin, which is widely used as amyloid aggregation promoter, has a dramatic effect on the structure and stability of β-endorphin amyloids. Not only did heparin effectively promote aggregation in β-endorphin, but it also enforced the peptide to form very stable amyloid fibrils. This effect was very pronounced and outcompeted the influence of all other factors. In the context of our hypothesis that hormone amyloids are the storage state of hormones, which are required to disassembly after secretion, our findings question the applicability of heparin as a model GAG and a universal aggregation promoter in hormone aggregation studies.

The reversibility of hormone amyloid aggregation has been unambiguously demonstrated here for the first time by the example of β-endorphin fibrils, whose

formation was promoted by the salts of polyprotic acids in the aggregation mixture. The observed rates of aggregation and dissociation were in a reasonable agreement with those expected *in vivo* and showed the dependence on the peptide ionic state. Thus, the neutralization of peptide charge by counter-anions is considered the major driving force of hormone aggregation, and the change of environment occurring upon secretion (such as change of the dominant salt ions, dilution) is sufficient to induce fibril dissociation. In addition, low-molecular-weight carbohydrates have been found to assist β-endorphin aggregation, but not to alter the structure and stability of the fibrils.

A number of questions have yet remained to be answered. First and foremost, is the heparin effect universal for all peptide hormones? The preliminary data obtained for the heparin-induced fibrils of SS14 indicate that heparin was tightly associated with the fibrils and stabilized their structure as well. In the case of β-endorphin, it is interesting to identify heparin concentrations in the aggregation buffer, which allow to observe the lag-phase during peptide aggregation and which is sufficient to switch the salt-promoted amyloid fold to the heparin-induced one. Is it possible to induce reversible aggregation in other peptide hormones by salts of polyprotic acids? The fact that CRF aggregated in the presence of sodium citrate encourages optimism. Obviously, determination of high-resolution 3D structure of salt-promoted functional hormone amyloids is of high interest because it may shed the light on the molecular mechanism responsible for reversible aggregation of hormones. While the dilution of β-endorphin fibrils into the buffer containing the salt of monoprotic acid has been demonstrated to be sufficient for amyloid disassembly, the role of the dissociation buffer's pH has not been examined yet.

Another interesting aspect of functional hormone aggregation, which can be studied, for example, on the CRF model system, is the role of prohormones in prevention of hormone amyloid aggregation. Pro-CRF delivers a single mature product – CRF. Therefore, the difference in behavior of pro-CRF and CRF can be unambiguously attributed to the prohormone. The prohormone sequence is rich in prolines. This hints that the prohormone is aimed to prevent amyloid aggregation by disturbance of secondary structure elements. Moreover, the pI of pro-CRF is much higher than that of CRF, 10.6 vs. 5.4. This fact also supports the tentative role of the prohormone as an internal inhibitor of amyloid aggregation at the level of hormone precursor, because the ionization state of pro-CRF precludes the direct association of prohormone molecules at pH values of the ER and GC. The ultimate experiment would include the observation of pro-CRF

stability in solution where amyloid aggregation of CRF occurs upon excision of the hormone from the prohormone sequence.

Despite the achieved progress in studying of functional aggregation of β-endorphin a number of specific questions remain open.

- What are the aggregation and dissociation pathways of β-endorphin? More specifically, what are the intermediates occurring in these pathways?

- Is the growth/dissociation bidirectional or unidirectional? Is the mechanism of growth/dissociation continuously monotonic, stop-and-go, or dynamic, going back and forth?

- Is there a monomer exchange between bulk solution and mature fibrils?

- What are the changes in aggregation pathway upon addition of heparin to the system?

- What is the relative arrangement of heparin and peptide molecules in mature fibrils?

Of course, the topics highlighted above are not limited to studies of β-endorphin aggregation. Fibrillization of other hormones than discussed in the current thesis can also be challenged on the same way. Practically, the questions listed above can be addressed by optical super-resolution microscopy, which has emerged recently as a powerful new approach to investigate protein aggregation [119, 302, 303]. Optical super-resolution microscopy has been successfully applied for visualization of amyloid fibril formation both *in vitro* [119, 302-304] and *in vivo* [304-307]. The technique resolves spatial structures below the diffraction limit of optical microscopy, increasing resolution from 250 nm to 9-18 nm, with the capability to track early oligomerization events [304, 308, 309]. Aside from static localization of single molecules [302-304, 308], super-resolution microscopy can provide insights into the dynamics of amyloid formation [119]. Finally, it is very important to bridge the gap between *in vitro* and *in vivo* studies. Optical super-resolution microscopy and in-cell NMR methods seem very promising to achieve this ambitious goal.

Bibliography

1. Sipe, J.D. and Cohen, A.S., *Review: history of the amyloid fibril.* J. Struct. Biol., 2000. **130**(2-3): p. 88-98.
2. Eanes, E.D. and Glenner, G.G., *X-ray diffraction studies on amyloid filaments.* J. Histochem. Cytochem., 1968. **16**(11): p. 673-677.
3. Chiti, F. and Dobson, C.M., *Protein misfolding, functional amyloid, and human disease.* Annu. Rev. Biochem, 2006. **75**: p. 333-366.
4. Dobson, C.M., *Protein folding and misfolding.* Nature, 2003. **426**(6968): p. 884-890.
5. Kelly, J.W. and Balch, W.E., *Amyloid as a natural product.* J. Cell Biol., 2003. **161**(3): p. 461-462.
6. Fowler, D.M., et al., *Functional amyloid formation within mammalian tissue.* PLoS Biol., 2006. **4**(1): p. 100-107.
7. Fowler, D.M., et al., *Functional amyloid - from bacteria to humans.* Trends Biochem. Sci, 2007. **32**(5): p. 217-224.
8. Greenwald, J. and Riek, R., *Biology of amyloid: structure, function, and regulation.* Structure, 2010. **18**(10): p. 1244-1260.
9. Hu, K.N., et al., *Segmental polymorphism in a functional amyloid.* Biophys. J., 2011. **101**(9): p. 2242-2250.
10. Seuring, C., et al., *The mechanism of toxicity in HET-S/HET-s prion incompatibility.* PLoS Biol., 2012. **10**(12).
11. Seuring, C., et al., *Hormone amyloids in sickness and in health*, in *Amyloid fibrils and prefibrillar aggregates*. 2013, Wiley-VCH Verlag GmbH & Co. KGaA. p. 395-410.
12. Romier, C., et al., *Solution structure of human corticotropin releasing factor by ^{1}H NMR and distance geometry with restrained molecular dynamics.* Protein Eng., 1993. **6**(2): p. 149-156.
13. Pioszak, A.A., et al., *Molecular recognition of corticotropin-releasing factor by its G-protein-coupled receptor CRFR1.* J. Biol. Chem., 2008. **283**(47): p. 32900-32912.
14. Han, S.L., Rivier, J.E., and Scheraga, H.A., *Conformational studies of somatostatin and selected analogs by Raman spectroscopy.* Int. J. Pept. Protein Res., 1980. **15**(4): p. 355-364.
15. Hallenga, K., et al., *The conformational properties of the peptide hormone somatostatin (III). Assignment and analysis of the ^{1}H and ^{13}C high-resolution NMR spectra of somatostatin in aqueous solution.* FEBS Lett., 1980. **119**(1): p. 47-52.
16. Lichtarge, O., Jardetzky, O., and Li, C.H., *Secondary structure determination of human β-endorphin by ^{1}H NMR spectroscopy.* Biochemistry, 1987. **26**(18): p. 5916-25.
17. Kyle, R.A., *Amyloidosis: a convoluted story.* Br. J. Haematol., 2001. **114**(3): p. 529-538.
18. Cohen, A.S. and Calkins, E., *Electron microscopic observations on a fibrous component in amyloid of diverse origins.* Nature, 1959. **183**(4669): p. 1202-1203.
19. Dobson, C.M., *The structural basis of protein folding and its links with human disease.* Philos. Trans. R. Soc. Lond. Ser. B-Biol. Sci., 2001. **356**(1406): p. 133-145.
20. Chiti, F., et al., *Rationalization of the effects of mutations on peptide and protein aggregation rates.* Nature, 2003. **424**(6950): p. 805-808.
21. Baldwin, A.J., et al., *Metastability of native proteins and the phenomenon of amyloid formation.* J. Am. Chem. Soc., 2011. **133**(36): p. 14160-14163.
22. Kayed, R., et al., *Common structure of soluble amyloid oligomers implies common mechanism of pathogenesis.* Science, 2003. **300**(5618): p. 486-489.
23. Walsh, D.M., et al., *Amyloid-β oligomers: their production, toxicity and therapeutic inhibition.* Biochem. Soc. Trans., 2002. **30**: p. 552-557.
24. Chromy, B.A., et al., *Self-assembly of Aβ(1-42) into globular neurotoxins.* Biochemistry, 2003. **42**(44): p. 12749-12760.
25. Chernoff, Y., *Amyloidogenic domains, prions and structural inheritance: rudiments of early life or recent acquisition?* Curr. Opin. Chem. Biol., 2004. **8**(6): p. 665-671.
26. King, C.Y., et al., *Prion-inducing domain 2-114 of yeast Sup35 protein transforms in vitro into amyloid-like filaments.* Proc. Natl. Acad. Sci. U. S. A., 1997. **94**(13): p. 6618-6622.
27. Coustou, V., et al., *The protein product of the het-s heterokaryon incompatibility gene of the fungus Podospora anserina behaves as a prion analog.* Proc. Natl. Acad. Sci. U. S. A., 1997. **94**(18): p. 9773-9778.
28. Saupe, S.J., *Molecular genetics of heterokaryon incompatibility in filamentous ascomycetes.* Microbiol. Mol. Biol. Rev., 2000. **64**(3): p. 489-502.

29. Si, K., Lindquist, S., and Kandel, E.R., *A neuronal isoform of the Aplysia CPEB has prion-like properties.* Cell, 2003. **115**(7): p. 879-891.

30. Leonhardt, R.M., et al., *Critical residues in the PMEL/Pmel17 N-terminus direct the hierarchical assembly of melanosomal fibrils.* Mol. Biol. Cell, 2013. **24**(7): p. 964-981.

31. Maji, S.K., et al., *Functional amyloids as natural storage of peptide hormones in pituitary secretory granules.* Science, 2009. **325**(5938): p. 328-332.

32. Kato, M., et al., *Cell-free formation of RNA granules: low complexity sequence domains form dynamic fibers within hydrogels.* Cell, 2012. **149**(4): p. 753-767.

33. Nilsson, M.R., *Techniques to study amyloid fibril formation in vitro.* Methods, 2004. **34**(1): p. 151-160.

34. Oakley, A.E., et al., *Electron microscopic appearances and implications of neuropeptide fibrillary forms.* Neuropeptides, 1981. **2**(1): p. 1-11.

35. Snell, C.R., *The receptor conformation of flexible peptides.* Biochem. Soc. Trans., 1978. **6**(1): p. 138-141.

36. Alberts, B., et al., *Molecular biology of the cell.* 5th ed. 2008, New York, NY: Garland Science. 1616pp.

37. Dannies, P.S., *Protein hormone storage in secretory granules: mechanisms for concentration and sorting.* Endocr. Rev., 1999. **20**(1): p. 3-21.

38. Giannattasio, G., Zanini, A., and Meldolesi, J., *Molecular organization of rat prolactin granules. 1. In vitro stability of intact and "membraneless" granules.* J. Cell Biol., 1975. **64**(1): p. 246-251.

39. Loh, Y.P., et al., *Secretory granule biogenesis and neuropeptide sorting to the regulated secretory pathway in neuroendocrine cells.* J. Mol. Neurosci., 2003. **22**(1-2): p. 63-71.

40. Rambourg, A., et al., *Formation of secretory granules in the Golgi apparatus of prolactin cells in the rat pituitary gland: a stereoscopic study.* The Anatomical Record, 1992. **232**(2): p. 169-179.

41. Hutton, J.C., Penn, E.J., and Peshavaria, M., *Low-molecular-weight constituents of isolated insulin-secretory granules. Bivalent cations, adenine nucleotides and inorganic phosphate.* Biochem. J, 1983. **210**(2): p. 297-305.

42. Oprins, A., et al., *The ER to Golgi interface is the major concentration site of secretory proteins in the exocrine pancreatic cell.* Traffic, 2001. **2**(11): p. 831-838.

43. Lodish, H., et al., *Molecular cell biology.* 4th edition ed. Molecular cell biology. 2000, New York: W. H. Freeman. l+1344p-l+1344p.

44. Cool, D.R., et al., *Identification of the sorting signal motif within pro-opiomelanocortin for the regulated secretory pathway.* J. Biol. Chem., 1995. **270**(15): p. 8723-8729.

45. Fricker, L.D., *Carboxypeptidase E.* Annu. Rev. Physiol., 1988. **50**: p. 309-321.

46. Cool, D.R., et al., *Carboxypeptidase E is a regulated secretory pathway sorting receptor: genetic obliteration leads to endocrine disorders in Cpe^{fat} mice.* Cell, 1997. **88**(1): p. 73-83.

47. Arvan, P. and Castle, D., *Sorting and storage during secretory granule biogenesis: looking backward and looking forward.* Biochem. J, 1998. **332**: p. 593-610.

48. Birk, J., et al., *Dominant pro-vasopressin mutants that cause diabetes insipidus form disulfide-linked fibrillar aggregates in the endoplasmic reticulum.* J. Cell Sci., 2009. **122**(21): p. 3994-4002.

49. King, L.S. and Agre, P., *Pathophysiology of the aquaporin water channels.* Annu. Rev. Physiol., 1996. **58**: p. 619-648.

50. Brownstein, M.J., Russell, J.T., and Gainer, H., *Synthesis, transport, and release of posterior pituitary hormones.* Science, 1980. **207**(4429): p. 373-378.

51. Wu, C.K., et al., *Structures of an unliganded neurophysin and its vasopressin complex: Implications for binding and allosteric mechanisms.* Protein Sci., 2001. **10**(9): p. 1869-1880.

52. Hansen, L.K., Rittig, S., and Robertson, G.L., *Genetic basis of familial neurohypophyseal diabetes insipidus.* Trends Endocrinol. Metab., 1997. **8**(9): p. 363-372.

53. Christensen, J.H. and Rittig, S., *Familial neurohypophyseal diabetes insipidus - an update.* Semin. Nephrol., 2006. **26**(3): p. 209-223.

54. Gerdes, H.H., et al., *The primary structure of human secretogranin II, a widespread tyrosine-sulfated secretory granule protein that exhibits low pH- and calcium-induced aggregation.* J. Biol. Chem., 1989. **264**(20): p. 12009-12015.

55. Paroutis, P., Touret, N., and Grinstein, S., *The pH of the secretory pathway: measurement, determinants, and regulation.* Physiology, 2004. **19**: p. 207-215.

56. Leblond, F.A., et al., *Reconstitution in vitro of the pH-dependent aggregation of pancreatic zymogens en route to the secretory granule: implication of GP-2.* Biochem. J, 1993. **291**: p. 289-296.

57. Colomer, V., Kicska, G.A., and Rindler, M.J., *Secretory granule content proteins and the luminal domains of granule membrane proteins aggregate in vitro at mildly acidic pH.* J. Biol. Chem., 1996. **271**(1): p. 48-55.

58. Jain, R.K., Joyce, P.B.M., and Gorr, S.U., *Aggregation chaperones enhance aggregation and storage of secretory proteins in endocrine cells.* J. Biol. Chem., 2000. **275**(35): p. 27032-27036.

59. Stoller, T.J. and Shields, D., *The propeptide of preprosomatostatin mediates intracellular transport and secretion of α-globin from mammalian cells.* J. Cell Biol., 1989. **108**(5): p. 1647-1655.

60. van den Berg, B., Ellis, R.J., and Dobson, C.M., *Effects of macromolecular crowding on protein folding and aggregation.* EMBO J., 1999. **18**(24): p. 6927-6933.

61. Kornreich, W.D., et al., *Alanine series of ovine corticotropin releasing factor (oCRF): a structure-activity relationship study.* J. Med. Chem., 1992. **35**(10): p. 1870-1876.

62. Majzoub, J.A., *Corticotropin-releasing hormone physiology.* European Journal of Endocrinology, 2006. **155**: p. S71-S76.

63. Oyarce, A.M., et al., *Dopaminergic regulation of secretory granule-associated proteins in rat intermediate pituitary.* J. Neurochem., 1996. **67**(1): p. 229-241.

64. Penman, E., et al., *Molecular forms of somatostatin in normal subjects and in patients with pancreatic somatostatinoma.* Clin. Endocrinol. (Oxf.), 1980. **12**(6): p. 611-620.

65. Soong, Y.K., et al., *Size heterogeneity of immunoreactive prolactin in hyperprolactinemic serum.* Clin. Endocrinol. (Oxf.), 1982. **16**(3): p. 259-265.

66. Humphries, D.E., et al., *Heparin is essential for the storage of specific granule proteases in mast cells.* Nature, 1999. **400**(6746): p. 769-772.

67. Esko, J., Kimata, K., and Lindahl, U., *Proteoglycans and sulfated glycosaminoglycans*, in *Essentials of glycobiology*, A. Varki, et al., Editors. 2009, Cold Spring Harbor Laboratory Press: Cold Spring Harbor (NY). p. xvii+653p.

68. Kolset, S.O., Prydz, K., and Pejler, G., *Intracellular proteoglycans.* Biochem. J, 2004. **379**: p. 217-227.

69. Lindahl, U. and Li, J.-p., *Interactions between heparan sulfate and proteins. Design and functional implications*, in *International Review of Cell and Molecular Biology, Vol 276*, K.W. Jeon, Editor. 2009. p. 105-159.

70. Snow, A.D. and Kisilevsky, R., *Temporal relationship between glycosaminoglycan accumulation and amyloid deposition during experimental amyloidosis. A histochemical study.* Lab. Invest., 1985. **53**(1): p. 37-44.

71. van Horssen, J., et al., *Heparan sulphate proteoglycans in Alzheimer's disease and amyloid-related disorders.* Lancet Neurol., 2003. **2**(8): p. 482-492.

72. Li, J.P., et al., *In vivo fragmentation of heparan sulfate by heparanase overexpression renders mice resistant to amyloid protein A amyloidosis.* Proc. Natl. Acad. Sci. U. S. A., 2005. **102**(18): p. 6473-6477.

73. Noborn, F., et al., *Heparan sulfate/heparin promotes transthyretin fibrillization through selective binding to a basic motif in the protein.* Proc. Natl. Acad. Sci. U. S. A., 2011. **108**(14): p. 5584-5589.

74. Ren, R., et al., *Role of glycosaminoglycan sulfation in the formation of immunoglobulin light chain amyloid oligomers and fibrils.* J. Biol. Chem., 2010. **285**(48): p. 37672-37682.

75. Cohlberg, J.A., et al., *Heparin and other glycosaminoglycans stimulate the formation of amyloid fibrils from α-synuclein in vitro.* Biochemistry, 2002. **41**(5): p. 1502-1511.

76. Nielsen, S.B., et al., *Multiple roles of heparin in the aggregation of p25α.* J. Mol. Biol., 2012. **421**(4-5): p. 601-615.

77. Kisilevsky, R., *Review: amyloidogenesis—unquestioned answers and unanswered questions.* J. Struct. Biol., 2000. **130**(2–3): p. 99-108.

78. McLaurin, J., et al., *Review: modulating factors in amyloid-β fibril formation.* J. Struct. Biol., 2000. **130**(2-3): p. 259-270.

79. Ancsin, J.B., *Amyloidogenesis: historical and modern observations point to heparan sulfate proteoglycans as a major culprit.* Amyloid: Journal of Protein Folding Disorders, 2003. **10**(2): p. 67-79.

80. Jha, S., et al., *Mechanism of amylin fibrillization enhancement by heparin.* J. Biol. Chem., 2011. **286**(26): p. 22894-22904.

81. Jose Valle-Delgado, J., et al., *Modulation of Aβ(42) fibrillogenesis by glycosaminoglycan structure.* FASEB J., 2010. **24**(11): p. 4250-4261.

82. Nielsen, S.B., et al., *β-Sheet aggregation of kisspeptin-10 is stimulated by heparin but inhibited by amphiphiles.* Biopolymers, 2010. **93**(8): p. 678-689.

83. Yamaguchi, I., et al., *Glycosaminoglycan and proteoglycan inhibit the depolymerization of β2-microglobulin amyloid fibrils in vitro.* Kidney Int., 2003. **64**(3): p. 1080-1088.

84. Dill, K.A., *Polymer principles and protein folding.* Protein Sci., 1999. **8**(6): p. 1166-1180.

85. Levinthal, C. *How to fold graciously.* in *Mossbauer Spectroscopy in Biological Systems.* 1969. Allerton house, Monticello, Illinois.

86. Antzutkin, O.N., *Amyloidosis of Alzheimer's Aβ peptides: solid-state nuclear magnetic resonance, electron paramagnetic resonance, transmission electron microscopy, scanning transmission electron microscopy and atomic force microscopy studies.* Magn. Reson. Chem., 2004. **42**(2): p. 231-246.

87. Li, H., et al., *Amyloids and protein aggregation. Analytical methods*, in *Encyclopedia of Analytical Chemistry.* 2006, John Wiley & Sons, Ltd.

88. Kourkoutis, L.F., Plitzko, J.M., and Baumeister, W., *Electron microscopy of biological materials at the nanometer scale.* Annual Review of Materials Research, Vol 42, 2012. **42**: p. 33-58.

89. Bitan, G., et al., *Amyloid β-protein (Aβ) assembly: Aβ40 and Aβ42 oligomerize through distinct pathways.* Proc. Natl. Acad. Sci. U. S. A., 2003. **100**(1): p. 330-335.

90. Petkova, A.T., et al., *Self-propagating, molecular-level polymorphism in Alzheimer's β-amyloid fibrils.* Science, 2005. **307**(5707): p. 262-265.

91. Walsh, D.M., et al., *Amyloid β-protein fibrillogenesis. Detection of a protofibrillar intermediate.* J. Biol. Chem., 1997. **272**(35): p. 22364-22372.

92. Gath, J., et al., *Unlike twins: an NMR comparison of two α-synuclein polymorphs featuring different toxicity.* PLoS One, 2014. **9**(3): p. e90659.

93. Tjernberg, L.O., et al., *A molecular model of Alzheimer amyloid β-peptide fibril formation.* J. Biol. Chem., 1999. **274**(18): p. 12619-12625.

94. Apetri, M.M., et al., *Secondary structure of α-synuclein oligomers: characterization by Raman and atomic force microscopy.* J. Mol. Biol., 2006. **355**(1): p. 63-71.

95. Zhang, S., et al., *Coexistence of ribbon and helical fibrils originating from hIAPP(20-29) revealed by quantitative nanomechanical atomic force microscopy.* Proc. Natl. Acad. Sci. U. S. A., 2013. **110**(8): p. 2798-2803.

96. Hepler, R.W., et al., *Solution state characterization of amyloid β-derived diffusible ligands.* Biochemistry, 2006. **45**(51): p. 15157-15167.

97. Collins, S.R., et al., *Mechanism of prion propagation: Amyloid growth occurs by monomer addition.* PLoS Biol., 2004. **2**(10): p. 1582-1590.

98. Lashuel, H.A., et al., *Protofilaments, filaments, ribbons, and fibrils from peptidomimetic self-assembly: Implications for amyloid fibril formation and materials science.* J. Am. Chem. Soc., 2000. **122**(22): p. 5262-5277.

99. Soldi, G., et al., *Amyloid formation of a protein in the absence of initial unfolding and destabilization of the native state.* Biophys. J., 2005. **89**(6): p. 4234-4244.

100. Bernstein, S.L., et al., *Amyloid-β protein oligomerization and the importance of tetramers and dodecamers in the aetiology of Alzheimer's disease.* Nat. Chem., 2009. **1**(4): p. 326-331.

101. Smith, A.M., et al., *Direct observation of oligomeric species formed in the early stages of amyloid fibril formation using electrospray ionisation mass spectrometry.* J. Mol. Biol., 2006. **364**(1): p. 9-19.

102. Lomakin, A., Benedek, G.B., and Teplow, D.B., *Monitoring protein assembly using quasielastic light scattering spectroscopy.* Amyloid, Prions, and Other Protein Aggregates, 1999. **309**: p. 429-459.

103. Jayasinghe, S.A. and Langen, R., *Identifying structural features of fibrillar islet amyloid polypeptide using site-directed spin labeling.* J. Biol. Chem., 2004. **279**(46): p. 48420-48425.

104. Alexandrescu, A.T., *An NMR-based quenched hydrogen exchange investigation of model amyloid fibrils formed by cold shock protein A.* Pac. Symp. Biocomput., 2001: p. 67-78.

105. Hoshino, M., et al., *Dimethylsulfoxide-quenched hydrogen/deuterium exchange method to study amyloid fibril structure.* Biochimica Et Biophysica Acta-Biomembranes, 2007. **1768**(8): p. 1886-1899.

106. Luhrs, T., et al., *3D structure of Alzheimer's amyloid-β(1-42) fibrils.* Proc. Natl. Acad. Sci. U. S. A., 2005. **102**(48): p. 17342-17347.

107. Wales, T.E. and Engen, J.R., *Hydrogen exchange mass spectrometry for the analysis of protein dynamics.* Mass Spectrom. Rev., 2006. **25**(1): p. 158-170.

108. Wang, L., et al., *Bacterial inclusion bodies contain amyloid-like structure.* PLoS Biol., 2008. **6**(8): p. 1791-1801.

109. Paterson, Y., Englander, S.W., and Roder, H., *An antibody binding site on cytochrome c defined by hydrogen exchange and two-dimensional NMR.* Science, 1990. **249**(4970): p. 755-759.

110. Konuma, T., et al., *Kinetic intermediates of β2-microglobulin fibril elongation probed by pulse-labeling H/D exchange combined with NMR analysis.* J. Mol. Biol., 2011. **405**(3): p. 851-862.

111. Qi, W., et al., *Simultaneous monitoring of peptide aggregate distributions, structure, and kinetics using amide hydrogen exchange: application to Aβ(1-40) fibrillogenesis.* Biotechnol. Bioeng., 2008. **100**(6): p. 1214-1227.

112. Kheterpal, I., et al., *Aβ protofibrils possess a stable core structure resistant to hydrogen exchange.* Biochemistry, 2003. **42**(48): p. 14092-14098.

113. Carulla, N., et al., *Molecular recycling within amyloid fibrils.* Nature, 2005. **436**(7050): p. 554-558.

114. Kumar, S., Mohanty, S.K., and Udgaonkar, J.B., *Mechanism of formation of amyloid protofibrils of barstar from soluble oligomers: evidence for multiple steps and lateral association coupled to conformational conversion.* J. Mol. Biol., 2007. **367**(4): p. 1186-1204.

115. Tougu, V., Karafin, A., and Palumaa, P., *Binding of zinc(II) and copper(II) to the full-length Alzheimer's amyloid-β peptide.* J. Neurochem., 2008. **104**(5): p. 1249-1259.

116. Maji, S.K., et al., *Conformational dynamics of amyloid β-protein assembly probed using intrinsic fluorescence.* Biochemistry, 2005. **44**(40): p. 13365-13376.

117. Lee, J.C., et al., *α-Synuclein structures from fluorescence energy-transfer kinetics: implications for the role of the protein in Parkinson's disease.* Proc. Natl. Acad. Sci. U. S. A., 2004. **101**(47): p. 16466-16471.

118. Roberti, M.J., et al., *Fluorescence imaging of amyloid formation in living cells by a functional, tetracysteine-tagged α-synuclein.* Nat. Methods, 2007. **4**(4): p. 345-351.

119. Pinotsi, D., et al., *Direct observation of heterogeneous amyloid fibril growth kinetics via two-color super-resolution microscopy.* Nano Lett., 2014. **14**(1): p. 339-45.

120. Brahms, S. and Brahms, J., *Determination of protein secondary structure in solution by vacuum ultraviolet circular dichroism.* J. Mol. Biol., 1980. **138**(2): p. 149-178.

121. Stohr, J., et al., *Mechanisms of prion protein assembly into amyloid.* Proc. Natl. Acad. Sci. U. S. A., 2008. **105**(7): p. 2409-2414.

122. Picotti, P., et al., *Amyloid fibril formation and disaggregation of fragment 1-29 of apomyoglobin: insights into the effect of pH on protein fibrillogenesis.* J. Mol. Biol., 2007. **367**(5): p. 1237-1245.

123. *Today's tests.* Br. Med. J., 1968. **4**(5630): p. 564-565.

124. Chiti, F., et al., *Designing conditions for in vitro formation of amyloid protofilaments and fibrils.* Proc. Natl. Acad. Sci. U. S. A., 1999. **96**(7): p. 3590-3594.

125. Howie, A.J. and Brewer, D.B., *Optical properties of amyloid stained by Congo red: history and mechanisms.* Micron, 2009. **40**(3): p. 285-301.

126. Howie, A.J., et al., *Physical basis of colors seen in Congo red-stained amyloid in polarized light.* Lab. Invest., 2008. **88**(3): p. 232-242.

127. Howie, A.J. and Brewer, D.B., *Apple-green birefringence?* The Bulletin of The Royal College of Pathologists, 2008(144): p. 263-266.

128. Ivanova, M.I., et al., *Role of the C-terminal 28 residues of β2-microglobulin in amyloid fibril formation.* Biochemistry, 2003. **42**(46): p. 13536-13540.

129. Schuetz, A.K., et al., *The amyloid-Congo Red interface at atomic resolution.* Angew. Chem.-Int. Edit., 2011. **50**(26): p. 5956-5960.

130. Findeis, M.A., *Approaches to discovery and characterization of inhibitors of amyloid β-peptide polymerization.* Biochim. Biophys. Acta-Mol. Basis Dis., 2000. **1502**(1): p. 76-84.

131. Heiser, V., et al., *Inhibition of huntingtin fibrillogenesis by specific antibodies and small molecules: implications for Huntington's disease therapy.* Proc. Natl. Acad. Sci. U. S. A., 2000. **97**(12): p. 6739-6744.

132. LeVine, H., *Thioflavine T interaction with synthetic Alzheimer's disease β-amyloid peptides: detection of amyloid aggregation in solution.* Protein Sci., 1993. **2**(3): p. 404-410.

133. LeVine, H., *Quantification of β-sheet amyloid fibril structures with thioflavin T.* Amyloid, Prions, and Other Protein Aggregates, 1999. **309**: p. 274-284.

134. Khurana, R., et al., *Mechanism of thioflavin T binding to amyloid fibrils.* J. Struct. Biol., 2005. **151**(3): p. 229-238.

135. Krebs, M.R.H., Bromley, E.H.C., and Donald, A.M., *The binding of thioflavin-T to amyloid fibrils: localisation and implications.* J. Struct. Biol., 2005. **149**(1): p. 30-37.

136. Ilanchelian, M. and Ramaraj, R., *Emission of thioflavin T and its control in the presence of DNA.* J. Photochem. Photobiol. A-Chem., 2004. **162**(1): p. 129-137.

137. LeVine, H., *Thioflavine T interaction with amyloid β-sheet structures.* Amyloid-International Journal of Experimental and Clinical Investigation, 1995. **2**(1): p. 1-6.

138. Suzuki, Y., et al., *Alternative pathways of human islet amyloid polypeptide aggregation distinguished by ^{19}F nuclear magnetic resonance-detected kinetics of monomer consumption.* Biochemistry, 2012. **51**(41): p. 8154-8162.

139. Wilcken, R., et al., *Kinetic mechanism of p53 oncogenic mutant aggregation and its inhibition.* Proc. Natl. Acad. Sci. U. S. A., 2012. **109**(34): p. 13584-13589.

140. Lee, C.-C., et al., *A three-stage kinetic model of amyloid fibrillation.* Biophys. J., 2007. **92**(10): p. 3448-3458.

141. Wolfe, L.S., et al., *Protein-induced photophysical changes to the amyloid indicator dye thioflavin T.* Proc. Natl. Acad. Sci. U. S. A., 2010. **107**(39): p. 16863-16868.

142. Nilsson, K.P.R., et al., *Imaging distinct conformational states of amyloid-β fibrils in Alzheimer's disease using novel luminescent probes.* ACS Chem. Biol., 2007. **2**(8): p. 553-560.

143. Nilsson, K.P.R., *Small organic probes as amyloid specific ligands. Past and recent molecular scaffolds.* FEBS Lett., 2009. **583**(16): p. 2593-2599.

144. Cavanagh, J., et al., *Protein NMR spectroscopy: principles and practice.* Protein NMR spectroscopy: principles and practice. 1996. xxiii+587p.

145. Zeeb, M. and Balbach, J., *Protein folding studied by real-time NMR spectroscopy.* Methods, 2004. **34**(1): p. 65-74.

146. Riek, R., et al., *NMR studies in aqueous solution fail to identify significant conformational differences between the monomeric forms of two Alzheimer peptides with widely different plaque-competence, Aβ(1-40)^{ox} and Aβ(1-42)^{ox}.* Eur. J. Biochem., 2001. **268**(22): p. 5930-5936.

147. Esposito, G., et al., *Solution structure of β2-microglobulin and insights into fibrillogenesis.* Biochimica Et Biophysica Acta-Proteins and Proteomics, 2005. **1753**(1): p. 76-84.

148. Shao, H.Y., et al., *Solution structures of micelle-bound amyloid β-(1-40) and β-(1-42) peptides of Alzheimer's disease.* J. Mol. Biol., 1999. **285**(2): p. 755-773.

149. Luginbuhl, P., Szyperski, T., and Wuthrich, K., *Statistical basis for the use of $^{13}C^{\alpha}$ chemical shifts in protein structure determination.* J. Magn. Reson., Ser B, 1995. **109**(2): p. 229-233.

150. Petkova, A.T., Yau, W.M., and Tycko, R., *Experimental constraints on quaternary structure in Alzheimer's β-amyloid fibrils.* Biochemistry, 2006. **45**(2): p. 498-512.

151. Jaroniec, C.P., et al., *High-resolution molecular structure of a peptide in an amyloid fibril determined by magic angle spinning NMR spectroscopy.* Proc. Natl. Acad. Sci. U. S. A., 2004. **101**(3): p. 711-716.

152. Van Melckebeke, H., et al., *Atomic-resolution three-dimensional structure of HET-s(218-289) amyloid fibrils by solid-state NMR spectroscopy.* J. Am. Chem. Soc., 2010. **132**(39): p. 13765-13775.

153. Iwata, K., et al., *3D structure of amyloid protofilaments of β2-microglobulin fragment probed by solid-state NMR.* Proc. Natl. Acad. Sci. U. S. A., 2006. **103**(48): p. 18119-18124.

154. Spera, S. and Bax, A., *Empirical correlation between protein backbone conformation and Cα and Cβ ^{13}C nuclear magnetic resonance chemical shifts.* J. Am. Chem. Soc., 1991. **113**(14): p. 5490-5492.

155. Balbach, J.J., et al., *Supramolecular structure in full-length Alzheimer's β-amyloid fibrils: evidence for a parallel β-sheet organization from solid-state nuclear magnetic resonance.* Biophys. J., 2002. **83**(2): p. 1205-1216.

156. Bockmann, A. and Meier, B.H., *Prions: en route from structural models to structures.* Prion, 2010. **4**(2).

157. Edwards, A.M., et al., *Protein production: feeding the crystallographers and NMR spectroscopists.* Nat. Struct. Biol., 2000. **7**: p. 970-972.

158. Laganowsky, A., et al., *Atomic view of a toxic amyloid small oligomer.* Science, 2012. **335**(6073): p. 1228-1231.

159. Colletier, J.-P., et al., *Molecular basis for amyloid-β polymorphism.* Proc. Natl. Acad. Sci. U. S. A., 2011. **108**(41): p. 16938-16943.

160. Razavi, H., et al., *Benzoxazoles as transthyretin amyloid fibril inhibitors: synthesis, evaluation, and mechanism of action.* Angew. Chem.-Int. Edit., 2003. **42**(24): p. 2758-2761.

161. Morais-de-Sa, E., et al., *The crystal structure of transthyretin in complex with diethylstilbestrol. A promising template for the design of amyloid inhibitors.* J. Biol. Chem., 2004. **279**(51): p. 53483-53490.

162. Wun, K.S., et al., *Crystallization and preliminary X-ray diffraction analysis of the Fab fragment of WO2, an antibody specific for the Aβ peptides associated with Alzheimer's disease.* Acta Crystallographica Section F-Structural Biology and Crystallization Communications, 2008. **64**: p. 438-441.

163. Basi, G.S., et al., *Structural correlates of antibodies associated with acute reversal of amyloid β-related behavioral deficits in a mouse model of Alzheimer disease.* J. Biol. Chem., 2010. **285**(5): p. 3417-3427.

164. Sawaya, M.R., et al., *Atomic structures of amyloid cross-β spines reveal varied steric zippers.* Nature, 2007. **447**(7143): p. 453-457.

165. Streltsov, V., *X-ray absorption and diffraction studies of the metal binding sites in amyloid β-peptide.* European Biophysics Journal with Biophysics Letters, 2008. **37**(3): p. 257-263.

166. Atwood, C.S., et al., *Copper mediates dityrosine cross-linking of Alzheimer's amyloid-β.* Biochemistry, 2004. **43**(2): p. 560-568.

167. LeVine, S.M., *Iron deposits in multiple sclerosis and Alzheimer's disease brains.* Brain Res., 1997. **760**(1-2): p. 298-303.

168. Vale, W., et al., *Characterization of a 41-residue ovine hypothalamic peptide that stimulates secretion of corticotropin and β-endorphin.* Science, 1981. **213**(4514): p. 1394-1397.

169. Owens, M.J. and Nemeroff, C.B., *Physiology and pharmacology of corticotropin-releasing factor.* Pharmacol. Rev., 1991. **43**(4): p. 425-473.

170. Vale, W., et al., *Chemical and biological characterization of corticotropin releasing factor.* Recent Prog. Horm. Res., 1983. **39**: p. 245-270.

171. Shibahara, S., et al., *Isolation and sequence analysis of the human corticotropin-releasing factor precursor gene.* EMBO J., 1983. **2**(5): p. 775-779.

172. Castro, M.G., et al., *Expression of biologically active human pre-procorticotropin releasing hormone in E. coli: characterization and purification.* Int. J. Biochem., 1990. **22**(11): p. 1341-1349.

173. Hauger, R.L., et al., *Corticotropin releasing factor (CRF) receptor signaling in the central nervous system: new molecular targets.* CNS & Neurological Disorders-Drug Targets, 2006. **5**(4): p. 453-479.

174. Spiess, J., et al., *Primary structure of corticotropin-releasing factor from ovine hypothalamus.* Proceedings of the National Academy of Sciences of the United States of America-Biological Sciences, 1981. **78**(10): p. 6517-6521.

175. Castro, M.G., et al., *Biosynthesis of corticotropin-releasing hormone (CRH) in mouse corticotropic tumor cells expressing the human proCRH gene: intracellular storage and regulated secretion.* J. Mol. Endocrinol., 1991. **7**(2): p. 97-104.

176. Dathe, M., et al., *Conformational differences of ovine and human corticotropin releasing hormone. A CD, IR, NMR and dynamic light scattering study.* Int. J. Pept. Protein Res., 1996. **47**(5): p. 383-393.

177. Gilligan, P.J., Robertson, D.W., and Zaczek, R., *Corticotropin releasing factor (CRF) receptor modulators: progress and opportunities for new therapeutic agents.* J. Med. Chem., 2000. **43**(9): p. 1641-1660.

178. Stohr, P.A., *On quantitative changes of "gomori-positive" substances in the median eminence and neural lobe of the rat hypophysis after bilateral adrenalectomy.* Z. Zellforsch. Mikrosk. Anat., 1969. **94**(3): p. 425-433.

179. Bock, R., *Morphometric investigations concerning the histological detection of the corticotropin-releasing factor in the median eminence of the rat.* Z. Anat. Entwicklungsgesch., 1972. **137**(1): p. 1-29.

180. Rinne, U.K., *Experimental electron microscopic studies on the neurovascular link between the hypothalamus and anterior pituitary.* Bargmann W. And B. Scharrer. 1970. 220-228.

181. Schwabedal, P.E., Partenheimer, U., and Bock, R., *Influence of sodium chloride on amount of CRF-granules and "classical" neurosecretory material (NSM) in neurohypophysis of bilaterally adrenalectomized rats.* Anat. Embryol. (Berl.), 1976. **149**(3): p. 307-313.

182. Mac, T.T., et al., *High yield expression and purification of isotopically labelled human endothelin-1 for use in NMR studies.* Protein Expression Purif., 2006. **48**(2): p. 253-260.

183. Marley, J., Lu, M., and Bracken, C., *A method for efficient isotopic labeling of recombinant proteins.* J. Biomol. NMR, 2001. **20**(1): p. 71-75.

184. Seo, E.S., et al., *Preparation of isotopically labelled recombinant β-defensin for NMR studies.* Protein Expression Purif., 2009. **65**(2): p. 179-184.

185. Rasband, W.S., *ImageJ.* 1997-2014.

186. Salzmann, M., et al., *TROSY-type triple-resonance experiments for sequential NMR assignments of large proteins.* J. Am. Chem. Soc., 1999. **121**(4): p. 844-848.

187. Fernandez-Escamilla, A.M., et al., *Prediction of sequence-dependent and mutational effects on the aggregation of peptides and proteins.* Nat. Biotechnol., 2004. **22**(10): p. 1302-1306.

188. Maurer-Stroh, S., et al., *Exploring the sequence determinants of amyloid structure using position-specific scoring matrices.* Nat. Methods, 2010. **7**(3): p. 237-U109.

189. Lewandowski, J.R., et al., *Structural complexity of a composite amyloid fibril.* J. Am. Chem. Soc., 2011. **133**(37): p. 14686-14698.

190. *ProteinCalculator v3.4.* 2013; Available from: http://protcalc.sourceforge.net/.

191. Kapust, R.B., Routzahn, K.M., and Waugh, D.S., *Processive degradation of nascent polypeptides, triggered by tandem AGA codons, limits the accumulation of recombinant tobacco etch virus protease in Escherichia coli BL21(DE3).* Protein Expression Purif., 2002. **24**(1): p. 61-70.

192. Laemmli, U.K., *Cleavage of structural proteins during assembly of head of bacteriophage-T4.* Nature, 1970. **227**(5259): p. 680-685.

193. Pervushin, K., et al., *Attenuated T$_2$ relaxation by mutual cancellation of dipole-dipole coupling and chemical shift anisotropy indicates an avenue to NMR structures of very large biological macromolecules in solution.* Proc. Natl. Acad. Sci. U. S. A., 1997. **94**(23): p. 12366-12371.

194. Vranken, W.F., et al., *The CCPN data model for NMR spectroscopy: development of a software pipeline.* Proteins-Structure Function and Bioinformatics, 2005. **59**(4): p. 687-696.

195. Patel, Y.C., *Somatostatin and its receptor family.* Front. Neuroendocrinol., 1999. **20**(3): p. 157-198.

196. Delfs, J.R. and Dichter, M.A., *Effects of somatostatin on mammalian cortical neurons in culture: physiological actions and unusual dose response characteristics.* J. Neurosci., 1983. **3**(6): p. 1176-1188.

197. Lamberts, S.W.J., et al., *Drug therapy. Octreotide.* New Engl. J. Med., 1996. **334**(4): p. 246-254.

198. Ramirez-Jarquin, J.O., et al., *Somatostatin modulates generation of inspiratory rhythms and determines asphyxia survival.* Peptides, 2012. **34**(2): p. 360-372.

199. Grace, C.R.R., et al., *Novel sst$_2$-selective somatostatin agonists. Three-dimensional consensus structure by NMR.* J. Med. Chem., 2006. **49**(15): p. 4487-4496.

200. Deleuze, C. and Hull, W.E., *Assignment and analysis of the 500 MHz ^{1}H NMR spectra of somatostatin and the acyclic precursor (S^{3,14}- Acm)-somatostatin in dimethyl sulfoxide.* Organic Magnetic Resonance, 1982. **18**(2): p. 112-116.

201. Grace, C.R.R., et al., *Novel sst$_4$-selective somatostatin (SRIF) agonists. 4. Three-dimensional consensus structure by NMR.* J. Med. Chem., 2003. **46**(26): p. 5606-5618.

202. Holladay, L.A. and Puett, D., *Somatostatin conformation: evidence for a stable intramolecular structure from circular dichroism, diffusion, and sedimentation equilibrium.* Proc. Natl. Acad. Sci. U. S. A., 1976. **73**(4): p. 1199-1202.

203. Nilsson, J., et al., *Affinity fusion strategies for detection, purification, and immobilization of recombinant proteins.* Protein Expression Purif., 1997. **11**(1): p. 1-16.

204. Arnau, J., et al., *Current strategies for the use of affinity tags and tag removal for the purification of recombinant proteins.* Protein Expression Purif., 2006. **48**(1): p. 1-13.

205. Sorensen, H.P. and Mortensen, K.K., *Soluble expression of recombinant proteins in the cytoplasm of Escherichia coli.* Microb. Cell. Fact., 2005. **4**.

206. Rozkov, A., et al., *Cost-effective production of labeled recombinant proteins in E. coli using minimal medium.* Microbial Cell Factories, 2006. **5**(Suppl 1): p. P44.

207. Turjanski, A.G., et al., *NMR and molecular dynamics studies of the interaction of melatonin with calmodulin.* Protein Sci., 2004. **13**(11): p. 2925-2938.

208. Tapaneeyakorn, S., et al., *Heterologous high yield expression and purification of neurotensin and its functional fragment in Escherichia coli.* Protein Expression Purif., 2010. **74**(1): p. 65-68.

209. Moon, W.J., et al., *Recombinant expression, isotope labeling, refolding, and purification of an antimicrobial peptide, piscidin.* Protein Expression Purif., 2007. **51**(2): p. 141-146.

210. Notani, J., et al., *High-level expression and efficient purification of recombinant somatostatin in Escherichia coli.* Biotechnol. Progr., 1989. **5**(1): p. 40-45.

211. Itakura, K., et al., *Expression in Escherichia coli of a chemically synthesized gene for the hormone somatostatin.* Science, 1977. **198**(4321): p. 1056-1063.

212. Canosi, U., et al., *Genetic expression of somatostatin as hybrid polypeptide.* 1993, Ist Farmacologico Serono Spa (Istf). p. 21.

213. Jakubowski, H. and Goldman, E., *Editing of errors in selection of amino acids for protein synthesis.* Microbiol. Rev., 1992. **56**(3): p. 412-429.

214. Calderone, T.L., Stevens, R.D., and Oas, T.G., *High-level misincorporation of lysine for arginine at AGA codons in a fusion protein expressed in Escherichia coli.* J. Mol. Biol., 1996. **262**(4): p. 407-412.

215. Goldman, E., et al., *Consecutive low-usage leucine codons block translation only when near the 5´ end of a message in Escherichia coli.* J. Mol. Biol., 1995. **245**(5): p. 467-473.

216.   McNulty, D.E., et al., *Mistranslational errors associated with the rare arginine codon CGG in Escherichia coli.* Protein Expression Purif., 2003. **27**(2): p. 365-374.

217.   Kawe, M., Horn, U., and Plückthun, A., *Facile promoter deletion in Escherichia coli in response to leaky expression of very robust and benign proteins from common expression vectors.* Microbial Cell Factories, 2009. **8**.

218.   Ferrer-Miralles, N., et al., *Microbial factories for recombinant pharmaceuticals.* Microbial Cell Factories, 2009. **8**.

219.   Rapley, R., *Recombinant DNA technology*, in *Molecular biology and biotechnology.* 2000, Royal Society of Chemistry {a} , Thomas Graham House, Science Park: Cambridge. p. 67-123.

220.   Hartley, J.L., *Cloning technologies for protein expression and purification.* Curr. Opin. Biotechnol., 2006. **17**(4): p. 359-366.

221.   Tu, G.F., et al., *C-terminal extension of truncated recombinant proteins in Escherichia coli with a 10Sa RNA decapeptide.* J. Biol. Chem., 1995. **270**(16): p. 9322-9326.

222.   de Valdivia, E.I.G. and Isaksson, L.A., *Abortive translation caused by peptidyl-tRNA drop-off at NGG codons in the early coding region of mRNA.* FEBS J., 2005. **272**(20): p. 5306-5316.

223.   Martin, S.L., Vrhovski, B., and Weiss, A.S., *Total synthesis and expression in Escherichia coli of a gene encoding human tropoelastin.* Gene, 1995. **154**(2): p. 159-66.

224.   Sanchez, J.C., et al., *Elimination of an $_{Hu}IFN_{\alpha\ 2b}$ readthrough species, produced in Escherichia coli, by replacing its natural translational stop signal.* J. Biotechnol., 1998. **63**(3): p. 179-186.

225.   Sipley, J. and Goldman, E., *Increased ribosomal accuracy increases a programmed translational frameshift in Escherichia coli.* Proc. Natl. Acad. Sci. U. S. A., 1993. **90**(6): p. 2315-2319.

226.   Spanjaard, R.A. and Vanduin, J., *Translation of the sequence AGG-AGG yields 50% ribosomal frameshift.* Proc. Natl. Acad. Sci. U. S. A., 1988. **85**(21): p. 7967-7971.

227.   Esipov, R.S., et al., *Production of thymosin α I via non-enzymatic acetylation of the recombinant precursor.* Biotechnol. Appl. Biochem., 2010. **56**: p. 17-25.

228.   Sambrook, J. and Russel, D.W., *Molecular cloning: a laboratory manual.* Vol. 3. 2001, New York: Cold Spring Harbor Laboratory Press, Cold Spring Harbor. 1954.

229.   Kapust, R.B., et al., *The P1' specificity of tobacco etch virus protease.* Biochem. Biophys. Res. Commun., 2002. **294**(5): p. 949-955.

230.   Poole, E.S., Brown, C.M., and Tate, W.P., *The identity of the base following the stop codon determines the efficiency of in vivo translational termination in Escherichia coli.* EMBO J., 1995. **14**(1): p. 151-158.

231.   Perkins, D.N., et al., *Probability-based protein identification by searching sequence databases using mass spectrometry data.* Electrophoresis, 1999. **20**(18): p. 3551-3567.

232.   Edman, P. and Begg, G., *A protein sequenator.* Eur. J. Biochem., 1967. **1**(1): p. 80-91.

233.   Novagen, *TB122VM pET-32a-c(+) Vector Map.* 1998.

234.   Covalt, J.C., et al., *Temperature, media, and point of induction affect the N-terminal processing of interleukin-1β.* Protein Expression Purif., 2005. **41**(1): p. 45-52.

235.   Novagen, *TB055 pET System Manual.* 2003.

236.   Invitrogen, *One Shot® BL21(DE3), One Shot® BL21(DE3)pLysS, One Shot® BL21(DE3)pLysE Competent cells.* 2010.

237.   Zwietering, M.H., et al., *Modeling of the bacterial growth curve.* Appl. Environ. Microbiol., 1990. **56**(6): p. 1875-1881.

238.   Rivier, J., et al., *Somatostatin analogs. Relative importance of the disulfide bridge and of the Ala-Gly side chain for biological activity.* J. Med. Chem., 1975. **18**(2): p. 123-126.

239.   de Marco, A., *Strategies for successful recombinant expression of disulfide bond-dependent proteins in Escherichia coli.* Microbial Cell Factories, 2009. **8**.

240.   Rivier, J., *Somatostatin. Total solid phase synthesis.* J. Am. Chem. Soc., 1974. **96**(9): p. 2986-2992.

241.   Chen, L., Annis, I., and Barany, G., *Disulfide bond formation in peptides*, in *Current Protocols in Protein Science.* 2001, John Wiley & Sons, Inc.

242.   Brazeau, P., et al., *Hypothalamic polypeptide that inhibits secretion of immunoreactive pituitary growth hormone.* Science, 1973. **179**(4068): p. 77-79.

243.   Fletcher, D.J., et al., *Characterization of the conversion of a somatostatin precursor to somatostatin by islet secretory granules.* Diabetes, 1980. **29**(8): p. 593-599.

244.   Noe, B.D., Debo, G., and Spiess, J., *Comparison of prohormone-processing activities in islet microsomes and secretory granules: evidence for distinct converting enzymes for separate islet prosomatostatins.* J. Cell Biol., 1984. **99**(2): p. 578-587.

245.   Patel, Y.C., *General aspects of the biology and function of somatostatin*, in *Somatostatin.* 1992, Springer Berlin Heidelberg. p. 1-16.

246. van Grondelle, W., et al., *Spontaneous fibrillation of the native neuropeptide hormone somatostatin-14*. J. Struct. Biol., 2007. **160**(2): p. 211-223.

247. van Grondelle, W., et al., *Lamination and spherulite-like compaction of a hormone's native amyloid-like nanofibrils: spectroscopic insights into key interactions*. Faraday Discuss., 2013. **166**: p. 163-180.

248. Lieu, V.H., et al., *Inhibition of amyloid fibrillization of hen egg-white lysozymes by rifampicin and p-benzoquinone*. Biotechnol. Progr., 2007. **23**(3): p. 698-706.

249. Sluzky, V., et al., *Kinetics of insulin aggregation in aqueous solutions upon agitation in the presence of hydrophobic surfaces*. Proc. Natl. Acad. Sci. U. S. A., 1991. **88**(21): p. 9377-9381.

250. Behrens, S.H. and Grier, D.G., *The charge of glass and silica surfaces*. J. Chem. Phys., 2001. **115**(14): p. 6716-6721.

251. Wasmer, C., et al., *Amyloid fibrils of the HET-s(218-289) prion form a β solenoid with a triangular hydrophobic core*. Science, 2008. **319**(5869): p. 1523-1526.

252. Heise, H., et al., *Molecular-level secondary structure, polymorphism, and dynamics of full-length α-synuclein fibrils studied by solid-state NMR*. Proc. Natl. Acad. Sci. U. S. A., 2005. **102**(44): p. 15871-15876.

253. Takegoshi, K., Nakamura, S., and Terao, T., *^{13}C-^{1}H dipolar-assisted rotational resonance in magic-angle spinning NMR*. Chem. Phys. Lett., 2001. **344**(5-6): p. 631-637.

254. Wishart, D.S. and Sykes, B.D., *The ^{13}C chemical-shift index: a simple method for the identification of protein secondary structure using ^{13}C chemical-shift data*. J. Biomol. NMR, 1994. **4**(2): p. 171-180.

255. Wishart, D.S. and Sykes, B.D., *Chemical shifts as a tool for structure determination*. Nuclear Magnetic Resonance, Pt C, 1994. **239**: p. 363-392.

256. Schuetz, A., et al., *Protocols for the sequential solid-state NMR spectroscopic assignment of a uniformly labeled 25 kDa protein: HET-s(1-227)*. ChemBioChem, 2010. **11**(11): p. 1543-1551.

257. Wang, Y.J. and Jardetzky, O., *Probability-based protein secondary structure identification using combined NMR chemical-shift data*. Protein Sci., 2002. **11**(4): p. 852-861.

258. Ippel, J.H., et al., *Probing solvent accessibility of amyloid fibrils by solution NMR spectroscopy*. Proc. Natl. Acad. Sci. U. S. A., 2002. **99**(13): p. 8648-8653.

259. Hosaka, M. and Watanabe, T., *Secretogranin III: a bridge between core hormone aggregates and the secretory granule membrane*. Endocr. J., 2010. **57**(4): p. 275-286.

260. Balabin, R.M., *Enthalpy difference between conformations of normal alkanes: Raman spectroscopy study of n-pentane and n-butane*. J. Phys. Chem. A, 2009. **113**(6): p. 1012-1019.

261. Savitzky, A. and Golay, M.J.E., *Smoothing and differentiation of data by simplified least squares procedures*. Anal. Chem., 1964. **36**(8): p. 1627-1639.

262. Dalayeun, J.F., Nores, J.M., and Bergal, S., *Physiology of β-endorphins. A close-up view and a review of the literature*. Biomed. Pharmacother., 1993. **47**(8): p. 311-320.

263. Li, C.H. and Chung, D., *Isolation and structure of an untriakontapeptide with opiate activity from camel pituitary glands*. Proc. Natl. Acad. Sci. U. S. A., 1976. **73**(4): p. 1145-1148.

264. Goldstein, A. and Lowery, P.J., *Effect of opiate antagonist naloxone on body temperature in rats*. Life Sci., 1975. **17**(6): p. 927-931.

265. Chretien, M., Seidah, N.G., and Scherrer, H., *Endorphins: structure, roles and biogenesis*. Can. J. Physiol. Pharmacol., 1981. **59**(5): p. 413-431.

266. Benjannet, S., et al., *PC1 and PC2 are proprotein convertases capable of cleaving proopiomelanocortin at distinct pairs of basic residues*. Proc. Natl. Acad. Sci. U. S. A., 1991. **88**(9): p. 3564-3568.

267. Pritchard, L.E., Turnbull, A.V., and White, A., *Pro-opiomelanocortin processing in the hypothalamus: impact on melanocortin signalling and obesity*. J. Endocrinol., 2002. **172**(3): p. 411-421.

268. Hollosi, M., Kajtar, M., and Graf, L., *Studies on the conformation of β-endorphin and its constituent fragments in water and trifluoroethanol by CD spectroscopy*. FEBS Lett., 1977. **74**(2): p. 185-189.

269. Li, C.H., *β-Endorphin*. Cell, 1982. **31**(3): p. 504-505.

270. Falcone, C., et al., *Correlation between β-endorphin plasma levels and anginal symptoms in patients with coronary artery disease*. J. Am. Coll. Cardiol., 1988. **11**(4): p. 719-723.

271. Straub, J., et al., *Role of β-endorphins in silent form of ischemic heart disease*. Sb. Lek., 1989. **91**(1): p. 5-10.

272. Rosenblatt, J.S., Mayer, A.D., and Giordano, A.L., *Hormonal basis during pregnancy for the onset of maternal behavior in the rat*. Psychoneuroendocrinology, 1988. **13**(1-2): p. 29-46.

273. Izquierdo, I., et al., *Construction and reconstruction of memories*. Braz. J. Med. Biol. Res., 1988. **21**(1): p. 9-25.

274. Schnabel, E., Mains, R.E., and Farquhar, M.G., *Proteolytic processing of pro-ACTH/endorphin begins in the Golgi complex of pituitary corticotropes and AtT-20 cells*. Mol. Endocrinol., 1989. **3**(8): p. 1223-1235.

275. Keeler, C., Hodsdon, M.E., and Dannies, P.S., *Is there structural specificity in the reversible protein aggregates that are stored in secretory granules?* J. Mol. Neurosci., 2003. **22**(1-2): p. 43-49.

276. Gath, J., *Amyloid fibrils seen by solid-state NMR: structure, dynamics, interactions.*, in *D-CHAB*. 2013, ETH Zurich. p. 197.

277. Seuring, C., *The mechanisms of toxicity in HET-S/HET-s prion incompatibility and high-resolution solid-state NMR spectra of the natural amyloid-like storage form of β-endorphin*, in *D-CHAB*. 2012, ETH Zurich. p. 226.

278. Finkelstein, A.V. and Ptitsyn, O.B., *Part II: Elementary interactions in and around proteins. Lecture 6*, in *Protein physics: a course of lectures*. 2002, Academic Press: London. p. 57-72.

279. Lindman, S., et al., *Electrostatic contributions to residue-specific protonation equilibria and proton binding capacitance for a small protein*. Biochemistry, 2006. **45**(47): p. 13993-14002.

280. Lide, D.R. Properties of amino acids, in *CRC handbook of chemistry and physics. Internet version 2014*. Available from: http://www.hbcpnetbase.com/.

281. McIntosh, L.P., et al., *The pK_a of the general acid/base carboxyl group of a glycosidase cycles during catalysis: a ^{13}C-NMR study of Bacillus circuluns xylanase*. Biochemistry, 1996. **35**(31): p. 9958-9966.

282. Lide, D.R. Typical pH values of biological materials and foods, in *CRC handbook of chemistry and physics. Internet version 2014*. Available from: http://www.hbcpnetbase.com/.

283. McGlinchey, R.P., et al., *Probing fibril dissolution of the repeat domain of a functional amyloid, Pmel17, on the microscopic and residue level*. Biochemistry, 2011. **50**(49): p. 10567-10569.

284. Li, C.H., et al., *β-endorphin: replacement of glutamic acid in position 8 by glutamine increases analgesic potency and opiate receptor-binding activity*. Biochem. Biophys. Res. Commun., 1981. **101**(1): p. 118-123.

285. Shine, J., et al., *Expression of cloned β-endorphin gene sequences by Escherichia coli*. Nature, 1980. **285**(5765): p. 456-461.

286. Burgoyne, R.D. and Morgan, A., *Secretory granule exocytosis*. Physiol. Rev., 2003. **83**(2): p. 581-632.

287. Campioni, S., et al., *The presence of an air-water interface affects formation and elongation of α-synuclein fibrils*. J. Am. Chem. Soc., 2014. **136**(7): p. 2866-2875.

288. Fung, B.M., Khitrin, A.K., and Ermolaev, K., *An improved broadband decoupling sequence for liquid crystals and solids*. J. Magn. Reson., 2000. **142**(1): p. 97-101.

289. Madine, J., et al., *Heparin promotes the rapid fibrillization of a peptide with low intrinsic amyloidogenicity*. Biochemistry, 2013. **52**(50): p. 8984-8992.

290. Motamedi-Shad, N., Monsellier, E., and Chiti, F., *Amyloid formation by the model protein muscle acylphosphatase is accelerated by heparin and heparan sulphate through a scaffolding-based mechanism*. J. Biochem., 2009. **146**(6): p. 805-814.

291. Ranganathan, S., et al., *Molecular interpretation of ACTH-β-endorphin coaggregation: relevance to secretory granule biogenesis*. PLoS One, 2012. **7**(3): p. 12.

292. Schmidt, R.F., Lang, F., and Heckmann, M., *Physiologie Des Menschen: Mit Pathophysiologie*. 2005: Springer London, Limited.

293. *Fenestrated capillary*, in *Functional Ultrastructure*. 2005, Springer Vienna. p. 232-233.

294. Kleine, B. and Rossmanith, W.G., *Hormone und hormonsystem*. 2010: Springer.

295. Macchi, F., et al., *The effect of osmolytes on protein fibrillation*. International Journal of Molecular Sciences, 2012. **13**(3): p. 3801-3819.

296. Nayak, A., et al., *Osmolyte controlled fibrillation kinetics of insulin: new insight into fibrillation using the preferential exclusion principle*. Biotechnol. Progr., 2009. **25**(5): p. 1508-1514.

297. Fung, J., Darabie, A.A., and McLaurin, J., *Contribution of simple saccharides to the stabilization of amyloid structure*. Biochem. Biophys. Res. Commun., 2005. **328**(4): p. 1067-1072.

298. Arora, A., Ha, C., and Park, C.B., *Inhibition of insulin amyloid formation by small stress molecules*. FEBS Lett., 2004. **564**(1-2): p. 121-125.

299. McIlvaine, T.C., *A buffer solution for colorimetric comparison*. J. Biol. Chem., 1921. **49**(1): p. 183-186.

300. de Groot, N.S., et al., *Ile-Phe dipeptide self-assembly: clues to amyloid formation*. Biophys. J., 2007. **92**(5): p. 1732-1741.

301.   Pedersen, J.S., et al., *Sulfates dramatically stabilize a salt-dependent type of glucagon fibrils.* Biophys. J., 2006. **90**(11): p. 4181-4194.

302.   Duim, W.C., et al., *Sub-diffraction imaging of huntingtin protein aggregates by fluorescence blink-microscopy and atomic force microscopy.* Chemphyschem, 2011. **12**(13): p. 2386-2389.

303.   Ries, J., et al., *Superresolution imaging of amyloid fibrils with binding-activated probes.* ACS Chem. Neurosci., 2013. **4**(7): p. 1057-1061.

304.   Heilemann, M., et al., *Subdiffraction-resolution fluorescence imaging with conventional fluorescent probes.* Angew. Chem.-Int. Edit., 2008. **47**(33): p. 6172-6176.

305.   Schierle, G.S.K., et al., *In situ measurements of the formation and morphology of intracellular β-amyloid fibrils by super-resolution fluorescence imaging.* J. Am. Chem. Soc., 2011. **133**(33): p. 12902-12905.

306.   Pinotsi, D., et al., *Localization microscopy for the study of amyloid fibril formation*, in *Nanoimaging and Nanospectroscopy*, P. Verma and A. Egner, Editors. 2013.

307.   Roberti, M.J., et al., *Imaging nanometer-sized α-synuclein aggregates by superresolution fluorescence localization microscopy.* Biophys. J., 2012. **102**(7): p. 1598-1607.

308.   Rust, M.J., Bates, M., and Zhuang, X., *Sub-diffraction-limit imaging by stochastic optical reconstruction microscopy (STORM).* Nat. Methods, 2006. **3**(10): p. 793-795.

309.   Thompson, M.A., Lew, M.D., and Moerner, W.E., *Extending microscopic resolution with single-molecule imaging and active control.* Annual Review of Biophysics, Vol 41, 2012. **41**: p. 321-342.

310.   *IsoPro 3.1*. Available from: https://sites.google.com/site/isoproms/home.

A. Abbreviations

1D, 2D, 3D	one-dimensional, two-dimensional, three-dimensional
ACTH	adrenocorticotropic hormone
CD	circular dichroism
CMC	critical micelle concentration
CP	citrate-phosphate buffer
cps	counts per second
CR	Congo red
CRF	corticotropin-releasing factor
Da	dalton (atomic mass unit)
DARR	dipolar assisted rotational resonance
DMSO	dimethyl sulfoxide
DTT	1,4-dithio-D-threitol
E. coli	*Escherichia coli*
EDTA	ethylenediaminetetraacetic acid
ER	endoplasmic reticulum
ESI	electrospray ionization
FRET	Förster resonance energy transfer/fluorescence resonance energy transfer
GAG	glycosaminoglycan
GC	Golgi complex, Golgi apparatus
HDX	hydrogen-deuterium exchange
HMQC	heteronuclear multiple-quantum correlation spectroscopy
hnRNP	heterogeneous nuclear ribonucleoprotein
HPA axis	hypothalamic-pituitary-adrenal axis
HPLC	high-performance liquid chromatography
IPTG	isopropyl β-D-1-thiogalactopyranoside
IR	infrared spectroscopy
LB	lysogeny broth (Luria broth)
LC	liquid chromatography

LCP	luminescent conjugated probe
LMW	low-molecular-weight
m/z	mass-to-charge ratio
MALDI	matrix-assisted laser desorption/ionization
MBP	maltose-binding protein
MPL	mass-per-length
MS	mass spectrometry
NMR	nuclear magnetic resonance
PAGE	polyacrylamide gel electrophoresis
PBS	phosphate buffered saline
pI	isoelectric point
PMSF	phenylmethylsulfonyl fluoride
POMC	pro-opiomelanocortin
ppm	parts per million
Q-TOF	quadrupole-time-of-flight mass spectrometer
rER	rough endoplasmic reticulum
RP	reversed phase
rpm	revolutions per minute
SDS	sodium dodecyl sulfate
SS14	somatostatin 14
ssNMR	solid-state nuclear magnetic resonance
TEV-protease	tobacco etch virus nuclear inclusion a endopeptidase
TFA	2,2,2-trifluoroethanoic acid
TGN	*trans*-Golgi network
TOF	time-of-flight analyzer
Tris	2-amino-2-hydroxymethyl-propane-1,3-diol
TROSY	transverse relaxation optimized spectroscopy
UV	ultraviolet
WT	wild-type
XAS	X-ray absorption spectroscopy

B. Supplementary tables and figures

```
ATGAGCGATAAAATTATTCACCTGACTGACGACAGTTTTGACACGGATGTACTCAAAGCG
M   S   D   K   I   I   H   L   T   D   D   S   F   D   T   D   V   L   K   A
GACGGGGCGATCCTCGTCGATTTCTGGGCAGAGTGGTGCGGTCCGTGCAAAATGATCGCC
D   G   A   I   L   V   D   F   W   A   E   W   C   G   P   C   K   M   I   A
CCGATTCTGGATGAAATCGCTGACGAATATCAGGGCAAACTGACCGTTGCAAAACTGAAC
P   I   L   D   E   I   A   D   E   Y   Q   G   K   L   T   V   A   K   L   N
ATCGATCAAAACCCTGGCACTGCGCCGAAATATGGCATCCGTGGTATCCCGACTCTGCTG
I   D   Q   N   P   G   T   A   P   K   Y   G   I   R   G   I   P   T   L   L
CTGTTCAAAAACGGTGAAGTGGCGGCAACCAAAGTGGGTGCACTGTCTAAAGGTCAGTTG
L   F   K   N   G   E   V   A   A   T   K   V   G   A   L   S   K   G   Q   L
AAAGAGTTCCTCGACGCTAACCTGGCCGGTTCTGGTTCTGGCCATATGCACCATCATCAT
K   E   F   L   D   A   N   L   A   G   S   G   S   G   H   M   H   H   H   H
CATCATTCTTCTGGTCTGGTGCCACGCGGTTCTGGTATGAAAGAAACCGCTGCTGCTAAA
H   H   S   S   G   L   V   P   R   G   S   G   M   K   E   T   A   A   A   K
TTCGAACGCCAGCACATGGACAGCCCAGATCTGGGTACCGACGACGACGACAAGGCCATG
F   E   R   Q   H   M   D   S   P   D   L   G   T   D   D   D   D   K   A   M
GCTGATATCGGATCCGAAAACCTGTATTTTCAGAGCGAAGAACCTCCGATTAGCCTGGAT
A   D   I   G   S   E   N   L   Y   F   Q   S   E   E   P   P   I   S   L   D
CTGACCTTTCATCTGCTGCGTGAAGTTCTGGAAATGGCACGTGCAGAACAGCTGGCACAG
L   T   F   H   L   L   R   E   V   L   E   M   A   R   A   E   Q   L   A   Q
CAGGCACATAGCAATCGTAAACTGATGGAAATTATTGGCTGAAAGCTTGCGGCCGCACTC
Q   A   H   S   N   R   K   L   M   E   I   I   G   *   K   L   A   A   A   L
GAGCACCACCACCACCACCACTGA
E   H   H   H   H   H   H   *
```

Figure S1. Nucleotide and amino acid sequence of the THX-CRF-G fusion protein. The displayed sequence contains also a segment of the downstream plasmid sequence. The 6His-tag is highlighted in green; the TEV-protease recognition site is highlighted in purple, and the sequence of CRF-G is in yellow. Shown DNA sequence was confirmed by DNA sequencing.
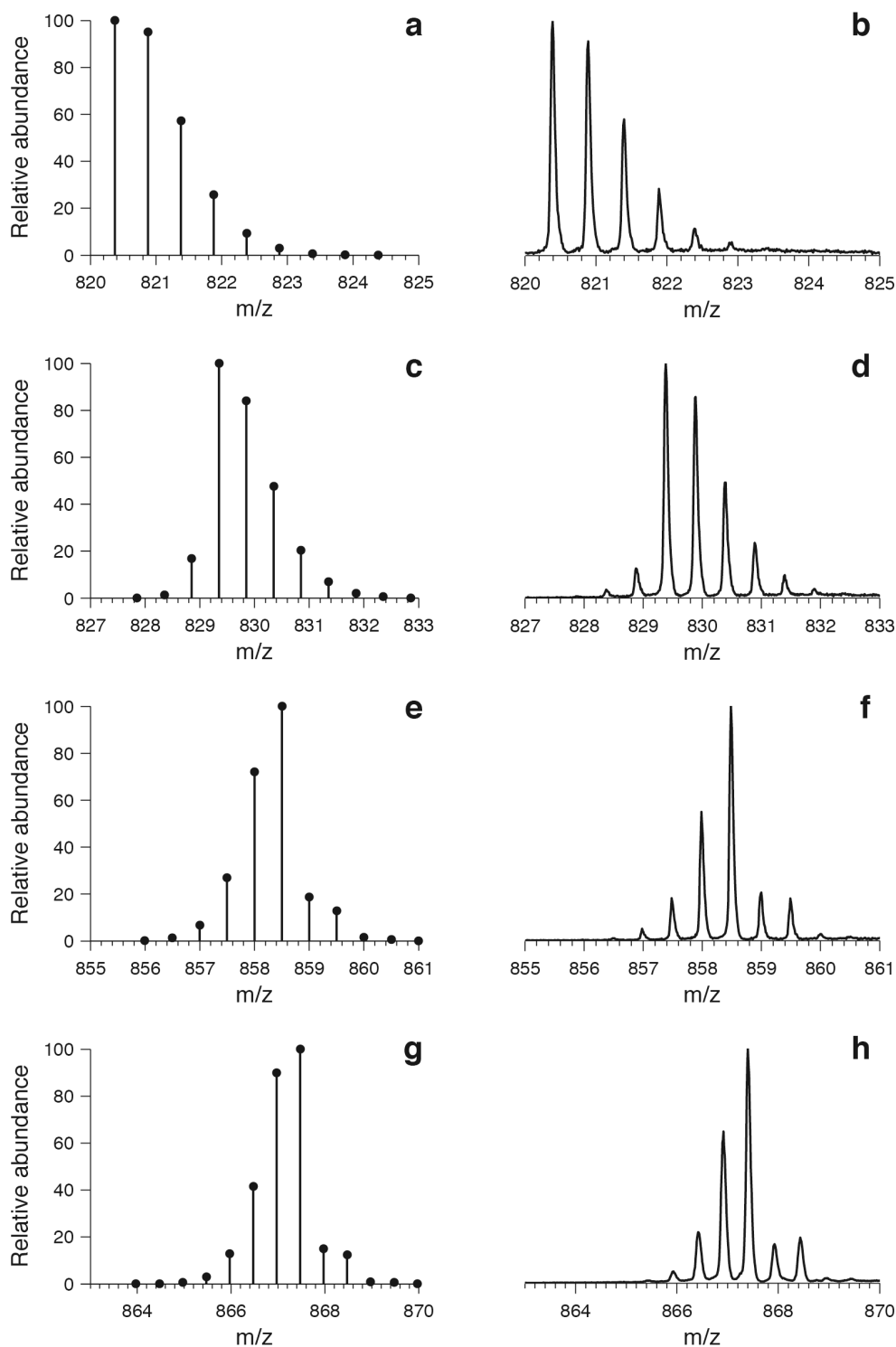
Figure S2. Analysis of ^{13}C and ^{15}N enrichment in ^{13}C, ^{15}N-labeled SS14 by high-resolution ESI-MS. Theoretically calculated (left panels: **a**, **c**, **e**, **g**) and corresponding experimental (right panels: **b**, **d**, **f**, **h**) isotopic distributions of SS14 with various stable isotope abundances are compared. The MS peaks on the left were simulated by IsoPro 3.1 software [310] for the following isotopic abundances: (**a**) natural abundance, (**c**) 99 % ^{15}N-enriched, (**e**) 99 % ^{13}C-enriched, (**g**) 99 % ^{13}C- and ^{15}N-enriched. On the right, the region of experimentally measured ESI-MS spectra corresponding to the signal of doubly charged [SS+2H]$^{2+}$ ion of SS14 is shown for the natural abundance (**b**), ^{15}N-labeled (**d**), ^{13}C-labeled (**f**), and ^{13}C, ^{15}N-labeled (**h**) samples.

Table S1

Fragment ions identified in ESI-CID-MS/MS spectra of the 5.5 kDa peptide

ion	slice	*m/z*	z	sequence	error, ppm
				precursor ion *m/z* 1105.3 (5+)	
b4	[1-4]	360.17	1	.AGCK.n	-5
b5-NH₃	[1-5]	457.1864	1	.AGCKN.f	5
b5	[1-5]	474.2129	1	.AGCKN.f	-0.7
b6	[1-6]	621.2813	1	.AGCKNF.f	2.6
b6-NH₃	[1-6]	604.2548	1	.AGCKNF.f	8.2
b7	[1-7]	768.3498	1	.AGCKNFF.g	2.2
b7-NH₃	[1-7]	751.3232	1	.AGCKNFF.g	4.3
b8	[1-8]	825.3712	1	.AGCKNFFG.k	2.2
b8-NH₃	[1-8]	808.3447	1	.AGCKNFFG.k	7.4
b9-NH₃	[1-9]	936.4396	1	.AGCKNFFGK.p	23.2
b9	[1-9]	953.4662	1	.AGCKNFFGK.p	0
b11	[1-11]	1163.603	1	.AGCKNFFGKPL.p	6.8
b14	[1-14]	1402.73	1	.AGCKNFFGKPLPAA.e	32.3
b15	[1-15]	1531.7726	1	.AGCKNFFGKPLPAAE.s	11.6
b16	[1-16]	1618.8046	1	.AGCKNFFGKPLPAAES.l	49.5
b16-H₂O	[1-16]	1600.7941	1	.AGCKNFFGKPLPAAES.l	-13.1
b17	[1-17]	1731.8887	1	.AGCKNFFGKPLPAAESL.r	16.1
b18	[1-18]	1887.9898	1	.AGCKNFFGKPLPAAESLR.p	16.6
b18-NH₃	[1-18]	1870.9633	1	.AGCKNFFGKPLPAAESLR.p	-11.9
b9	[1-9]	477.2367	2	.AGCKNFFGK.p	-17.2
b10	[1-10]	525.7631	2	.AGCKNFFGKP.l	2
b11-NH₃	[1-11]	573.7919	2	.AGCKNFFGKPL.p	10.5
b11	[1-11]	582.3051	2	.AGCKNFFGKPL.p	-3.8
b12	[1-12]	630.8315	2	.AGCKNFFGKPLP.a	28.1
b13	[1-13]	666.3501	2	.AGCKNFFGKPLPA.a	-17
b18-NH₃	[1-18]	935.9853	2	.AGCKNFFGKPLPAAESLR.p	16.3
b18	[1-18]	944.4985	2	.AGCKNFFGKPLPAAESLR.p	-6.4
b18-H₂O	[1-18]	935.4933	2	.AGCKNFFGKPLPAAESLR.p	-10.5
b29	[1-29]	1516.2507	2	.AGCKNFFGKPLPAAESLRPHSSTTTTTTE.i	7.4
b37	[1-37]	1328.0334	3	.AGCKNFFGKPLPAAESLRPHSSTTTTTTTEIRLLTKPE.r	16.9
b44	[1-44]	1626.8866	3	.AGCKNFFGKPLPAAESLRPHSSTTTTTTTEIRLLTKPERKLSWLL.p	18.5
b40	[1-40]	1095.5969	4	.AGCKNFFGKPLPAAESLRPHSSTTTTTTTEIRLLTKPERKL.s	-10
b43-NH₃	[1-43]	1187.8891	4	.AGCKNFFGKPLPAAESLRPHSSTTTTTTTEIRLLTKPERKLSWL.l	-31.4
b44	[1-44]	1220.4167	4	.AGCKNFFGKPLPAAESLRPHSSTTTTTTTEIRLLTKPERKLSWLL.p	18
b47	[1-47]	1297.2141	4	.AGCKNFFGKPLPAAESLRPHSSTTTTTTTEIRLLTKPERKLSWLLPPL.s	-6.3
b48-H₂O	[1-48]	1314.4695	4	.AGCKNFFGKPLPAAESLRPHSSTTTTTTTEIRLLTKPERKLSWLLPPLS.n	-4.4
b48	[1-48]	1318.9721	4	.AGCKNFFGKPLPAAESLRPHSSTTTTTTTEIRLLTKPERKLSWLLPPLS.n	-24.7
b48-NH₃	[1-48]	1314.7155	4	.AGCKNFFGKPLPAAESLRPHSSTTTTTTTEIRLLTKPERKLSWLLPPLS.n	40.2
a5-NH₃	[1-5]	429.1915	1	.AGCKN.f	17
a5	[1-5]	446.218	1	.AGCKN.f	20.7
a6	[1-6]	593.2864	1	.AGCKNF.f	-0.2
a6-NH₃	[1-6]	576.2599	1	.AGCKNF.f	11.8
a7	[1-7]	740.3548	1	.AGCKNFF.g	6.5
a7-NH₃	[1-7]	723.3283	1	.AGCKNFF.g	10
a8	[1-8]	797.3763	1	.AGCKNFFG.k	8.5
a8-NH₃	[1-8]	780.3498	1	.AGCKNFFG.k	3.3
a11	[1-11]	568.3077	2	.AGCKNFFGKPL.p	3.8
a42	[1-42]	1156.876	4	.AGCKNFFGKPLPAAESLRPHSSTTTTTTTEIRLLTKPERKLSW.l	10.2
y15	[36-50]	1763.9803	1	k.PERKLSWLLPPLSNN.	8.6
y7-NH₃	[44-50]	737.3828	1	l.LPPLSNN.	4.3
y7	[44-50]	754.4094	1	l.LPPLSNN.	3.1
y7-H₂O	[44-50]	736.3988	1	l.LPPLSNN.	-11.1
y6-NH₃	[45-50]	624.2988	1	l.PPLSNN.	0

ion	slice	*m/z*	z	sequence	error, ppm
y6-H₂O	[45-50]	623.3148	1	l.PPLSNN.	-14.9
y6	[45-50]	641.3253	1	l.PPLSNN.	-1
y5-NH₃	[46-50]	527.246	1	p.PLSNN.	33.7
y5	[46-50]	544.2726	1	p.PLSNN.	3.8
y5-H₂O	[46-50]	526.262	1	p.PLSNN.	4.6
y4	[47-50]	447.2198	1	p.LSNN.	12.4
y4-H₂O	[47-50]	429.2092	1	p.LSNN.	-24.4
y4-NH₃	[47-50]	430.1932	1	p.LSNN.	41.4
y3-H₂O	[48-50]	316.1252	1	l.SNN.	-18.4
y3-NH₃	[48-50]	317.1092	1	l.SNN.	-13.1
y3	[48-50]	334.1357	1	l.SNN.	-12
y2-NH₃	[49-50]	230.0771	1	s.NN.	-37.4
y2	[49-50]	247.1037	1	s.NN.	-28.9
y15	[36-50]	882.4938	2	k.PERKLSWLLPPLSNN.	-39.1
y43	[8-50]	1584.5451	3	f.GKPLPAAESLRPHSSTTTTTTEIRLLTKPERKLSWLLPPLSNN.	9.9
y41	[10-50]	1522.8396	3	k.PLPAAESLRPHSSTTTTTTEIRLLTKPERKLSWLLPPLSNN.	18.2
y39-NH₃	[12-50]	1447.1185	3	l.PAAESLRPHSSTTTTTTEIRLLTKPERKLSWLLPPLSNN.	9.6
y39	[12-50]	1452.794	3	l.PAAESLRPHSSTTTTTTEIRLLTKPERKLSWLLPPLSNN.	-7.2
y38-NH₃	[13-50]	1414.7675	3	p.AAESLRPHSSTTTTTTEIRLLTKPERKLSWLLPPLSNN.	3
y38	[13-50]	1420.4431	3	p.AAESLRPHSSTTTTTTEIRLLTKPERKLSWLLPPLSNN.	11.9
y38-H₂O	[13-50]	1414.4395	3	p.AAESLRPHSSTTTTTTEIRLLTKPERKLSWLLPPLSNN.	-24
y41	[10-50]	1142.3815	4	k.PLPAAESLRPHSSTTTTTTEIRLLTKPERKLSWLLPPLSNN.	4

precursor ion *m/z* 1380.8 (4+)

ion	slice	*m/z*	z	sequence	error, ppm
a3	[1-3]	204.0801	1	.AGC.k	10.1
a4	[1-4]	332.1751	1	.AGCK.n	-45
b4	[1-4]	360.17	1	.AGCK.n	-10
a5	[1-5]	446.218	1	.AGCKN.f	-10.5
b5-NH₃	[1-5]	457.1864	1	.AGCKN.f	-1.7
a5-NH₃	[1-5]	429.1915	1	.AGCKN.f	3.2
b5	[1-5]	474.2129	1	.AGCKN.f	-10.5
a6-NH₃	[1-6]	576.2599	1	.AGCKNF.f	-8.5
a6	[1-6]	593.2864	1	.AGCKNF.f	-11.5
b6-NH₃	[1-6]	604.2548	1	.AGCKNF.f	-7.4
b6	[1-6]	621.2813	1	.AGCKNF.f	-11.9
b7	[1-7]	768.3498	1	.AGCKNFF.g	-10.5
b7-NH₃	[1-7]	751.3232	1	.AGCKNFF.g	-2.9
a7-NH₃	[1-7]	723.3283	1	.AGCKNFF.g	1
a7	[1-7]	740.3548	1	.AGCKNFF.g	-9.2
a8	[1-8]	797.3763	1	.AGCKNFFG.k	22.6
b8-NH₃	[1-8]	808.3447	1	.AGCKNFFG.k	-0.8
b8	[1-8]	825.3712	1	.AGCKNFFG.k	-3.5
a8-NH₃	[1-8]	780.3498	1	.AGCKNFFG.k	9.8
b9-NH₃	[1-9]	936.4396	1	.AGCKNFFGK.p	22.3
b9	[1-9]	953.4662	1	.AGCKNFFGK.p	-10.4
a9	[1-9]	925.4713	1	.AGCKNFFGK.p	36.8
a9-NH₃	[1-9]	908.4447	1	.AGCKNFFGK.p	38.6
b10	[1-10]	1050.5189	1	.AGCKNFFGKP.l	-7.2
b10-NH₃	[1-10]	1033.4924	1	.AGCKNFFGKP.l	24.8
a10-NH₃	[1-10]	1005.4975	1	.AGCKNFFGKP.l	6.4
a10	[1-10]	1022.524	1	.AGCKNFFGKP.l	6.9
a11	[1-11]	1135.6081	1	.AGCKNFFGKPL.p	-9.1
a11-NH₃	[1-11]	1118.5815	1	.AGCKNFFGKPL.p	-3.6
b11	[1-11]	1163.603	1	.AGCKNFFGKPL.p	-6.3
b11-NH₃	[1-11]	1146.5765	1	.AGCKNFFGKPL.p	-1.8
a12-NH₃	[1-12]	1215.6343	1	.AGCKNFFGKPLP.a	30.8
b12	[1-12]	1260.6558	1	.AGCKNFFGKPLP.a	13.2
a12	[1-12]	1232.6609	1	.AGCKNFFGKPLP.a	5
b12-NH₃	[1-12]	1243.6292	1	.AGCKNFFGKPLP.a	30.8

ion	slice	_m/z_	_z_	sequence	error, ppm
b13-NH₃	[1-13]	1314.6663	1	.AGCKNFFGKPLPA.a	38.9
b13	[1-13]	1331.6929	1	.AGCKNFFGKPLPA.a	5.7
a13	[1-13]	1303.698	1	.AGCKNFFGKPLPA.a	-1.5
a13-NH₃	[1-13]	1286.6714	1	.AGCKNFFGKPLPA.a	35.3
b14	[1-14]	1402.73	1	.AGCKNFFGKPLPAA.e	23
a15	[1-15]	1503.7777	1	.AGCKNFFGKPLPAAE.s	11.2
b15	[1-15]	1531.7726	1	.AGCKNFFGKPLPAAE.s	7.8
a16	[1-16]	1590.8097	1	.AGCKNFFGKPLPAAES.l	26.7
a16-NH₃	[1-16]	1573.7832	1	.AGCKNFFGKPLPAAES.l	40.7
a16-H₂O	[1-16]	1572.7991	1	.AGCKNFFGKPLPAAES.l	42.2
b16	[1-16]	1618.8046	1	.AGCKNFFGKPLPAAES.l	40.2
a17	[1-17]	1703.8938	1	.AGCKNFFGKPLPAAESL.r	20.3
b18	[1-18]	944.4985	2	.AGCKNFFGKPLPAAESLR.p	-15.1
b18-NH₃	[1-18]	1870.9633	1	.AGCKNFFGKPLPAAESLR.p	4.4
b18	[1-18]	1887.9898	1	.AGCKNFFGKPLPAAESLR.p	11.9
a18-H₂O	[1-18]	1841.9843	1	.AGCKNFFGKPLPAAESLR.p	4.3
a18-NH₃	[1-18]	1842.9683	1	.AGCKNFFGKPLPAAESLR.p	8.7
b18-H₂O	[1-18]	1869.9792	1	.AGCKNFFGKPLPAAESLR.p	-14.8
a18	[1-18]	1859.9949	1	.AGCKNFFGKPLPAAESLR.p	23.9
b20	[1-20]	1061.5544	2	.AGCKNFFGKPLPAAESLRPH.s	-11.8
b21-NH₃	[1-21]	2192.107	1	.AGCKNFFGKPLPAAESLRPHS.s	20.9
a21-NH₃	[1-21]	2164.112	1	.AGCKNFFGKPLPAAESLRPHS.s	26.2
b21	[1-21]	2209.1335	1	.AGCKNFFGKPLPAAESLRPHS.s	26.7
a21-H₂O	[1-21]	2163.128	1	.AGCKNFFGKPLPAAESLRPHS.s	13.3
a21	[1-21]	2181.1386	1	.AGCKNFFGKPLPAAESLRPHS.s	34.4
b21-NH₃	[1-21]	1096.5571	2	.AGCKNFFGKPLPAAESLRPHS.s	33
b21	[1-21]	1105.0704	2	.AGCKNFFGKPLPAAESLRPHS.s	45.1
y35	[16-50]	1330.0708	3	e.SLRPHSSTTTTTTEIRLLTKPERKLSWLLPPLSNN.	18.7
y34-H₂O	[17-50]	1942.0813	2	s.LRPHSSTTTTTTEIRLLTKPERKLSWLLPPLSNN.	1
y34-NH₃	[17-50]	1942.5733	2	s.LRPHSSTTTTTTEIRLLTKPERKLSWLLPPLSNN.	6.9
y33-H₂O	[18-50]	1885.5392	2	l.RPHSSTTTTTTEIRLLTKPERKLSWLLPPLSNN.	0.6
y33-NH₃	[18-50]	1886.0312	2	l.RPHSSTTTTTTEIRLLTKPERKLSWLLPPLSNN.	2.9
y32-NH₃	[19-50]	1807.9807	2	r.PHSSTTTTTTEIRLLTKPERKLSWLLPPLSNN.	1.5
y32	[19-50]	1816.4939	2	r.PHSSTTTTTTEIRLLTKPERKLSWLLPPLSNN.	-1.1
y31-NH₃	[20-50]	1759.4543	2	p.HSSTTTTTTEIRLLTKPERKLSWLLPPLSNN.	16.3
y31-H₂O	[20-50]	1758.9623	2	p.HSSTTTTTTEIRLLTKPERKLSWLLPPLSNN.	1
y30-NH₃	[21-50]	1690.9248	2	h.SSTTTTTTEIRLLTKPERKLSWLLPPLSNN.	21.8
y30	[21-50]	1699.4381	2	h.SSTTTTTTEIRLLTKPERKLSWLLPPLSNN.	-6.2
y29-NH₃	[22-50]	1647.4088	2	s.STTTTTTEIRLLTKPERKLSWLLPPLSNN.	7.1
y29	[22-50]	1655.9221	2	s.STTTTTTEIRLLTKPERKLSWLLPPLSNN.	-11.3
y22-NH₃	[29-50]	1300.7498	2	t.EIRLLTKPERKLSWLLPPLSNN.	-32.3
y21-H₂O	[30-50]	1235.7365	2	e.IRLLTKPERKLSWLLPPLSNN.	-37.4
y21-NH₃	[30-50]	1236.2285	2	e.IRLLTKPERKLSWLLPPLSNN.	-14
y21	[30-50]	1244.7418	2	e.IRLLTKPERKLSWLLPPLSNN.	-12.6
y20	[31-50]	1188.1997	2	i.RLLTKPERKLSWLLPPLSNN.	-3.6
y19	[32-50]	2219.291	1	r.LLTKPERKLSWLLPPLSNN.	-1.2
y19-NH₃	[32-50]	2202.2645	1	r.LLTKPERKLSWLLPPLSNN.	7.2
y18	[33-50]	2106.207	1	l.LTKPERKLSWLLPPLSNN.	0.2
y18-NH₃	[33-50]	2089.1804	1	l.LTKPERKLSWLLPPLSNN.	8.3
y18-H₂O	[33-50]	2088.1964	1	l.LTKPERKLSWLLPPLSNN.	-1.8
y17-NH₃	[34-50]	1976.0964	1	l.TKPERKLSWLLPPLSNN.	11.7
y17	[34-50]	1993.1229	1	l.TKPERKLSWLLPPLSNN.	-4
y16-NH₃	[35-50]	1875.0487	1	t.KPERKLSWLLPPLSNN.	-1.4
y16	[35-50]	1892.0752	1	t.KPERKLSWLLPPLSNN.	-7
y15	[36-50]	1763.9803	1	k.PERKLSWLLPPLSNN.	-2.6
y15-H₂O	[36-50]	1745.9697	1	k.PERKLSWLLPPLSNN.	11.7
y15-NH₃	[36-50]	1746.9537	1	k.PERKLSWLLPPLSNN.	3.6
y14-H₂O	[37-50]	1648.917	1	p.ERKLSWLLPPLSNN.	-9.2
y14-NH₃	[37-50]	1649.901	1	p.ERKLSWLLPPLSNN.	0.4

ion	slice	m/z	z	sequence	error, ppm
y14	[37-50]	1666.9275	1	p.ERKLSWLLPPLSNN.	-9.1
y13	[38-50]	1537.8849	1	e.RKLSWLLPPLSNN.	-7.2
y10	[41-50]	1140.6048	1	l.SWLLPPLSNN.	10.6
y10-H_2O	[41-50]	1122.5942	1	l.SWLLPPLSNN.	33.8
y9-H_2O	[42-50]	1035.5622	1	s.WLLPPLSNN.	-26.8
y9	[42-50]	1053.5728	1	s.WLLPPLSNN.	-15.1
y9-NH_3	[42-50]	1036.5462	1	s.WLLPPLSNN.	12
y8	[43-50]	867.4934	1	w.LLPPLSNN.	-20.9
y8-NH_3	[43-50]	850.4669	1	w.LLPPLSNN.	-37.8
y7	[44-50]	754.4094	1	l.LPPLSNN.	-26.4
y7-NH_3	[44-50]	737.3828	1	l.LPPLSNN.	-33.9
y7-H_2O	[44-50]	736.3988	1	l.LPPLSNN.	-49
y6-NH_3	[45-50]	624.2988	1	l.PPLSNN.	-12.9
y6	[45-50]	641.3253	1	l.PPLSNN.	-13.2
y6-H_2O	[45-50]	623.3148	1	l.PPLSNN.	-43.9
y5	[46-50]	544.2726	1	p.PLSNN.	-8.7
y5-NH_3	[46-50]	527.246	1	p.PLSNN.	27.4
y5-H_2O	[46-50]	526.262	1	p.PLSNN.	11.7
y4	[47-50]	447.2198	1	p.LSNN.	-4
y4-H_2O	[47-50]	429.2092	1	p.LSNN.	-38.2
y3	[48-50]	334.1357	1	l.SNN.	7.7
y3-NH_3	[48-50]	317.1092	1	l.SNN.	11.9
y3-H_2O	[48-50]	316.1252	1	l.SNN.	14.9
y2-NH_3	[49-50]	230.0771	1	s.NN.	7.3
y2	[49-50]	247.1037	1	s.NN.	-20.4

Table S2

Experimental details of 20 ms DARR experiment on acquired on ^{13}C, ^{15}N-SS14 fibrils obtained in 10 mM sodium citrate buffer containing 5 % D-mannitol and 2 mg/ml heparin (pH 5.5).

Spectrometer	850 MHz
MAS frequency/kHz	18
Measurement Time	14 h
Number of Scans	16
Transfer 1	**HC-CP**
Time/ms	0.7
Field/kHz	77(H)/62(C)
Shape	tangent(H)
Transfer 2	**MIRROR**
Time/ms	20
Field/kHz	18(H)
Shape (*)	-
t1 Increments	1536
Sweep width/kHz	80
acq. time/ms	9.6
t2 Increments	2048
Sweep width/kHz	80
acq. time/ms	12.8
Decoupling	SPINAL64
Field/kHz	100
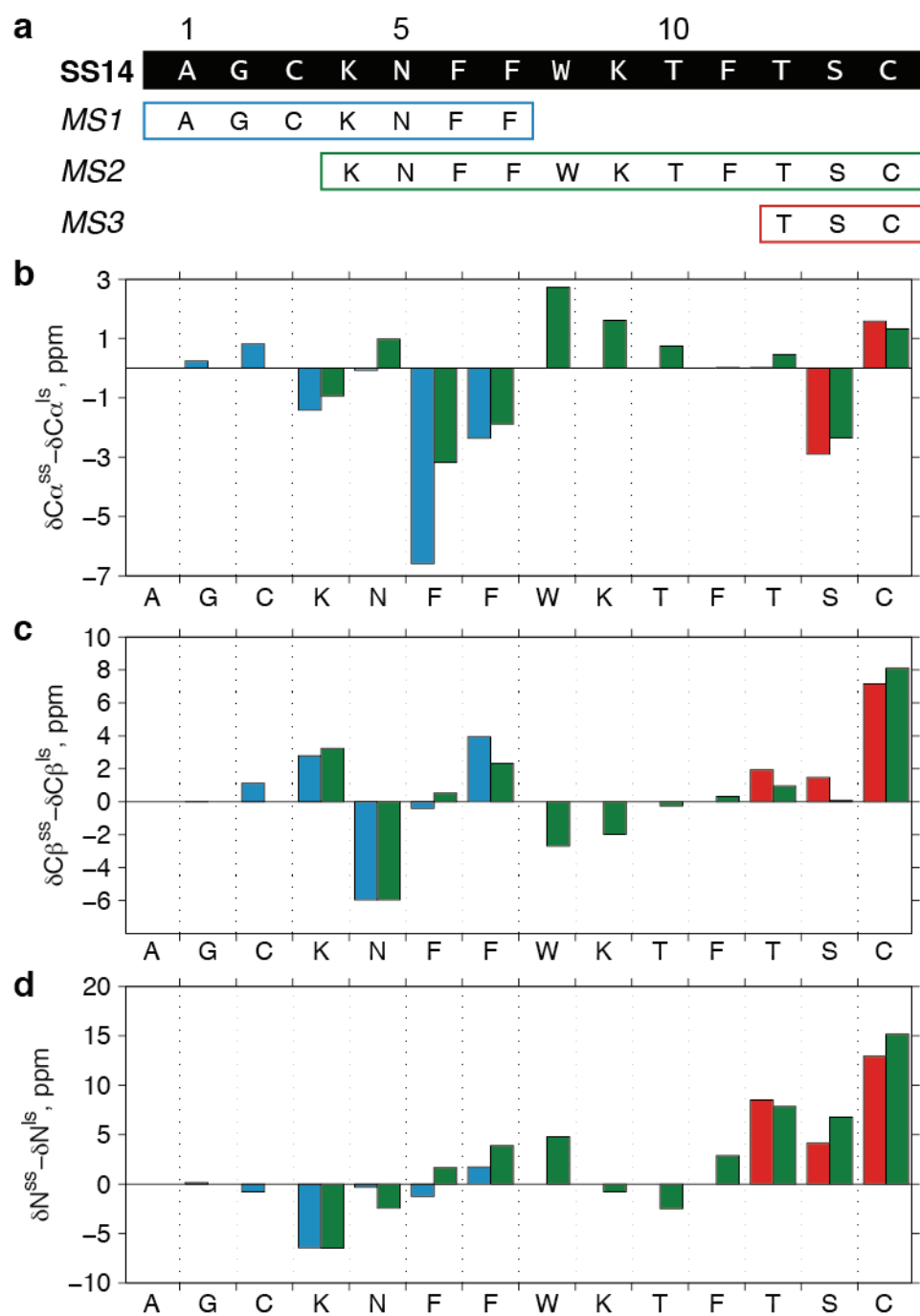
Figure S3. Comparison of chemical shifts of SS14 in the amyloid and soluble state. (**a**) MS (1-3) – molecular systems with distinct intramolecular interactions determined by ssNMR., Differences in chemical shifts of Cα (**b**), Cβ (**c**), and N backbone atoms (**d**) of SS14 in the amyloid (ss) and soluble state (ls). Molecular systems are color-coded: the sequentially assigned stretch is shown in the same color as the corresponding differences in chemical shifts in **b**, **c**, and **d**: MS1 – blue, MS2 – green; MS3 – red.

Table S3

Aggregation conditions tested for β-endorphin

Buffer composition	pH	Additives	Fibrillization
WT			
50 mM sodium phosphate 2 mM citric acid	5.5-8.0		yes
50 mM sodium phosphate 2 mM citric acid	5.0		no
50 mM sodium phosphate 2 mM citric acid	5.0-8.0	2 mg/ml heparin	yes
50 mM Tris, 50 mM maleic acid	5.5		yes
50 mM Tris, 50 mM maleic acid	7.4		yes
10 mM sodium citrate	5.5		yes
10 mM ammonium acetate 200 mM NaCl	5.5		no
10 mM ammonium acetate 200 mM NaCl	5.5	2 mg/ml heparin disaccharide I-S	yes
10 mM ammonium acetate 200 mM NaCl	5.5	2 mg/ml glucosamine	yes
10 mM ammonium acetate 200 mM NaCl	5.5	2 mg/ml glucosamine-6-sulfate	yes
10 mM ammonium acetate 200 mM NaCl	5.5	2 mg/ml glucuronic acid	yes
10 mM ammonium acetate 200 mM NaCl	5.5	2 mg/ml glucose	yes
10 mM ammonium acetate 200 mM NaCl	5.5	2 mg/ml mannitol	yes
10 mM ammonium acetate 200 mM NaCl	5.5	2 mg/ml heparin	yes
10 mM ammonium acetate 200 mM NaCl	5.5	10 mM sodium sulfate	yes
PBS	7.4		yes
PBS	7.4	2 mg/ml heparin	yes
PBS	7.4	10 mM sodium sulfate	yes
PBS	7.4	0.1 mg/ml heparin	yes[a]
PBS	7.4		yes[a]
10 mM Tris-HCl 150 mM NaCl	7.4		yes[b]
10 mM Tris-HCl 150 mM NaCl	7.4	2 mg/ml heparin	yes
10 mM Tris-HCl 150 mM NaCl	7.4	10 mM sodium sulfate	yes
10 mM Tris-HCl	7.4	10 mM sodium phosphate	yes
10 mM Tris-HCl	7.4	1 mM sodium phosphate	yes
10 mM Tris-HCl	7.4	100 μM sodium phosphate	no
10 mM Tris-HCl	7.4	10 μM sodium phosphate	no
10 mM Tris-HCl	7.4	1 μM sodium phosphate	no
10 mM Tris-HCl	7.4		no

Concentration of β-endorphin is 2 mg/ml, unless stated otherwise.

a – peptide concentration 0.1 mg/ml

b – fibrillization occurred more then in 72 h

Table S3 (continued)

Aggregation conditions tested for β-endorphin

Buffer composition	pH	Additives	Fibrillization
E8Q			
10 mM ammonium acetate, 200 mM NaCl	5.5		yes
10 mM ammonium acetate, 200 mM NaCl	5.5	2 mg/ml heparin	yes
PBS	7.4		yes
PBS	7.4	2 mg/ml heparin	yes
PBS	7.4	10 mM sodium sulfate	yes
10 mM Tris-HCl, 150 mM NaCl	7.4		no
10 mM Tris-HCl, 150 mM NaCl	7.4	2 mg/ml heparin	yes
10 mM Tris-HCl, 150 mM NaCl	7.4	10 mM sodium sulfate	no
10 mM Tris-HCl	7.4		no
50 mM sodium phosphate, 2 mM sodium citrate	5.5		yes
E8L			
PBS	7.4		yes
PBS	7.4	2 mg/ml heparin	yes
PBS	7.4	10 mM sodium sulfate	yes
10 mM Tris-HCl, 150 mM NaCl	7.4		yes
10 mM Tris-HCl, 150 mM NaCl	7.4	2 mg/ml heparin	yes
10 mM Tris-HCl, 150 mM NaCl	7.4	10 mM sodium sulfate	yes
10 mM Tris-HCl	7.4		no
10 mM ammonium acetate, 200 mM NaCl	5.5		yes
10 mM ammonium acetate, 200 mM NaCl	5.5	10 mM sodium sulfate	yes
10 mM ammonium acetate	5.5		no
50 mM sodium phosphate, 2 mM sodium citrate	5.5		yes

Concentration of β-endorphin is 2 mg/ml, unless stated otherwise.

Table S3 (continued)

Aggregation conditions tested for β-endorphin

Buffer composition	pH	Additives	Fibrillization
E8K			
10 mM ammonium acetate, 200 mM NaCl	5.5		no
10 mM ammonium acetate, 200 mM NaCl	5.5	2 mg/ml heparin	yes
10 mM ammonium acetate, 200 mM NaCl	5.5	10 mM sodium sulfate	yes
PBS	7.4		yes
PBS	7.4	2 mg/ml heparin	yes
PBS	7.4	10 mM sodium sulfate	yes
10 mM Tris-HCl, 150 mM NaCl	7.4		no
10 mM Tris-HCl, 150 mM NaCl	7.4	2 mg/ml heparin	yes
10 mM Tris-HCl, 150 mM NaCl	7.4	10 mM sodium sulfate	no
10 mM Tris-HCl	7.4		no
50 mM sodium phosphate, 2 mM sodium citrate	5.5		no
E8R			
10 mM ammonium acetate, 200 mM NaCl	5.5		no
10 mM ammonium acetate, 200 mM NaCl	5.5	2 mg/ml heparin	yes
10 mM ammonium acetate, 200 mM NaCl	5.5	10 mM sodium sulfate	yes
PBS	7.4		yes
PBS	7.4	2 mg/ml heparin	yes
PBS	7.4	10 mM sodium sulfate	yes
10 mM Tris-HCl, 150 mM NaCl	7.4		no
10 mM Tris-HCl, 150 mM NaCl	7.4	2 mg/ml heparin	yes
10 mM Tris-HCl, 150 mM NaCl	7.4	10 mM sodium sulfate	no
10 mM Tris-HCl	7.4		no
50 mM sodium phosphate, 2 mM sodium citrate	5.5		no

Concentration of β-endorphin is 2 mg/ml, unless stated otherwise.
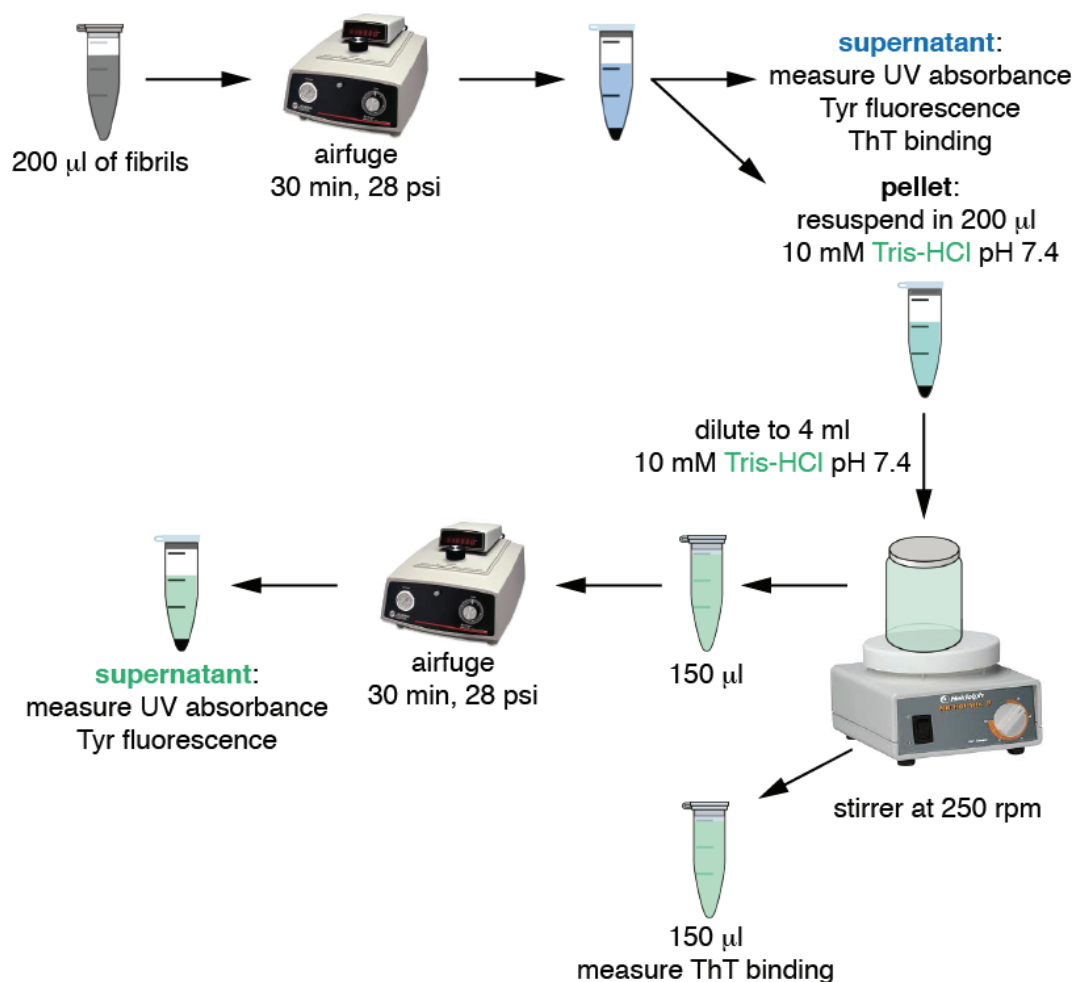
Figure S4. Dissociation assay. 200 µl of preformed fibrils were centrifuged for 30 min at 28 psi in Airfuge® Air-Driven centrifuge. The supernatant obtained was analyzed by UV absorbance, Tyr fluorescence, and ThT binding measurements. The pellet was resuspended in 200 µl of 10 mM Tris-HCl buffer at pH 7.4. The suspension was immediately transferred to 4 ml of the same buffer under constant stirring at 250 rpm, room temperature. Samples for analysis were taken at different time points. The residual content of β-endorphin amyloid fibrils was analyzed by ThT binding assay, in which 150 µl of the dissociation mixture were stained by 1 µl of 1.5 mM ThT solution. Appearance of soluble β-endorphin was detected by UV absorbance and Tyr fluorescence measurements of the supernatant obtained after ultracentrifugation of 150 µl of the dissociation mixture.

```
ATGAGCGATAAAATTATTCACCTGACTGACGACAGTTTTGACACGGATGTACTCAAAGCG
M   S   D   K   I   I   H   L   T   D   D   S   F   D   T   D   V   L   K   A
GACGGGGCGATCCTCGTCGATTTCTGGGCAGAGTGGTGCGGTCCGTGCAAAATGATCGCC
D   G   A   I   L   V   D   F   W   A   E   W   C   G   P   C   K   M   I   A
CCGATTCTGGATGAAATCGCTGACGAATATCAGGGCAAACTGACCGTTGCAAAACTGAAC
P   I   L   D   E   I   A   D   E   Y   Q   G   K   L   T   V   A   K   L   N
ATCGATCAAAACCCTGGCACTGCGCCGAAATATGGCATCCGTGGTATCCCGACTCTGCTG
I   D   Q   N   P   G   T   A   P   K   Y   G   I   R   G   I   P   T   L   L
CTGTTCAAAAACGGTGAAGTGGCGGCAACCAAAGTGGGTGCACTGTCTAAAGGTCAGTTG
L   F   K   N   G   E   V   A   A   T   K   V   G   A   L   S   K   G   Q   L
AAAGAGTTCCTCGACGCTAACCTGGCCGGTTCTGGTTCTGGCCATATGCACCATCATCAT
K   E   F   L   D   A   N   L   A   G   S   G   S   G   H   M   H   H   H   H
CATCATTCTTCTGGTCTGGTGCCACGCGGTTCTGGTATGAAAGAAACCGCTGCTGCTAAA
H   H   S   S   G   L   V   P   R   G   S   G   M   K   E   T   A   A   A   K
TTCGAACGCCAGCACATGGACAGCCCAGATCTGGGTACCGACGACGACGACAAGGCCATG
F   E   R   Q   H   M   D   S   P   D   L   G   T   D   D   D   D   K   A   M
GCTGATATCGGATCCGAAAACCTGTATTTTCAGTATGGTGGCTTTATGACCAGCGAAAAA
A   D   I   G   S   E   N   L   Y   F   Q   Y   G   G   F   M   T   S   E   K
AGCCAGACACCGCTGGTTACCCTGTTTAAAAATGCCATTATTAAAAATGCCTATAAAAAA
S   Q   T   P   L   V   T   L   F   K   N   A   I   I   K   N   A   Y   K   K
GGCGAATGAAAGCTTGCGGCCGCACTCGAGCACCACCACCACCACCACTGA
G   E   *   K   L   A   A   A   L   E   H   H   H   H   H   H   *
```

Figure S5. Nucleotide and amino acid sequence of the THX-β-endorphin fusion protein. The displayed sequence contains also a segment of the downstream plasmid sequence. The 6His-tag is highlighted in green; the TEV-protease recognition site is highlighted in purple, and the sequence of β-endorphin is in yellow. Shown DNA sequence was confirmed by DNA sequencing.
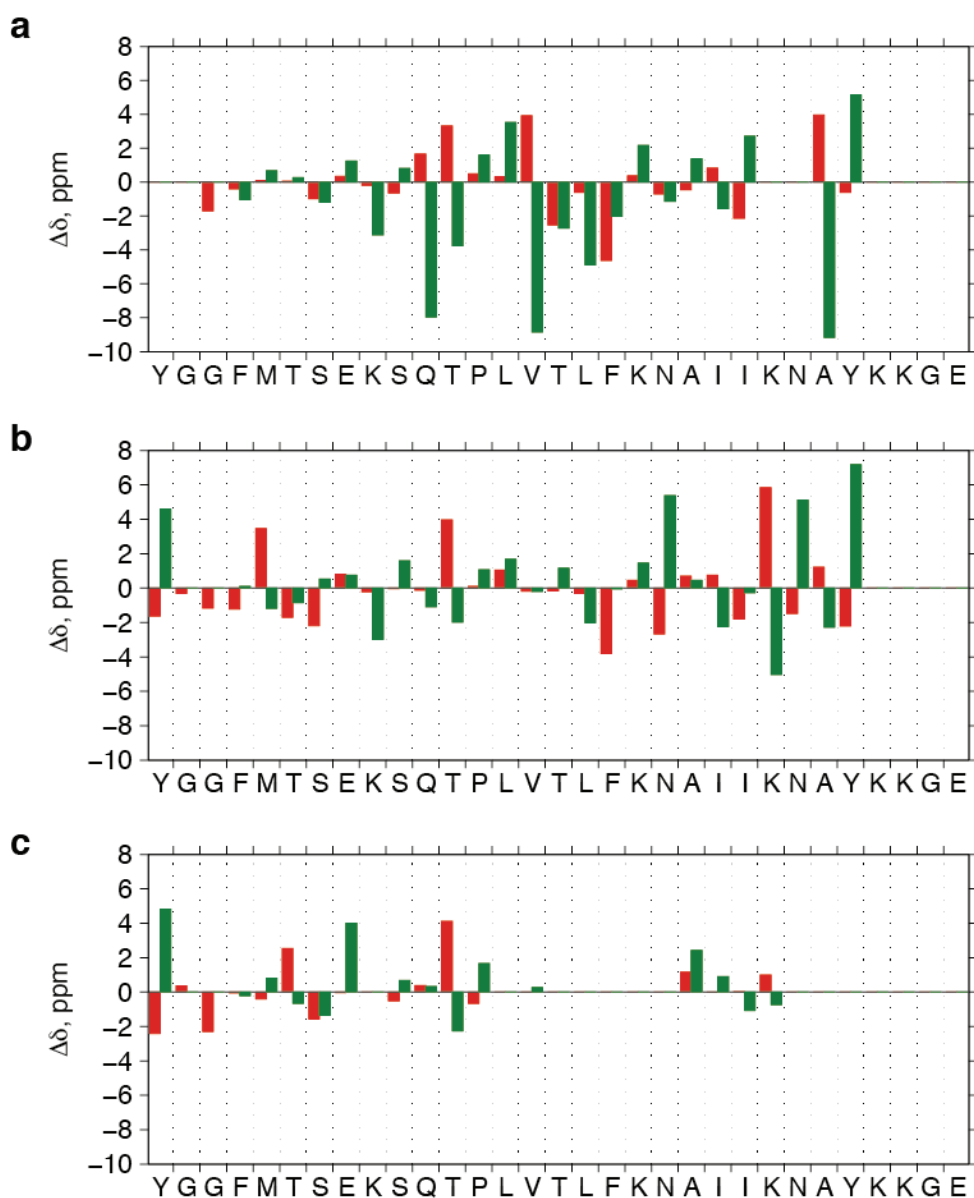
Figure S6. Differences in chemical shifts of β-endorphin fibrils formed in CP buffer at pH 6.0 ("δ_{CP}") and 10 mM ammonium acetate buffer at pH 5.5 in the presence of 200 mM NaCl and 2 mg/ml heparin ("$\delta_{heparin}$"). The values plotted are obtained by subtracting the $\delta_{heparin}$ from the δ_{CP} value for a given amino acid residue. Red and green bars represent differences in Cα and Cβ chemical shifts, respectively. The analysis is performed for the β-endorphin amyloid polymorph A, B, and C (see **Chapter 7** for details) individually (**a**, **b**, and **c**, respectively)

Figure S7. 20 ms DARR spectra of amyloid fibrils formed by ^{13}C, ^{15}N-labeled β-endorphin in 50 mM sodium phosphate, 2 mM sodium citrate buffer at pH 6.0. Peaks assigned to the polymorph A are labeled. The assignment is tentative.

Figure S8. 20 ms DARR spectra of amyloid fibrils formed by ^{13}C, ^{15}N-labeled β-endorphin in 50 mM sodium phosphate, 2 mM sodium citrate buffer at pH 6.0. Peaks assigned to the polymorph B are labeled. The assignment is tentative.

Figure S9. 20 ms DARR spectra of amyloid fibrils formed by ¹³C, ¹⁵N-labeled β-endorphin in 50 mM sodium phosphate, 2 mM sodium citrate buffer at pH 6.0. Peaks assigned to the polymorph C are labeled. The assignment is tentative.

Figure S10. 20 ms DARR spectra of amyloid fibrils formed by ^{13}C, ^{15}N-labeled β-endorphin in 50 mM sodium phosphate, 2 mM sodium citrate buffer at pH 6.0. Spin systems, which were not assigned to any polymorphic form, are labeled. The assignment is tentative.
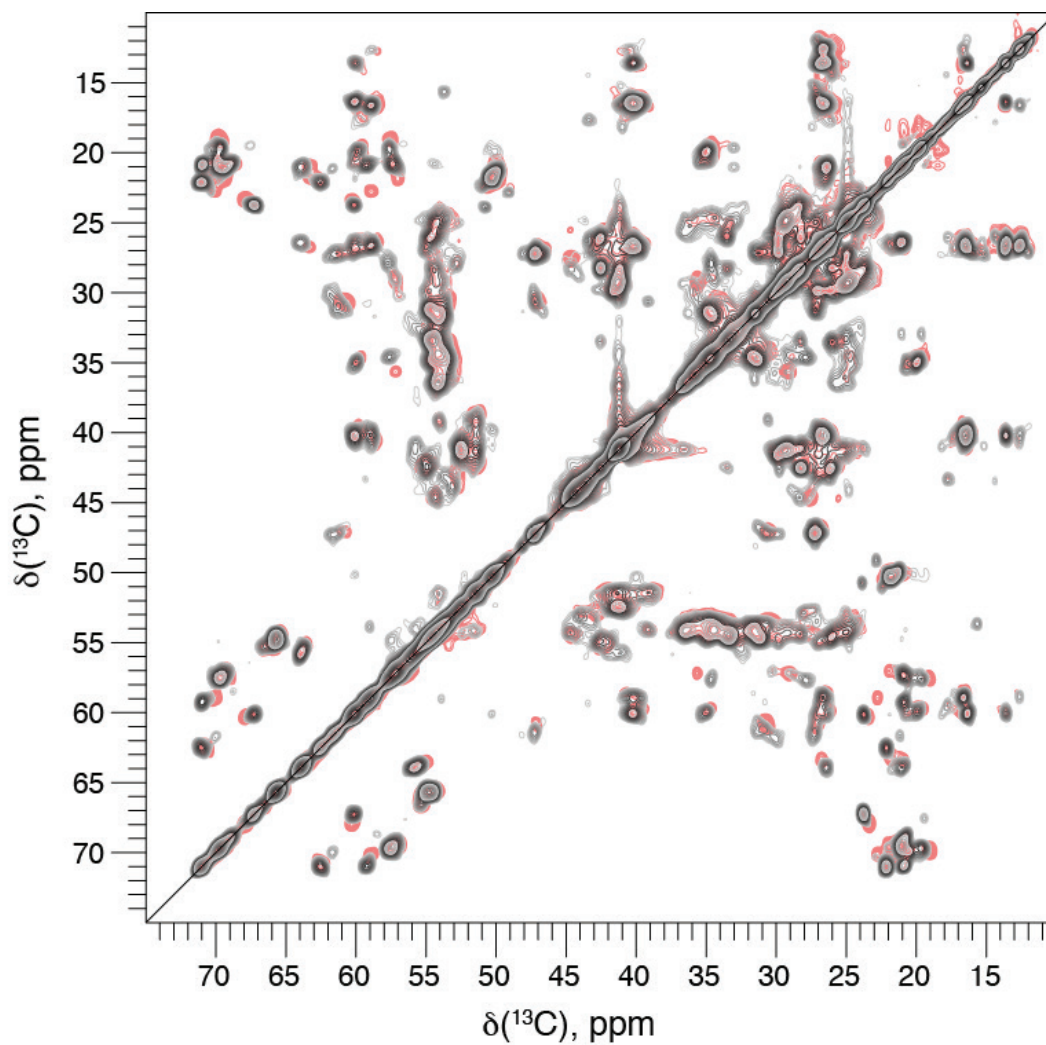
Figure S11. 20 ms DARR spectra of amyloid fibrils formed by ^{13}C, ^{15}N-labeled β-endorphin in 50 mM sodium phosphate, 2 mM sodium citrate buffer at pH 6.0 (gray) and in 55 mM sodium phosphate at pH 6.0 (pink).
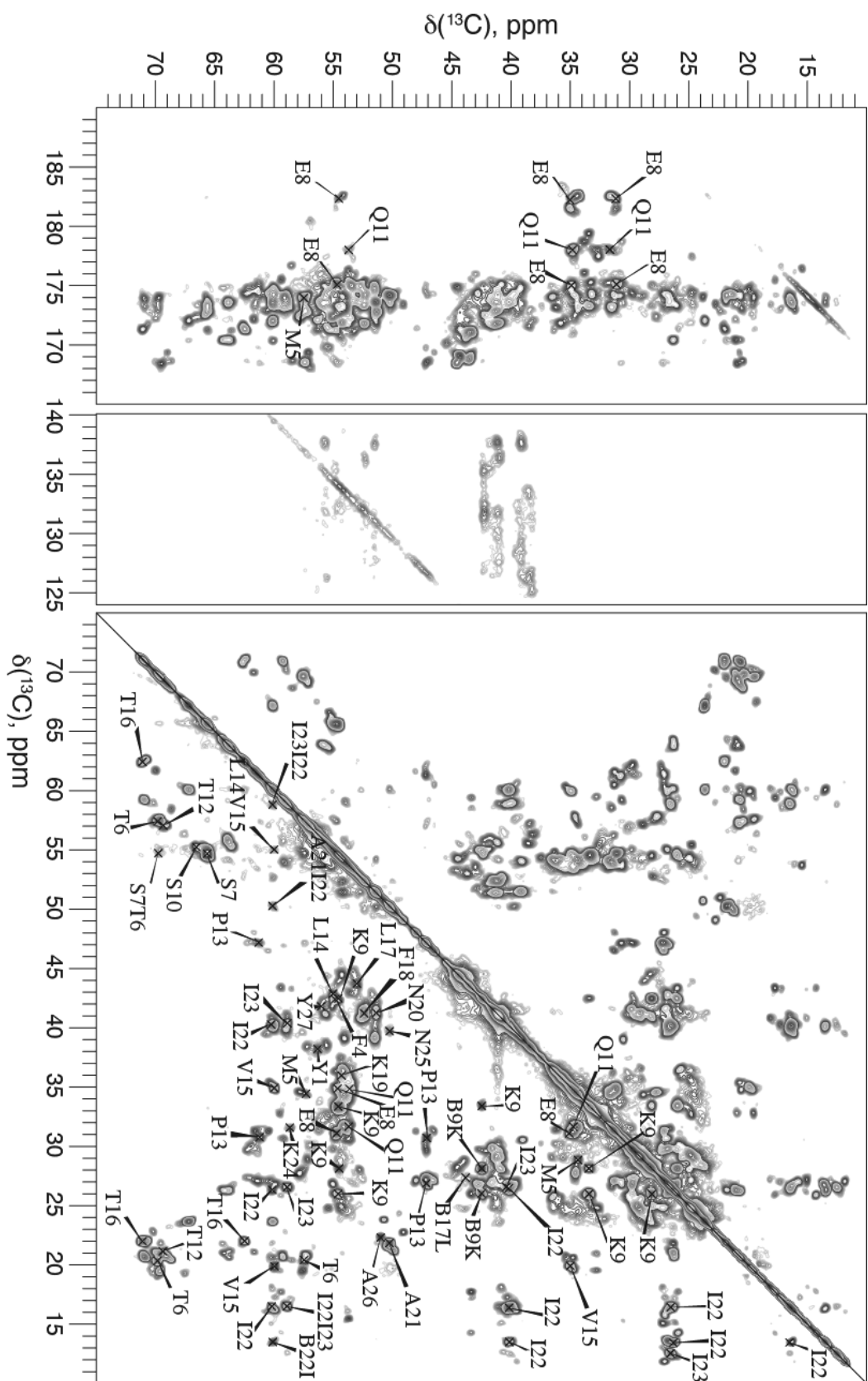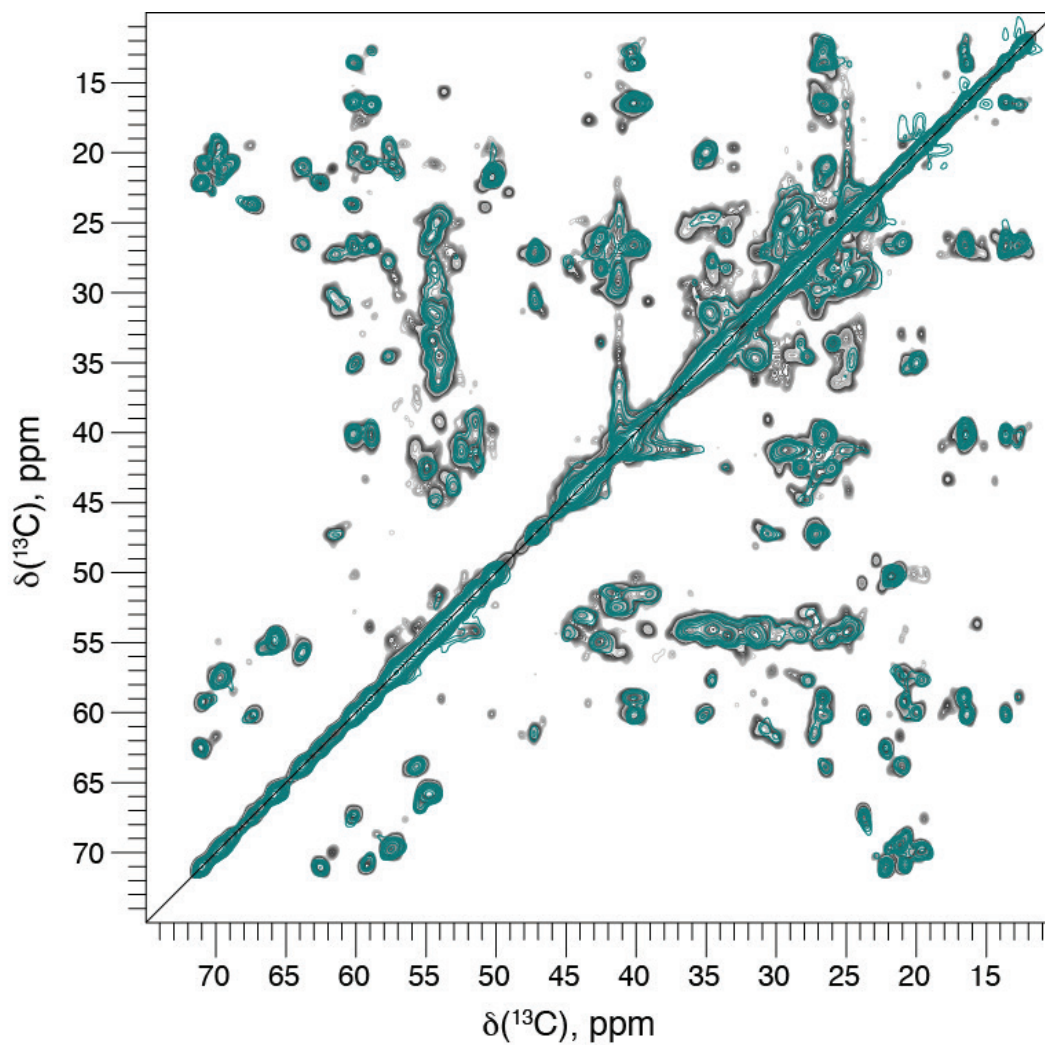
Figure S12. 20 ms DARR spectra of amyloid fibrils formed by ^{13}C, ^{15}N-labeled β-endorphin in 50 mM sodium phosphate, 2 mM sodium citrate buffer at pH 6.0 (grey) and in 14 mM sodium citrate buffer at pH 6.0 (green).
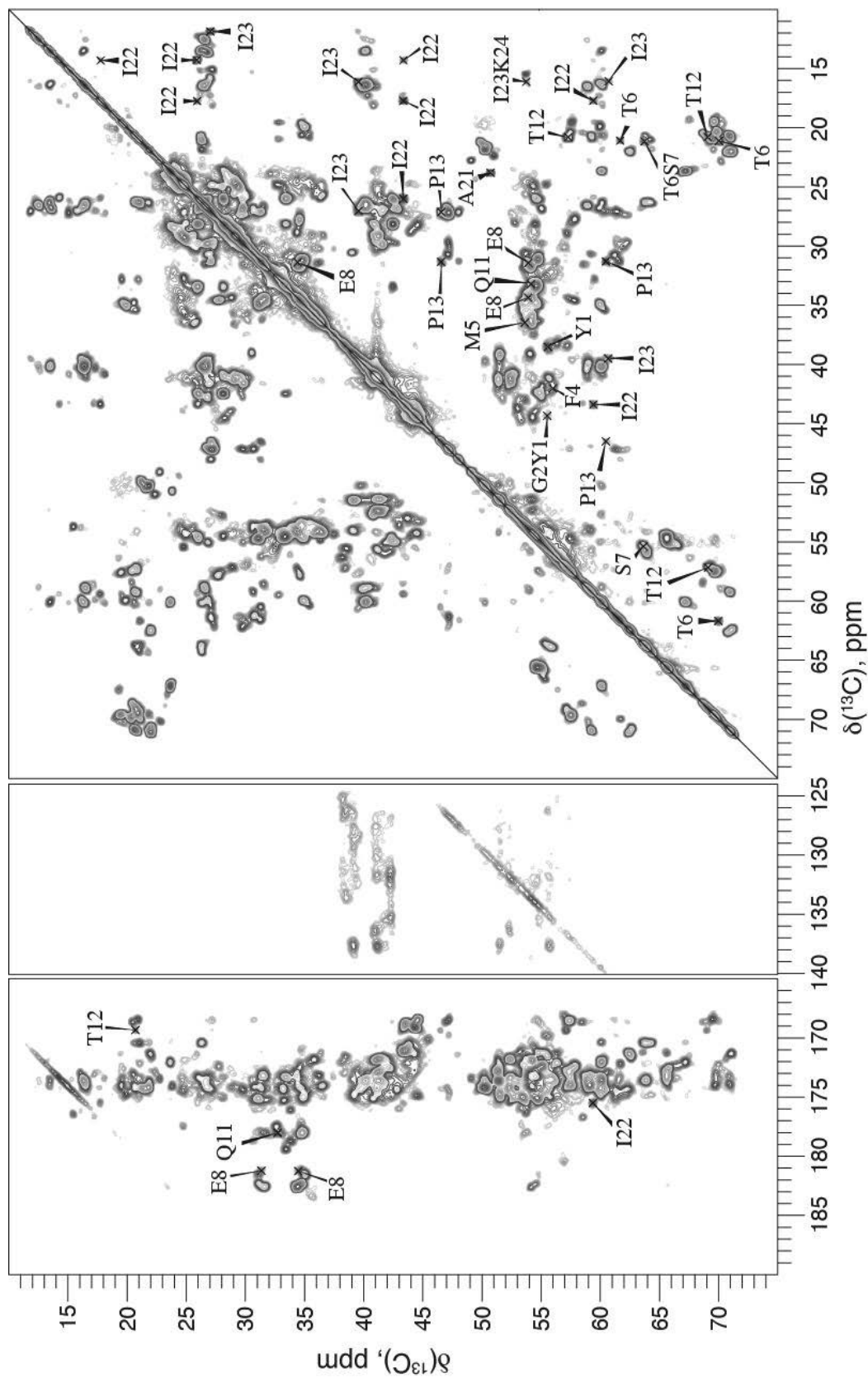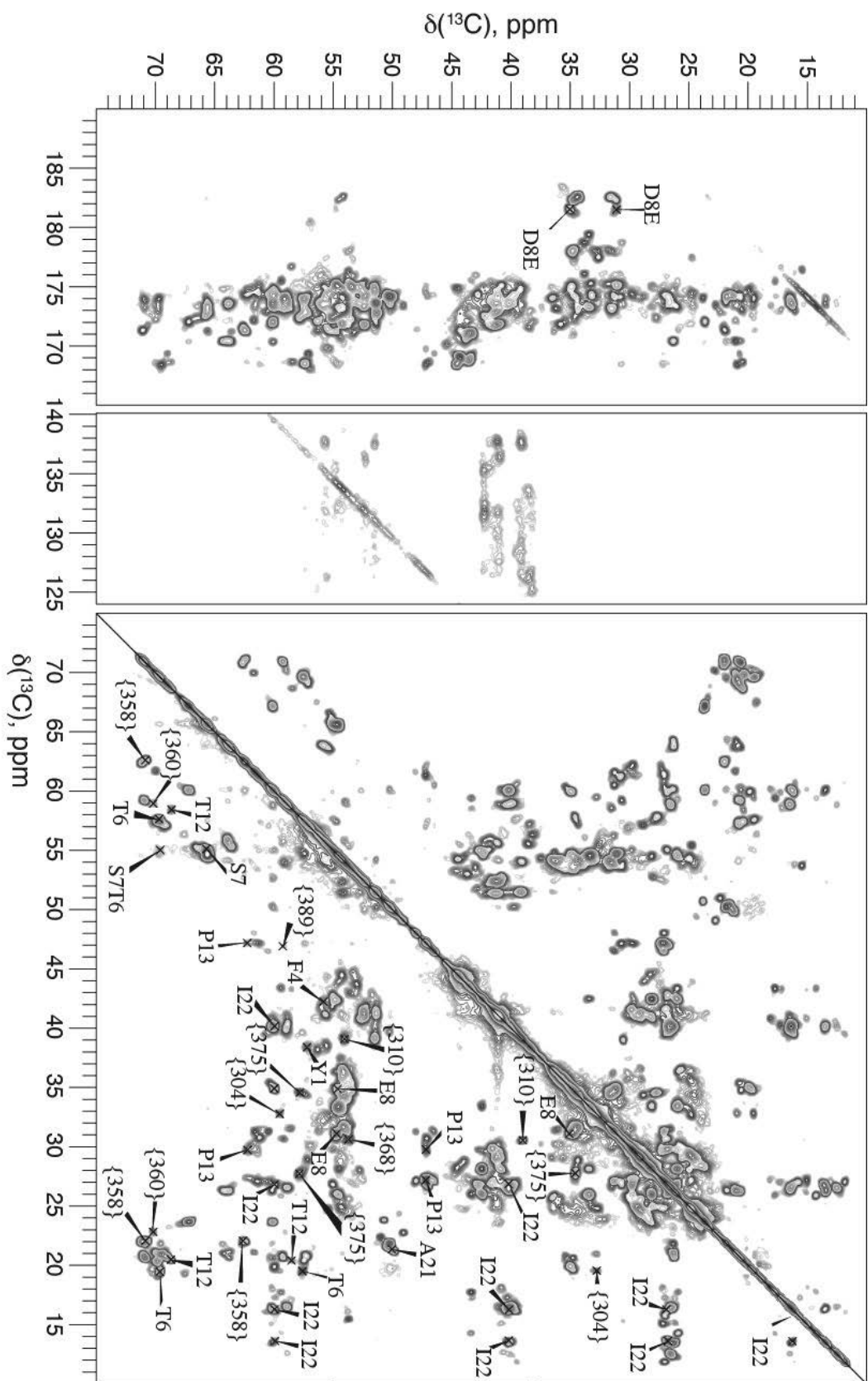
Figure S13. 20 ms DARR spectra of amyloid fibrils formed by ^{13}C, ^{15}N-labeled β-endorphin in 50 mM sodium phosphate, 2 mM sodium citrate buffer at pH 6.0 (grey) and pH 5.5 (light purple).
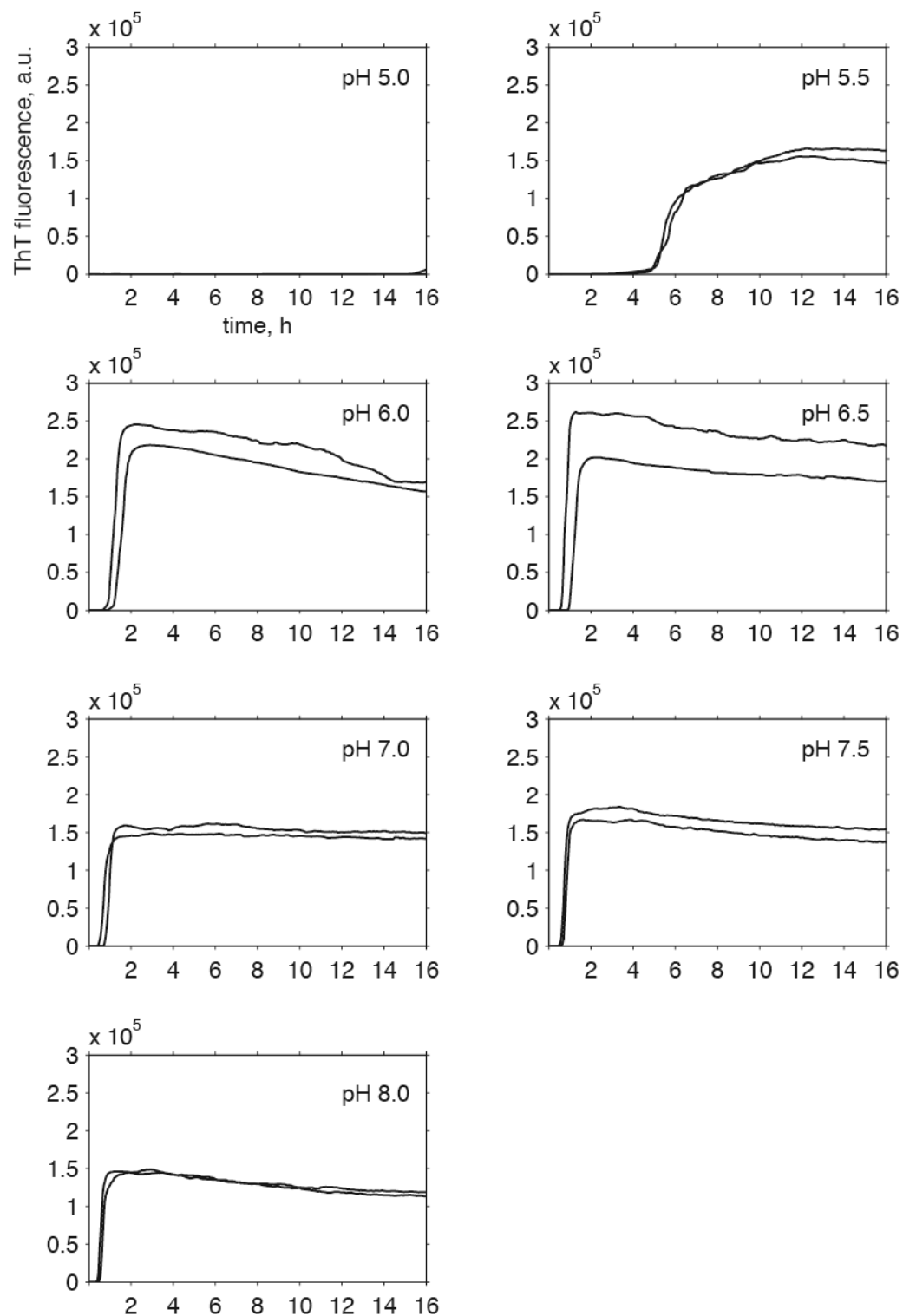
Figure S14. Aggregation of β-endorphin in 50 mM sodium phosphate, 2 mM sodium citrate buffer at different pH tracked by ThT fluorescence. The respective pH is labeled on each graph. Each curve represents the average of 4-5 replicas of the experiment repeated on the same 96-well plate. Each curve corresponds to independent repetition of the experiment in different 96-well plates. The fluorescence intensity plotted is baseline-subtracted.
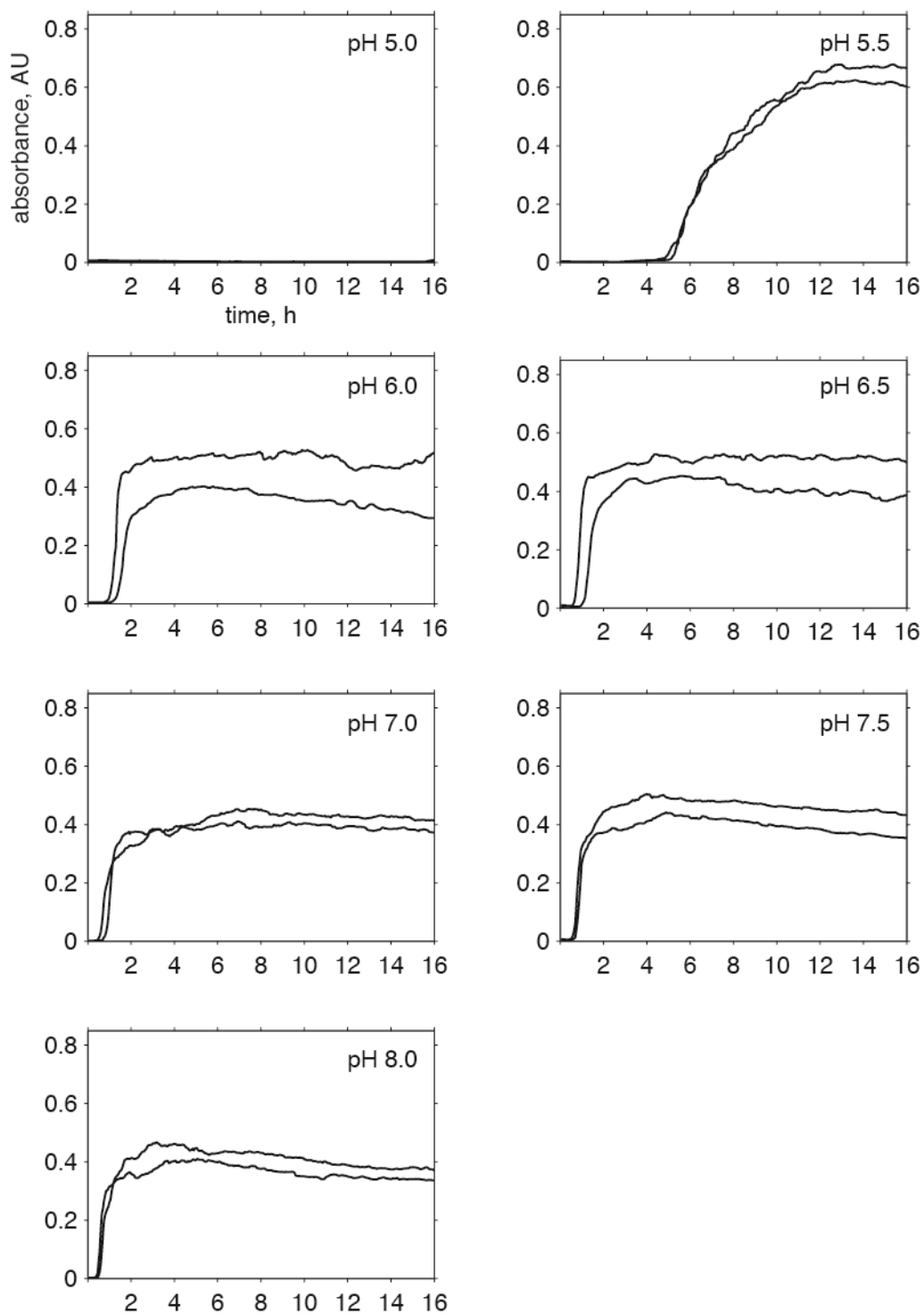
Figure S15. Aggregation of β-endorphin in 50 mM sodium phosphate, 2 mM sodium citrate buffer at different pH tracked by absorbance at 600 nm. The respective pH is labeled on each graph. Each curve represents the average of 4-5 replicas of the experiment repeated on the same 96-well plate. Each curve corresponds to independent repetition of the experiment in different 96-well plates. The absorbance intensity plotted is baseline-subtracted.
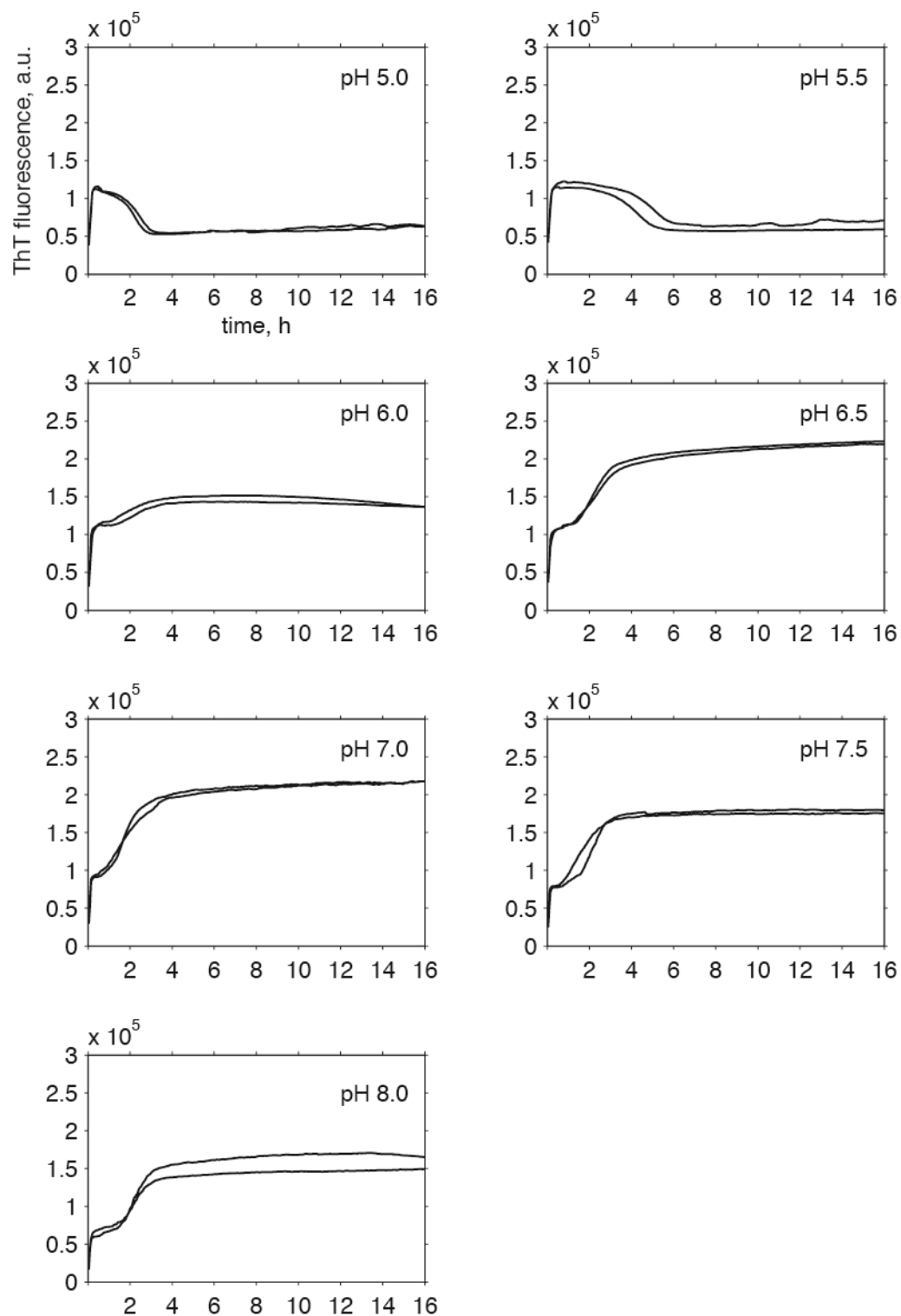
Figure S16. Aggregation of β-endorphin in 50 mM sodium phosphate, 2 mM sodium citrate buffer containing 2 mg/ml heparin at different pH tracked by ThT fluorescence. The respective pH is labeled on each graph. Each curve represents the average of 4-5 replicas of the experiment repeated on the same 96-well plate. Each curve corresponds to independent repetition of the experiment in different 96-well plates. The fluorescence intensity plotted is baseline-subtracted.
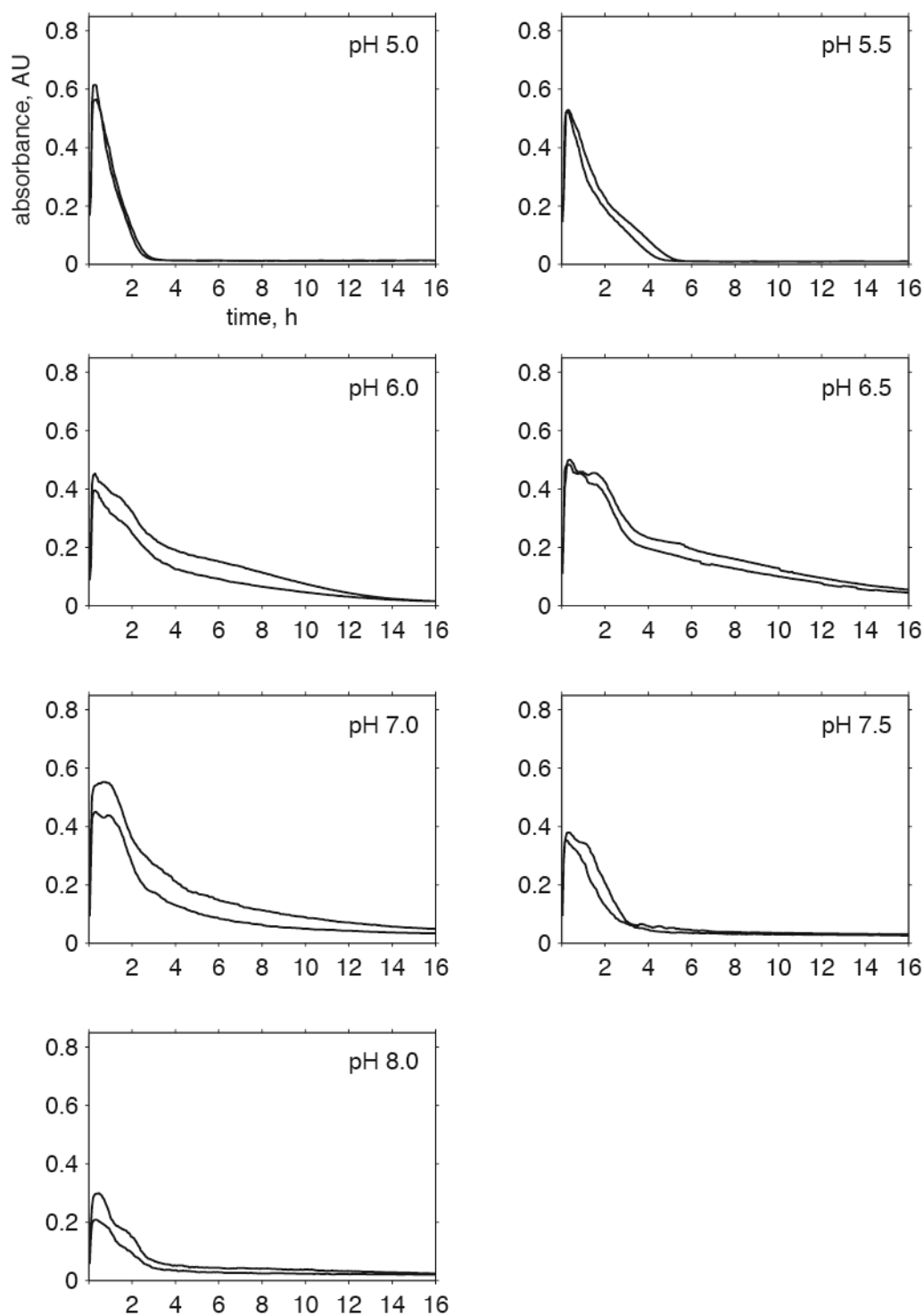
Figure S17. Aggregation of β-endorphin in 50 mM sodium phosphate, 2 mM sodium citrate buffer containing 2 mg/ml heparin at different pH tracked by absorbance at 600 nm. The respective pH is labeled on each graph. Each curve represents the average of 4-5 replicas of the experiment repeated on the same 96-well plate. Each curve corresponds to independent repetition of the experiment in different 96-well plates. The absorbance intensity plotted is baseline-subtracted.
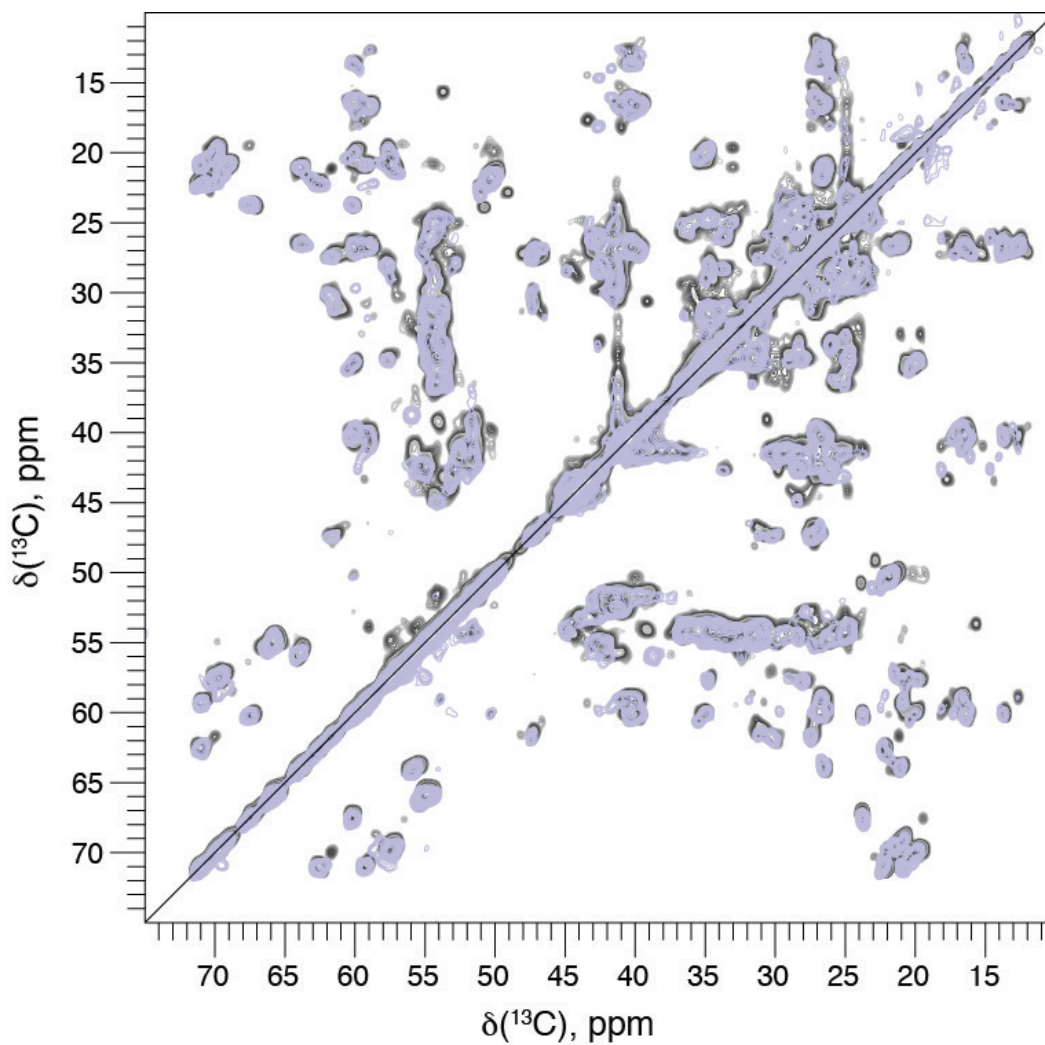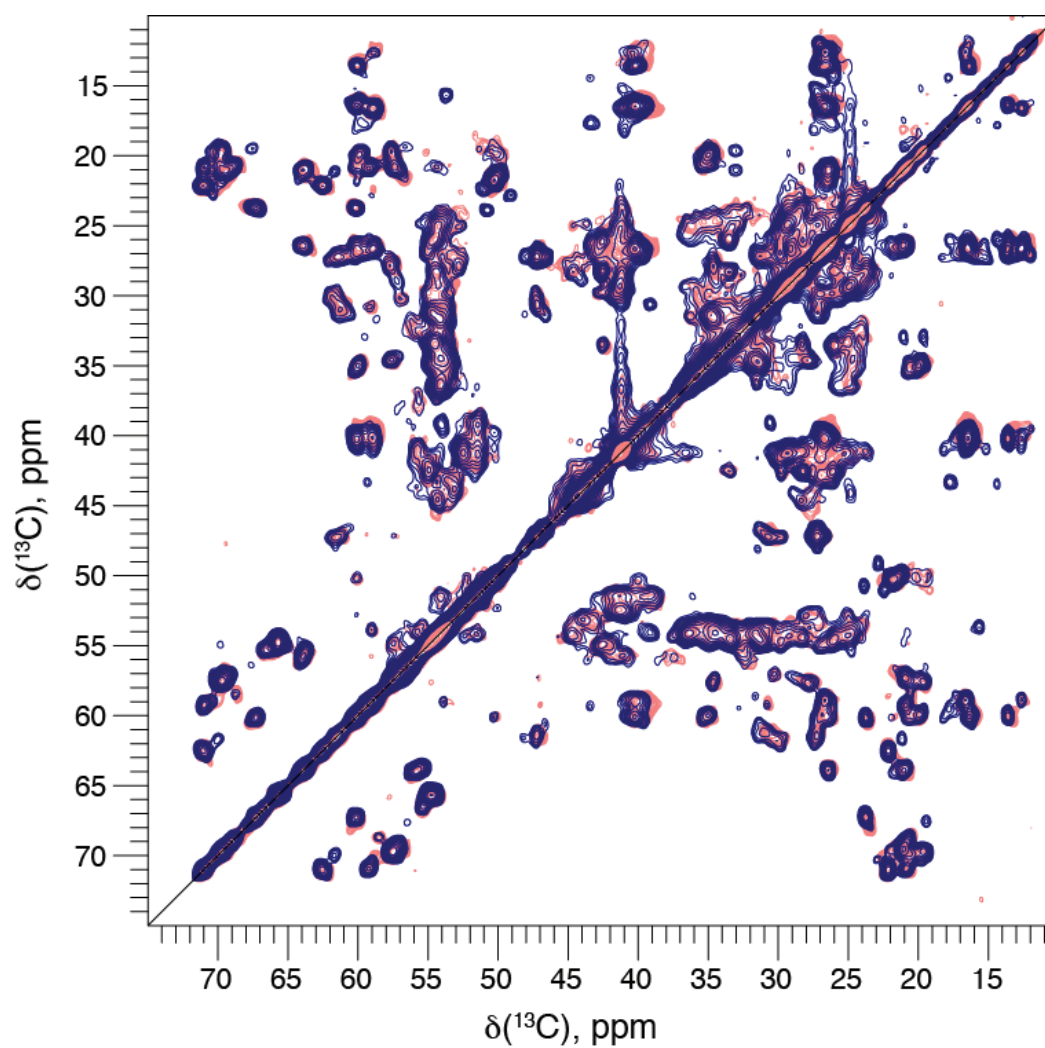
Figure S18. 20 ms DARR spectra of amyloid fibrils formed by ^{13}C, ^{15}N-labeled β-endorphin in 50 mM sodium phosphate, 2 mM sodium citrate buffer at pH 6.0 in the presence (pink) and absence (dark blue) of heparin disaccharide I-S.
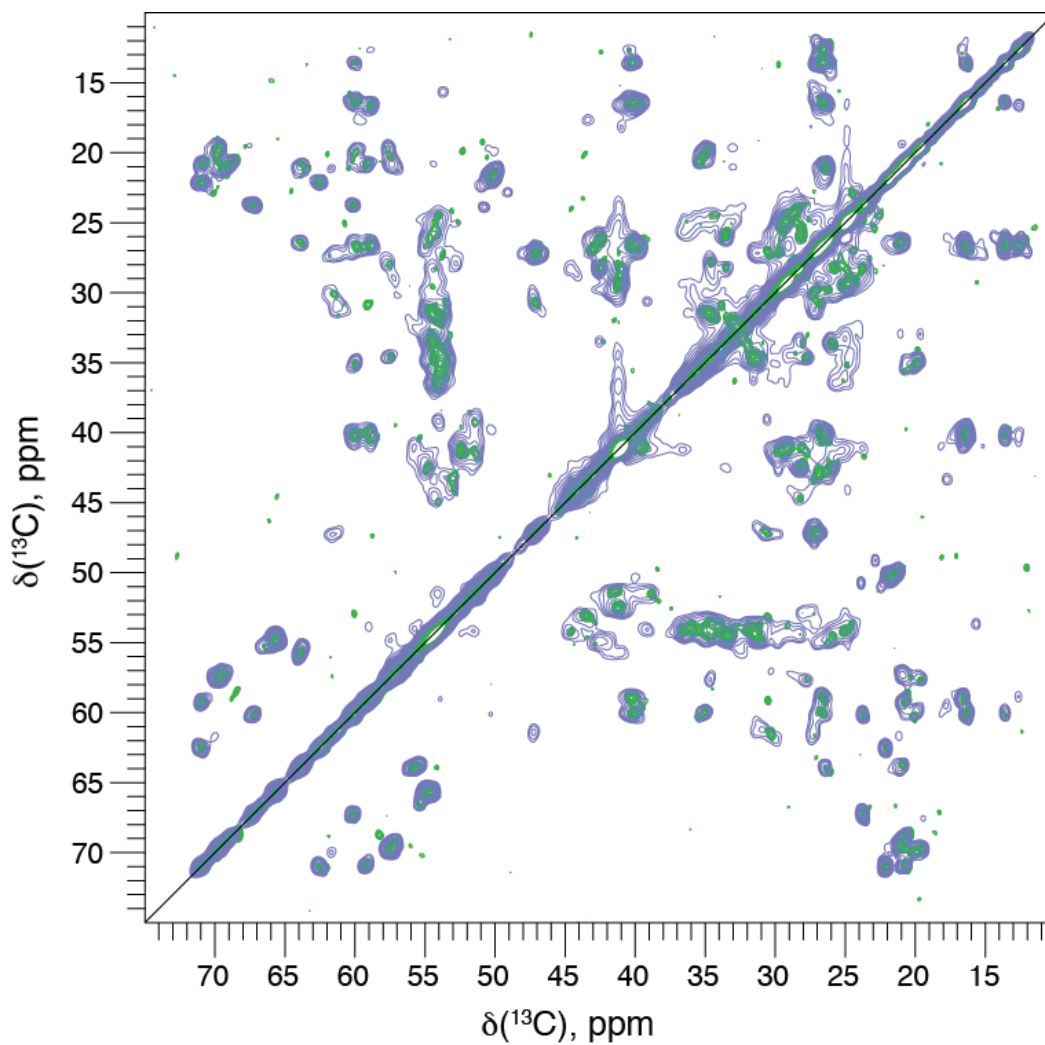
Figure S19. 20 ms DARR spectra of amyloid fibrils formed by ^{13}C, ^{15}N-labeled β-endorphin in 50 mM sodium phosphate, 2 mM sodium citrate buffer at pH 6.0 in the presence (green) and absence (light purple) of heparin glucosamine-6-sulfate.
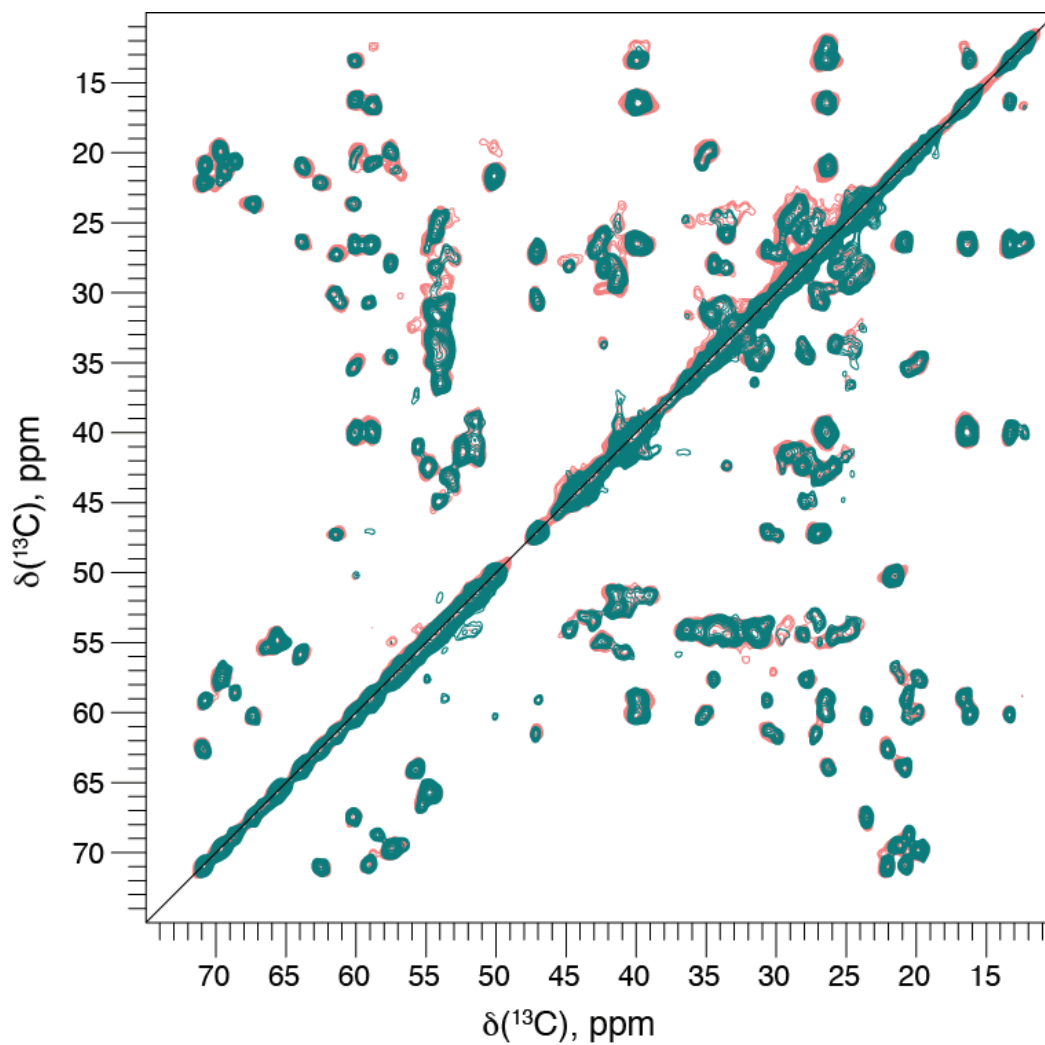
Figure S20. 20 ms DARR spectra of amyloid fibrils formed by ^{13}C, ^{15}N-labeled β-endorphin in the presence of heparin disaccharide I-S in 50 mM sodium phosphate, 2 mM sodium citrate buffer at pH 6.0 (pink) and 10 mM ammonium acetate, 200 mM NaCl buffer at pH 5.5 (green).

Table S4

Experimental details of ^{13}C-^{13}C DARR spectra acquired on WT, E8Q and E8R variants of ^{13}C, ^{15}N-β-endorphin fibrils obtained at different conditions

Sample	E8Q[1]	E8R[1]	WT[2]	WT[1]
Spectrometer	600 MHz	600 MHz	600 MHz	850 MHz
Measurement Time	18 h	15 h	18 h	8.5h
Number of Scans	32	24	32	8
Transfer 1	**HC-CP**	**HC-CP**	**HC-CP**	**HC-CP**
Time/ms	0.7	1	0.7	0.5
Field/kHz	62(H)/50(C)	62(H)/50(C)	62(H)/50(C)	80(H)/63(C)
Shape (*)	tangent(H)	tangent(H)	tangent(H)	tangent(H)
	D=12kHz	D=12kHz	D=12kHz	D=16kHz
Carrier/ppm	97	99	97	47
Transfer 2	**DARR**	**DARR**	**DARR**	**DARR**
Time/ms	20	20	20	20
Field/kHz	13(H)	13(H)	13(H)	17(H)
Shape (*)	-	-	-	-
Carrier/ppm	-	-	-	-
t1 Increments	1024	1024	1024	1536
Sweep width/kHz	50	50	50	85
carrier/ppm	97	99	97	100
acq. time/ms	10.2	10.2	10.2	9
td proc	2048	2048	2048	4096
window function	qsine 3.0	qsine 3.0	qsine 3.0	qsine 2.5
t2 Increments	1536	1536	1536	4096
Sweep width/kHz	50	50	50	100
carrier/ppm	97	99	97	100
acq. time/ms	15.4	15.4	15.4	20.5
td proc	4096	4096	4096	8192
window function	qsine 3.0	qsine 3.0	qsine 3.0	qsine 3.0
Decoupling	SPINAL64	SPINAL64	SPINAL64	SPINAL64
Field/kHz	90	100	90	100

* – The width D of the tangent shape refers to the difference between maximal and the minimal rf amplitude.
Fibrillization conditions:
1 – 10 mM ammonium acetate buffer (pH 5.5) containing 200 mM NaCl and 2 mg/ml heparin.
2 – 10 mM ammonium acetate buffer (pH 7.4) containing 200 mM NaCl and 2 mg/ml heparin.

Table S4 (continued)

Experimental details of ^{13}C-^{13}C DARR spectra acquired on WT, E8Q and E8R variants of ^{13}C, ^{15}N-β-endorphin fibrils obtained at different conditions

Sample	WT[1]	WT[2]	WT[3] pH5.5	WT[3] pH6
Spectrometer	600 MHz	600 MHz	600 MHz	600 MHz
Measurement Time	15 h	15 h	23 h	20 h
Number of Scans	24	24	36	32
Transfer 1	**HC-CP**	**HC-CP**	**HC-CP**	**HC-CP**
Time/ms	0.7	0.7	0.7	0.7
Field/kHz	62(H)/50(C)	62(H)/50(C)	62(H)/50(C)	62(H)/50(C)
Shape (*)	tangent(H)	tangent(H)	tangent(H)	tangent(H)
	D=12kHz	D=12kHz	D=12kHz	D=12kHz
Carrier/ppm	102	102	97	102
Transfer 2	**DARR**	**DARR**	**DARR**	**DARR**
Time/ms	20	20	20	20
Field/kHz	13(H)	13(H)	13(H)	13(H)
Shape (*)	-	-	-	-
Carrier/ppm	-	-	-	-
t1 Increments	1024	1024	1024	1024
Sweep width/kHz	50	50	50	50
carrier/ppm	102	102	97	102
acq. time/ms	10.2	10.2	10.2	10.2
td proc	2048	2048	2048	2048
window function	qsine 3.0	qsine 3.0	qsine 3.0	qsine 3.0
t2 Increments	1536	1536	1536	1536
Sweep width/kHz	50	50	50	50
carrier/ppm	102	102	97	102
acq. time/ms	15.4	15.4	15.4	15.4
td proc	4096	4096	4096	4096
window function	qsine 3.0	qsine 3.0	qsine 3.0	qsine 3.0
Decoupling Field/kHz	SPINAL64 90	SPINAL64 90	SPINAL64 90	SPINAL64 90

* – The width D of the tangent shape refers to the difference between maximal and the minimal rf amplitude.
Fibrillization conditions:
1 – 55 mM sodium phosphate buffer (pH 6.0).
2 – 14 mM sodium citrate buffer (pH 6.0).
3 – 50 mM sodium phosphate, 2 mM sodium citrate buffer.

Table S4 (continued)

Experimental details of ^{13}C-^{13}C DARR spectra acquired on WT, E8Q and E8R variants of ^{13}C, ^{15}N-β-endorphin fibrils obtained at different conditions

Sample	WT[1]+heparin	WT[1]+GlcN-6-SO$_4$	WT[2]	WT[3]
Spectrometer	600 MHz	600 MHz	600 MHz	600 MHz
Measurement Time	18 h	15 h	20 h	20 h
Number of Scans	28	24	32	32
Transfer 1	**HC-CP**	**HC-CP**	**HC-CP**	**HC-CP**
Time/ms	1	1	1	1
Field/kHz	62(H)/50(C)	62(H)/50(C)	62(H)/50(C)	62(H)/50(C)
Shape (*)	tangent(H)	tangent(H)	tangent(H)	tangent(H)
	D=12kHz	D=12kHz	D=12kHz	D=12kHz
Carrier/ppm	100	100	100	100
Transfer 2	**DARR**	**DARR**	**DARR**	**DARR**
Time/ms	20	20	20	20
Field/kHz	13(H)	13(H)	13(H)	13(H)
Shape (*)	-	-	-	-
Carrier/ppm	-	-	-	-
t1 Increments	1024	1024	1024	1024
Sweep width/kHz	50	50	50	50
carrier/ppm	100	100	100	100
acq. time/ms	10.2	10.2	10.2	10.2
td proc	2048	2048	2048	2048
window function	qsine 3.0	qsine 3.0	qsine 3.0	qsine 3.0
t2 Increments	1536	1536	1536	1536
Sweep width/kHz	50	50	50	50
carrier/ppm	100	100	100	100
acq. time/ms	15.4	15.4	15.4	15.4
td proc	4096	4096	4096	4096
window function	qsine 3.0	qsine 3.0	qsine 3.0	qsine 3.0
Decoupling	SPINAL64	SPINAL64	SPINAL64	SPINAL64
Field/kHz	100	100	100	100

* – The width D of the tangent shape refers to the difference between maximal and the minimal rf amplitude.

Fibrillization conditions:

1 – 50 mM sodium phosphate, 2 mM sodium citrate buffer (pH 6.0).

2 – 50 mM sodium phosphate, 2 mM sodium citrate buffer (pH 6.0) containing 2 mg/ml heparin disaccharide I-S.

3 – 10 mM ammonium acetate buffer (pH 5.5) containing 200 mM NaCl and 2 mg/ml heparin disaccharide I-S.

Table S5

Experimental details of the ssNMR spectra acquired on ^{13}C, ^{15}N-β-endorphin fibrils obtained in 50 mM sodium phosphate, 2 mM sodium citrate buffer at pH 6.0

Experiment	NCO	NCA	NCACB
Spectrometer	850 MHz	850 MHz	850 MHz
Measurement Time	10.5 h	10.5 h	21 h
Recycle delay/s	2.3	2.3	2.2
Number of Scans	8	8	4
Transfer 1	**HN-CP**	**HN-CP**	**HN-CP**
Time/ms	0.7	0.7	0.7
Field/kHz	67(H)/50(N)	67(H)/50(N)	67(H)/50(N)
Shape (*)	tangent(H)	tangent(H)	tangent(H)
	D=27kHz	D=27kHz	D=27kHz
Carrier/ppm	120	120	121
Transfer 2	**NCO-CP**	**NCA-CP**	**NCA-CP**
Time/ms	5	5	5
Field/kHz	90(H)/9.5(C)/8.1(N)	90(H)/9.5(C)/7.3(N)	90(H)/9.5(C)/7.3(N)
Shape (*)	tangent(C) D=2kHz	tangent(C) D=2kHz	tangent(C) D=2kHz
Carrier/ppm	0:now	50	50
Transfer 3	-	-	**DREAM**
Time/ms			4
Field/kHz			90(H)/8.3(C)
Shape (*)			tangent(C) D=3kHz
Carrier/ppm			48
t1 Increments	2048	2048	68
Sweep width/kHz	77	77	5.2
carrier/ppm	120	120	121
acq. time/ms	13.3	13.3	6.5
td proc	4096	4096	256
window function	qsine 3.0	qsine 3.0	qsine 2.6
t2 Increments	3072	3072	128
Sweep width/kHz	100	100	10
carrier/ppm	94	94	59
acq. time/ms	15.4	15.4	6.4
td proc	8192	8192	512
window function	qsine 3.0	qsine 3.0	qsine 2.6
t3 Increments	-	-	1280
Sweep width/kHz			50
carrier/ppm			94
acq. time/ms			12.8
td proc			4096
window function			qsine 2.6
Decoupling	SPINAL64	SPINAL64	SPINAL64
Field/kHz	90	90	90

Table S5 (continued)

Experimental details of the ssNMR spectra acquired on ^{13}C, ^{15}N-β-endorphin fibrils obtained in 50 mM sodium phosphate, 2 mM sodium citrate buffer at pH 6.0

Experiment	NCOCA	CANCO	NCACO
Spectrometer	850 MHz	850 MHz	850 MHz
Measurement Time	42 h	19 h	21 h
Recycle delay/s	2.2	2.2	2.2
Number of Scans	8	4	4
Transfer 1	**HN-CP**	**HC-CP**	**HN-CP**
Time/ms	0.7	0.3	0.7
Field/kHz	67(H)/50(N)	80(H)/63(C)	67(H)/50(N)
Shape (*)	tangent(H) D=27kHz	tangent(H) D=32kHz	tangent(H) D=27kHz
Carrier/ppm	121	59	121
Transfer 2	**NCO-CP**	**NCA-CP**	**NCA-CP**
Time/ms	5	5	5
Field/kHz	90(H)/9.5(C)/8.1(N)	90(H)/9.5(C)/7.3(N)	90(H)/9.5(C)/7.3(N)
Shape (*)	tangent(C) D=2kHz	tangent(C) D=2kHz	tangent(C) D=2kHz
Carrier/ppm	183	50	50
Transfer 3	**DARR**	**NCO-CP**	**DARR**
Time/ms	50	5	30
Field/kHz	17(H)	90(H)/9.5(C)/8.1(N)	17(H)
Shape (*)	-	tangent(C) D=2kHz	-
Carrier/ppm	-	183	-
t1 Increments	68	112	68
Sweep width/kHz	5.2	10	5.2
carrier/ppm	121	59	121
acq. time/ms	6.5	5.6	6.5
td proc	256	256	256
window function	qsine 2.6	qsine 2.6	qsine 2.6
t2 Increments	128	68	128
Sweep width/kHz	10	5.2	10
carrier/ppm	173	121	59
acq. time/ms	6.4	6.5	6.4
td proc	512	256	512
window function	qsine 2.6	qsine 2.6	qsine 2.6
t3 Increments	1280	1280	1280
Sweep width/kHz	50	50	50
carrier/ppm	94	94	94
acq. time/ms	12.8	12.8	12.8
td proc	4096	4096	4096
window function	qsine 2.6	qsine 2.6	qsine 2.6
Decoupling	SPINAL64	SPINAL64	SPINAL64
Field/kHz	90	90	90

Table S5 (continued)

Experimental details of the ssNMR spectra acquired on ^{13}C, ^{15}N-β-endorphin fibrils obtained in 50 mM sodium phosphate, 2 mM sodium citrate buffer at pH 6.0

Experiment	DARR 20ms	DARR 80ms
Spectrometer	850 MHz	850 MHz
Measurement Time	22 h	22 h
Recycle delay/s	2.3	2.3
Number of Scans	16	16
Transfer 1	**HC-CP**	**HC-CP**
Time/ms	0.3	0.3
Field/kHz	80(H)/63(C)	80(H)/63(C)
Shape (*)	tangent(H)	tangent(H)
	D=32kHz	D=32kHz
Carrier/ppm	38	38
Transfer 2	**DARR**	**DARR**
Time/ms	20	80
Field/kHz	17(H)	17(H)
Shape (*)	-	-
Carrier/ppm	-	-
Transfer 3	-	-
Time/ms		
Field/kHz		
Shape (*)		
Carrier/ppm		
t1 Increments	2176	2176
Sweep width/kHz	80	80
carrier/ppm	38	38
acq. time/ms	13.6	13.6
td proc	4096	4096
window function	qsine 3.0	qsine 3.0
t2 Increments	3072	3072
Sweep width/kHz	100	100
carrier/ppm	94	94
acq. time/ms	15.4	15.4
td proc	8192	8192
window function	qsine 3.0	qsine 3.0
t3 Increments	-	-
Sweep width/kHz		
carrier/ppm		
acq. time/ms		
td proc		
window function		
Decoupling	SPINAL64	SPINAL64
Field/kHz	90	90

C. List of publications

Nadezhda Nespovitaya, Konstantin Barylyuk, Cédric Eichmann, Renato Zenobi, Roland Riek. The production of recombinant ^{15}N,^{13}C-labelled somatostatin 14 for NMR spectroscopy. *Protein Expr. Purif.* (2014), 99: 78-86.

Simon Weidmann, Konstantin Barylyuk, **Nadezhda Nespovitaya**, Stefanie Maedler, Renato Zenobi. A new, modular mass calibrant for high-mass MALDI-MS. *Anal. Chem.* (2013), 85 (6): 3425-3432.

Carolin Seuring, **Nadezhda Nespovitaya**, Jonas Rutishauser, Martin Spiess, Roland Riek. Hormone Amyloids in Sickness and in Health. In *Amyloid fibrils and prefibrillar aggregates: molecular and biological properties*. Daniel Otzen (ed.). Wiley-VCH, Weinheim. 2013: 395-410.

D. Conference contributions

Oral presentations

Nadezhda Nespovitaya, Roland Riek (2013). FEBS/EMBO lecture course and IUBMB advanced school "Protein interactions, assemblies and human disease", Island of Spetses, Greece, September 16-26. Title: Exploring the influence of environmental factors on the assembly/disassembly of the functional β-endorphin amyloid.

Poster presentations

Nadezhda Nespovitaya, Roland Riek (2013). FEBS/EMBO lecture course and IUBMB advanced school "Protein interactions, assemblies and human disease", Island of Spetses, Greece, September 16-26. Title: Exploring the influence of environmental factors on the assembly/disassembly of the functional β-endorphin amyloid.

Nadezhda Nespovitaya, Carolin Seuring, Julia Gath, Anja Böckmann, Beat Meier, and Roland Riek (2013). FASEB Science Research Conference "Molecular Mechanisms and Physiological Consequences of Protein Aggregation", Big Sky, Montana, USA, June 23-28. Title: The Mechanism of β-endorphin amyloid aggregation/disaggregation depends on the Glu8 protonation state?

Nadezhda Nespovitaya, Carolin Seuring, Julia Gath, Beat Meier, and Roland Riek (2012). "SCS Meeting", ETH Zurich, Zurich, Switzerland, September 13. Title: Structural studies of hormone functional amyloids by NMR-based quenched hydrogen/deuterium exchange.

Nadezhda Nespovitaya, Carolin Seuring, Julia Gath, Francesco Ravotti, Beat Meier, and Roland Riek (2012). "XXVth ICMRBS", Lyon, France, August 19-24. Title: DMSO quenched hydrogen/deuterium exchange in combination with solution state NMR provide an insight into the 3D structure of functional hormone amyloids.